

**ÉCOLE DOCTORALE DE PHYSIQUE ET CHIMIE PHYSIQUE**

**Institut de Chimie, UMR 7177**

**THÈSE** présentée par :

**Jordan APPLETON**

soutenue le : **02 Décembre 2022**

pour obtenir le grade de : **Docteur de l'Université de Strasbourg**

Discipline/ Spécialité : Chimie / Chimie-Physique

**Interactions électroniques et  
magnétiques dans des dimères de  
porphyrines et nouveaux complexes de  
cuivre(I) luminescents**

**THÈSE dirigée par :**

**Madame CHOUA Sylvie**  
**Monsieur RUPPERT Romain**

Professeur, Université de Strasbourg  
Chargé de recherche, Université de Strasbourg

**RAPPORTEURS :**

**Madame DUBOC Carole**  
**Monsieur ODOBEL Fabrice**

Directeur de recherche, Université Grenoble Alpes  
Directeur de recherche, Nantes Université

**AUTRES MEMBRES DU JURY :**

**Madame DESAGE-EL MURR Marine**  
**Monsieur WENGER Oliver**

Professeur, Université de Strasbourg  
Professeur, University of Basel

*For Dad, forever my inspiration*

## Acknowledgements

I would like to thank the members of the jury: Dr C. Duboc, Dr. F. Odobel, Pr. M. Desage-El Murr and Pr. O. Wenger for having accepted to be a part of my PhD jury.

My thanks first and foremost go out to my two PhD supervisors: Pr. Sylvie Choua and Dr. Romain Ruppert for having accepted me as a PhD student and helping me progress as a chemist and physical chemist throughout the three years of my PhD.

**Sylvie** Merci d'avoir transformer un chimiste en physico-chemiste. Je te remercie pour tous les conseils et soutien que tu m'as donnés sur la RPE. Je te remercie également d'avoir eu la confiance en moi de m'accepter en thèse.

**Romain** I remember when you picked me up from the airport when I was an Erasmus student with a little sign saying 'Jordan Appleton.' I thought to myself 'this man could be a good boss.' This proved to be the case! Thank you very much for teaching me how to carry out synthesis in a correct way and more importantly for showing me the great wine in France. You have always been present to help with any issues that I have had in the lab or just to discuss about the history of Chemistry. You have been more than just a boss to me for the past three years.

**Nolwenn** Comment puis-je te remercier ? Tu as toujours été présent pour m'aider avec des manips, des simulations et l'interprétation des deux. Tu as fait beaucoup plus que ce que tu étais censée de faire et je te remercie pour tout ce que tu as fait pour moi.

**Jean** Le grand chef avec des bonnes blagues de papa et le rire qui va avec ! Malgré ton emploi du temps hyper chargé tu as toujours le temps pour discuter avec moi. Je te remercie pour toutes les discussions et pour tout le soutien que tu m'as donné.

**Jennifer** I never thought that my English would improve when I moved to France but I will miss the "Jordan, I have an English question for you," even though the response was normally "I will check with my mum." Thank you for the discussions that we have had over the past three years about chemistry and also the nuances between the British and American way of life.

**Jean-Claude** Je te remercie pour l'aide que tu m'as apportée pendant ma thèse avec tes énormes connaissances de la chimie de phénanthroline et des porphyrines. Je te remercie également pour les

soirées qu'on a passées ensemble à regarder l'orchestre philharmonique ou l'opéra et pour les discussions sur la musique qu'on a eues ensemble. T'inquiète pas, je vais continuer à chanter après ma thèse. Bon courage pour le Mont Blanc.

**Christophe J.** Merci pour les conseils que tu m'as donnés pour l'enseignement et pour l'aide avec la chimie. J'ai bien rigolé avec tes histoires de bêtise des constructeurs. J'espère qu'ils mettront le mur au bon endroit bientôt.

**Bertrand** Merci pour l'aide que tu m'as donné avec le RPE et pour les discussions en général qu'on a eu ensemble.

**Christophe G.** Toujours présent pour m'aider. Merci de m'avoir expliquer comment faire le coding et comment faire des calculs DFT. Tes connaissances en complexes de cuivre phénanthroline sont très larges et je te remercie de les avoir partagées avec moi.

**Thannasis** Thank you for taking the time to explain the difficult concepts of pulsed EPR spectroscopy and for all your help with the interpretation of the data.

**Nicholas** Days spent underground in ISIS doesn't sound too appealing, yet you made the experience a lot more enjoyable. Thank you for taking the time to teach me how to use an STM machine and for all the help afterwards when analysing the images.

**Jean** On est arrivé ensemble et on va finir ensemble. Ça a été un plaisir. Tu as bien travaillé pendant ta thèse et je te félicite pour ce que tu as fait.

**Mathilde** Quand tu es arrivée au labo je me suis dit « elle a l'air d'être un peu folle elle », maintenant je le pense toujours et je sais que c'est un de tes meilleures qualités ! Ça a été un plaisir d'avoir été voisin de bureau avec toi. Bon courage pour le reste de ta thèse.

**Vincent** On a partagé deux années ensemble dans le labo et c'était un plaisir de partager ces années avec toi. On a eu des bonnes discussions sur la galère de la synthèse des porphyrines. Merci de m'avoir aidé au début de ma thèse.

**Laurie** Une nouvelle membre de l'équipe qui a déjà trouvé sa place. Bon courage pour tes trois années de thèse.

Je remercie les deux anciens thésards qui ont travaillé sur mon sujet, Mary-Ambre et Hervé, pour toute l'aide que vous m'avez donné sur les porphyrines et toutes les discussions qu'on a eues ensemble.

**Ryan** Mon « gros » frère, merci pour toutes les soirées qu'on a passées ensemble. Mon temps à Strasbourg n'aurait pas été le même si toi tu n'étais pas là ! Merci de m'avoir poussé et de m'avoir montré la beauté de la cuisine française.

**Merwan** Merci de m'avoir rassuré pendant la période de rédaction pendant nos pauses cannettes. Je te remercie également d'avoir été un très bon pote à moi pendant ma thèse. Merci khouya.

Je remercie également tous les membres de l'équipe de Faller qui m'ont invité plusieurs fois à leurs pots, je suis le thésard adopté de votre groupe même si vous faites de la bio. Merci Peter, Angélique, Vincent, Laurent, Maxime, Thibaut, Michael, Enrico, Katharina et Susheela pour votre accueil. Je remercie l'autre côté de notre étage, l'équipe de Heitz et l'équipe Cecchini. Toujours un plaisir de passer mes journées avec vous à nos côtés. Je remercie l'équipe de Pale pour toutes les bières qu'on a bues ensemble à la Kfet.

**Services communs RMN** Lionel, Bruno et Maurice toujours disponible pour m'aider avec mes spectres ou juste pour bavarder sur la vie en général. **RX** Corinne, Lydia et Nathalie merci pour les structures que tu as passées pour moi c'est toujours un plaisir de passer chez vous pour dire « J'ai peut-être des cristaux pour vous » **Masse** Merci Stéphanie et Hélène pour tous les spectres que vous avez passés pour moi. **AE** Merci à Noémi et Martine pour les analyses élémentaires.

Je remercie également tous mes bons amis à Strasbourg de m'avoir intégré dans vos groupes d'amis. Pour toutes les soirées à Strasbourg, en Martinique, en Suisse pour faire la luge et beaucoup plus de bons moments avec vous. Merci Jerem, Aurel, Myngoc, Hervé, Seb, Regis, Salen et Julien.

Thanks also to my friends from England for keeping in contact, despite the distance. Thanks for having supported me throughout the years. Thanks Callum, James, Ness, Liam, Dan, Kayleigh and Keir. We will have a pint of newcy brown after, don't worry!

My final and greatest thanks go to my family for always being there for me through rain or shine.

**Mum** Moving away from England wasn't the easiest of decisions, but I hope you can see that it was worth it. Thank you for supporting me through thick and thin. Our Saturday morning chats remain a highlight of my week. Thank you for everything that you have done throughout my life, for your unconditional love and above all, for shaping me into the man that I am today.

**Nana** Speaking on the internet isn't always the easiest of operations, but we always work it out and it is always a pleasure to have the catch up. Thank you for supporting me through all my major life events be it singing, piano or musical theatre.

**Gem** The kindest and most loving sister anyone could ask for. Will drop everything at a moment's notice to help. Thanks Gem, for always having my back and helping me through.

**Dad** This is what I promised you I would do and here I am. I hope you're looking down on me with pride. Thank you for all our conversations that we had that helped shape me into the man I am today. Your people skills were second to none and the qualities that you passed down to me have really helped me progress in life.

## Summary

List of abbreviations	10
General introduction	12
<b>Introduction 1 - An introduction to copper(I) phenanthroline complexes</b>	<b>13</b>
I1.1 1,10-phenanthroline	14
I1.1.2 Coordination Chemistry	15
I1.2 Applications	15
I1.3 Absorption and luminescence properties	19
I1.4.1 Substituent effects	22
I1.4.2 Copper(I) phenanthroline complexes with non-symmetric ligands	25
I1.5 Template effect to direct the topologies of the complexes	26
I1.6 Heteroleptic copper(I) complexes	28
I1.7 Copper(I)(phenanthroline)(phosphine)	30
I1.8 Conclusion and project plan	33
I1.9 References	34
<b>CHAPTER 1 - Heteroleptic copper(I) phenanthroline complexes: Synthesis and properties</b>	<b>39</b>
1.1 Introduction	40
1.2 Lithium Source	40
1.2.1 n-Butyl lithium	40
1.2.2 t-Butyl lithium	41
1.2.3 Lithium metal	44
1.3 Heteroleptic complexes	45
1.3.1 Structural properties	47
1.3.2 Electronic properties	54
1.3.3 Photoluminescence properties	58
1.4 Conclusion	64
1.5 References	66

<b>CHAPTER 2 - Homoleptic copper(I) phenanthroline complexes: Synthesis and properties</b>	<b>67</b>
2.1 Ligand synthesis	68
2.2.1 Homoleptic complexes	74
2.2.2 Structural property	75
2.2.3 Electronic properties	79
2.2.4 Photoluminescent properties	81
2.3 Photoluminescent Pt phenanthroline complexes	87
2.4 Conclusion	88
2.5 General conclusions	90
2.6 References	92

<b>INTRODUCTION 2 – Porphyrins -The properties of dimers, oligomers and more</b>	<b>93</b>
I2.1 Porphyrins	94
I2.1.1 Optical properties	95
I2.1.2 Electronic properties	95
I2.1.3 Magnetic properties	96
I2.2 Assembling porphyrins	98
I2.2.1 Changing the position of the linking unit	100
I2.2.2 Changing the linking unit	101
I2.2.3 Fused porphyrins	104
I2.2.4 Metal ion linked porphyrins	105
I2.3 To trimers, tetramers, oligomers and supramolecular assemblies	110
I2.3.1 Self-assembly of porphyrins at the solid-liquid interface	112
I2.4 Conclusions and project plan	114
I2.5 References	115

<b>Chapter 3 - Synthesis of porphyrin dimers and the study of their magnetic and electronic properties</b>	<b>119</b>
3.1 Introduction	120
3.2 Porphyrin synthesis	120
3.3 Electronic properties	126
3.3.1 Vanadyl porphyrins	126

3.3.2 Copper porphyrins	131
3.4 Magnetic properties	132
3.4.1 Vanadyl porphyrins	133
3.4.2 Copper porphyrins	140
3.5 Enaminothioketone Porphyrins	144
3.5.1 Synthesis	144
3.5.2 Electronic properties	145
3.5.3 Magnetic properties	147
3.6 Qubits for quantum computing	149
3.6.1 Hahn echo	150
3.6.2 Saturation recovery	151
3.6.3 Vanadyl monomer M4	152
3.6.4 2-Qubit systems	156
3.7 Conclusions and perspectives	159
3.8 References	161
<b>Chapter 4 - Self-assembly of porphyrin dimers at a solid-liquid interface</b>	<b>163</b>
4.1 Introduction	164
4.2 Porphyrin synthesis	165
4.3 Surface studies	166
4.3.1 Ni monomer	166
4.3.2 Ni dimer	169
4.3.2.1 2D surface chirality	170
4.3.3 Pd monomer	172
4.3.4 Pd dimer	174
4.3.4.1 Pd cis dimer	175
4.4 Towards porphyrin nano-ribbons	177
4.5 Conclusions and perspectives	181
4.6 General conclusions	183
4.7 References	185
<b>Résumé en français</b>	<b>186</b>
<b>Experimental part</b>	<b>199</b>
<b>List of molecules</b>	<b>269</b>

## List of abbreviations

<i>A</i>	hyperfine coupling
acac	acetylacetone
AFM	atomic force microscopy
Ar	aryl
BODIPY	boron-dipyrromethene
B3LYP	Becke, 3-parameter, Lee-Yang-Parr
([Cu(ditBuphen) <sub>2</sub> ] <sup>+</sup> )	[copper(I)(2,9-ditert-butylphenanthroline) <sub>2</sub> ] <sup>+</sup>
CV	cyclic voltammetry
CW	continuous wave
<i>D</i>	dipolar interaction
DDQ	2,3-dichloro-5,6-dicyano-1,4-benzoquinone
DFT	density functional theory
DPPZ	dipyridophenazine
DSSCs	dye-sensitised solar cells
EDFS	echo detected field sweep
ENDOR	electron-nuclear double resonance
EPR	electron paramagnetic resonance
ESEEM	electron spin echo envelope modulation
ESI	electrospray ionisation
<i>et al.</i>	<i>et alli</i>
eq.	equation
$\varepsilon$	molar extinction coefficient
Fc	ferrocene
<i>g</i>	<i>g</i> factor
$g_{\perp}$	perpendicular <i>g</i> factor
$g_{\parallel}$	parallel <i>g</i> factor
HETPHEN	heteroleptic phenanthroline
HOMO	highest occupied molecular orbital
HOPG	highly ordered pyrolytic graphite
HSAB	hard-soft acid base principle
<i>I</i>	nuclear spin
<i>J</i>	isotropic exchange coupling
$\lambda_{\max}$	maximum absorption
LC	ligand-centred

LMCT	ligand-metal charge transfer
LLCT	ligand-ligand charge transfer
LUMO	lowest unoccupied molecular orbital
M	mol/L
MALDI	matrix-assisted laser desorption/ionization
MATLAB	matrix laboratory
MC	metal-centred
mnt	1,2-dicyanoethylene-1,2-dithiolate
MOFs	metal-organic frameworks
NCI	non-covalent interaction
NCP	N-confused porphyrins
NIR	near infrared
NMR	nuclear magnetic resonance
POP	2-(diphenylphosphino)phenyl
MLCT	metal-ligand charge transfer
NMP	N-methyl-2-pyrrolidone
ppm	parts per million
QC	quantum computing
qubit	quantum bit
rt	room temperature
<i>S</i>	electronic spin
SOMO	singly occupied molecular orbital
SQUID	superconducting quantum interference device
STM	scanning tunnelling microscopy
TADF	thermally activated delayed fluorescence
tBu	<i>tert</i> -butyl
TheoDORE	Theoretical Density, Orbital Relaxation and Exciton
TFA	trifluoroacetic acid
TLC	thin layer chromatography
$T_m$	phase-memory time
$T_2$	spin-spin relaxation time
$T_1$	spin-spin relaxation time
UV	ultraviolet
VO	vanadyl

# General Introduction

This thesis focuses on two topics: the first of which being the study of new luminescent copper(I) complexes and the second being the study of magnetic and electronic interactions between porphyrin dimers. These two projects have been carried out thanks to many successful collaborations between four groups at the University of Strasbourg.

The first topic details the synthesis of heteroleptic (Chapter 1) and homoleptic (Chapter 2) copper(I) phenanthroline complexes and the study of the ground state electronic properties and their excited state properties. Properties observed experimentally were explained by a combined experimental-computational study, in order to try and gain a further understanding of the excited state properties of such complexes. I would like to take to thank, at this point, Christophe Gourlaouen for teaching me coding and how to carry out such DFT calculations.

The second topic describes the synthesis of porphyrin monomers and the assembly of porphyrin dimers with a linking metal ion. Once synthesised, the electronic and magnetic properties of these porphyrin monomers and dimers were analysed by absorption spectroscopy, cyclic voltammetry and electron paramagnetic resonance (EPR) spectroscopy (Chapter 3). I would like to thank Nolwenn Le Breton for her “EPR driving licence” and her further help that allowed me to carry out the EPR measurements and simulations. Similar porphyrin monomer and dimers were self-assembled at a solid-liquid interface and the assemblies were imaged using Scanning Tunnelling Microscopy (STM) (Chapter 4). I would like to thank Nicolas Turreta from the lab of Paolo Samori (ISIS, University of Strasbourg) for having taught me how to use the STM machine.

# Introduction 1

## An introduction to copper(I) phenanthroline complexes

I1.1 1,10-phenanthroline	14
I1.1.2 Coordination Chemistry	15
I1.2 Applications	15
I1.3 Absorption and luminescence properties	19
I1.4.1 Substituent effects	22
I1.4.2 Copper(I) phenanthroline complexes with non-symmetric ligands	25
I1.5 Template effect to direct the topologies of the complexes	26
I1.6 Heteroleptic copper(I) complexes	28
I1.7 Copper(I)(phenanthroline)(phosphine)	30
I1.8 Conclusion and project plan	33
I1.9 References	34

## I1.1 1,10-phenanthroline

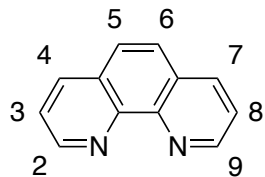


Figure 1: 1,10-phenanthroline and the nomenclature for numbering the positions

Phenanthroline and other  $\alpha$ -diimines are well established chelating agents. Their first use was in analytical chemistry with phenanthroline and 2,9-dimethylphenanthroline being used to detect iron and copper salts present in solutions by colorimetric methods. This led to their respective trivial names of ferroine and cuproine. In the literature, there are a wide variety of applications for such ligands and the applications are still heavily reliant on coordination chemistry. The main application that will be discussed in this introduction will be in solar energy conversion, an issue that has become more and more prominent in recent years.<sup>1</sup>

One of the main reasons why phenanthroline chemistry became more present in the literature was thanks to the pioneering work of Sauvage and Dietrich-Buchecker<sup>2</sup> who majorly simplified the substitution of phenanthroline at the 2 and 9 positions with aryl or alkyl groups by a simple nucleophilic addition with an aryl or alkyl lithium reagent, followed by aromatisation with an oxidant (see Figure 2).

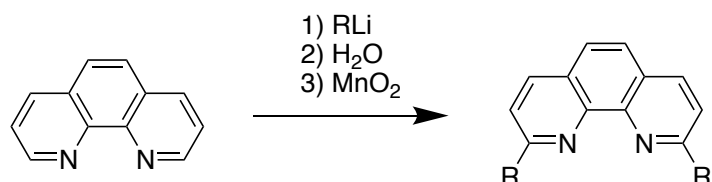


Figure 2: Substitution pattern for 1,10-phenanthroline developed by Sauvage and co-workers

This synthetic process avoided long and tedious reactions such as the Skraup<sup>3</sup> reaction, where the tarry mixture formed led to more challenging work-up procedures. The facile functionalisation designed by Dietrich-Buchecker avoided such issues, as functional groups could be relatively easily added and this meant that the properties of such complexes could be more easily tuned. With the discovery of this synthetic pathway and the wide variety of metal ions that can coordinate to phenanthroline, synthetic chemists quickly grasped the opportunity to research deeper into this field.

## I1.1.2 Coordination Chemistry

These ligands were then used to complex a multitude of metal ions such as Cu(I),<sup>4</sup> Ru(II), Zn(II),<sup>5</sup> Ir(III),<sup>6</sup> Au(I),<sup>7</sup> Ag(I)<sup>8</sup> and Li(I).<sup>9</sup> The coordination geometry would be either tetrahedral, square planar or octahedral depending on the metal ion employed.<sup>10</sup> Such a vast range of metals can be coordinated, as  $\alpha$ -diimines are able to stabilise metal centres in both high and low oxidation states by either donating or accepting electron density. Low oxidation states are stabilised, as a radical-anion can be formed in the  $\pi^*$  orbital of the ligand *via* a metal-ligand charge transfer (MLCT). It is this MLCT that gives the complexes their colour and their extensive properties, as the electron present in the  $\pi^*$  orbital of the photoexcited complex is a powerful reductant. A hole is also formed at the metal centre and consequently the excited complex presents oxidising character.

## I1.2 Applications

Such complexes can be envisaged for a multitude of applications, for example: renewable fuel sources such as CO<sub>2</sub> reduction,<sup>11</sup> in catalysis for the water gas shift reaction when the phenanthroline is used as a ligand for Rh or Ir,<sup>12</sup> the charge transfer properties of copper(I) phenanthroline complexes have been used for photoredox-catalysis.<sup>13</sup> Platinum complexes are also of upmost interest as they have phosphorescent properties at room temperature that can be easily tuned by changing the ligand. Such properties are enhanced on the formation of NNC complexes,<sup>14</sup> where the platinum is coordinated to two nitrogen atoms and a carbon atom, leading to a very intense emission at room temperature. These enhanced properties are on account of a decrease in non-radiative decay, due to optimisation of the geometry, and also the Pt-carbon bond granting the ligand a greater  $\pi$ -donating ability. These complexes have hence been optimised by modifying the ligands for potential applications in organic light emitting devices.<sup>15</sup>

By far the most extensively studied  $\alpha$ -diimine complex is [Ru(bipyridine)<sub>3</sub>]<sup>2+</sup>,<sup>16</sup> as despite its simplicity, the complex presents impressive properties in both the ground state (light absorption in the visible region and electrochemically reversible oxidation and reduction) and the excited state (intense luminescence and long lived excited state lifetimes). These types of complexes were quickly sought after by photochemists for applications in light to energy conversion. Work was initially carried out by Honda as early as 1972,<sup>17</sup> research on increasing the efficiency of the so-called dye-sensitised solar cells (DSSCs) was then furthered in the 1990s by Grätzel<sup>18</sup> and Scandola<sup>19</sup> who used

Ru polypyridine complexes that achieved power conversion efficiencies higher than 10%.<sup>20</sup> Sauvage<sup>21</sup> switched metals to Cu(I) but kept the  $\alpha$ -diimine ligands.

A schematic representation of an n-Type DSSCs<sup>22</sup> is shown in Figure 3. Taking a ruthenium(II) complex as an example, the process can be described in four steps: (i) the photosensitiser is excited using natural light; (ii) the excited complex ( $\text{Ru}^{\text{II}*}$ ) is then able to inject an electron into the conduction band of  $\text{TiO}_2$  nanoparticles *via* a charge transfer process; (iii) the photosensitiser is hence oxidised ( $\text{Ru}^{\text{III}}$ ), and the neutral complex ( $\text{Ru}^{\text{II}}$ ) is obtained by a reducing agent that is also present in the electrolyte which is often iodide ions ( $\text{I}^-$ ) and the iodide is reformed from  $\text{I}_3^-$  at the Pt counter electrode (iv).

On injection of the electrons into the conduction band, photoenergy conversion processes then occur in order to transform the light absorbed into electrical current. The efficiencies of the above processes are hence of fundamental importance in order to achieve an efficient solar cell. The obvious factor not listed above is the ability of the photosensitiser to absorb visible light and this is a factor that can easily be tuned by synthetic chemists by modifying the ligands and their substituents.

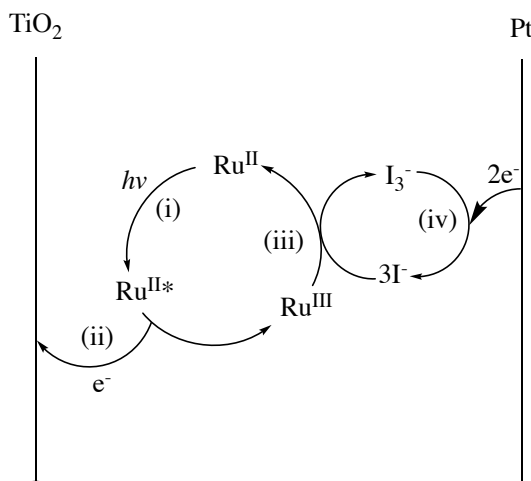


Figure 3: Schematic representation of an n-type DSSCs

The complex in Figure 4 was used for DSSCs,<sup>23</sup> with the carboxylic acids of one of the bipyridines being used as an anchoring group onto the surface of  $\text{TiO}_2$ . The thiocyanate groups support the electron donation into the  $\text{TiO}_2$  conduction band and help delay counterproductive back electron transfer. The complex however has poor photophysical properties in solution, with a luminescence quantum yield of 0.4% (at 125K) and a lifetime of 50 ns (at 298K), these properties can hence be optimised.<sup>24</sup> The remainder of this introduction will focus on the optimisation of the excited state properties of transition metal complexes.

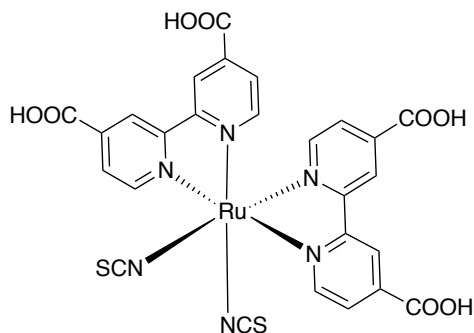


Figure 4: Schematic representation of ruthenium(II) complex N3

The major drawback of N3 (Figure 4) and other ruthenium sensitizers, is the cost and availability of ruthenium, consequently a less scarce metal has been sought after for use as a photosensitizer. Perovskites<sup>25</sup> have proven to be efficient photosensitizers with perovskite/silicon tandem solar cells reaching efficiencies as high as 25.2%. A perovskite is any material with the same crystal structure as the mineral calcium titanium oxide, which was the first perovskite to be discovered. They have proven to be highly efficient, surpassing ruthenium complexes, and using perovskite/silicon tandem solar cells conversion efficiencies as high as 25.2%<sup>26</sup> have been achieved which is almost as efficient as standard silicon based solar cells. These versatile molecules have also been used for water photolysis.<sup>27</sup> Grätzel<sup>28</sup> pointed out that the drawbacks to perovskites were their stability and toxicity. Quantum dots<sup>29</sup> are also a potential alternative, like with perovskites, the metal lead has appeared to present more optimal properties.

First row transition metals appeared as a viable alternative,<sup>30</sup> however their efficiencies for photoconversion were considerably less than that of ruthenium(II) complexes. However, considerable research is still ongoing in this field as they are less-expensive, more abundant, easier to synthesise and handle than alternative photosensitizers. The discovery of the excited state properties of  $[\text{Cu(I)}(2,9\text{-dimethylphenanthroline})_2]^{+}$ <sup>31</sup> and  $[\text{Cu(I)}(2,9\text{-diphenylphenanthroline})_2]^{+}$ <sup>32</sup> complexes led to this inexpensive and abundant metal appearing as a viable option. Copper was advantageous as it lacked d-d transitions that quickly quenched the triplet state by thermal equilibration or energy transfer. This was a fundamental flaw of iron(II) complexes, where no intersystem crossing to a triplet state was able to occur, consequently decreasing the lifetime substantially.<sup>33</sup> Copper presented the same type of properties as ruthenium, with absorption in the visible region granted by an MLCT between the metal centre and the ligand and reversible redox states from Cu(I) to Cu(II). With steric hindrance at the 2,9-positions of the phenanthroline, the complex became luminescent and thanks to Dietrich-Buchecker's work (Figure 2), these properties could be easily tuned. These points quickly led to copper(I) complexes being used in DSSCs.<sup>34</sup>

Copper(I) phenanthroline complexes have a tetrahedral structure in the ground state. How perfectly tetrahedral the complex is, very much depends on the substituents, with alkyl groups leading to more tetrahedral complexes and aryl groups leading to distorted complexes. This distortion is on account of  $\pi$ - $\pi$  interactions between the phenanthroline and one of the aryl groups at the 2 or 9 position of the other phenanthroline; such interactions do however stabilise the complex. Consequently, there are two potential motifs for phenanthroline complexes, these have been coined as either the centred motif, meaning the copper(I) phenanthroline is near-perfectly tetrahedral, or the pac-man motif where the  $\pi$ - $\pi$  interaction described above leads to a non-perfectly tetrahedral complex. These two motifs are shown below in Figure 5.

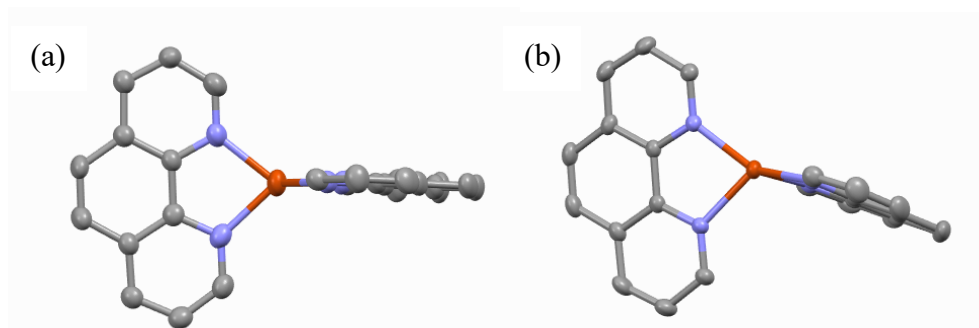


Figure 5: The two potential motifs for copper(I) phenanthroline complexes. (a) Centred motif; (b) pac-man motif. Phenanthroline substituents omitted for clarity

The electron injection using copper(I) phenanthroline complexes to the  $\text{TiO}_2$  proved to be efficient and could be monitored by electron paramagnetic resonance (EPR). This was carried out successfully by Lin Chen and co-workers<sup>35</sup> using copper(I) phenanthroline complexes with sulfonate groups to coordinate to the  $\text{TiO}_2$ . The intensity of the black line in Figure 6 clearly shows an efficient charge transfer that then decreases on switching off the visible light (grey line).

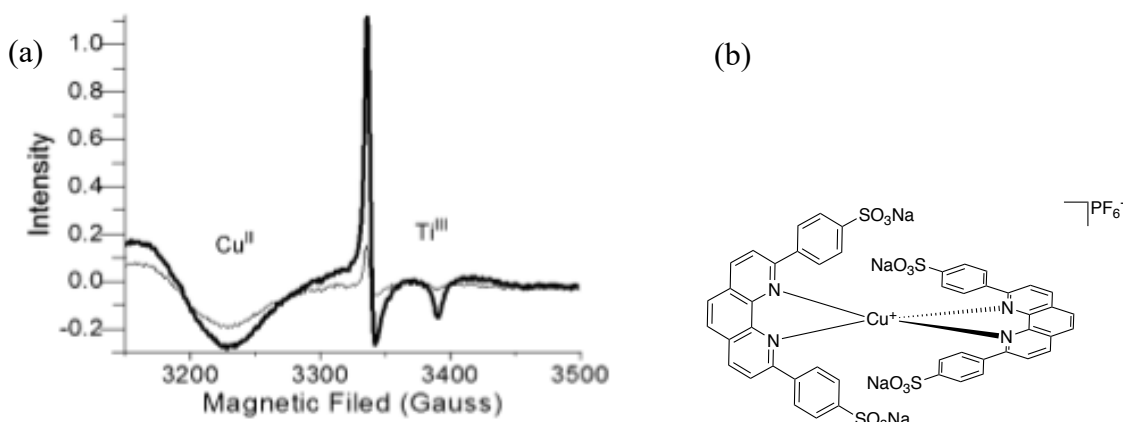


Figure 6: (a) EPR spectra of copper(I) complex (b) adsorbed onto  $\text{TiO}_2$  nanoparticles. Black line of the EPR spectra when light turned on (440 nm) and the grey line when light was turned off

There are other potential sensitizers for DSSCs. A more recent area of development is using organic sensitizers for p-type DSSCs,<sup>36</sup> these can then be combined with n-type DSSCs and increase the efficiency of the process. Organic dyes have also been combined with BODIPYs by Gibson and co-workers,<sup>37</sup> to make NiO solar cells instead of TiO<sub>2</sub>.

### 11.3 Absorption and luminescence properties

Copper(I) phenanthroline complexes show two major absorption bands: one of which is in the UV region of the spectra and is a ligand based ( $\pi$ - $\pi^*$ ) transition that occurs at around 300 nm and the second is in the visible region of the spectrum at around 460 nm. This is the interesting part of the spectrum in terms of potential applications, with the absorption at 460 nm being an MLCT between the metal centre and the  $\pi^*$  orbital of the phenanthroline ligand. The MLCT is low lying in energy due to the facile oxidation of the copper(I) and the good electron accepting properties of the  $\pi^*$  orbital of the phenanthroline. The broadness of this absorption is highly dependent on the substituents present on the phenanthroline. For applications in photochemistry, a broad absorption would be the most optimal as there would be a greater efficiency of light absorption for the solar cell.

Knowledge of the luminescent properties of copper(I) phenanthroline complexes dates back to 1980 when McMillin and Blaskie<sup>38</sup> discovered that  $[\text{Cu}(2,9\text{-dimethylphenanthroline})_2]^+$  was luminescent on excitation of the MLCT band at around 460 nm. The excited state properties have been extensively studied, notably in transient absorption spectroscopy by Lin Chen.<sup>39</sup> The decay pathway from the excited to ground state is composed of three stages. Firstly, the formation of a <sup>1</sup>MLCT excited state which involves the transfer of a 3d electron from the copper(I) to the  $\pi^*$  orbital of one of the phenanthrolines. This process leads to the oxidation of the copper(I) to copper(II) and consequently a Jahn-Teller flattening distortion as the system passes from d<sup>10</sup> to d<sup>9</sup>. This leads to a change in geometry around the metal centre from the tetrahedral Franck-Condon structure to the more favourable square-planar geometry. An intersystem crossing (ISC) then occurs from the <sup>1</sup>MLCT to the <sup>3</sup>MLCT excited state and finally the triplet state relaxes down to the ground state *via* phosphorescence.

The relaxation down to the ground state can occur in one of two ways, either *via* fluorescence or phosphorescence, the difference being the excited state either has the same or a different spin than the ground state, respectively. This final step is largely affected by steric hindrance at the 2 and 9 positions with the lifetime for this step increasing from 20 ps for a non-substituted copper(I) phenanthroline complex, to 2  $\mu$ s for a complex with considerable steric bulk, for example with *tert*-

butyl groups at the 2 and 9 positions.<sup>40</sup> Hence, the limiting factor for quantum efficiency of the electron transfer for potential applications is the competition with, potentially, rapid non-radiative decay processes. The decay pathway is summarised in terms of a Jablonski diagram (Figure 7) with  $[\text{Cu(I)(2,9-dimethylphenanthroline)}_2]^+$  as an example complex.

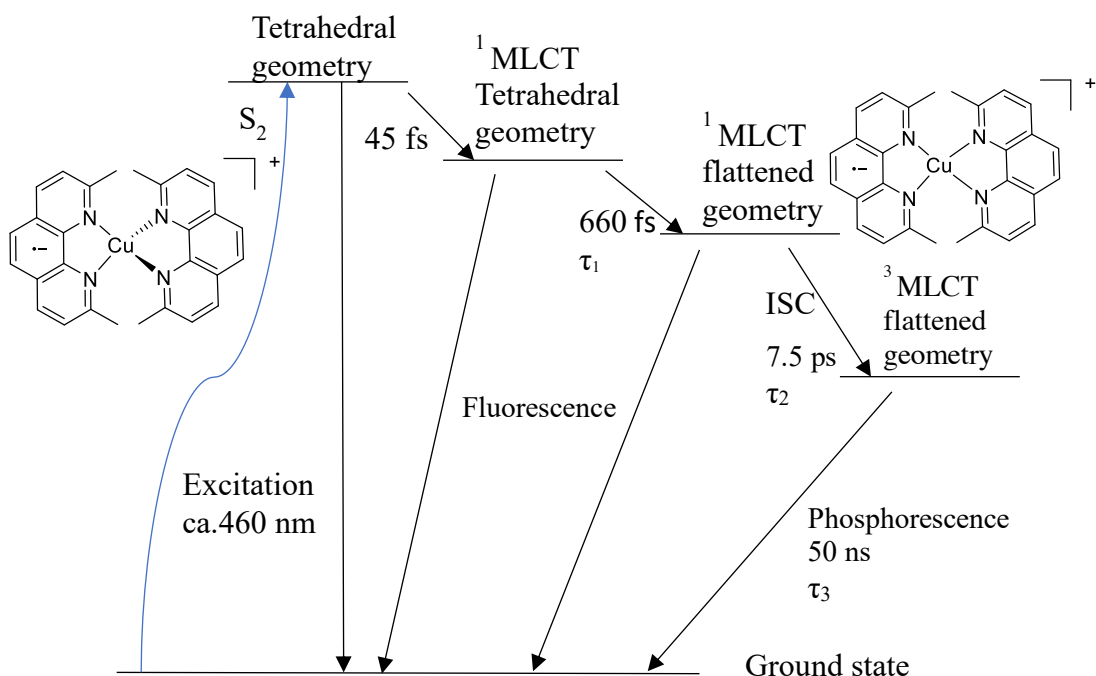


Figure 7: Jablonski diagram showing the decay pathway for  $[\text{Cu(I)(2,9-dimethylphenanthroline)}_2]^+$

Longer lifetimes are recorded at lower temperatures, hinting at the fact that the quenching is diffusional. This can be seen as  $[\text{Cu(I)(2,9-dimethylphenanthroline)}_2]^+$  is still emissive in an ethanol/methanol (4:1) solution at 100 K.<sup>41</sup> The entire process is also highly solvent dependent, with coordinating solvents leading to a considerably lower lifetime on account of the solvent molecule being able to coordinate to the flattened copper(II) complex. This leads to a stabilised excited state complex (an exciplex) that relaxes more easily to the ground state *via* a fluorescent pathway. This is apparent by Figure 8 with a smaller  $\Delta E$  for the exciplex compared to the excited state complex leading to more facile quenching from this energy minima.

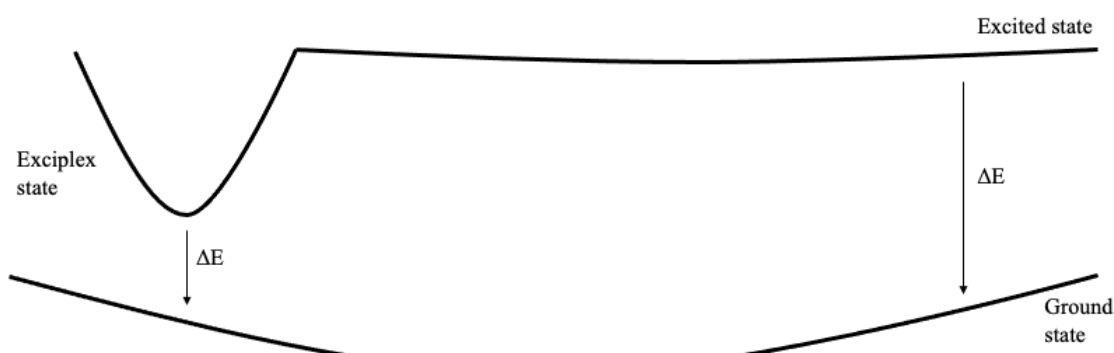


Figure 8: Potential energies of the ground state, excited state and the exciplex state.

The goal is to limit solvent interactions, as this lessens the likelihood of the formation of an exciplex ( $M^*$  and a quencher). Formation of an exciplex (Figure 9) decreases the lifetime because the charge stabilisation granted by the electronegative solvent with the metal centre leads to a lower energy excited state and consequently a smaller energy gap, leading to more favourable non-radiative processes.<sup>41</sup>

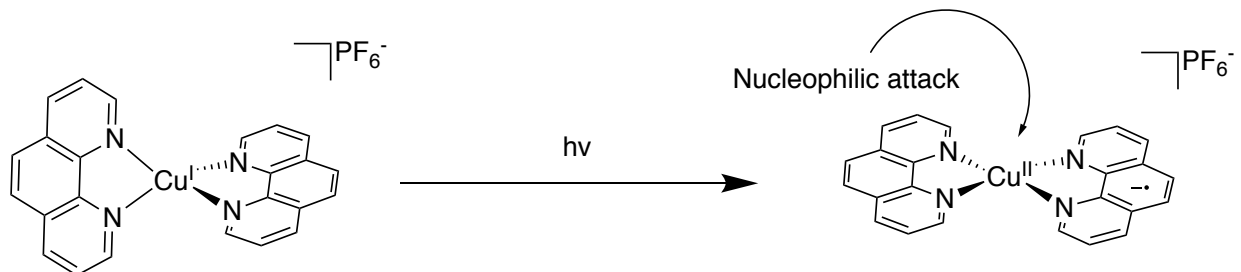


Figure 9: Formation of the exciplex complex

This can be prevented by using non-coordinating solvents and by increasing the steric hindrance at the coordination site. An example of this is the fact that  $[\text{Cu(I)}(2,9\text{-dimethylphenanthroline})_2]^+$ 's luminescence is quenched in methanol however the luminescence of  $[\text{Cu(I)}(2,9\text{-diphenylphenanthroline})_2]^+$  remains in this coordinating solvent, on account of the increased steric bulk. In addition to more optimal excited state properties, the ground state properties are also improved on addition of the phenyl groups as there is a red shift in the absorption and the absorption spectrum itself is much broader.<sup>42</sup> This leads to light absorption over a larger range of the visible region and consequently an optimised light sensitisier.

Another difference between these two complexes is that  $[\text{Cu(I)}(2,9\text{-dimethylphenanthroline})_2]^+$  adopts a  $D_{2d}$  symmetry, whereas because of the  $\pi\text{-}\pi$  stacking between the phenyl and the phenanthroline,  $[\text{Cu(I)}(2,9\text{-phenylphenanthroline})_2]^+$  adopts a  $D_2$  symmetry. This means that there is a greater coupling between the ground state and the lowest energy  $^1\text{MLCT}$  state for copper(I)(2,9-phenylphenanthroline)<sub>2</sub> compared to  $[\text{Cu(I)}(2,9\text{-dimethylphenanthroline})_2]^+$ .<sup>43</sup> Looking specifically at the excited state properties of such complexes, by changing the substituents at the 2,9-positions of the phenanthroline from phenyl groups<sup>44</sup> to *tert*-butyl groups<sup>40</sup> an increase in the lifetime from 250 ns to 3260 ns is observed. Consequently, a major push was made in the literature to see the effects of different substituents on the phenanthroline. McMillin *et al*<sup>45</sup> and Karpishin *et al*<sup>46</sup> carried out most of this pioneering work in an attempt to optimise both the ground and the excited state. When considering aryl substituents, distortion from the tetrahedral geometry is a battle between steric repulsion and  $\pi\text{-}\pi$  interactions. Lack of steric repulsion will lead to  $\pi\text{-}\pi$  interactions being more favourable, however it will also lead to a shorter lifetime as the exciplex is easily quenched as the

coordination site is less well protected and also because there is a greater coupling between the excited and the ground state on distortion, as mentioned above. The more prolonged the excited state is, ( $>10$  ns) the greater the probability of energy transfer and increasing the lifetime as much as possible is hence the desired goal.

### 11.4.1 Substituent effects

It was found that it was not only the 2,9-positions that affected the lifetime but also the 4,7-positions. For  $[\text{Ru(II)}(\text{phenanthroline})_3]^{2+}$ , the lifetime could be doubled by substituting methyl groups at the 4 and 7 positions and it could become five times larger by substituting phenyl groups at these positions.<sup>47</sup> Interestingly, adding groups to the 2,9-positions decreased the lifetime of the complex due to an increase in interligand steric repulsion. McMillin reported<sup>32</sup> that like Ru complexes, the lifetimes of copper complexes were also largely affected by the substituents, however the trend was not the same. The issue of steric repulsion observed for ruthenium complexes is not an issue for copper due to the lack of a third phenanthroline and it is this additional steric hindrance at the 2 and 9 positions that grants these complexes their luminescent properties (*vide supra*). Substitution at the 4 and 7 positions has a more limited effect on the lifetime of copper(I) phenanthroline complexes. Knowledge of the energy gap law can be advantageous as substituents can affect the energy of the excited state and by increasing energy gap, the lifetime should increase due to decreased non-radiative decay.<sup>45</sup> Favouring the intersystem crossing process will also lead to a favoured thermally activated delayed fluorescence.<sup>48</sup>

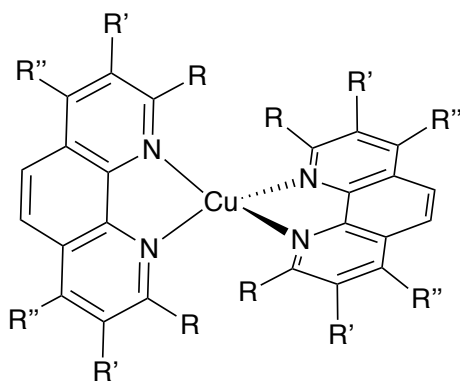


Figure 10:  $\text{Cu(I)}$  phenanthroline complex with varying  $R$  groups shown in Table 1

The effect of different substituents at the 2,9 (R), 3,8 (R'), and 4,7 (R'') positions (Figure 10) on the excited state lifetime of copper phenanthroline complexes in  $\text{CH}_2\text{Cl}_2$  is shown in Table 1.

Table 1: Effect of R groups on the lifetime of copper(I) phenanthroline complexes. R, R' and R'' defined in Figure 10.

Substituent	Lifetimes (ns)
R = n-butyl, R' = H, R'' = Me <sup>45</sup>	145
R = Ph, R' = H, R'' = Ph <sup>44</sup>	230
R = paramethylbenzene, R' = H, R'' = H <sup>49</sup>	237
R = Ph, R' = H, R'' = H <sup>44</sup>	270
R = Ph, R' = H, R'' = Me <sup>45</sup>	310
R = Ph, R' = Me, R'' = Me <sup>45</sup>	480
R = n-butyl, R' = Me, R'' = Me <sup>45</sup>	920
R = isopropyl, R' = Me, R'' = Me <sup>50</sup>	2300
R = sec-butyl, R' = Me, R'' = Me <sup>51</sup>	2800
R = <i>tert</i> -butyl, R' = H, R'' = H <sup>40</sup>	3260

Clearly the substituents have a large effect on the lifetime. The amount of hindrance present at the 2 and 9 positions has large effects on the stability of the complexes and if too large, the homoleptic complex will not form. For example with *tert*-butyl<sup>40</sup> as the R group, these complexes have limited stability. Yet their lifetimes are clearly optimal due to their perfectly tetrahedral geometry and maximum protection of the coordination site from solvent attack. The crystal structure in Figure 11 demonstrates how perfect the geometry is.

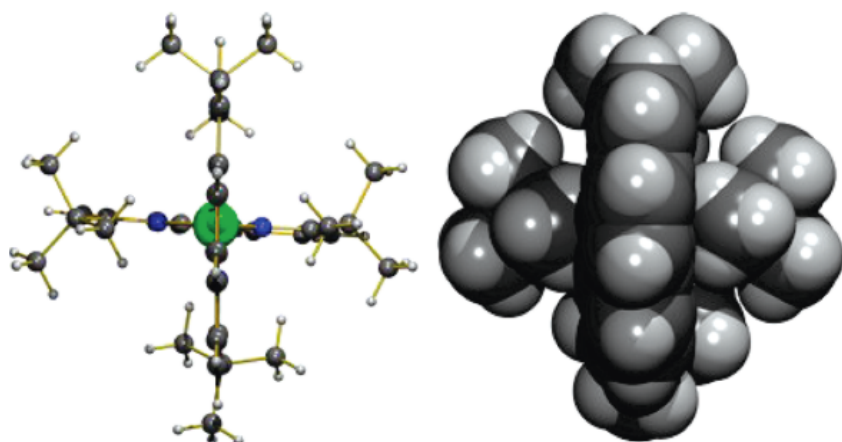


Figure 11: Crystal structure of  $[\text{Cu}(\text{I})(2,9\text{-ditert-butylphenanthroline})_2]^+$

Lack of stability was however still a major issue for this complex. This led Castellano and co-workers to decrease the steric hindrance at the 2,9-positions and add steric hindrance at the 7,8-positions.<sup>51</sup> This led to what Castellano defined as a cooperative steric effect with the methyl groups at the 3,4,7,8-positions forcing the *sec*-butyl groups to hinder the coordination site even more efficiently, which

increased the lifetime considerably compared to the same complexes without the methyl groups. DFT calculations showed that this complex also had minimal distortion in the excited state, demonstrating the rigidity of the system and hinting at explanations for such unprecedented excited state lifetimes (Figure 12). These two groups complement each other and lead to a highly sterically hindered copper(I) complex with optimal properties and good stability.

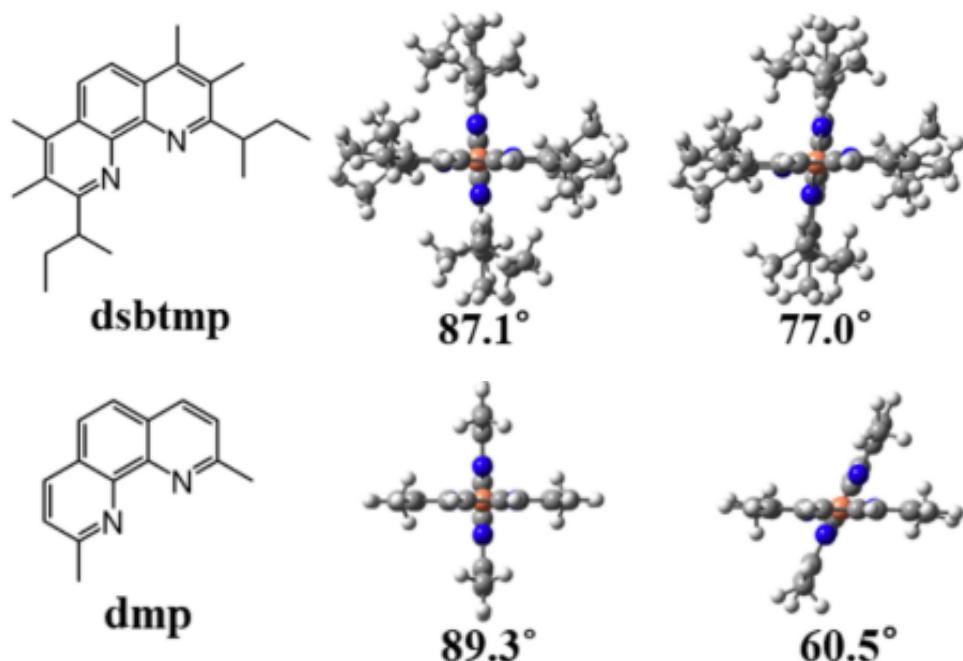


Figure 12: Ligands used for complexation (left), calculated ground state (middle) and excited state (right) geometries for two copper(I) phenanthroline complexes, showing the deformation from ground to excited state<sup>52</sup>

Comparison of the excited state properties with a complex without the methyl groups at the 3,8-positions proved that these substituents were leading to an increased steric contribution from the *sec*-butyl groups.<sup>53</sup> Similar positive effects were also seen for isopropyl groups at the 2,9-positions<sup>50</sup> and the steric hindrance was also increased to as much as a cyclohexane group at the 2,9-positions<sup>52</sup> leading to a lifetime of 2.6  $\mu$ s in dichloromethane. This shows the major impact of the 3,8-methyl substituents, as without the 3,8-methyl substituents, alkyl groups perform worse than aryl groups.

Addition of 3,8-methyl substituents, also leads to a positive effect for aryl substituents at the 2,9-positions, as demonstrated by the increased lifetime on addition of methyl groups in the sixth example of Table 1. Looking at the effect of groups at the 4,7-positions (R''), taking the second and fifth example of Table 1, it would appear that methyl groups have a positive effect on the lifetime and phenyl groups a negative one, whether this is due to an increased amount of rotamers or due to electron withdrawing effects is unsure; the effect of substituents at the 4,7-positions remains less

compared to the 3,8. However, the fact that there is still a difference in the lifetime on changing the 4,7-positions shows that the cooperative steric effect, mentioned previously, is not the effect at play.

As well as adjusting the steric hindrance, the electronic properties can also be adjusted to favour long excited state lifetimes. The homoleptic complex with an anthracene moiety at the 2-position of the phenanthroline and a methyl at the 9-position leads to a lifetime of  $1.2\text{ }\mu\text{s}$ .<sup>54</sup> The reason for this major increase in lifetime is because the anthracene is acting as an energy reservoir. This means that the lifetime of the triplet state of the anthracene moiety,  ${}^3(\pi-\pi^*)$ , is very long. This state and the singlet and triplet MLCT states are able to interact efficiently due to their close proximity in energy. Having stored the energy, an efficient transfer to the emissive metal centre can then occur.

The counter ion of the complex is also of paramount importance for optimal excited state properties. As stated above the most efficient way to quench the excited state is by forming an exciplex with a solvent molecule. The exciplex formation can be mediated by the counterion; this phenomenon occurs at concentrations higher than  $30\text{ }\mu\text{M}$ . Looking at the excited state properties of  $[\text{Cu(I)}(2,9\text{-dimethylphenanthroline})_2]^+$ , changing the counter ion from  $\text{ClO}_4^-$  to  $\text{PF}_6^-$  led to an increase in the lifetime from  $38\text{ ns}$  to  $78\text{ ns}$ , respectively.<sup>55</sup>

#### 11.4.2 Copper(I) phenanthroline complexes with non-symmetric ligands

Non-symmetric ligands were synthesised in an attempt to increase the steric hindrance around the metal site, yet still render the homoleptic complex accessible. The idea was to make complexes with long-excited state lifetimes and high quantum yields, without sacrificing the stability of the complex, looking notably at the group of Pellegrin, where ligand with both alkyl and aryl groups have been synthesised (Figure 13).

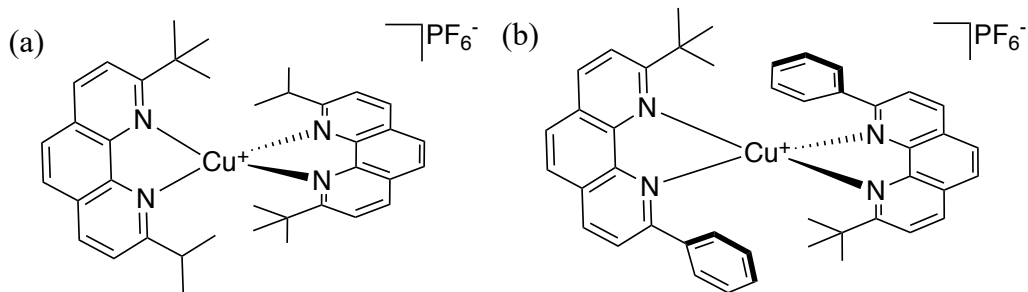


Figure 13: Two copper(I) complexes recently reported by Pellegrin that have non-symmetric phenanthroline ligands

The two above examples are adapted from well-known examples in the literature. Burstyn's copper(I) complex with *tert*-butyl groups at the 2,9-positions<sup>40</sup> possesses highly sought after properties with a lifetime of 3260 ns, however the complex's fundamental flaw is its stability. In order to remove this problem, Pellegrin replaced one of the *tert*-butyl groups with either an isopropyl group<sup>56</sup> or a phenyl group.<sup>57</sup> This was an attempt to find a perfect balance between photophysical properties and stability, with less steric hindrance in the alkyl complex (Figure 13a) and  $\pi$ - $\pi$  interactions between the phenanthroline and the adjacent phenyl group for the complex (Figure 13b) granting increased stability. This hypothesis proved correct and stable complexes were formed with near-perfect tetrahedral geometries. However, protection of the metal is not the only contributing factor to a long-lasting excited state, the issue being that the rate constant for non-radiative processes increases with two different substituents at the 2,9-positions of the phenanthroline, leading to lower emission and shorter lifetimes; this is a recurring theme in the literature.<sup>58</sup>

## I1.5 Template effect to direct the topologies of the complexes

It would be impossible to discuss copper(I) phenanthroline complexes without mentioning its use as a templating agent, developed by Sauvage and co-workers.<sup>59</sup>

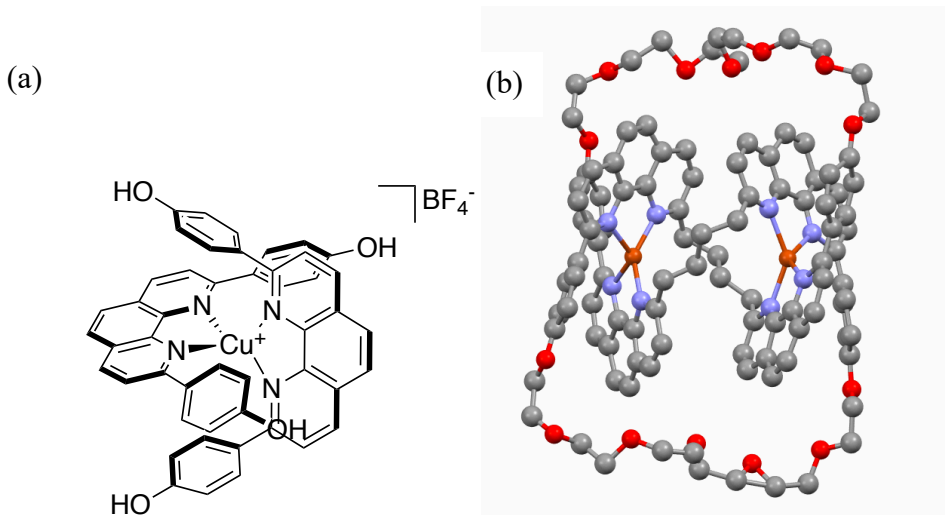


Figure 14: Copper(I) phenanthroline complex used to synthesise catenanes (a) and the crystal structure of Sauvage's trefoil knot (b)

The coordination geometry around the metal centre led to the phenol groups of the [Cu(I)(2,9-diphenolphenanthroline)]<sup>+</sup> being in four well-defined directions (Figure 14a). This observation allowed Sauvage's group to prepare catenanes,<sup>60</sup> rotaxanes<sup>61</sup> and other topologically complex architectures.<sup>62</sup> On cyclisation of the phenols with a polyethylene glycol group, followed by the removal of copper by the addition of KCN, two interlocked rings, a catenane was obtained. The

knotted rings (Figure 14b), where two phenanthroline complexes were used, is known as a trefoil knot.<sup>63</sup> Among the examples that were reported by Sauvage's group,<sup>64</sup> one exhibited spontaneous resolution on recrystallisation, meaning that only one of the enantiomers was observed in the crystal structure.<sup>8</sup>

The increased rigidity gained by using a catenane leads to increased  $^1\text{MLCT}$  state and hence optimised excited state properties.<sup>65</sup> As well as this, the reversible oxidation states were also applied to molecular machines with the development of a movable shuttle in a catenane,<sup>66</sup> where oxidation of the copper(I) to copper(II) led to more favourable coordination with the terpyridine as opposed to the phenanthroline and hence caused a rotation of the ring in a matter of minutes. This process can then be reversed and the reduction of copper(II) leads to more favourable coordination with the phenanthroline and the ring rotates again in a matter of seconds.

The template effect has been employed by Fallis and co-workers<sup>67</sup> to assemble copper(I) phenanthroline complexes in a fused macrocycle (Figure 15a). The coordination of the copper allows for the coupling of two acetylenes due to their close proximity using a Glaser-Hay acetylene homocoupling. Without the template effect, the yield is considerably lower, 15%; compared to 84% for the templated process.

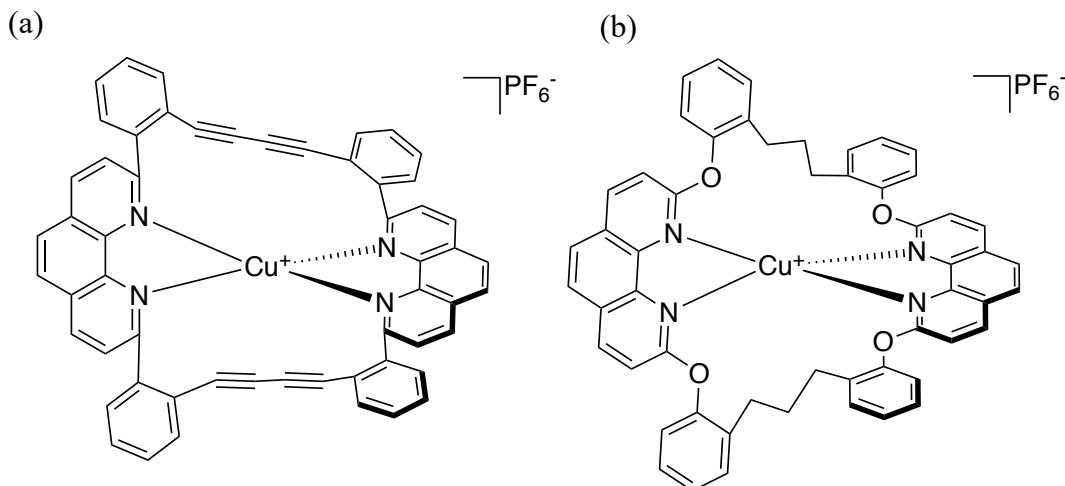


Figure 15: Two macrocyclic copper(I) phenanthroline complexes presented by Fallis (a) and Mayor (b)

On demetallating, the ligand did fluoresce however the copper(I) complex itself did not. Some years later, Mayor and co-workers<sup>68</sup> went on to improve the photostability of such complexes by decreasing the strain on the molecule by changing the linking chains from acetylene to a more flexible chain (Figure 15b). In doing so, an emission was obtained for the copper(I) complex. As well as the synthetic challenge, these complexes are interesting ways to block the phenanthroline in place, in an attempt to limit deformation from a near-perfect tetrahedral geometry on excitation. The stability that

this complex gained by decreasing the steric strain unfortunately had negative effects on the excited state properties, with DFT calculations still showing a distortion from the ground to the excited state of 15°. The authors concluded that this led to short excited state lifetimes by exciplex quenching. Added strain would prevent this deformation however, as shown, hinders the stability. Another advantage to these complexes is the fact that ligand exchange would be impossible.<sup>69</sup>

## 11.6 Heteroleptic copper(I) complexes

A phenomenon that is not seen in homoleptic complexes is the dynamic character of these complexes, where a ligand is able to dissociate and complex with another copper ion and this could continue without any effect as all the ligands are the same. However, issues start to arise when the two ligands are non-identical, this is what is known as a heteroleptic complex. The dynamic aspect of copper(I) phenanthroline complexes was an advantage to supramolecular chemists, as it allowed for the most thermodynamically stable product to be formed leading to high yielding supramolecular nanostructures.<sup>70</sup> Yet, there are ways around the problem of ligand exchange. In Sauvage's synthesis of catenanes he favours the formation of the heteroleptic complex by mixing the copper(I) source with one phenanthroline that has already been cyclised and a second non-cyclised phenanthroline (Figure 16).

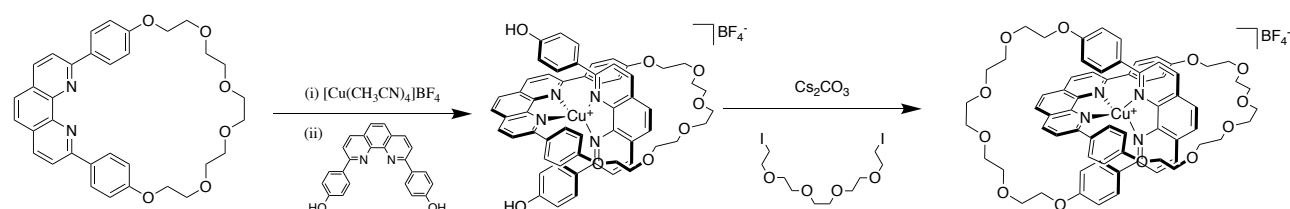


Figure 16: Synthesis of catenanes

Thermodynamically, the heteroleptic complex will be favoured as the cyclised phenanthrolines cannot form homoleptic complexes and this would hence lead to a frustrated system as not all the metal binding sites would be in use. Hence the non-cyclised phenanthroline would be forced to form the heteroleptic complex as opposed to the homoleptic complex with another non-cyclised phenanthroline in order to obey the maximum occupancy principle.<sup>71</sup> Lehn used this technique to self-assemble helical complexes<sup>72</sup> and Nierengarten also extended this work and used phosphine ligands (*vide infra*) as the second ligand and was able to form heteroleptic complexes thanks to the metal-ligand saturation arguments made above.

A second way to prevent the formation of the homoleptic complex was designed by Schmittel<sup>73</sup> and is known as the HETPHEN (HETeroleptic PHENanthroline) process. Here, one of the phenanthroline

moieties contains a significant amount of steric hindrance at the 2,9-positions and hence is unable to form the homoleptic complex at room temperature. Then, on addition of one equivalent of the copper(I) source and finally one equivalent of a less hindered phenanthroline, heteroleptic complexes are formed. These complexes should then be stable and ligand scrambling should be minimal as the hindered phenanthroline is unable to form a homoleptic complex. If the non-hindered phenanthroline formed a homoleptic complex, the system would once again be frustrated due to vacant metal-binding sites; despite this, mixtures of the homoleptic and heteroleptic complexes are sometimes observed, but this is usually when the steric hindrance at the coordination site reaches its limit. This facile two-step, one pot synthesis proved highly efficient to synthesise HETPHEN complexes.

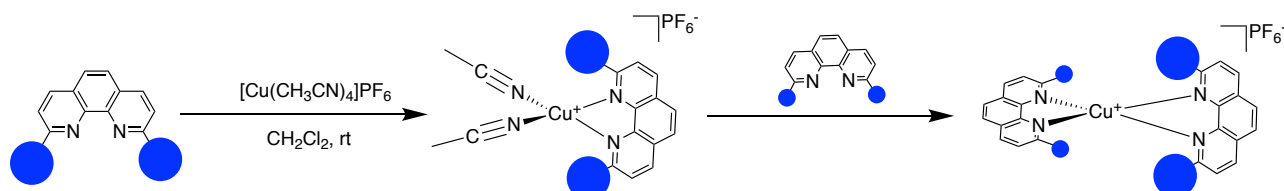


Figure 17: The HETPHEN synthesis presented by Schmittel and co-workers

The HETPHEN process overcame the problem of too much steric hindrance at the coordination site limiting the stability of such complexes, as seen for  $[\text{Cu(I)}(2,9\text{-ditert-butylphenanthroline})_2]^+$ . As stated above, a perfectly tetrahedral geometry is desired, consequently it could potentially be advantageous to have greater steric hindrance at the coordination site. These complexes were hence stable but still presented a large amount of steric hindrance at the coordination site. Also the introduction of a second different ligand allowed for there to be a preferential formation of the radical anion when the MLCT occurred. This leads to a directionality for the charge transfer process as demonstrated for N3 (*vide supra*) with the thiocyanate groups donating charge density and the carboxylic acids adsorbing onto the  $\text{TiO}_2$  surface. This type of directionality was demonstrated by Odobel and co-workers (Figure 18).<sup>74</sup> Calculations clearly showed that the radical anion is solely delocalised onto one of the  $\alpha$ -diimines moieties (Figure 19).

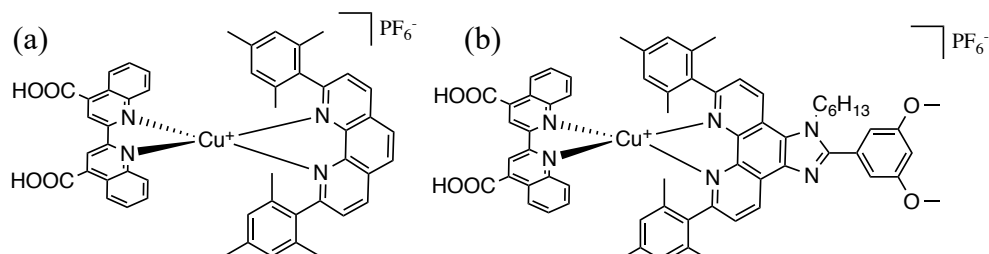


Figure 18: An example of a push-pull heteroleptic complex developed by Odobel and co-workers

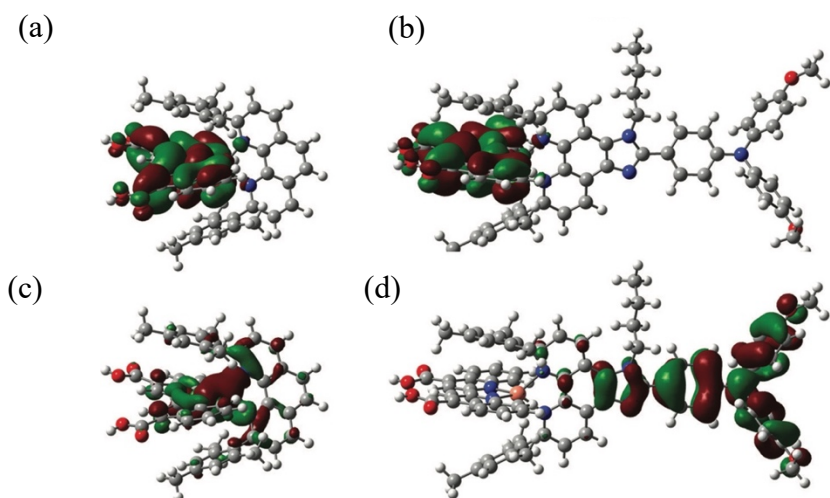


Figure 19: DFT calculations for the HOMO (c) and LUMO (a) of complex Figure 18a and the HOMO (d) and LUMO (b) of complex Figure 18b

These complexes, although more complicated, unfortunately have lower lifetimes in the excited state due to an increased number of conformers. However, HETPHEN complexes are still advantageous as the tunability of the complex has been increased. A wide variety of heteroleptic complexes have been made with varying steric hindrance and a more centred motif, with more steric hindrance leading to optimised properties both in solution<sup>75</sup> and on a surface.<sup>76</sup> These push-pull systems have also been applied to organic dyes.<sup>77</sup>

Schmittel has also exploited the HETPHEN approach to assemble beautiful supramolecular structures like the nanobox,<sup>78</sup> or a ring-in-ring complex,<sup>79</sup> with the steric hindrance provided by the mesityl groups preventing the formation of the homoleptic complex. These self-assembled structures demonstrate the magnitude of potential complexes that can be envisaged. Copper(I) complexes, incorporating other types of molecules or subunits, have also been synthesised by Schmittel, for example a phenanthroline-porphyrin tweezer complex.<sup>80</sup>

## I1.7 Copper(I)(phenanthroline)(phosphine)

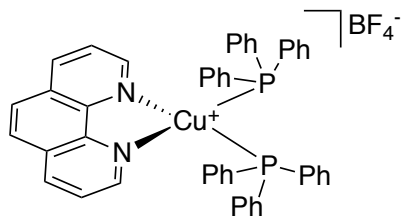


Figure 20:  $[\text{Cu(I)(phenanthroline)(PPh}_3)_2]^+$  presented by McMillin

The luminescent properties of copper(I)(phenanthroline)(phosphine) were first discovered by McMillin<sup>81</sup> in 1980 when copper(I)bis(triphenylphosphine)phenanthroline was found to be luminescent (Figure 20).

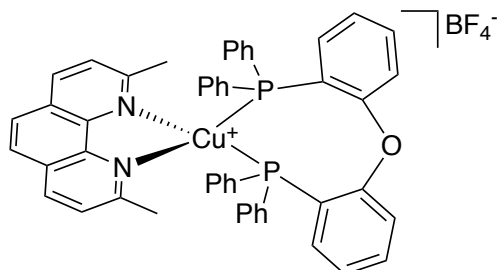


Figure 21:  $[\text{Cu(I)(phenanthroline)(POP)}]^+$  presented by McMillin

$[\text{Cu(I)(phenanthroline)(POP)}]^+$  (Figure 21), synthesised in 2001 by McMillin and co-workers,<sup>82</sup> allowed the way for a new branch in copper(I) photosensitiser with the addition of diphosphine as the second ligand giving unprecedented results for the excited state properties. The absorption maximum of such complexes lies lower than that of copper(I) phenanthroline complexes, for example, the complex above (Figure 21) has an absorption maximum of 383 nm compared to 457 nm for the homoleptic counterpart,  $[\text{Cu(2,9-dimethylphenanthroline)}_2]^+$ . This still lies just within the visible region, so applications in solar cells are still viable. Comparing  $[\text{Cu(2,9-dimethylphenanthroline)(POP)}]^+$  and  $[\text{Cu(2,9-dimethylphenanthroline)(PPh}_3)_2]^+$  there is a 100-fold increase in the emission lifetime and an increase in lifetime from 0.33  $\mu\text{s}$  to 14.3  $\mu\text{s}$  in dichloromethane, demonstrating the advantage of additional sturdiness in the complex, by switching from  $\text{PPh}_3$  to POP. Even in coordinating solvents the complexes perform well. The lifetime of  $[\text{Cu(2,9-dimethylphenanthroline)(PPh}_3)_2]^+$  decreases to 330 ns when in methanol (a coordinating solvent) whereas  $[\text{Cu(2,9-dimethylphenanthroline)(POP)}]^+$  has a lifetime of 2.4  $\mu\text{s}$ , meaning limited solvent induced quenching has occurred. As is the case for copper(I) bis-phenanthroline complexes, changing the substituents will have effects on energy levels and consequently the bite angle of the phosphine ligand can be adjusted in order to optimise the excited state properties. Increasing the steric hindrance at the 2,9-positions increases the lifetime substantially.<sup>82</sup>

A big advantage of adding a phosphine moiety is the increase in energy of the excited MLCT state; this leads to non-radiative deactivation being less favourable. The advantageous properties mean that these complexes are starting to be used in devices.<sup>83</sup> Much like with copper phenanthroline complexes, substitution at the 4,7-positions of the phenanthroline<sup>84</sup> presents the highest reported luminescent quantum yield for a copper phenanthroline complex, with phenyl groups at the 4,7-positions of the phenanthroline and keeping POP as the second ligand and the methyl groups at the 2,9-positions, the quantum yield is 28 % for this complex and the lifetime is 17.3  $\mu\text{s}$  (Figure 22a). n-

Bu substituents at the 2,9-positions (Figure 22b), also has a very high quantum yield of 26% and a lifetime of 17.4  $\mu$ s. The importance of working in an inert atmosphere is also apparent as a 40-fold decrease in the quantum yield is observed when oxygen is not removed from the sample.

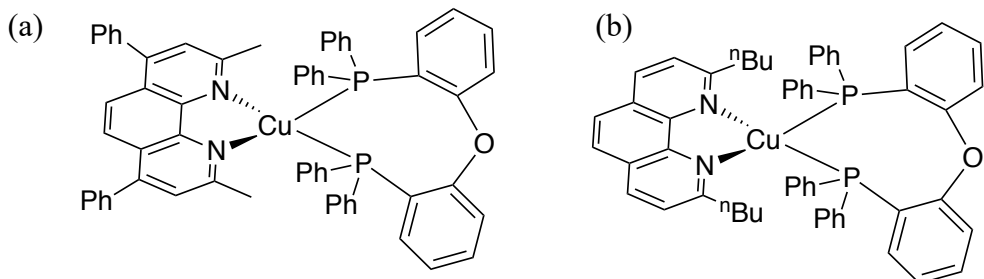


Figure 22: Different substitution patterns for copper(I)(phenanthroline)(diphosphine) complexes

Homoleptic copper(I) phosphine complexes have also been synthesised. The same applies for copper phenanthroline complexes where increased steric hindrance favours longer lifetimes for example using bis(diphenylphosphine)methane as a ligand for the copper leads to a lifetime of 2440 ns. The greater lifetime for this complex is deemed to be on account of the difficulty of the distortion from pseudo-tetrahedral geometry, whereas a complex which is more susceptible to deformation has a shorter lifetime. This is also corroborated by electrochemistry with the first oxidation potential being more positive due to the destabilisation of the copper(II) complex.<sup>85</sup>

Adjusting the number of coordination sites of the copper from four to three has also been a method developed in order to optimise properties. Introducing bulky substituents on the phosphine ligands inhibits the formation of a  $\text{Cu}_2\text{X}_2$  and hence leads to a  $\text{CuX}$  complex with one additional halide ligand.

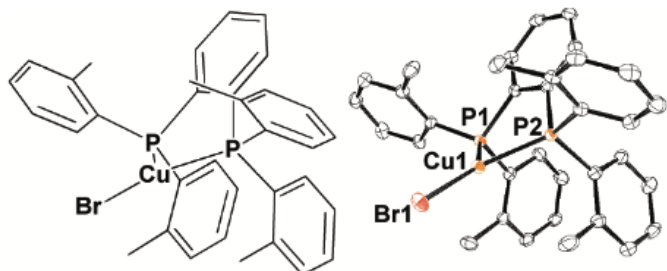


Figure 23: Three-coordinate copper(I)(diphosphine) complex

The three-coordinate copper(I) diphosphine complex (Figure 23), has a lifetime of 5.4  $\mu$ s and a phosphorescence quantum yield of 0.47. This is owed to only a mild Jahn-Teller distortion of the trigonal planar complex on excitation as progressing from a Y to a T shape would clearly be quite

unfavourable. This mild distortion leads to low non-radiative decay and hence high quantum yields.<sup>86</sup> There is a very small energy gap between the singlet and the triplet state.

One of the main issues with copper(I)(phenanthroline)(phosphine) type complexes is the fact that the homoleptic copper complex is the most thermodynamically stable product and consequently when the complex is placed in solution, ligand displacement is likely to occur and the homoleptic complex is formed. Nierengarten<sup>87,88</sup> avoided this problem by applying Sauvage's technique described above (Figure 16) and hence synthesising heteroleptic complexes without the risk of ligand displacement by applying the metal-ligand saturation arguments (Figure 24).

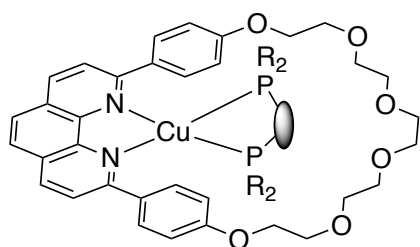


Figure 24: Technique to favour the formation of  $[\text{Cu}(\text{phenanthroline})(\text{phosphine})]^+$  complexes developed by Nierengarten

## 11.8 Conclusion and project plan

The literature shows us that steric hindrance is of paramount importance to prolong the excited state lifetime. It would appear that a near-perfectly tetrahedral ground state geometry renders optimal excited state properties as an exciplex is less likely to form. Our aim was to form copper(I) phenanthroline complexes with minimal steric hindrance at the coordination site, however the complexes were still near-perfectly tetrahedral. This goal would be achieved by adding steric hindrance away from the coordination site and, similar to Castellano, with the addition of the methyl groups pushing the *sec*-butyl groups to block the coordination site more. It was hoped that we too would have a complementary steric effect and that the hindrance away from the coordination site would force the copper(I) to be near tetrahedral and that this optimised geometry would have optimal excited state properties. To verify the change in coordination geometry on excitation, the excited state geometry was studied by DFT calculations. The result was that a new pathway has been developed to create near-perfect tetrahedral copper(I) complex with a small amount of steric hindrance at the coordination site.

## I1.9 REFERENCES

- 1 N. Armaroli and V. Balzani, *Angew. Chem. Int. Ed.*, 2007, **46**, 52–66.
- 2 C. O. Dietrich-Buchecker, P. A. Marnot and J. P. Sauvage, *Tetrahedron Lett.*, 1982, **23**, 5291–5294.
- 3 C. R. Smith, *J. Am. Chem. Soc.*, 1930, **52**, 397–403.
- 4 C. O. Dietrich-Buchecker, J. P. Sauvage and J. P. Kintzinger, *Tetrahedron Lett.*, 1983, **24**, 5095–5098.
- 5 Q. Liu, R. Wang and S. Wang, *Dalton Trans.*, 2004, 2073–2079.
- 6 F. Nastasi, F. Punzoriero, S. Campagna, S. Schergna, M. Maggini, F. Cardinali, B. Delavaux-Nicot and J. F. Nierengarten, *Chem. Commun.*, 2007, 3556–3558.
- 7 A. Kaeser, B. Delavaux-Nicot, C. Duhayon, Y. Coppel and J. F. Nierengarten, *Inorg. Chem.*, 2013, **52**, 14343–14354.
- 8 C. Dietrich-Buchecker, G. Rapenne, J. P. Sauvage, A. De Cian and J. Fischer, *Chem. Eur. J.*, 1999, **5**, 1432–1439.
- 9 L. X. Sun, T. Okada, J. P. Collin and H. Sugihara, *Anal. Chim. Acta*, 1996, **329**, 57–64.
- 10 A. Barbieri, G. Accorsi and N. Armaroli, *Chem. Commun.*, 2008, 2185–2193.
- 11 N. Elgrishi, M. B. Chambers, X. Wang and M. Fontecave, *Chem. Soc. Rev.*, 2017, **46**, 761–796.
- 12 J. P. Collin, R. Ruppert and J. P. Sauvage, *Nouv. J. Chem.*, 1985, **9**, 395.
- 13 M. Knorn, T. Rawner, R. Czerwieniec and O. Reiser, *ACS Catal.*, 2015, **5**, 5186–5193.
- 14 X. G. Liu and W. Sun, *Eur. J. Inorg. Chem.*, 2013, 4732–4742.
- 15 J. A. Gareth Williams, S. Develay, D. L. Rochester and L. Murphy, *Coord. Chem. Rev.*, 2008, **252**, 2596–2611.
- 16 D. W. Thompson, A. Ito and T. J. Meyer, *Pure Appl. Chem.*, 2013, **85**, 1257–1305.
- 17 K. Fujishima, A. Honda, *Nature*, 1972, **238**, 37–38.
- 18 B. C. O'Regan and M. Grätzel, *Nature*, 1991, **353**, 737–740.
- 19 R. Amadelli, R. Argazzi, C. A. Bignozzi and F. Scandola, *J. Am. Chem. Soc.*, 1990, **112**, 7099–7103.
- 20 M. Grätzel, *J. Photochem. Photobiol. C Photochem. Rev.*, 2003, **4**, 145–153.
- 21 N. Alonso-Vante, J. F. Nierengarten and J. P. Sauvage, *J. Chem. Soc. Dalton Trans.*, 1994, **11**, 1649–1654.
- 22 M. Urbani, M. Grätzel, M. K. Nazeeruddin and T. Torres, *Chem. Rev.*, 2014, **114**, 12330–12396.
- 23 M. K. Nazeeruddin, A. Kay, R. Rodicio, R. Humphry-Baker, E. Müller, P. Liska, N.

Vlachopoulos and Grätzel, *J. Am. Chem. Soc.*, 1993, **115**, 6382–6390.

24 M. T. Rupp, N. Shevchenko, G. S. Hanan and D. G. Kurth, *Coord. Chem. Rev.*, 2021, **446**, 214127.

25 J. P. Correa-Baena, A. Abate, M. Saliba, W. Tress, T. Jesper Jacobsson, M. Grätzel and A. Hagfeldt, *Energy Environ. Sci.*, 2017, **10**, 710–727.

26 F. Sahli, J. Werner, B. A. Kamino, M. Bräuninger, R. Monnard, B. Paviet-Salomon, L. Barraud, L. Ding, J. J. Diaz Leon, D. Sacchetto, G. Cattaneo, M. Despeisse, M. Boccard, S. Nicolay, Q. Jeangros, B. Niesen and C. Ballif, *Nat. Mater.*, 2018, **17**, 820–826.

27 J. Luo, J. H. Im, M. T. Mayer, M. Schreier, M. K. Nazeeruddin, N. G. Park, S. D. Tilley, H. J. Fan and M. Grätzel, *Science*, 2014, **345**, 1593–1596.

28 M. Grätzel, *Nat. Mater.*, 2014, **13**, 838–842.

29 G. H. Carey, A. L. Abdelhady, Z. Ning, S. M. Thon, O. M. Bakr and E. H. Sargent, *Chem. Rev.*, 2015, **115**, 12732–12763.

30 C. E. Housecroft and E. C. Constable, *Chem. Sci.*, 2022, **13**, 1225–1262.

31 D. R. McMillin, M. T. Buckner and B. Tae Ahn, *Inorg. Chem.*, 1977, **16**, 943–945.

32 C. O. Dietrich-Buchecker, P. A. Marnot, J. P. Sauvage, J. R. Kirchhoff and D. R. McMillin, *J. Chem. Soc. Chem. Commun.*, 1983, 513–515.

33 S. Ferrere and B. A. Gregg, *J. Am. Chem. Soc.*, 1998, **120**, 843–844.

34 T. Bessho, E. C. Constable, M. Grätzel, A. Hernandez Redondo, C. E. Housecroft, W. Kylberg, M. K. Nazeeruddin, M. Neuburger and S. Schaffner, *Chem. Commun.*, 2008, 3717–3719.

35 J. Huang, O. Buyukcakir, M. W. Mara, A. Coskun, N. M. Dimitrijevic, G. Barin, O. Kokhan, A. B. Stickrath, R. Ruppert, D. M. Tiede, J. F. Stoddart, J. P. Sauvage and L. X. Chen, *Angew. Chem. Int. Ed.*, 2012, **51**, 12711–12715.

36 F. Odobel, Y. Pellegrin, E. A. Gibson, A. Hagfeldt, A. L. Smeigh and L. Hammarström, *Coord. Chem. Rev.*, 2012, **256**, 2414–2423.

37 G. H. Summers, J. F. Lefebvre, F. A. Black, E. Stephen Davies, E. A. Gibson, T. Pullerits, C. J. Wood and K. Zidek, *Phys. Chem. Chem. Phys.*, 2016, **18**, 1059–1070.

38 M. W. Blaskie and D. R. McMillin, *Inorg. Chem.*, 1980, **19**, 3519–3522.

39 L. X. Chen, G. B. Shaw, I. Novozhilova, T. Liu, G. Jennings, K. Attenkofer, G. J. Meyer and P. Coppens, *J. Am. Chem. Soc.*, 2003, **125**, 7022–7034.

40 O. Green, B. A. Gandhi and J. N. Burstyn, *Inorg. Chem.*, 2009, **48**, 5704–5714.

41 D. R. McMillin, J. R. Kirchhoff and K. V. Goodwin, *Coord. Chem. Rev.*, 1985, **64**, 83–92.

42 M. T. Miller and T. B. Karpishin, *Inorg. Chem.*, 1999, **38**, 5246–5249.

43 M. T. Miller, P. K. Gantzel and T. B. Karpishin, *Inorg. Chem.*, 1998, **37**, 2285–2290.

44 A. K. Ichinaga, J. R. Kirchhoff, D. R. McMillin, C. O. Dietrich-Buchecker, P. A. Marnot and J. P. Sauvage, 1987, **26**, 4290–4292.

45 C. T. Cunningham, K. L. H. Cunningham, J. F. Michalec and D. R. McMillin, *Inorg. Chem.*, 1999, **38**, 4388–4392.

46 M. T. Miller, P. K. Gantzel and T. B. Karpishin, *Inorg. Chem.*, 1999, **38**, 3414–3422.

47 C. T. Lin, W. Böttcher, M. Chou, C. Creutz and N. Sutin, *J. Am. Chem. Soc.*, 1976, **98**, 6536–6544.

48 P. K. Samanta, D. Kim, V. Coropceanu and J. L. Brédas, *J. Am. Chem. Soc.*, 2017, **139**, 4042–4051.

49 F. Vögtle, I. Lüer, V. Balzani and N. Armaroli, *Angew. Chemie Int. Ed.*, 1991, **30**, 1333–1336.

50 S. Garakyanaghi, P. D. Crapps, C. E. McCusker and F. N. Castellano, *Inorg. Chem.*, 2016, **55**, 10628–10636.

51 C. E. McCusker and F. N. Castellano, *Inorg. Chem.*, 2013, **52**, 8114–8120.

52 M. C. Rosko, K. A. Wells, C. E. Hauke and F. N. Castellano, *Inorg. Chem.*, 2021, **60**, 8394–8403.

53 S. Garakyanaghi, E. O. Danilov, C. E. McCusker and F. N. Castellano, *J. Phys. Chem. A*, 2015, **119**, 3181–3193.

54 Y. Leydet, D. M. Bassani, G. Jonusauskas and N. D. McClenaghan, *J. Am. Chem. Soc.*, 2007, **129**, 8688–8689.

55 R. M. Everly and D. R. McMillin, *Photochem. Photobiol.*, 1989, **50**, 711–716.

56 L. Gimeno, B. T. Phelan, E. A. Sprague-Klein, T. Roisnel, E. Blart, C. Gourlaouen, L. X. Chen and Y. Pellegrin, *Inorg. Chem.*, 2022, **61**, 7296–7307.

57 L. Gimeno, E. Blart, J. N. Rebilly, M. Coupeau, M. Allain, T. Roisnel, A. Quarré de Verneuil, C. Gourlaouen, C. Daniel and Y. Pellegrin, *Chem. Eur. J.*, 2020, **26**, 11887–11899.

58 D. Felder, J. F. Nierengarten, F. Barigelli, B. Ventura and N. Armaroli, *J. Am. Chem. Soc.*, 2001, **123**, 6291–6299.

59 C. O. Dietrich-Buchecker and J. P. Sauvage, *Tetrahedron Lett.*, 1983, **24**, 5091–5094.

60 C. Dietrich-Buchecker, B. Colasson, M. Fujita, A. Hori, N. Geum, S. Sakamoto, K. Yamaguchi and J. P. Sauvage, *J. Am. Chem. Soc.*, 2003, **125**, 5717–5725.

61 N. Solladié, J. C. Chambron and J. P. Sauvage, *J. Am. Chem. Soc.*, 1999, **121**, 3684–3692.

62 F. Niess, V. Duplan and J. P. Sauvage, *J. Am. Chem. Soc.*, 2014, **136**, 5876–5879.

63 S. D. P. Fielden, D. A. Leigh and S. L. Woltering, *Angew. Chem. Int. Ed.*, 2017, **56**, 11166–11194.

64 G. Rapenne, C. Dietrich-Buchecker and J. P. Sauvage, *J. Am. Chem. Soc.*, 1999, **121**, 994–

1001.

65 M. W. Mara, D. N. Bowman, O. Buyukcakir, M. L. Shelby, K. Haldrup, J. Huang, M. R. Harpham, A. B. Stickrath, X. Zhang, J. F. Stoddart, A. Coskun, E. Jakubikova and L. X. Chen, *J. Am. Chem. Soc.*, 2015, **137**, 9670–9684.

66 A. Livoreil, C. O. Dietrich-Buchecker and J. P. Sauvage, *J. Am. Chem. Soc.*, **116**, 1994, 9399–9400.

67 M. A. Heuft and A. G. Fallis, *Angew. Chem. Int. Ed.*, 2002, **41**, 4520–4523.

68 T. Brandl, C. Kerzig, L. Le Pleux, A. Prescimone, O. S. Wenger and M. Mayor, *Chem. Eur. J.*, 2020, **26**, 3119–3128.

69 B. Ralhy, U. Hahn, E. Wasielewski and J. F. Nierengarten, *Eur. J. Inorg. Chem.*, 2021, **2021**, 2625–2635.

70 R. Chakrabarty, P. S. Mukherjee and P. J. Stang, *Chem. Rev.*, 2011, **111**, 6810–6918.

71 V. G. Machado, P. N. W. Baxter and J. M. Lehn, *J. Braz. Chem. Soc.*, 2001, **12**, 431–462.

72 R. Kramer, J. M. Lehn and A. Marquis-Rigault, *Proc. Natl. Acad. Sci. USA.*, 1993, **90**, 5394–5398.

73 M. Schmittel, U. Lüning, M. Meder, A. Ganz, C. Michel and M. Herderich, *Heterocycl. Commun.*, 1997, **3**, 493–498.

74 M. Sandroni, M. Kayanuma, A. Planchat, N. Szwarski, E. Blart, Y. Pellegrin, C. Daniel, M. Boujtita and F. Odobel, *Dalton Trans.*, 2013, **42**, 10818–10827.

75 L. Kohler, R. G. Hadt, D. Hayes, L. X. Chen and K. L. Mulfort, *Dalton Trans.*, 2017, **46**, 13088–13100.

76 M. S. Eberhart, B. T. Phelan, J. Niklas, E. A. Sprague-Klein, D. M. Kaphan, D. J. Gosztola, L. X. Chen, D. M. Tiede, O. G. Poluektov and K. L. Mulfort, *Chem. Commun.*, 2020, **56**, 12130–12133.

77 K. S. Keremane, Y. Pellegrin, D. Jacquemin, F. Odobel and A. V. Adhikari, *J. Phys. Chem. C*, 2022, **126**, 12383–12390.

78 M. Schmittel, H. Ammon, V. Kalsani, A. Wiegrefe and C. Michel, *Chem. Commun.*, 2002, 2566–2567.

79 M. Schmittel, A. Ganz and D. Fenske, *Org. Lett.*, 2002, **4**, 2289–2292.

80 S. De, K. Mahata and M. Schmittel, *Chem. Soc. Rev.*, 2010, **39**, 1555–1575.

81 G. Blasse and D. R. McMillin, *Chem. Phys. Lett.*, 1980, **70**, 1–3.

82 D. G. Cuttell, S. M. Kuang, P. E. Fanwick, D. R. McMillin and R. A. Walton, *J. Am. Chem. Soc.*, 2002, **124**, 6–7.

83 Q. Zhang, Q. Zhou, Y. Cheng, L. Wang, D. Ma, X. Jing and F. Wang, *Adv. Mater.*, 2004, **16**, 432–436.

84 N. Armaroli, G. Accorsi, M. Holler, O. Moudam, J. F. Nierengarten, Z. Zhou, R. T. Wegh and R. Welter, *Adv. Mater.*, 2006, **18**, 1313–1316.

85 O. Moudam, A. Kaeser, B. Delavaux-Nicot, C. Duhayon, M. Holler, G. Accorsi, N. Armaroli, I. Séguy, J. Navarro, P. Destruel and J. F. Nierengarten, *Chem. Commun.*, 2007, 3077–3079.

86 S. Igawa, M. Hashimoto, I. Kawata, M. Yashima, M. Hoshino and M. Osawa, *J. Am. Chem. Soc.*, 2011, **113**, 10348–10351.

87 M. Mohankumar, M. Holler, J. F. Nierengarten and J. P. Sauvage, *Chem. Eur. J.*, 2012, **18**, 12192–12195.

88 M. Mohankumar, M. Holler, M. Schmitt, J. P. Sauvage and J. F. Nierengarten, *Chem. Commun.*, 2013, **49**, 1261–1263.

# CHAPTER 1

## Heteroleptic copper(I) phenanthroline complexes: Synthesis and properties

1.1 Introduction	40
1.2 Lithium Source	40
1.2.1 n-Butyl lithium	40
1.2.2 t-Butyl lithium	41
1.2.3 Lithium metal	44
1.3 Heteroleptic complexes	45
1.3.1 Structural properties	47
1.3.2 Electronic properties	54
1.3.3 Photoluminescence properties	58
1.4 Conclusion	64
1.5 References	66

## 1.1 Introduction

It is well established in the literature that steric hindrance at the metal coordination site is of paramount importance to optimise the electronic properties of copper(I) phenanthroline complexes. The use of heteroleptic complexes allows for greater tunability of the complex and a directionality for the charge transfer. The heteroleptic approach uses one sterically hindered phenanthroline and a second phenanthroline with less steric hindrance. Maximising the steric hindrance will lead to optimised excited state properties as there is a reduced geometrical deformation on excitation of the tetrahedral copper(I) complex to a square-planar copper(II) complex. Steric hindrance prevents this flattening distortion and prevents the formation of the exciplex, yet it is important not to sacrifice the stability of the complex; as is the case for the unstable  $[\text{Cu(I)}(2,9\text{-ditert-butylphenanthroline})_2]^+$  complex.<sup>1</sup> Despite optimal excited state properties, this complex lacks stability and is highly susceptible to ligand exchange. This chapter focuses on the synthesis and analysis of sterically hindered copper(I) heteroleptic phenanthroline complexes, in an attempt to optimise the ground and excited state properties.

A sterically hindered phenanthroline complex was therefore synthesised with 2,6-dimethyl-4-(*tert*-butyl)phenyl group at the 2 and 9 positions of 1,10-phenanthroline (this ligand was mentioned briefly in a Japanese patent,<sup>2</sup> where it was coordinated to zinc(II) to catalyse polymerisation reactions). The lithio-aryl was formed *via* a halogen-lithium exchange between 2-bromo-5-(*tert*-butyl)-1,3-dimethylbenzene and a lithium source. Three different lithium sources were tested for this reaction. The steric hindrance of this aryl group meant that the reaction needed to be heated (65 °C) for the nucleophilic aromatic addition on the phenanthroline to occur. After quenching with water, the phenanthroline was rearomatised with MnO<sub>2</sub>. The lithium source proved to be of paramount importance for the formation of the desired product.

## 1.2 Lithium Source

The three lithium sources were as follow: n-butyl lithium, *tert*-butyl lithium and lithium metal.

### 1.2.1 n-Butyl lithium

The use of n-butyl lithium led purely to the formation of the monofunctionalised product (Figure 26), despite a 5:1 ratio of aryl:phenanthroline. A possible reason for this could be due to electrophilic side

products formed after the halogen-lithium exchange reaction, resulting in the ArLi reacting with other electrophilic molecules as opposed to the phenanthroline. Nevertheless, the monosubstituted product is still useful for the formation of non-symmetrical phenanthrolines (see Chapter 2).

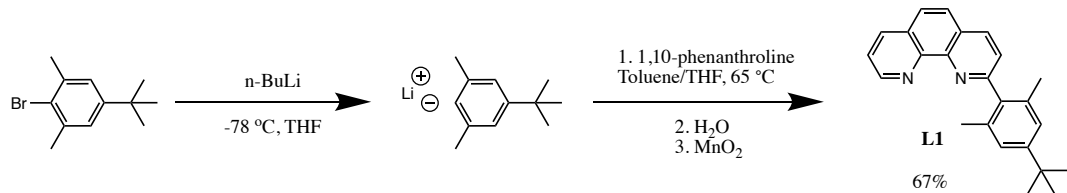


Figure 26: Preparation of the monofunctionalised phenanthroline

### 1.2.2 *t*-Butyl lithium

In order to prevent these electrophilic side-products, *n*-butyl lithium was replaced with *tert*-butyl lithium (Figure 27). The halogen-lithium exchange, first described by Seebach,<sup>3</sup> using *tert*-butyl lithium led to the desired difunctionalised product with a yield of 26%; surprisingly this was not the major product of the reaction. The major product obtained in 56% yield was the phenanthroline with the expected aryl at the 2 position and a benzyl group at the 7 position.

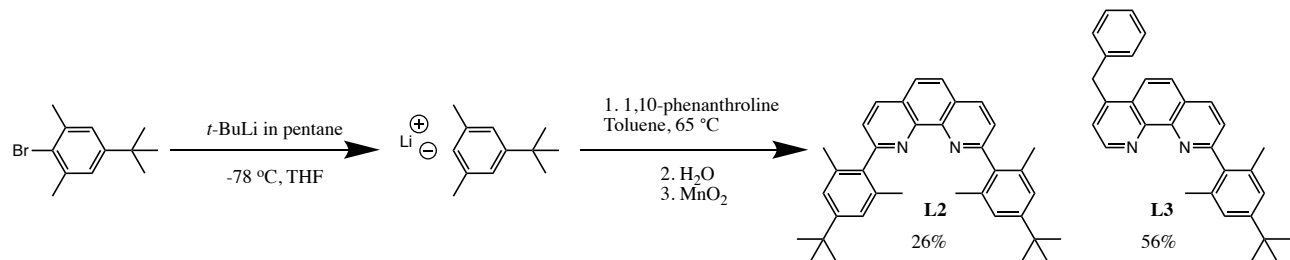


Figure 27: Preparation of the difunctionalised phenanthroline and a new substitution pattern

This reaction was reproducible, performed multiple times and L3 was always the major product. Therefore, a deprotonation of the toluene had occurred *in situ* and we hypothesise that a lithium cluster had formed<sup>4</sup> between the negatively charged nitrogen and the positively charged lithio-aryl, hence blocking the 9-position and leading to substitution of the benzyl at the 7 position. The 4 position was not available due to the lack of aromaticity after the addition of the aryl at the 2 position. This potential substitution pattern is pictured in Figure 28.

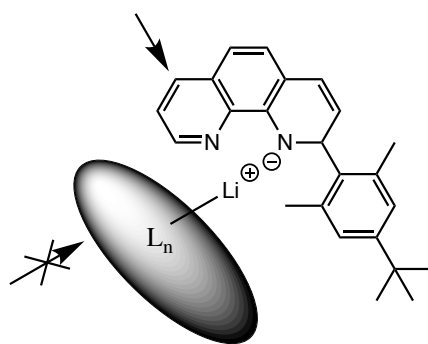


Figure 28: Potential substitution pattern for the formation of **L3**

This new substitution pattern at the 7-position in a one-step process is novel with only one example in the literature as a two-step process.<sup>5</sup> The hypothesis for the substitution cannot be confirmed. However, to quote Pr. Marc Julia “*il vaut mieux un kilo de produit dans le ballon sans explication qu'un kilo de papier pour expliquer que la réaction espérée ne s'est pas faite!*” (translation: It is better to have a kilogram of product in a round-bottom flask with no explanation than a kilogram of paper explaining why a reaction did not occur!).<sup>6</sup>

Characteristic peaks in the <sup>1</sup>H NMR spectrum (Figure 29) proved the formation of this product, with a doublet at 9.12 ppm that could only belong to a proton next to the nitrogen atom, meaning that there was no substituent at the 9 position of the phenanthroline. The methylene protons of the benzyl group appeared as a singlet at 4.54 ppm. Coupling between H<sub>9</sub> and H<sub>8</sub> proved that addition had occurred at the 7-position of the phenanthroline. This ligand was then used to prepare the homoleptic copper(I) complex, **C1** (the complexation reaction is described in Chapter 2).

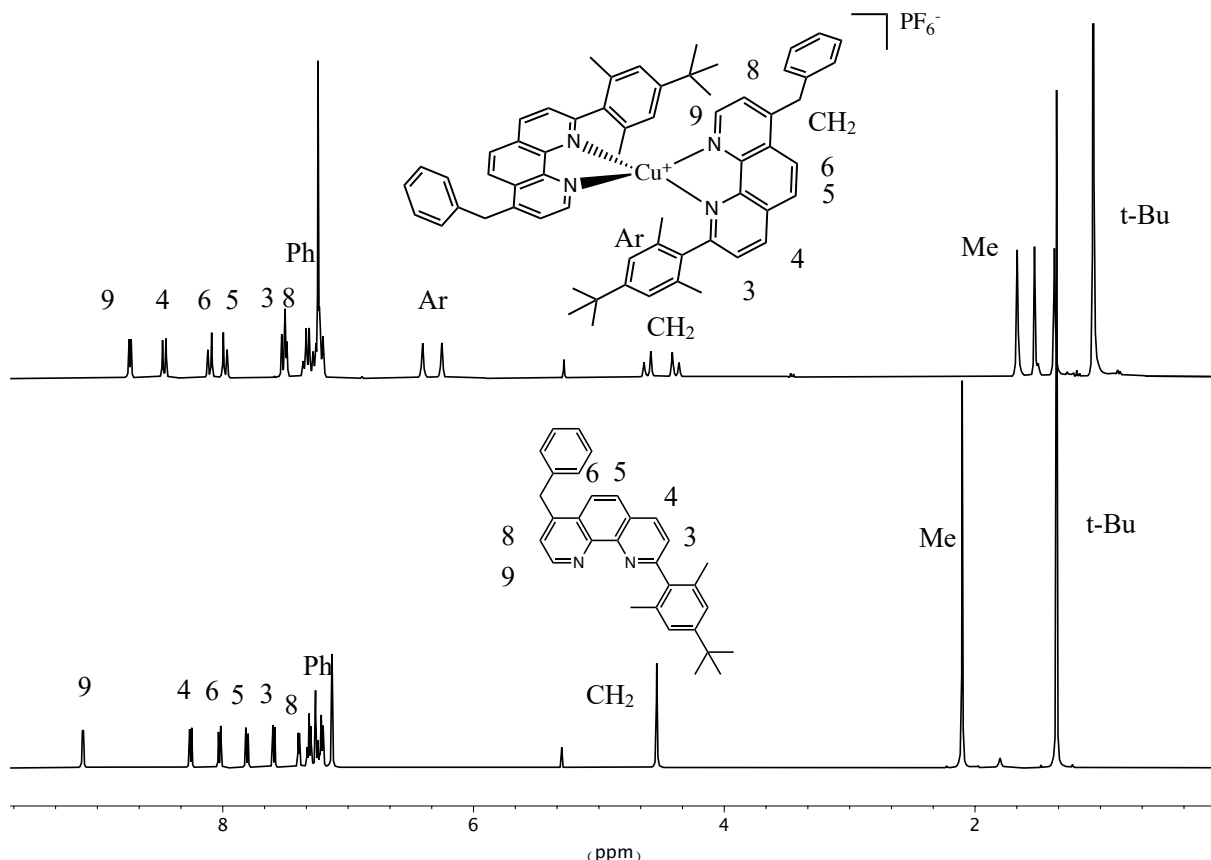


Figure 29:  $^1\text{H}$ NMR of **C1** (top) and **L3** (bottom) in  $\text{CDCl}_3$

Interestingly, the singlet at 4.5 ppm becomes two tenting doublets on complexation, meaning that the two protons of the  $\text{CH}_2$  have become diastereotopic. The reason for this can be explained as the ligand is non-symmetric and consequently on complexation, a stereogenic centre is formed at the  $\text{Cu(I)}$  and hence **C1** is a chiral complex.

The crystal structure shown in Figure 30 confirmed that the tolyl group had indeed been substituted at the 7-position, hence meaning that a new substitution pattern for phenanthroline ligands had been found. Interestingly there was spontaneous resolution on crystallisation, with only one enantiomer being observed in the crystal data. This is quite a rare finding with only one other copper(I) complex having demonstrated this property, the trefoil knot developed by Sauvage and co-workers.<sup>7</sup> Other examples of enantiomerically pure copper(I) complexes were obtained with chiral anions.<sup>8</sup> This is only the case in the solid state as with ligand dissociation in solution a racemic mixture will be present.

From the crystal structure it is apparent that  $\pi$ - $\pi$  stacking is occurring between the aryl and the phenanthroline, this hence explains the large upfield shift of the aromatic aryl protons (from 7.1 ppm to 6.25 and 6.41 ppm) and the methyl groups (from 2.10 ppm to 1.68 and 1.38 ppm) on complexation

(Figure 29) and the hindering of the rotation on complexation means that the protons can now be differentiated.

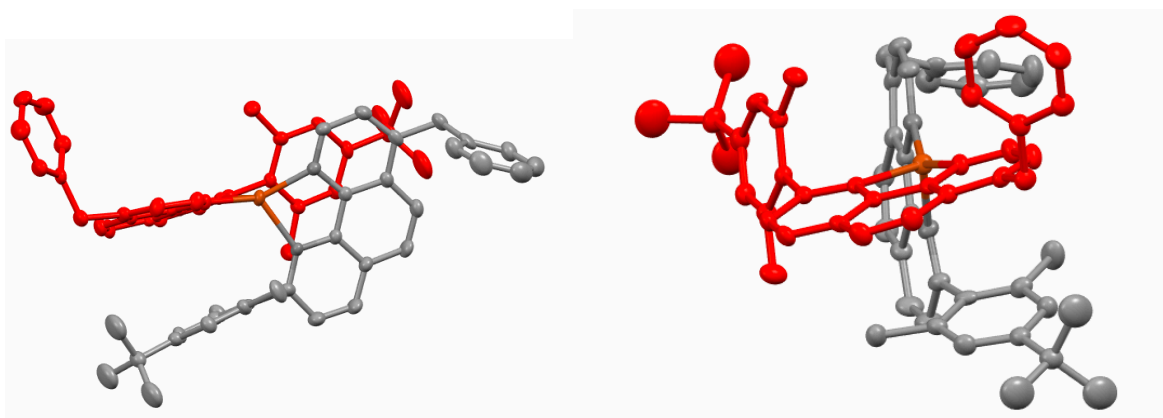


Figure 30: X-ray structure of **C1**. Hydrogen atoms omitted for clarity

### 1.2.3 Lithium metal

The final source of lithium was lithium metal (Figure 31). This reaction led to the formation of the desired product in respectable yields. In this case, neither electrophilic nor nucleophilic side-products were a problem.

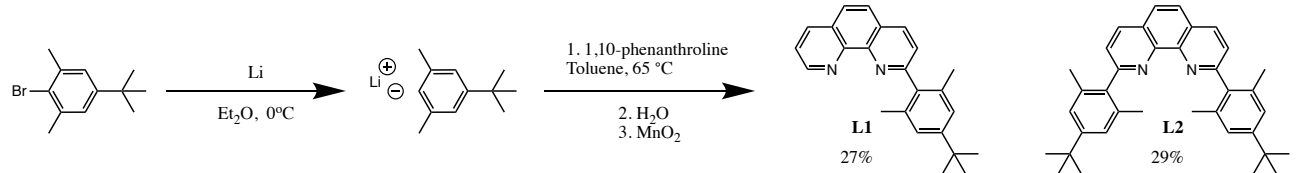


Figure 31: Preparation of the difunctionalised phenanthroline.

A crystal structure of the desired difunctionalised phenanthroline was obtained *via* slow diffusion of ether into dichloromethane and the spacefilling model (Figure 32) demonstrates clearly just how sterically hindered the ligand is.

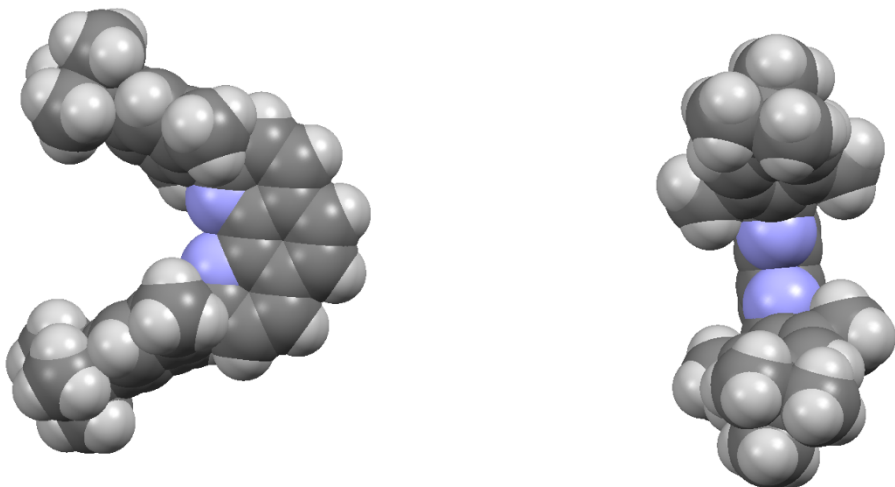


Figure 32: Two orthogonal spacefilling views of the X-ray structure of **L2**. N, blue; C, dark grey; H light grey

The phenyl groups are orthogonal to the plane of the phenanthroline and the distance between the centroids of the two aryl groups is 8.23 nm. The methyl and *tert*-butyl groups will help protect the coordination site from solvent attack and minimise distortion from a tetrahedral geometry on complexation with copper(I) and a second phenanthroline. The *tert*-butyl group also has a second purpose of providing additional steric hindrance away from the coordination site.

The difunctionalised ligand could hence be used to make heteroleptic complexes, yet the monofunctionalised phenanthroline still has a utility for the formation of unsymmetric ligands that could then be used to make homoleptic complexes (see Chapter 2).

### 1.3 Heteroleptic complexes

The heteroleptic complexes were synthesised in a two-step, one pot synthesis utilising the HETPHEN process (Figure 33) developed by Schmittel and co-workers.<sup>9</sup> One equivalent of the copper(I) source was added to the sterically hindered phenanthroline dissolved in distilled dichloromethane, (the steric hindrance prevents the formation of the bis-homoleptic complex) followed by one equivalent of the less-hindered phenanthroline. On addition of the second phenanthroline, an instantaneous colour change was observed from yellow to red (other colours also formed depending on the diimine used) as an MLCT occurs between the metal ion and the phenanthroline in the visible region.

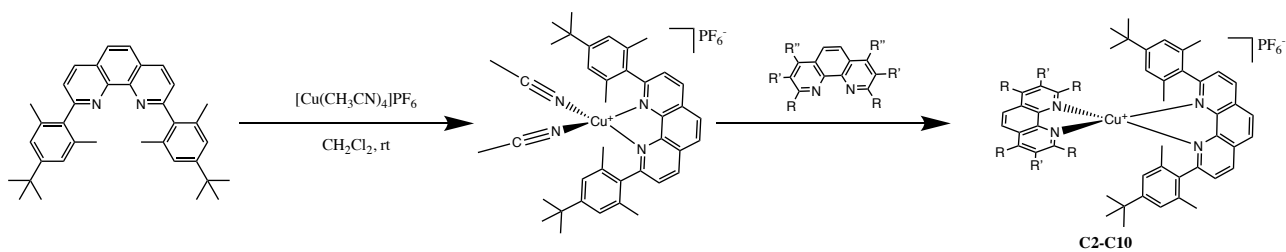


Figure 33: Formation of heteroleptic copper(I) diimine complexes

A wide variety of less-hindered ligands was used to synthesise nine heteroleptic complexes (Figure 34) with varying substituents at the 2,3,4,5,6,7,8,9-positions. The yields for this process were always high (60 - 84%) and varied depending on the amount of steric hindrance on the aforementioned positions. The complexes were then recrystallised by slow diffusion of diethyl ether/pentane (1:1) into the complex dissolved in dichloromethane. The air stable copper(I) complexes are shown below:

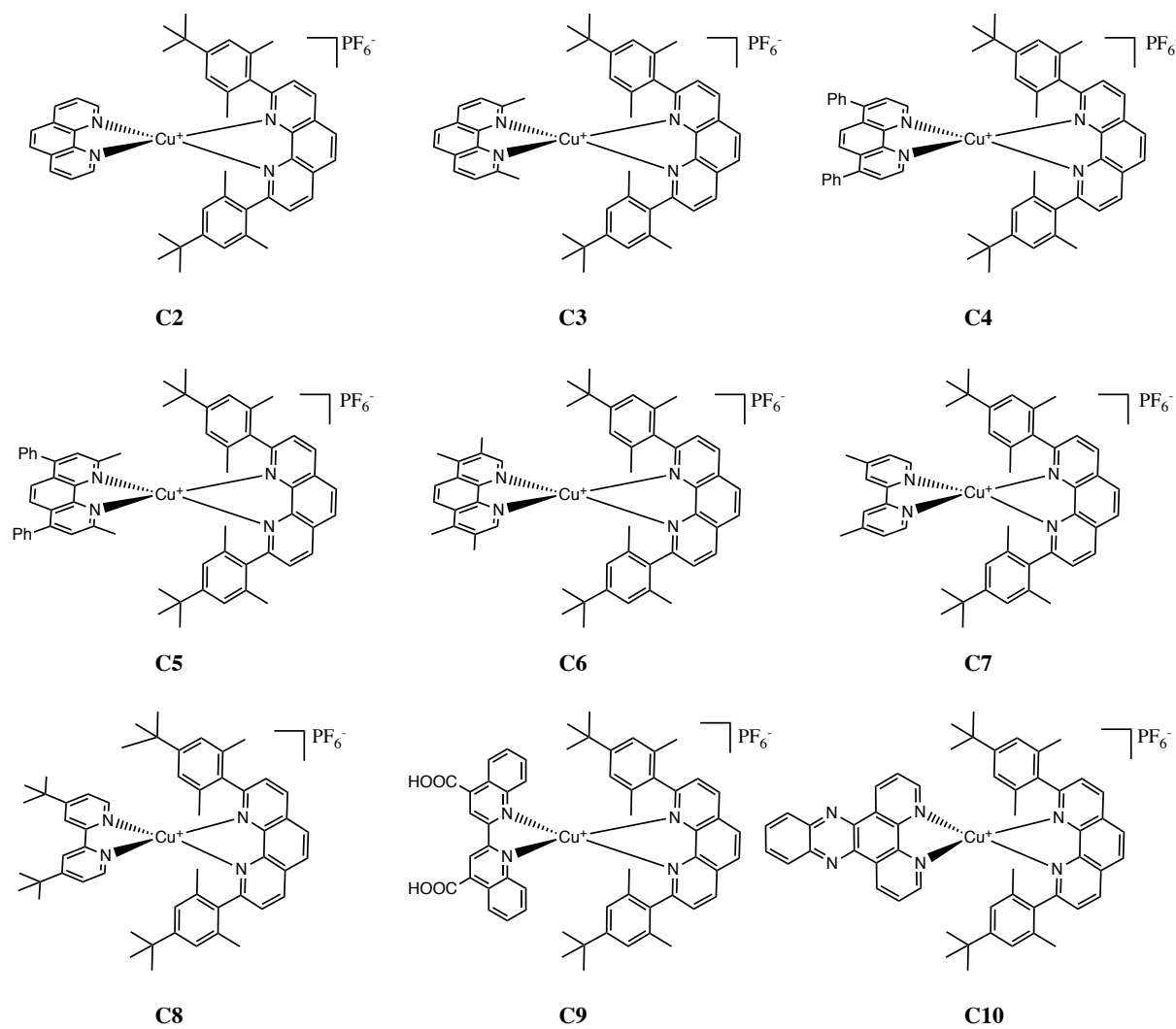


Figure 34: Heteroleptic copper(I) diimine complexes

This wide range of copper(I) (bis)diimine complexes shows the versatility of the synthesis. They were chosen in order to optimise the steric hindrance at the coordination site (addition of methyl groups at the 2,9-positions of the phenanthroline) and to optimise the electronic properties (addition of phenyl and methyl groups at the 3,4,7,8-positions). The efficiency of the HETPHEN processes was demonstrated by the high purity of the complexes, an example of which is **C2** in Figure 35. The signal of the protons of the aryl group were shifted upfield from 7.11 to 6.15 ppm due to the ring current of the second phenanthroline and those of the phenanthroline were shifted downfield due to the metal complexation.

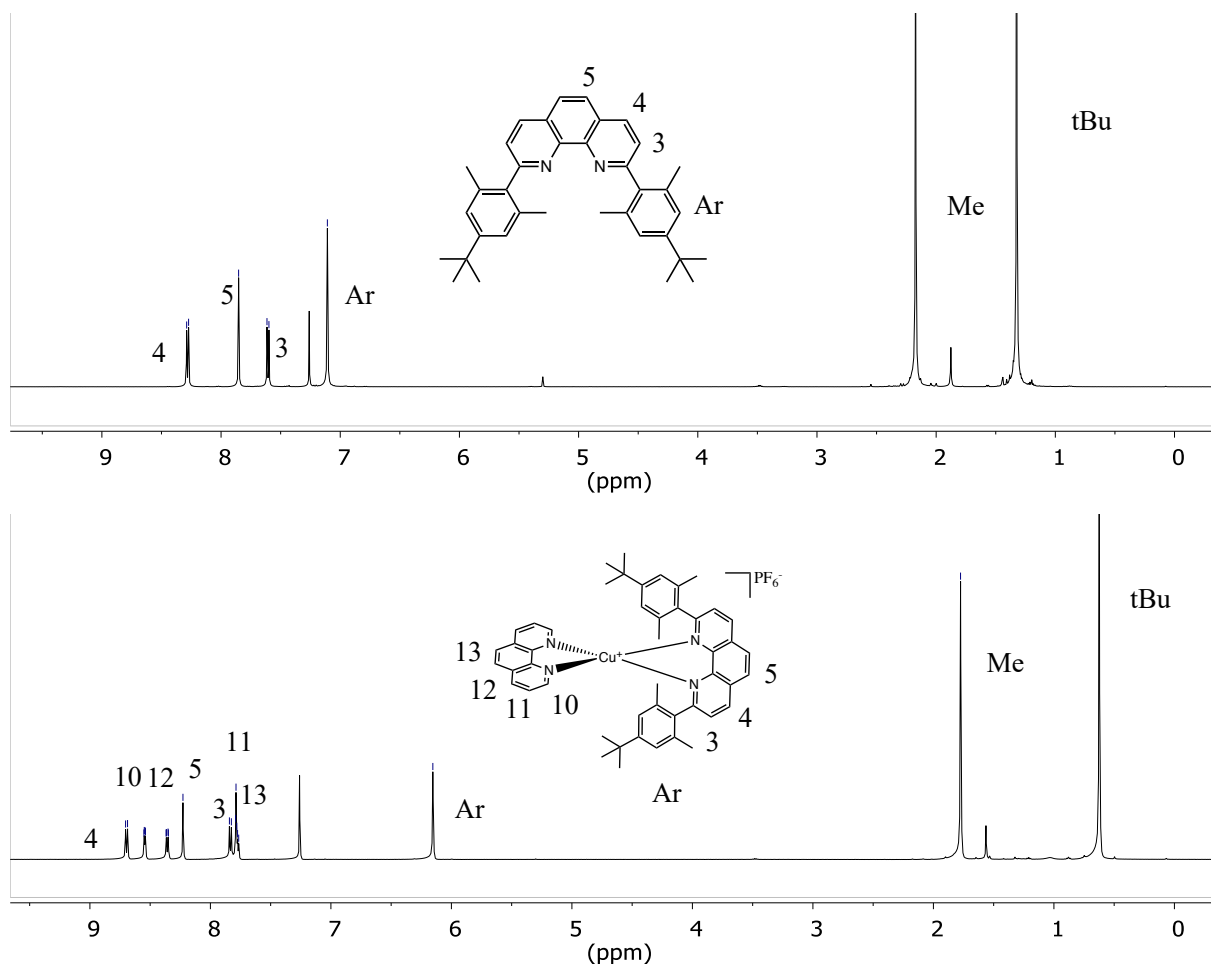


Figure 35:  $^1\text{H}$  NMR of **L2** (top) and **C2** (bottom) in  $\text{CDCl}_3$

### 1.3.1 Structural properties

X-ray crystal structures allowed for the coordination geometry of the copper(I) complexes to be determined. The geometry should be tetrahedral, however other factors are at play that can influence the geometry. Without steric hindrance, it is preferential for the phenanthroline to undergo  $\pi$ - $\pi$  interactions with the aryl group of the neighbouring phenanthroline, leading to what is known as a

“pac-man” motif, as one of the phenanthrolines distorts in order for this  $\pi$ - $\pi$  interaction to occur. However, introducing steric hindrance at the coordination site prevents this deformation and consequently leads to a more perfectly tetrahedral geometry, known as a “centred” motif. The latter motif normally leads to better electronic properties, as the steric hindrance will hinder the distortion to a square-planar geometry on excitation to the copper(II) species and consequently prevents the formation of an exciplex as the fifth coordination site is less available due to this increased hindrance. This is favourable as it prevents the fastest way to quench the excited state.

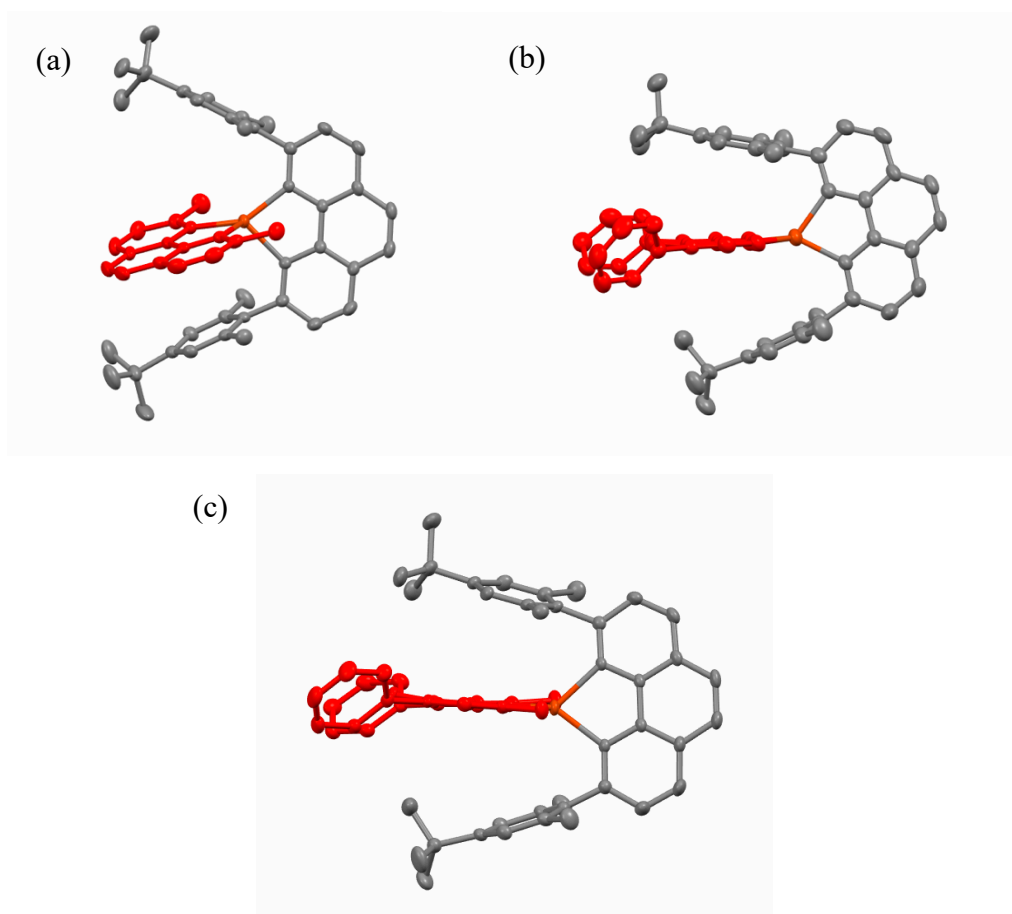


Figure 36: X-ray crystal structures of **C3** (a), **C4** (b), **C5** (c). Hydrogen atoms omitted for clarity

The aim was consequently to form near-perfect tetrahedral complexes. Several crystal structures were obtained in order to verify the geometry. In the literature, the steric hindrance is present close to the metal coordination site (2,9-positions of the phenanthroline). Here a new system design for forming near-perfect tetrahedral complexes is presented, where the steric hindrance is away from the coordination site (4,7-positions of the phenanthroline). Hence, despite small groups being present at the 2,9-positions, a near-perfect tetrahedral geometry was still observed. This was due to the steric interactions between the phenyl groups at the 4,7-positions of the phenanthroline in complexes **C4** and **C5** and the *tert*-butyl groups of the aryl groups present at the 2,9-positions of the other

phenanthroline (Figure 36). This system design appears to be highly efficient for the formation of near-perfect tetrahedral copper(I) complexes in the ground state. Proof of concept was demonstrated with **C4**, as no steric hindrance was present at the coordination site, however a near-perfect tetrahedral geometry was still observed. Without these phenyl groups, **C3** adopted the “pac-man” motif. **C4** and **C5** also proved to be stable in deuterated acetonitrile, with no decomplexation even after a month in solution, demonstrating the rigidity of these complexes.

A standard was chosen as a means to compare the geometries found here with those in the literature,  $[\text{copper(I)}(2,9\text{-ditert-butylphenanthroline})_2]^+$  (Figure 37, left). This complex is widely regarded as being the most geometrically optimised complex. Its X-ray parameters along with those of **C3**, **C4** and **C5** are shown in Table 2.

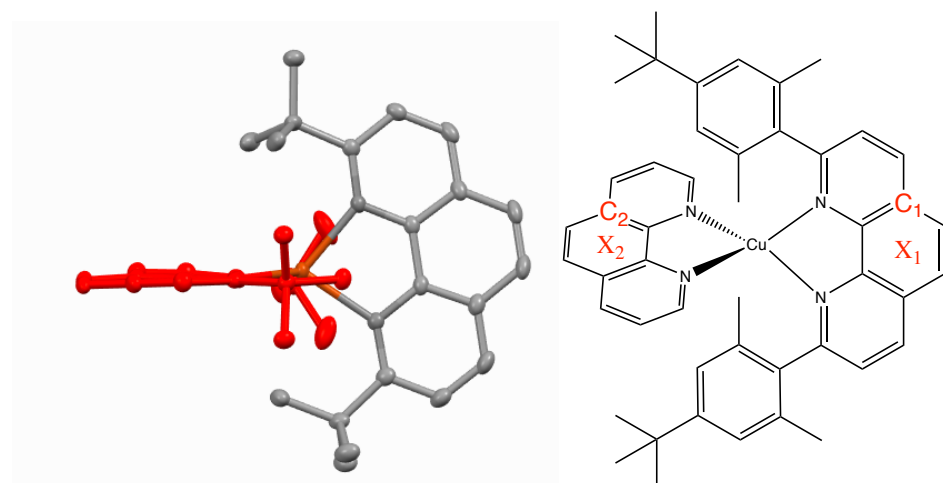


Figure 37: X-ray structures of  $[\text{copper(I)}(2,9\text{-ditert-butylphenanthroline})_2]^+$  (left) and a representation of the phenanthroline for analysis in Table 1 (right);  $X_n$  is the centroid of the central phenanthroline ring. Hydrogen atoms and anions omitted for clarity

Table 2: X-ray parameters of **C3**, **C4**, **C5** and  $[\text{copper(I)}(2,9\text{-ditert-butylphenanthroline})_2]^+$  ( $[\text{Cu}(\text{ditBuphen})_2]^+$ )

Experimental	<b>C3</b>	<b>C4</b>	<b>C5</b>	$[\text{Cu}(\text{ditBuphen})_2]^+$
Cu-N <sub>1</sub> (Å)	2.015	2.016	2.049	2.096
Cu-N <sub>2</sub> (Å)	2.083	2.063	2.076	2.129
Cu-N <sub>3</sub> (Å)	2.085	2.023	2.050	2.103
Cu-N <sub>4</sub> (Å)	1.996	2.038	2.035	2.120
X1-Cu-X2°	148	169	173	175
C1-X1-X2-C2°	51	80	81	80

The phenanthroline substituents have a strong influence on the Cu-N bond lengths. Hence, they can give an indication as to the stability of the coordination sphere with a shorter bond implying a more stable complex. The severity of the distortion from the “centred” to the “pac-man” motif was evaluated by looking at the X1-Cu-X2 and C1-X1-X2-C2 angles (parameters in Figure 37, right), values closer to 180° and 90°, respectively, are closer to a centred motif. The X1-Cu-X2 value determines the distortion in the vertical plane and the C1-X1-X2-C2 determines the distortion in the horizontal plane. The angles in Table 2 clearly showed that **C4** and **C5** were near perfectly tetrahedral and **C3**, lacking the additional phenyl rings at the 4,7-positions, was deformed to the “pac-man” motif, quantitatively demonstrating the effect of this novel remote control. The efficiency of this remote control was confirmed by comparing the angles found for the complexes with that of the standard, [copper(I)(2,9-ditert-butylphenanthroline)<sub>2</sub>]<sup>+</sup> (Table 2). The geometries for the complexes with the remote control were exceedingly close to the standard, demonstrating the efficiency of the remote control and also that the stability of the complexes had not been compromised, as seen for the standard which had longer Cu-N bond lengths. This is therefore a positive result for this new system design as the ground state properties appear to be optimal with near-perfectly tetrahedral geometries.

*Table 3: Calculated parameters for **C3**, **C4** and **C5***

Computational	<b>C3</b>	<b>C4</b>	<b>C5</b>
Cu-N <sub>1</sub> (Å)	2.040	2.056	2.090
Cu-N <sub>2</sub> (Å)	2.111	2.078	2.062
Cu-N <sub>3</sub> (Å)	2.033	2.056	2.069
Cu-N <sub>4</sub> (Å)	2.097	2.052	2.045
X1-Cu-X2°	154	174	169
C1-X1-X2-C2°	79	83	77

DFT calculations were used to confer the lowest energy ground state (Table 3). The calculated values coincided relatively well with the experimental data with the exception of **C3**, where the phenanthroline will most likely oscillate between the two aryl groups to undergo  $\pi$ - $\pi$  stacking with a very low energy barrier. This oscillation makes it difficult to compare the solid state X-ray structures and the calculations carried out in the gaseous state. This effect is not seen for **C4** and **C5** as steric hindrance prevents oscillation and fixes the phenanthroline in the centred geometry. The addition of Grimme’s corrections to the coding calculation means that the Van der Waals interactions will be calculated more exactly, yet the oscillation described above prevents more accurate calculations.

When steric hindrance was not present, as well as the distortion in the vertical plane, there was also a distortion in the horizontal plane, known as a rocking distortion. X-ray structures (Figure 38) showed that this second distortion was also prevented for **C4** and **C5**. The two structures with phenyl group (**C4** and **C5**) presented a central phenanthroline, whereas **C3**, which lacks these phenyl groups, had this distortion. This distortion was once again principally due to  $\pi$ - $\pi$  interactions and by avoiding this interaction, as was the case for **C4** and **C5**, the distortion was minimal.

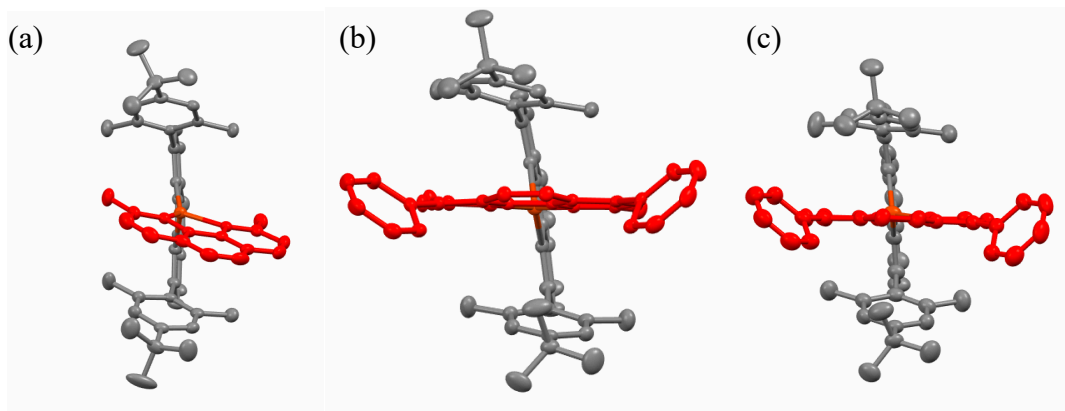


Figure 38: Orthogonal view of (a) **C3**, (b) **C4** and (c) **C5**

The preference for the deformation of the phenanthroline from a “centred” to a “pac-man” motif can be demonstrated visually by carrying out non-covalent interaction (NCI) calculations (Figure 39).

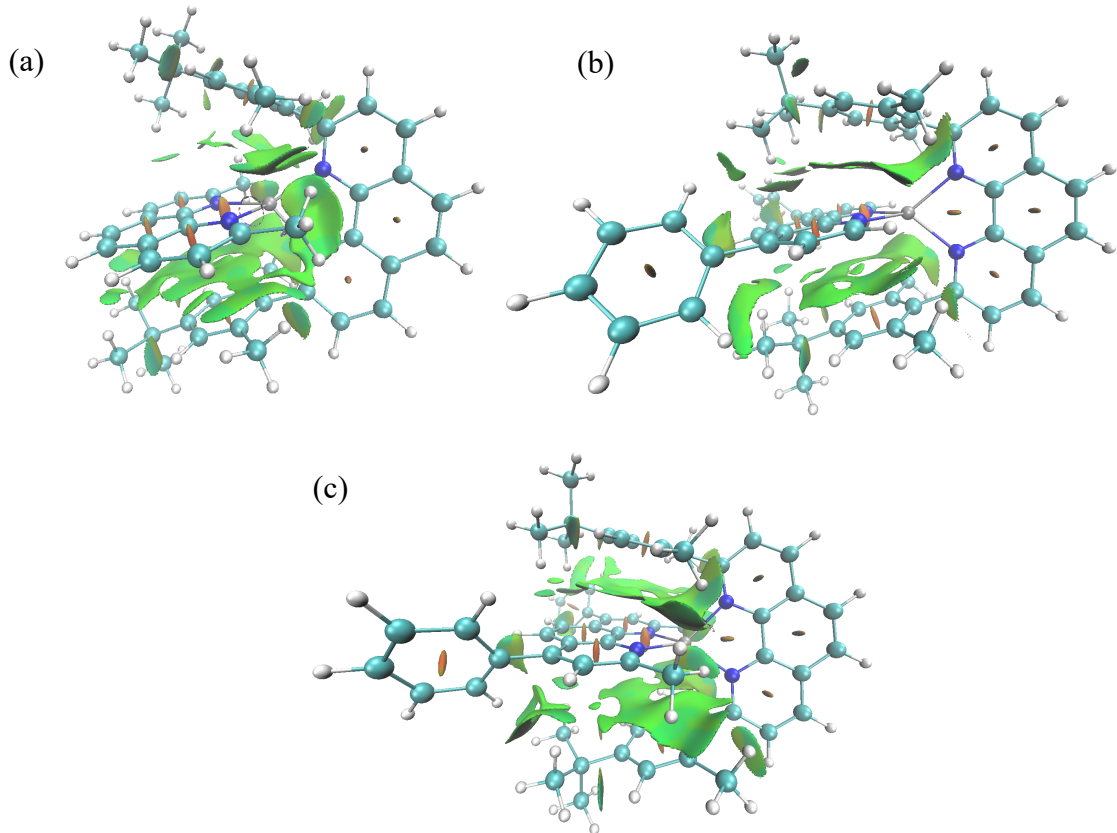


Figure 39: Non-covalent interactions present (a) **C3**, (b) **C4** and (c) **C5**

In Figure 39 the green colour represents these non-covalent interactions. It is apparent that the non-hindered ligand of **C3** (Figure 39a) has shifted to one of the aryl groups in order to undergo  $\pi$ - $\pi$  stacking, as there is a larger amount of green below the second phenanthroline than above. Whereas for **C4** and **C5** (Figure 39b and 39c) it is apparent that the green colour/NCI above and below the second phenanthroline is the same, hence demonstrating that there is no preferential interaction between the phenanthroline and the aryl groups, verifying the reason for a centred geometry.

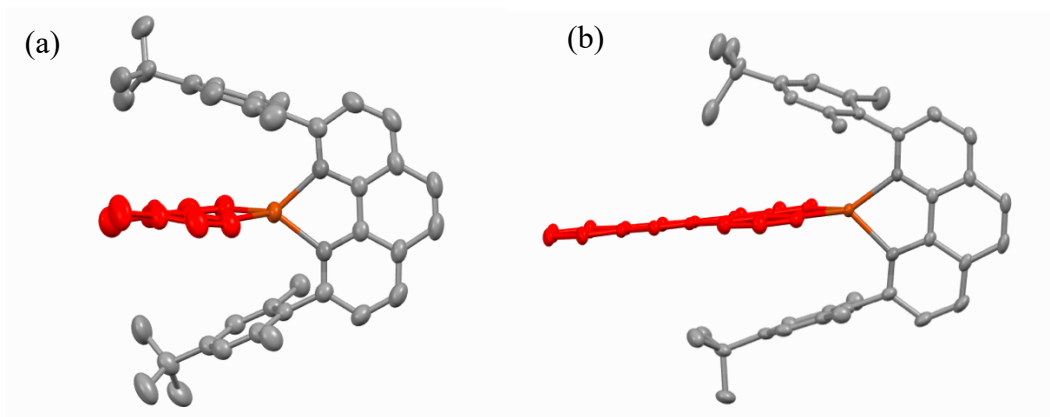


Figure 40: X-ray structures of (a) **C7** and (b) **C10**

The X-ray crystal structure of **C7** (Figure 40a) shows that even with a methyl group interacting with the *tert*-butyl, this was still enough steric hindrance to form a “centred” motif. On the other hand, bipyridine would undergo less  $\pi$ - $\pi$  stacking than phenanthroline, on account of the lack of an additional aromatic ring, hence direct comparison could not be made.

Complexes with the dipyridophenazine (DPPZ) ligand,<sup>10</sup> notably ruthenium(II) or rhodium(III) complexes,<sup>11</sup> have been widely used as molecules intercalating into DNA. Copper(I) complexes are photoactive, and present similar photophysical and photochemical properties, hence it might be interesting to study the intercalating properties of a heteroleptic complex containing the DPPZ ligand, such as **C10**, because its X-ray structure (Figure 40b) shows the planar character of DPPZ.

Table 4: Experimental X-ray parameters of **C7** and **C10**

Experimental parameters	<b>C7</b>	<b>C10</b>
Cu-N <sub>1</sub> (Å)	2.051	2.013
Cu-N <sub>2</sub> (Å)	2.044	2.047
Cu-N <sub>3</sub> (Å)	2.043	2.022
Cu-N <sub>4</sub> (Å)	2.031	2.035
X1-Cu-X2°	175	172
C1-X1-X2-C2°	94	98

Once again, looking at the bond lengths, rigid complexes were observed and the experimental results (Table 4) coincided with the calculated geometry for **C7** (Table 5), demonstrating that this was the most stable geometry for the complex.

Table 5: Computational parameters for **C7**

Computational parameters	<b>C7</b>
Cu-N <sub>1</sub> (Å)	2.069
Cu-N <sub>2</sub> (Å)	2.057
Cu-N <sub>3</sub> (Å)	2.051
Cu-N <sub>4</sub> (Å)	2.039
X1-Cu-X2°	177
C1-X1-X2-C2°	74

### 1.3.2 Electronic properties

The electronic properties of **C1-10** were analysed by cyclic voltammetry (CV) in dichloromethane with tetra-n-butylammonium hexafluorophosphate being used as the supporting electrolyte. The cyclic voltammograms of **C1-C10** showed the oxidation of copper(I) to copper(II) (Table 6), with this oxidation leading to a flattening distortion of the complex. Consequently, quite large potential differences were observed. The values obtained provided an indication of the reversibility of the redox process, with large potential differences hinting at a less reversible process, meaning there was more of a geometry change on passing from copper(I) to copper(II). This meant that the steric bulk was less efficient in such complexes.

Table 6: Summary of electrochemical data for **C1-10**<sup>a</sup>

	Anodic peak potential (Volt)	Cathodic peak potential (Volt)	Potential difference (Volt)
<b>C1</b>	0.52	0.05	0.47
<b>C2</b>	0.38	0.26	0.12
<b>C3</b>	0.47	0.36	0.11
<b>C4</b>	0.51	0.28	0.23
<b>C5</b>	0.60	0.36	0.24
<b>C6</b>	0.23	0.13	0.10
<b>C7</b>	0.32	0.065	0.26
<b>C8</b>	0.42	0.076	0.34
<b>C9</b>	0.55	0.47	0.08
<b>C10</b>	0.54	0.32	0.22

<sup>a</sup>  $CH_2Cl_2$ ,  $NBu_4PF_6$  (0.1M), 100 mV/s, vs.  $Fe^{+}/Fe$

The oxidation potentials are in accordance with what would be expected for HETPHEN complexes. Generally, increasing the steric bulk leads to more positive oxidation potentials. Greater potential differences are observed for the HETPHEN complexes with bipyridine moieties (**C7** and **C8**) as these are less-hindered ligands, potentially demonstrating the instability of the complex and/or a large distortion on oxidation of the copper(I). The potentials are also dependent on the substituents, with electron-donating groups leading to lower oxidation potentials (notably **C6**) and electron withdrawing groups presenting higher oxidation potentials (notably **C5**). This is most likely due to the apparent stabilisation or destabilisation of the HOMO.

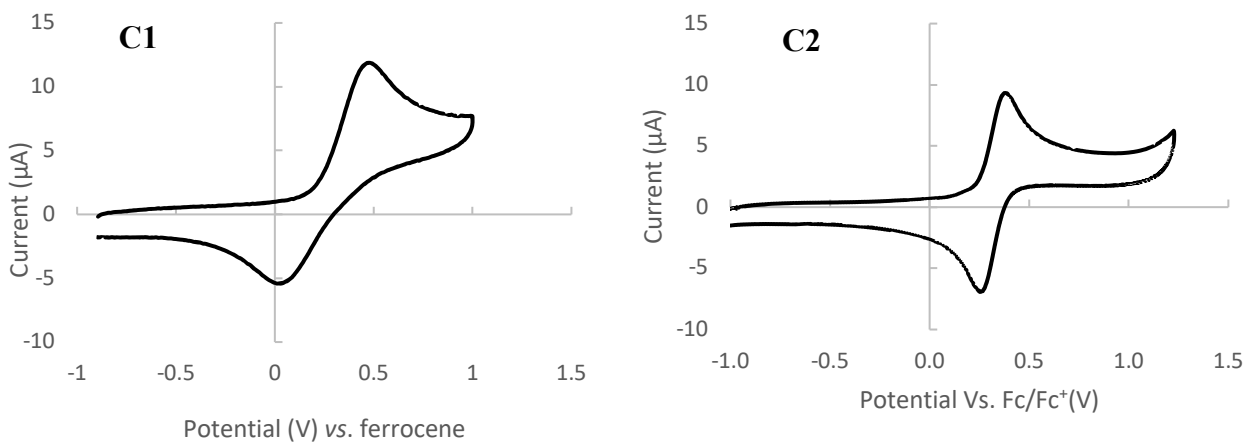


Figure 41: CV of **C1** (left) and **C2** (right) in dichloromethane with tetrabutylammonium hexafluorophosphate (0.1 M) at a scan rate of 100 mV/s.

Compared to the homoleptic complex **C1** (Figure 41, left), all of these complexes show a much more reversible process with the potential difference for **C1** being 0.46, with the larger flattening distortion leading to a less reversible process. For the heteroleptic complexes where the geometrical change is less accessible on account of the steric hindrance, much smaller potential differences are observed, an example of which is **C2** in Figure 41.

The electronic spectra of **C1-C10** show two characteristic peaks one of which being in the UV-region (around 280 nm), corresponding to a  $\pi-\pi^*$  transition of the phenanthroline moiety and the second being in the visible region (around 450 nm) corresponding to an MLCT between the copper(I) and the phenanthroline. The wavelength of these transitions is dependent on the substituents present on the phenanthroline, with the greatest bathochromic shift and highest molar extinction coefficient ( $\epsilon$ ) being for **C4**, thanks to the phenyl groups at the 4,7-positions of the phenanthroline. As an example, **C5** is shown in Figure 42. The data for all of the complexes is summarised in Table 7.

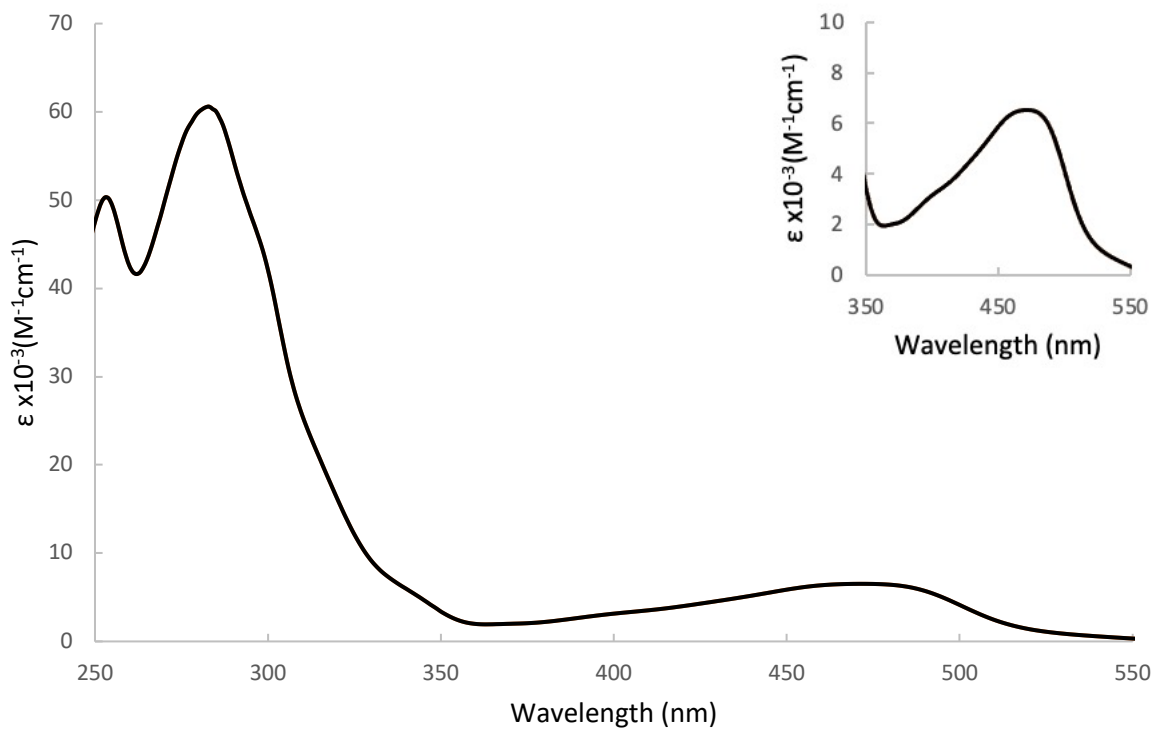


Figure 42: UV-Visible spectrum of **C5**, with a zoom of the visible region in dichloromethane at room temperature

Table 7: Summary of electronic properties of **C1-C9**

Complex	<b>C1</b>	<b>C2</b>	<b>C3</b>	<b>C4</b>	<b>C5</b>	<b>C6</b>	<b>C7</b>	<b>C8</b>	<b>C9</b>	<b>C10</b>
$\lambda_{\max}$ (nm)	276 461	276 461	277 468	285 496	286 477	279 470	275 475	276 478	279 442 577	275 476
$\epsilon \times 10^{-3}$ (M⁻¹cm⁻¹)	5100 6100	47900 6700	56100 5600	69200 8100	60000 6500	57200 6300	43600 6300	43500 6500	39200 2200 2300	81200 6800

These results are in accordance with other copper(I)  $\alpha$ -diimines present in the literature.<sup>12</sup> The MLCT band observed is also broad, demonstrating additional advantages for these complexes to be used for potential applications in light to energy conversion. Generally, a blue shift is observed for complexes with increased steric hindrance. **C9**, with a biquinoline moiety, presents an additional MLCT band at 577 nm between the copper and the biquinoline. Addition of phenyl groups at the 4,7-positions enhances the absorption properties with higher visible light absorption for **C4** and **C5**. This is in accordance with the literature.<sup>13</sup>

A greater understanding of these electronic transitions was gained by utilising TheoDORE (Theoretical Density, Orbital Relaxation and Exciton) analysis (Figure 43) on four of these complexes (**C3**, **C4**, **C5** and **C7**). The spectrum was originally calculated using ADF software and the data was then converted to TheoDORE. Here, the complex was divided into three parts: copper(I), ligand 1 and ligand 2, with the contribution from each part coming from the occupation or emptying of orbitals.

The graphs below show the first 50 excitation singlet states of complexes **C3**, **C4**, **C5** and **C7** respectively. Each bar represents a transition from 1-50. The y axis shows the character of said transition, be it MC, LC, MLCT, LMCT or LLCT. The type of transition is represented by the colour of the bar which is shown in the key on the right of Figure 43. The x-axis shows the transition state from 1 to 50 in ascending order. These results are comparable with the experimental observations, with low energy transitions being the MLCT state (s1 to  $\sim$  s20). The MLCT is also broad, which is evident from the number of MLCT transitions present. This is most likely due to the large number of rotamers possible for the complexes (notably, rotating *tert*-butyl and phenyl groups) and higher transitions being the LC and LLCT ( $\sim$ s20 -s50) i.e. the  $\pi$ - $\pi^*$  transitions observed at  $\sim$ 280 nm. The results also demonstrate that MC transfers and LMCT are not present.

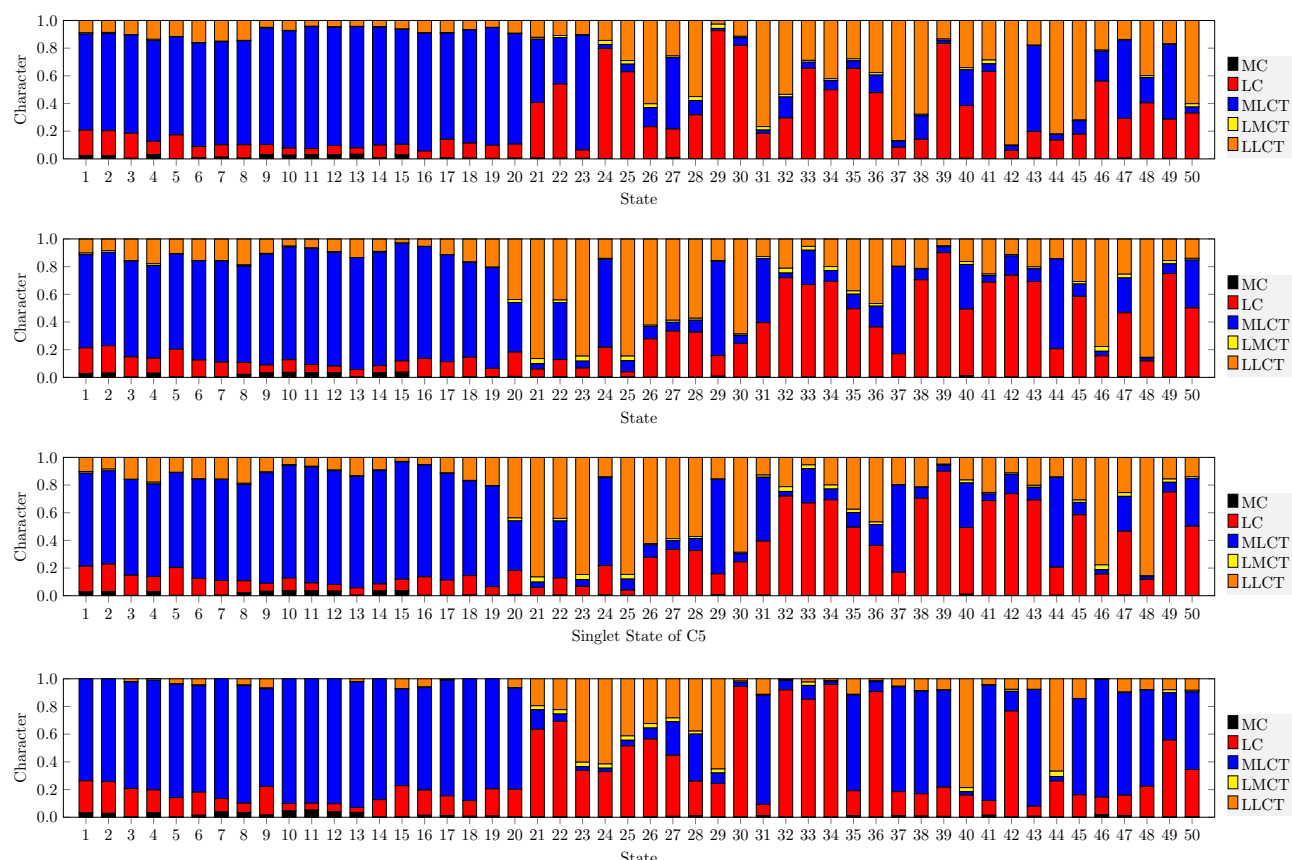


Figure 43: TheoDORE analysis of **C3**, **C4**, **C5** and **C7**, respectively. This shows the nature of the transitions in the calculated absorption spectra

### 1.3.3 Photoluminescence properties

The photoluminescent properties of **C2-C10** were then studied using a fluorimeter and excitation at 456 nm. The results of these studies are displayed in Table 8 and an example is shown in Figure 44. Unfortunately, emission was only observed for the complexes **C3** and **C5** with the other seven complexes showing no emission between 470 nm and 800 nm.

*Table 8: Summary of emission properties of **C3** and **C5**. The other complexes did not emit at a measurable wavelength*

	<b>C3</b>	<b>C5</b>
Lifetime (ns)	58	44
Emission (nm)	680	697

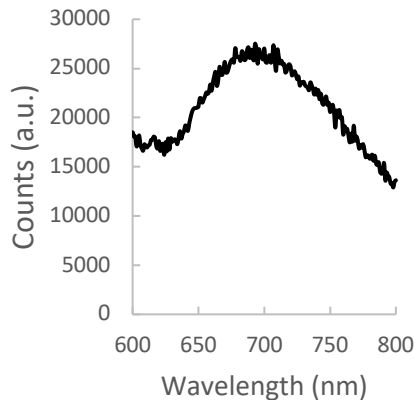


*Figure 44: Emission spectrum of **C5** in dichloromethane on excitation at 456 nm.*

The only two complexes where an emission was observed was with methyl groups at the 2,9-positions (**C3** and **C5**), demonstrating the necessity of the steric hindrance at the coordination site for optimal photoluminescent properties. The emission for **C5** (Figure 44) is not very intense showing an inefficient excited state process. Hence, the starting hypothesis that steric hindrance away from the coordination site was sufficient to prevent quenching of the exciplex appears to be inaccurate. This could be on account of a lower energy level of the excited state with less steric hindrance. Comparing **C2** and **C3** shows the dramatic effect of simply adding a methyl group at the 2,9-positions of the phenanthroline, with this methyl group leading to an observable emission for **C3** and a lifetime of 58 ns.

Comparison of **C3** and **C5**, where the difference is the substitution of phenyl groups at the 4,7-positions, surprisingly shows that the lifetime is longer for **C3** (58 ns) without the phenyl groups

compared to the 44 ns measured for **C5**. This demonstrates that for these complexes, the concept of remote control away from the coordination site is a futile way to try and improve the excited state properties. This could be due to the increased amount of rotamers present on addition of phenyl groups, which could potentially lead to a more preferential non-radiative decay pathway (*vide infra*). The fact that neither **C4** nor **C6** have an observable lifetime shows that additional substitution away from the coordination site does not optimise the lifetime. Yet, the additional charge density from the donating methyl groups could also destabilise the excited state which could lead to a decrease in the excited state lifetime. The two  $[\text{Cu(I)(phenanthroline)(bipyridine)}]^+$  complexes, **C7** and **C8**, show that increasing the steric bulk at the 4,4'-positions from a methyl to a *tert*-butyl has limited effect as neither of these complexes emit at a measurable wavelength.

Comparing **C4**, **C5** and **C6** shows that electron withdrawing and electron donating groups have limited impact on the excited state properties for the complexes. The lack of emission or **C9** shows changes need to be made before progressing onto using these complexes for DSSCs.

From these results, it is apparent that the alkyl groups at the 2,9-positions are necessary for prolonged excited state lifetimes.

A greater understanding of the excited state properties of these complexes is therefore necessary in order to account for these poor lifetimes. DFT calculations (Table 9) were thus carried out on four selected complexes among the nine studied (**C3**, **C4**, **C5** and **C7**). It is assumed that a greater geometrical distortion will lead to a shorter lifetime in the excited state. However, the excited state geometries showed minimal distortion from the tetrahedral geometry compared to the ground state, most likely due to the large amount of steric hindrance present between the *tert*-butyl and the phenyl, as **C3** displays a larger distortion, with the lack of the phenyl moiety. Consequently, other factors must be at play, as these complexes prevent distortion yet still low lifetimes.

Table 9: Calculated geometrical properties of the excited state complexes **C3**, **C4**, **b** and **C7**. ES= excited state

Computational ES	<b>C3</b>	<b>C4</b>	<b>C5</b>	<b>C7</b>
Cu-N <sub>1</sub> (Å)	1.966	2.038	1.976	1.968
Cu-N <sub>2</sub> (Å)	1.972	2.027	1.966	1.970
Cu-N <sub>3</sub> (Å)	2.050	1.964	2.030	2.00
Cu-N <sub>4</sub> (Å)	2.044	1.949	2.049	2.01
X1-Cu-X2°	178	176	176	179
C1-X1-X2-C2°	70	64	70	72

Table 10: Differences between the calculated geometrical properties of the excited and ground state complexes **C3**, **C4**, **C5** and **C7**

Difference between excited and ground state geometries	<b>C3</b>	<b>C4</b>	<b>C5</b>	<b>C7</b>
Cu-N <sub>1</sub> (Å)	0.074	0.018	0.11	0.101
Cu-N <sub>2</sub> (Å)	0.139	0.051	0.096	0.087
Cu-N <sub>3</sub> (Å)	0.017	0.092	0.039	0.051
Cu-N <sub>4</sub> (Å)	0.053	0.103	0.004	0.038
X1-Cu-X2°	24	2	7	2
C1-X1-X2-C2°	9	19	7	2

Comparing the ground state with the excited state geometrical values (Table 10), large differences in bond lengths is one way of showing on which phenanthroline the radical anion occupies, as an increase in the Cu-N bond length is observed on passing from the ground to the excited state. The SOMO of **C5** (Figure 45) shows the radical anion is positioned on the sterically hindered phenanthroline for this complex.

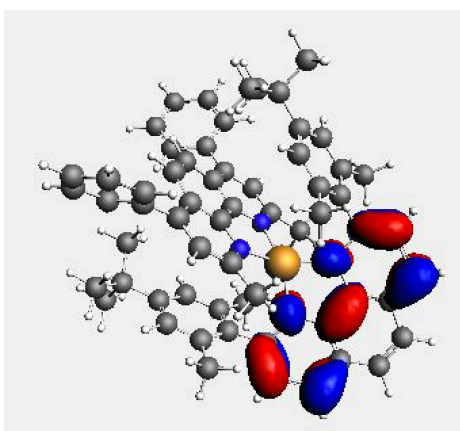


Figure 45: SOMO of excited complex **C5**

The calculated geometries of the ground state and excited state complexes show the efficiency of the blocking provided by the phenyl and *tert*-butyl groups (for **C4** and **C5**) as there is minimal change in the X1-Cu-X2° values between the ground and excited states, differences of 7° and 2° respectively, shown visually in Figure 46. The lack of distortion could mean that the formation of an exciplex would most likely occur due to lack of steric hindrance at the coordination site, as opposed to a distortion from the near-tetrahedral geometry.

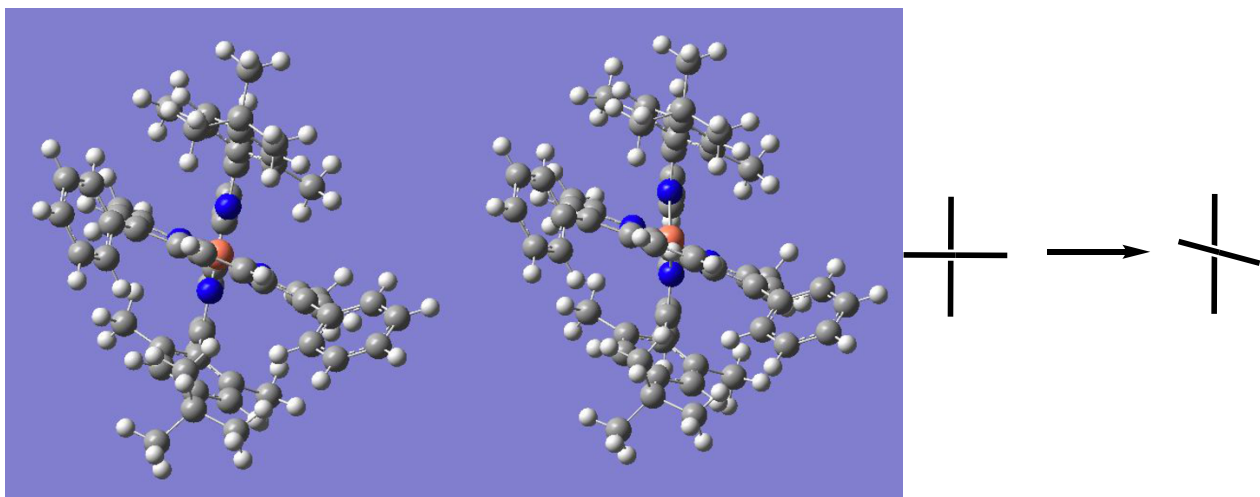


Figure 46: Calculated optimised geometries of **C5**. Complex in the ground state (left) and excited state (middle) with the expected distortion (right)

For the complex without remote steric hindrance (**C3**), there is a difference of 24° between the ground and excited state for the X1-Cu-X2° value. For the complex with remote steric hindrance (**C4**), there is a difference of 19° for the C1-X1-X2-C2° value. When steric hindrance is present both at and away from the coordination site (**C5**) the differences for both of these values is minimal, demonstrating that the steric hindrance away and at the coordination site is necessary in these complexes in order to have minor geometrical deformation on excitation.

These results potentially show an optimisation of the geometry in the vertical plane on utilisation of steric hindrance away from the coordination site, consequently blocking the disfavoured  $\pi$ - $\pi$  stacking, yet a limited optimisation of distortion into the vertical plane due to the lack of steric hindrance. This would be backed up experimentally as **C3** and **C5** were the two complexes with the longest lifetimes of the series and the only two showing measurable emissions. A tentative conclusion could be that horizontal distortion is more significant than vertical distortion. Prevention of horizontal distortion can be provided by larger groups at the 2,9-positions. This is however not a parameter that can be easily changed for heteroleptic complexes as the steric hindrance is already large because of the sterically hindered phenanthroline. Yet, these results do not explain the differences in luminescent properties between **C3** and **C5**.

Table 11: Calculated excited state properties of the complexes **C3**, **C4**, **C5** and **C7**. Phen=phenanthroline

	Triplet (kcal/mol)	Singlet (kcal/mol)	Triplet (on other Phen) (kcal/mol)	Emission (nm)	$\Delta E_{ST}$ (kcal/mol)
<b>C3</b>	-17514.24	-17501.87	-17514.32	832	12.37
<b>C4</b>	-20196.76	-20188.239	-20196.18	855	8.52
<b>C5</b>	-21058.78	-21087.09	Didn't work	819	28.31
<b>C7</b>	-17042.66	-17059.32	Didn't work	907	16.66

Looking at the emission values, it is apparent why no emission could be recorded as these values are considerably higher than the max emission range of the fluorimeter.

Greater understanding of the excited state properties was gained by calculating the energies of the triplet and singlet states and the coupling between these two states (Table 11). Calculations showed that apart from **C4**, the radical anion was present on the sterically hindered phenanthroline ligand. Considering the fact that **C3** and **C5** had the longest lifetimes, calculations were carried out in order to place the radical anion on the other phenanthroline in order to see whether there was a large difference in energy depending on which phenanthroline the radical anion was located. This proved not to be the case, with minimal differences in the excited state energy when the radical anion was placed on either phenanthroline for **C3** and **C4**. For **C5** and **C7**, these calculations were not possible as the radical anion always went onto the sterically hindered phenanthroline. Calculations showed that the energy difference of the triplet states of **C4** and **C5** was minimal, yet their lifetimes were considerably different. Consequently, stabilisation of the radical anion was not a viable hypothesis for optimisation of the excited state properties. This is a very tentative conclusion.

The difference in energy between the singlet and triplet state,  $\Delta E_{ST}$ , could be a potential factor that affected the excited state lifetime, with smaller differences between these two states meaning that interconversion between the singlet and triplet state will be facile. This led to two observations: one, that the relaxation pathway was most likely thermally activated delayed fluorescence (TADF), as the ground and singlet state have a greater coupling than the ground and triplet state, meaning that relaxation *via* the singlet state is favoured and hence relaxation most likely occurs from the singlet state. Two, that this small difference in  $\Delta E_{ST}$  would lead to a shorter lifetime, because of a more favourable relaxation pathway from the singlet to the ground state *cf.* the triplet to the ground state leading to a shorter excited state lifetime. **C7** has other fundamental issues, such as the lack of rigidity

in the bipyridine and the number of potential rotamers that hinders its excited state properties, as these factors increase non-radiative decay.

The experimental emission value for **C5**, 697 nm, is far away from the value calculated, 819 nm. One explanation for this could be the fact that the calculation was carried out from the triplet state, whereas it is possible that the emission occurs from the singlet state through thermally activated delayed fluorescence (TADF). This state can be populated *via* a reverse intersystem crossing, the similar energies of the triplet and singlet state would allow this to be possible. Switching from the triplet to the singlet state will obviously have a major impact on the value observed. Another possible reason could be that the value calculated comes from one possible energy state minimum and what is observed experimentally is not what is observed computationally. This hypothesis was tested by calculating the emission from three of these possible rotamers (Table 12), with the phenyl groups being either central, to the left or to the right. This hypothesis proved to be correct with the second rotamer giving a value similar to the first (821 nm) and the third giving a value closer to that observed experimentally (662 nm). This was the rotamer with the phenanthroline in a near-perfect tetrahedral geometry, once again demonstrating that distortion of the exciplex to a square-planar geometry is not the deciding factor for the short lifetime of these complexes. The energy difference between these three rotamers is 3 kcal/mol and consequently they will probably oscillate between each other in the excited state.

Table 12: Comparison of excited state properties for rotamers of **C5**

Rotamer of <b>C5</b>	Excited state energy (kcal/mol)	Emission (nm)
1	-21058.78	819
2	-21061.49	821
3	-21058.33	662

Apart from quenching of the exciplex by forming a fifth coordination site on distortion from the tetrahedral geometry, another possible hypothesis for the relaxation pathway could be that many possible rotamers are possible for these complexes (*vide supra*). Consequently, favouring non-radiative pathways, this is backed up by the fact that the complexes are low emitting and therefore the decay that is observed is more likely to be fluorescence than phosphorescence.

The fact that the crystal structure of **C7** displays a near-perfect tetrahedral geometry (Figure 40a) shows that the phenyl groups could potentially be replaced by methyl groups. This would avoid the problem of rotamers but keep the steric hindrance at the 4,7-positions allowing for the formation of

near-perfectly tetrahedral complexes. Therefore, complexes with 2,4,7,9-positions substituted should be considered.

## 1.4 Conclusion

To conclude this chapter, nine heteroleptic complexes have been synthesised and their ground state and excited electronic properties have been studied. The sterically hindered phenanthroline chosen was one with 2,6-dimethyl-4-(*tert*-butyl)phenyl at the 2 and 9 positions of the phenanthroline, hence maximising steric hindrance. When the complexes contained phenyl groups at the 4,7-positions of the phenanthroline, they presented a near-perfect tetrahedral ground state geometry on account of steric interactions between the *tert*-butyl of the aryl group of the adjacent phenanthroline and the phenyl groups at the 4,7-positions of the phenanthroline. This allowed for the development of a new way to form near perfectly tetrahedral copper(I) complexes with steric hindrance away from the coordination site. Multiple X-ray structures allowed proof of concept and demonstrated the necessity of these two parameters in order to form tetrahedral complexes. Unfortunately, the excited state properties were not as optimal as the ground state properties and low emitting complexes with short excited state lifetimes were observed. This demonstrated the necessity of steric hindrance at the coordination site in order to obtain optimal excited state properties.

DFT calculations allowed for a greater understanding of the relaxation pathways. Minimal distortion in the vertical plane was observed when steric hindrance away from the coordination site was present and minimal distortion in the vertical plane when steric hindrance was present at the coordination site. Multiple rotamers are possible for such highly substituted molecules, therefore potentially this is the downfall of these complexes with an increase in the amount of non-radiative decay processes being possible.

In order to improve these properties, greater steric hindrance should be added at the 2,9-positions of the phenanthroline in order to prevent distortion in the horizontal plane, without impeding the stability of the complex. Potentially decreasing the number of rotamers by replacing the aryl substituents at the 2,9-positions with a mesityl group could also be advantageous. However, this would lead to less protection of the metal site so this potentially outweighs the other factors, but the calculations would become simpler. Also, replacing the phenyl groups at the 4,7 positions with methyl groups would decrease the number of rotamers. A complex like **C6** with additional steric hindrance at the 2,9-positions (methyl groups for example) would be an interesting complex to synthesise. Alternatively, a different approach could be envisaged where the second phenanthroline could be replaced by a

biphosphine ligand.<sup>14</sup> In doing so, non-radiative decay would be disfavoured as the MLCT state is higher in energy. Yet, the simplicity and stability of these complexes are still very important points that lead to their ever prominence in the literature.

Considering what has been learned from this project and the results present in the literature, potentially an interesting complex to synthesise would be the one shown in Figure 47. Where the complex is well protected at the coordination site from the aryl groups of the sterically hindered phenanthroline, the methyl substituents at the 3,8-positions will lead to an amplified steric hindrance of the *sec*-butyl groups at the 2,9-positions. The methyl groups at the 4,7-positions will be able to undergo steric interactions with the *tert*-butyl groups of the adjacent aryl substituent. This would block the complex in a centred motif and there would be considerable steric hindrance at the coordination site granted by the alkyl and aryl substituents at the 2,9 positions. If the complex turns out to be too sterically hindered to be stable, the *sec*-butyl groups can be replaced by isopropyl groups.

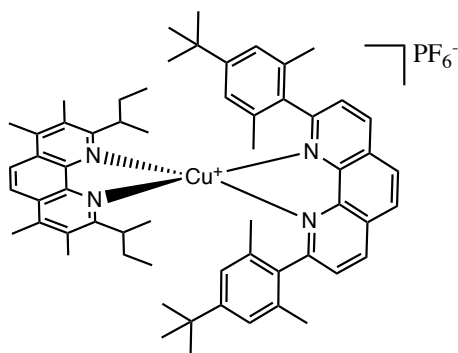


Figure 47: Perspective heteroleptic complex that could potentially be synthesised in the future

## 1.5 References

- 1 O. Green, B. Gandhi, and J. Burstyn, *Inorg. Chem.* 2009, **48**, 5704–5714.
- 2 Mitsui Chem., Japanese Patent, JP 2003342287.
- 3 D. Seebach and H. Neumann, *Chem. Ber.* 1974, **107**, 847–853.
- 4 Q. Dufrois, J.C. Daran, L. Vendier, C. Dinoi and M. Etienne, *Angew. Chem. Int. Ed.*, 2018, **57**, 1786 –1791.
- 5 M. Schmittel, C. Michel, S.-X. Liu, D. Schilbach and D. Fenske, *Eur. J. Inorg. Chem.* 2001, 1155–1166.
- 6 Daniel Uguen, University of Strasbourg, personal communications.
- 7 C. O. Dietrich-Buchecker, J. Guilhem, C. Pascard and J.-P. Sauvage, *Angew. Chem. Int. Ed. Engl.* 1990, **29**, 1154–1156.
- 8 C. O. Dietrich-Buchecker, G. Rapenne, J.-P. Sauvage, A. De Cian and J. Fischer, *Chem. Eur. J.* 1999, **5**, 1432–1439.
- 9 M. Schmittel and A. Ganz, *Chem. Commun.*, 1997, 99-100; M. Schmittel, U. Lüning, M. Meder, A. Ganz, C. Michel and M. Herderich, *Heterocycl. Commun.*, 1997, **3**, 493-498.
- 10 A. Friedman, J.-C. Chambron, J.-P. Sauvage, N. Turro and J. Barton, *J. Am. Chem. Soc.*, 1990, **112**, 4960-4962.
- 11 B. Zeglis, V. Pierre and J. Barton, *Chem. Comm.*, 2007, 4594-4696.
- 12 L. Kohler, R. G. Hadt, D. Hayes, L. X. Chen and K. L. Mulfort *et al*, *Dalton Trans.*, 2017, **46**, 13088–13100.
- 13 S. Garakyaraghi, C. E. McCusker, S. Khan, P. Koutnik, A. T. Bui and F. N. Castellano, *Inorg. Chem.*, 2018, **57**, 2296-2307.
- 14 D. G. Cuttell, S-M. Kuang, P. E. Fanwick, D. R. McMillin, and R. A. Walton, *J. Am. Chem. Soc.*, 2002, **124**, 6-7.

# CHAPTER 2

## Homoleptic copper(I) phenanthroline complexes: Synthesis and properties

2.1 Ligand synthesis	68
2.2.1 Homoleptic complexes	74
2.2.2 Structural properties	75
2.2.3 Electronic properties	79
2.2.4 Photoluminescent properties	81
2.3 Photoluminescent Pt phenanthroline complexes	87
2.4 Conclusion	88
2.5 General conclusions	90
2.6 References	92

## 2.1 Ligand synthesis

Having discovered the concept of remote control (see Chapter 1), a new series of ligands was designed with steric interactions away from the coordination site in the hope that this would lead to a near-perfect tetrahedral structure. The ligands chosen were 1,10-phenanthroline, as a control, and then with either methyl (3,4,7,8-tetramethylphenanthroline) or phenyl (bathophenanthroline) at the back of the phenanthroline. Homoleptic complexes could then be synthesised as there was limited steric hindrance at the coordination site. The phenyl substituent at the 2,9-positions of the phenanthroline was *p*-*tert*-butylphenyl and it was hoped that the strategically placed methyl and phenyl groups would interact sterically with these *tert*-butyl groups present on the aryl substituents of the phenanthroline and that this interaction would lead to a near-perfect tetrahedral geometry (as seen for C7 in Chapter 1).

A series of non-symmetric phenanthroline ligands was also synthesised with *tert*-butylphenyl at the 2-position and 2,6-dimethyl-4-*tert*-butylphenyl at the 9-position. This would allow for the synthesis of stable homoleptic complexes as, if both of the 2,9 substituents were 2,6-dimethyl-4-*tert*-butylphenyl, there would be too much steric hindrance to form a homoleptic complex (see Chapter 1). These non-symmetric ligands contained a large amount of steric hindrance but in the complex the steric hindrance would be away from the coordination site. Hence, it was assumed that once again the phenyl groups at the 4,7-positions of bathophenanthroline would interact sterically with the *tert*-butyl groups of the aryl substituent and that replacing the phenyl with methyl groups would lead to an optimisation of the excited state properties (Chapter 1 shows that phenyl groups may not be optimal for excited state properties).

The starting hypothesis was that methyl groups at the 4,7-positions would be substantial enough to have steric interactions with the *tert*-butyl groups. The series of ligands synthesised in this chapter is summarised in Figure 48.

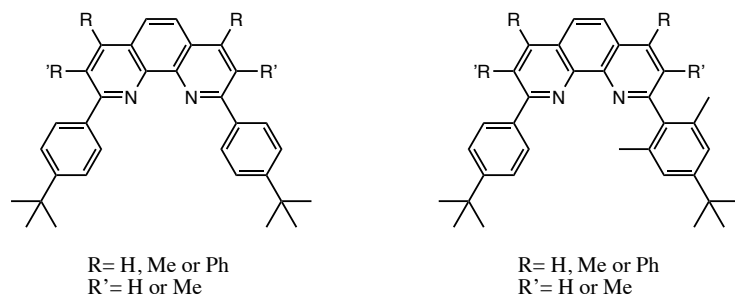


Figure 48: Proposed ligands to form homoleptic complexes

The choice of lithium source proved to be of paramount importance in order to obtain the desired product and once again unexpected substitution patterns were observed depending on the lithium source (as seen for **L3** in Chapter 1).

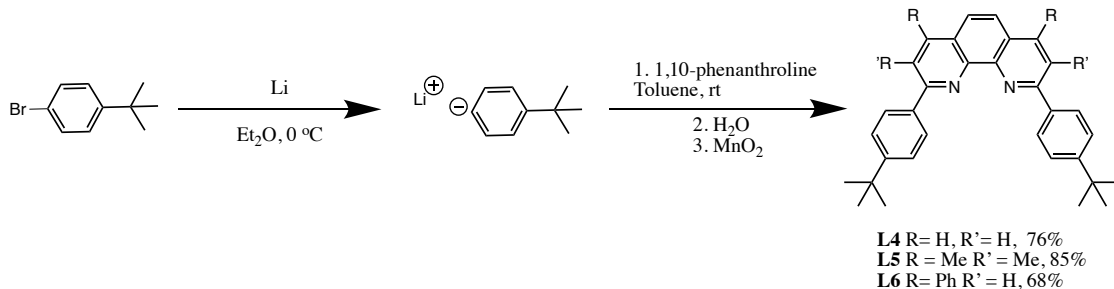


Figure 49: Symmetric ligand synthesis for **L4 – L6**

As seen in Chapter 1, Li metal was the most efficient way to substitute the phenanthroline, with high yields for the formation of the disubstituted product from the starting materials (Figure 49): 1,10-phenanthroline (76%), 3,4,7,8-tetramethyl-1,10-phenanthroline (85%) and bathophenanthroline (68%). In this reaction, only the disubstituted product was observed due to the lack of steric hindrance at the ortho positions of the aryl. These yields are comparable with those in the literature.<sup>1</sup>

Using n-BuLi for the above reaction led to exceedingly low yields, 5-9%, for the three starting phenanthrolines. A potential reason for this could be that the lack of steric hindrance at the ortho position of the aryl means that two aryl groups are able to react with each other: a lithio aryl and a bromoaryl. This cannot occur for 2,6-dimethyl-4-*tert*-butylphenyl as there is too much steric strain with the additional methyl groups for a diaryl to form. The two aryl groups could potentially react with one another during the time allowed for the halogen-lithium exchange process, before the phenanthroline is added, and form the sort of molecule shown in Figure 50, considerably limiting the quantity of aryl-lithium available to react; alternatively the aryl-lithium could be reacting with other electrophilic side products. *tert*-BuLi was not attempted, as the same side reaction would most likely have occurred.

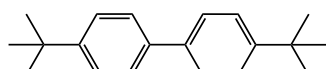


Figure 50: Potential side reaction

In order to synthesise the non-symmetric ligands, the monosubstituted phenanthroline with 2,6-dimethyl-4-*tert*-butylphenyl was the desired starting product. It was synthesised (Figure 51) by adding only two equivalents of the aryl-lithium reagent in order to favour the monosubstituted product. On optimisation of the reaction parameters (Figure 51), the yields for this process were high,

especially for the bathophenanthroline (87%). Large excesses of aryl-lithium proved problematic in reactions and also led to decreased yields in certain cases due to side products (*vide infra*). The heat required for this reaction to occur probably favoured side reactions. Yet, optimisation of the process led to the monosubstituted phenanthroline being the major product.

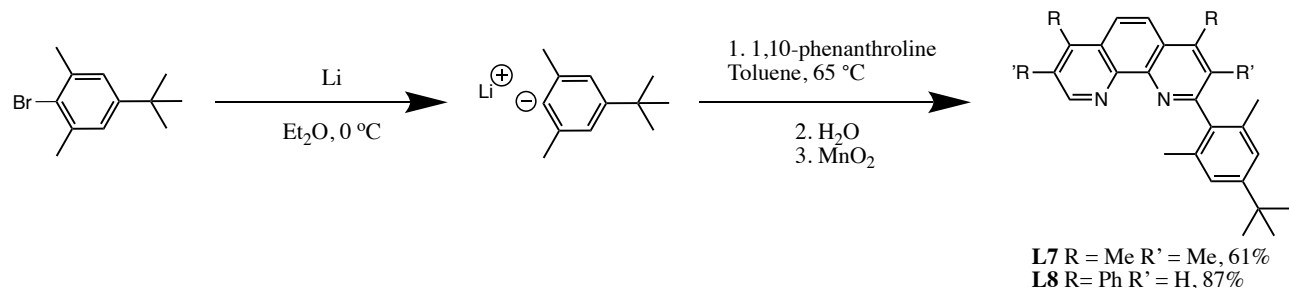


Figure 51: Non-symmetric ligand synthesis for **L1**, **L7** and **L8**

Once the monosubstituted product had been obtained, the non-symmetric ligand was obtained by using lithium metal for the halogen-lithium exchange and lower equivalents of the non-hindered aryl (4-*tert*-butylphenyl, 2 eq.) gave the best result with a high yield of 61% for this reaction to form **L11**. Different synthetic routes were attempted for the synthesis shown in Figure 52. On addition of higher equivalents of aryl substituents (5 eq.) the reaction worked considerably less efficiently (22% yield for **L9**) probably on account of the aryl side products formed (*vide supra*).

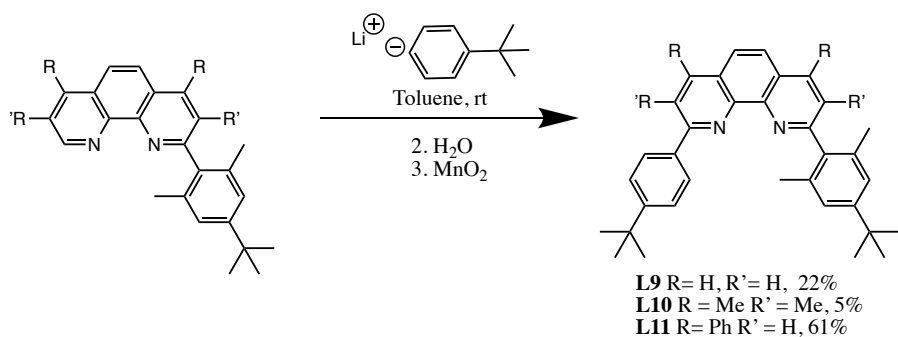


Figure 52: Second step of non-symmetric ligand synthesis

Using n-BuLi for the halogen lithium-exchange in **L10** proved to be highly inefficient with a 5% yield for the monosubstituted product. This could potentially be due to excess n-BuLi deprotonating one of the methyl groups of the phenanthroline, which can then lead to a multitude of side reactions. This was indeed the case as the side product shown below was isolated (Figure 53).

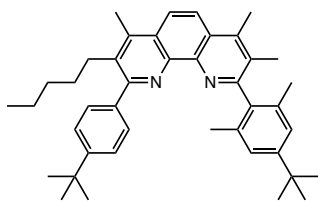


Figure 53: Side-product for synthesis of **L10**

Even when using lithium metal, if larger amounts of the aryl substituent (5 eq.) and high temperatures were used, side products formed. The most interesting side product observed was for the substitution of bathophenanthroline with 2,6-dimethyl-4-*tert*-butylphenyl, where alongside the disubstituted bathophenanthroline (60%), the two other major products formed during this reaction (**L12** and **L13**) are shown in Figure 54.

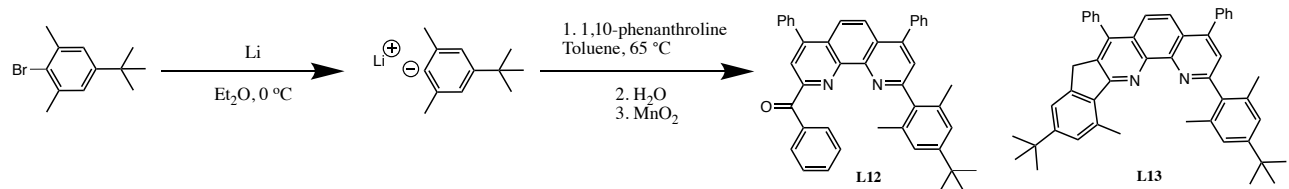


Figure 54: Side reactions during ligand synthesis

As seen in Chapter 1, it is possible to add a tolyl group to the phenanthroline, the addition occurred at the 7 position of the phenanthroline in Chapter 1 and it was hypothesised that the reason for this was due to a lithium cluster sterically blocking the 9-position from nucleophilic attack. The 7-position was already substituted by a phenyl group in bathophenanthroline and consequently substitution could not occur at this position, leading to substitution of the tolyl group at the 9-position of the phenanthroline. As the reaction was heterogeneous, a large excess of  $\text{MnO}_2$  was used to rearomatise the phenanthroline, meaning that this step also leads to the oxidation of the benzyl position to a ketone (**L12**).

Cyclising to form a carbon-carbon bond is a very sought-after process in synthetic chemistry. The cyclisation to form **L13** occurred in a slightly peculiar way, with the most likely reaction pathway being the deprotonation of the methyl group of the aryl substituent *via* a lithium source, potentially one that was in close proximity as the nitrogen will be negatively charged after addition of the aryl group. This methyl anion can then attack the 8-position of the phenanthroline and lead to the cyclised product **L13**. The blocking of the 4,7-positions with phenyl groups obviously prevents substitution and renders the phenanthroline more electrophilic, which could be another possible explanation for these unexpected and unprecedented substitution pathways.

The  $^1\text{H}$  NMR of **L12** and **L13** are shown in Figure 55 and 56, respectively and the spectra coincide with the proposed structures; mass spectrometry also helps to confirm this. Unfortunately, crystals suitable for X-ray diffraction were not able to be grown in order to have a conclusive response, yet these two structures coincide with NMR ( $^1\text{H}$  and  $^{13}\text{C}$ ) and HR-MS. These were both side products for the reactions, with only very small amounts of each product being produced.

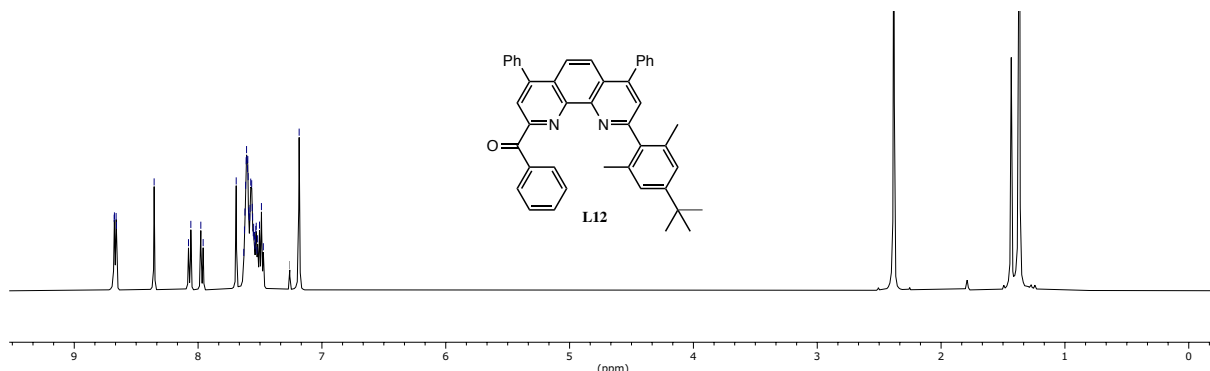


Figure 55:  $^1\text{H}$  NMR of **L12** in  $\text{CDCl}_3$

The crucial parts of this spectrum are that the 9-positions have been substituted as no peaks are present above 9 ppm and the phenanthroline is non-symmetrical as the 5,6-positions are non-equivalent at 8 ppm. The deciding factor was the presence of a ketone signal at 192.8 ppm in the  $^{13}\text{C}$  NMR spectrum.

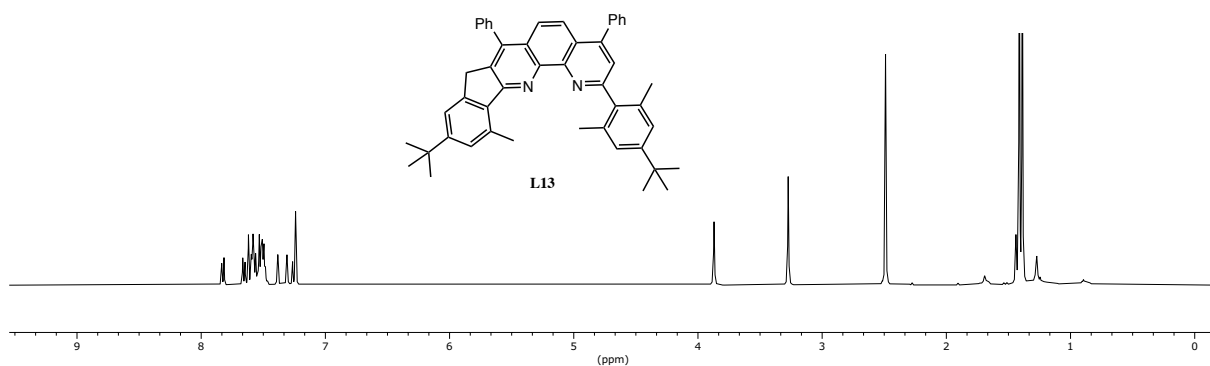


Figure 56:  $^1\text{H}$  NMR of **L13** in  $\text{CDCl}_3$

Once again, **L13** was substituted at the 2,9-positions as no peaks were present higher than 9 ppm. The aryl groups at about 7.3 ppm are non-equivalent (3 peaks), demonstrating that the symmetry had been broken. As for **L12**, the 5 and 6 positions are non-equivalent just below 8 ppm. Looking at the aliphatic part of the spectrum, the peak at 3.9 ppm integrated for 2, at 3.3 ppm it integrated for 3 and at 2.5 ppm the peak integrated for 6, meaning that one of the protons belonging to the methyl group of the aryl substituent was no longer present. The lack of a proton at the 8 position hints that a cyclisation has occurred.

Another set of non-symmetric ligands (**L14** and **L15**, Figure 57) was also synthesised in an attempt to gain a greater understanding of these complexes. To assess whether the *tert*-butyl substituent on the aryl was having a positive or negative effect on the photoluminescent properties, a non-symmetric ligand was synthesised with the sterically demanding 2,6-dimethyl-4-*tert*-butylphenyl at the 2-position and with a simple phenyl group at the 9-position. The effect of adding aliphatic groups was assessed by synthesising a phenanthroline with 2,6-dimethyl-4-*tert*-butylphenyl at the 2-position and an n-butyl group at the 9-position. Both reactions were carried out by simply adding the appropriate lithium source: phenyl lithium or n-butyl lithium, respectively.

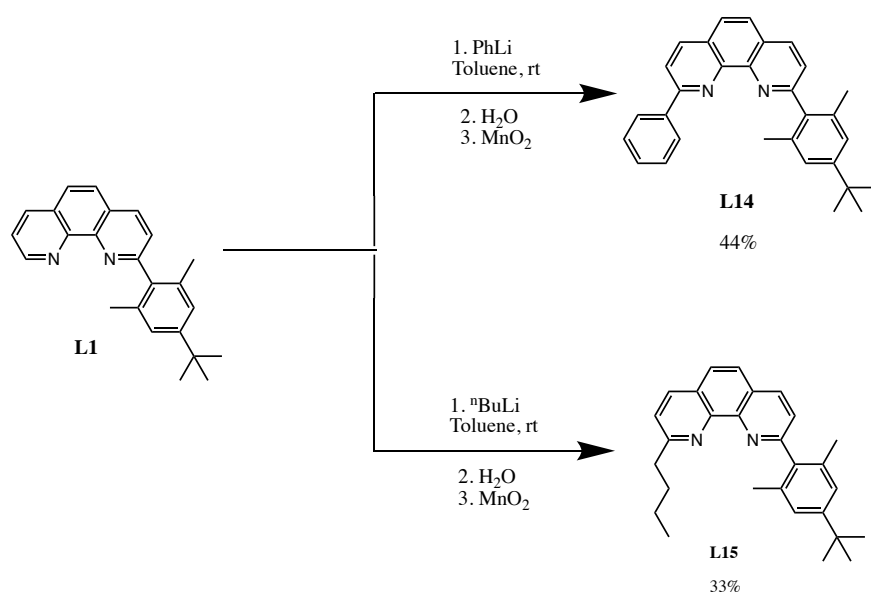


Figure 57: Non-symmetric ligand synthesis

To summarise the ligand synthesis, the synthesis of substituted phenanthrolines is not always predictable as many side reactions are able to occur. Some tentative conclusions are that utilising Li metal in order to prevent nucleophilic and electrophilic side products after the halogen-lithium exchange leads to a more efficient synthesis. Decreasing the number of equivalents in order to obtain solely the monosubstituted product with minimal side reactions is always a good way to optimise these reactions. On heating, the reaction becomes more complicated with more side-products, however this unfortunately cannot be avoided as the heat is needed to substitute the bulky aryl groups.

## 2.2.1 Homoleptic complexes

The symmetric homoleptic complexes (**C11-C13**) were synthesised by using  $[\text{Cu}(\text{CH}_3\text{CN})_4]\text{PF}_6$  as a copper(I) source (Figure 58) and formed the products in high yields: **C11** (74%), **C12** (91%) and **C13** (63%).

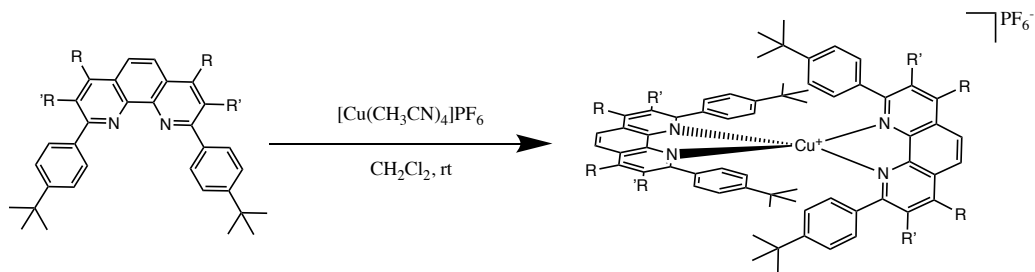


Figure 58: Formation of the homoleptic copper(I) complexes (**C11 – C13**)

The non-symmetric complexes (**C14-C19**) were also synthesised in the same way with similarly high yields and equally high purity. The following complexes (Figure 59) have thus been synthesised:

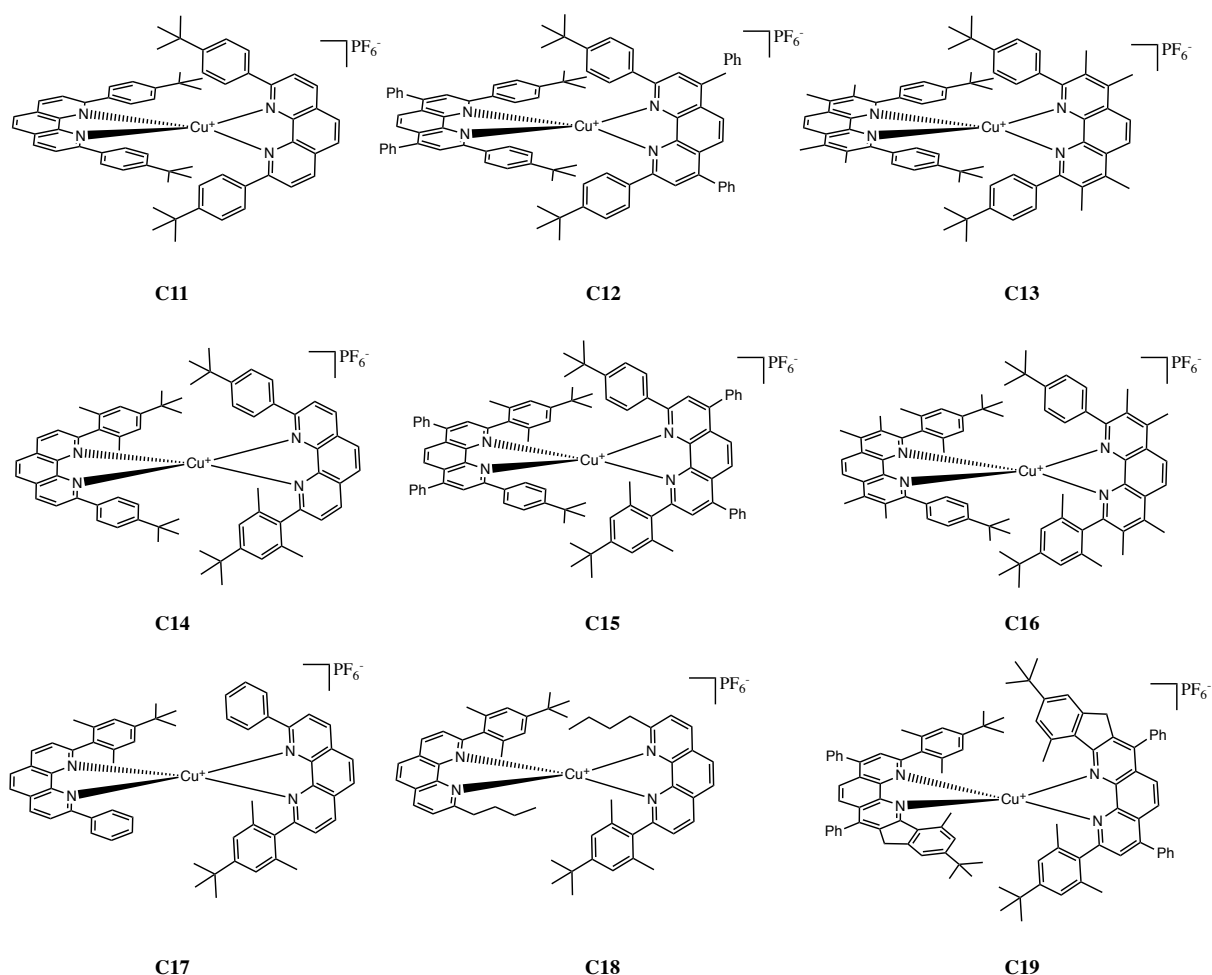


Figure 59: Homoleptic copper(I) phenanthroline complexes

## 2.2.2 Structural properties

X-ray structures were a crucial way to determine the coordination geometry around the metal centre. The same arguments put forward in Chapter 1 apply to the structures here, with a near-perfect tetrahedral geometry being the desired end product. The same model as used in Chapter 1 was applied here with the X1-Cu-X2 angle being most optimal at  $180^\circ$  and the C1-X1-X2-C2 angle being most optimal at  $90^\circ$ .  $[\text{Copper(I)}(2,9\text{-diphenylphenanthroline})_2]^+$  was also synthesised and used as a comparison with **C11 - C19**.

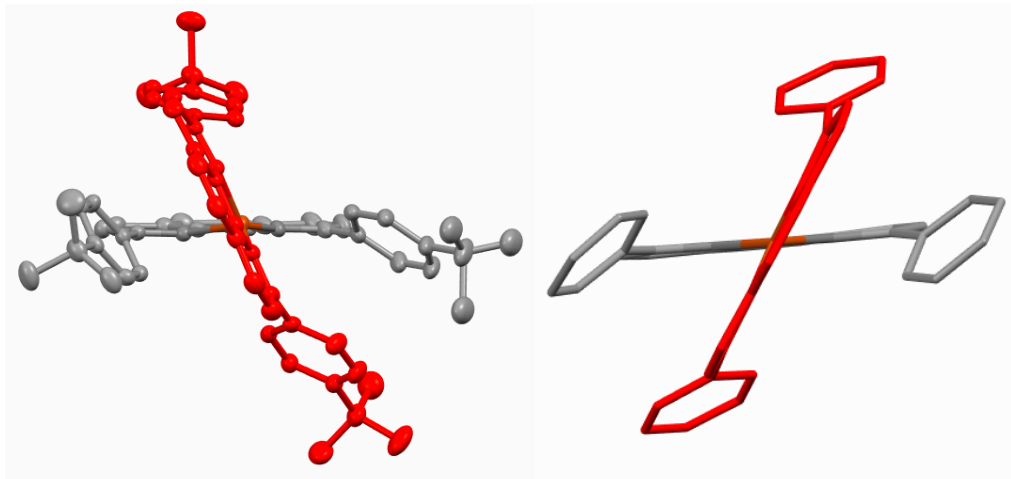


Figure 60: Crystal structure of **C11** (left) and copper(diphenylphenanthroline)<sub>2</sub> (right)

Table 13: Geometric parameters for **C11** and copper(diphenylphenanthroline)<sub>2</sub> (Cu(dpp)<sub>2</sub>)

Experimental	<b>C11</b>	Cu(dpp) <sub>2</sub>
Cu-N <sub>1</sub> (Å)	2.067	1.997
Cu-N <sub>2</sub> (Å)	2.043	1.994
Cu-N <sub>3</sub> (Å)	2.018	1.980
Cu-N <sub>4</sub> (Å)	2.099	1.993
X1-Cu-X2°	156	178
C1-X1-X2-C2°	68	56

As **C11** has a similar coordination geometry to Cu(dpp)<sub>2</sub> (as demonstrated by Figure 60 and Table 13) the control complex, **C11**, served its purpose. This means that the near-perfect tetrahedral geometry demonstrated in **C12** and **C13** (Figure 61) are on account of the remote control of the coordination geometry and not other factors. The Cu-N bond lengths increase for **C11**, demonstrating that the complex is more sterically hindered than Cu(dpp)<sub>2</sub>, which is expected as the *tert*-butyl groups will provide some steric bulk. **C11** also appears to be more distorted in the horizontal plane, judging by the X1-Cu-X2 angle,  $156^\circ$ . Looking slightly more closely at the crystal structure of **C11** (Figure

60), it is apparent that the aryl group on the left is orientated towards the phenanthroline. This could mean that there is preferential  $\pi$ - $\pi$  stacking between this aryl group and the phenanthroline, which is normal when there is a minimal amount of steric hindrance. The aryl on the right of **C11** is not orientated towards the phenanthroline and hence does not appear to be undergoing  $\pi$ - $\pi$  interactions. For Cu(dpp)<sub>2</sub>, aryl orientations hint that  $\pi$ - $\pi$  stacking may be occurring between both aryls and the phenanthrolines.

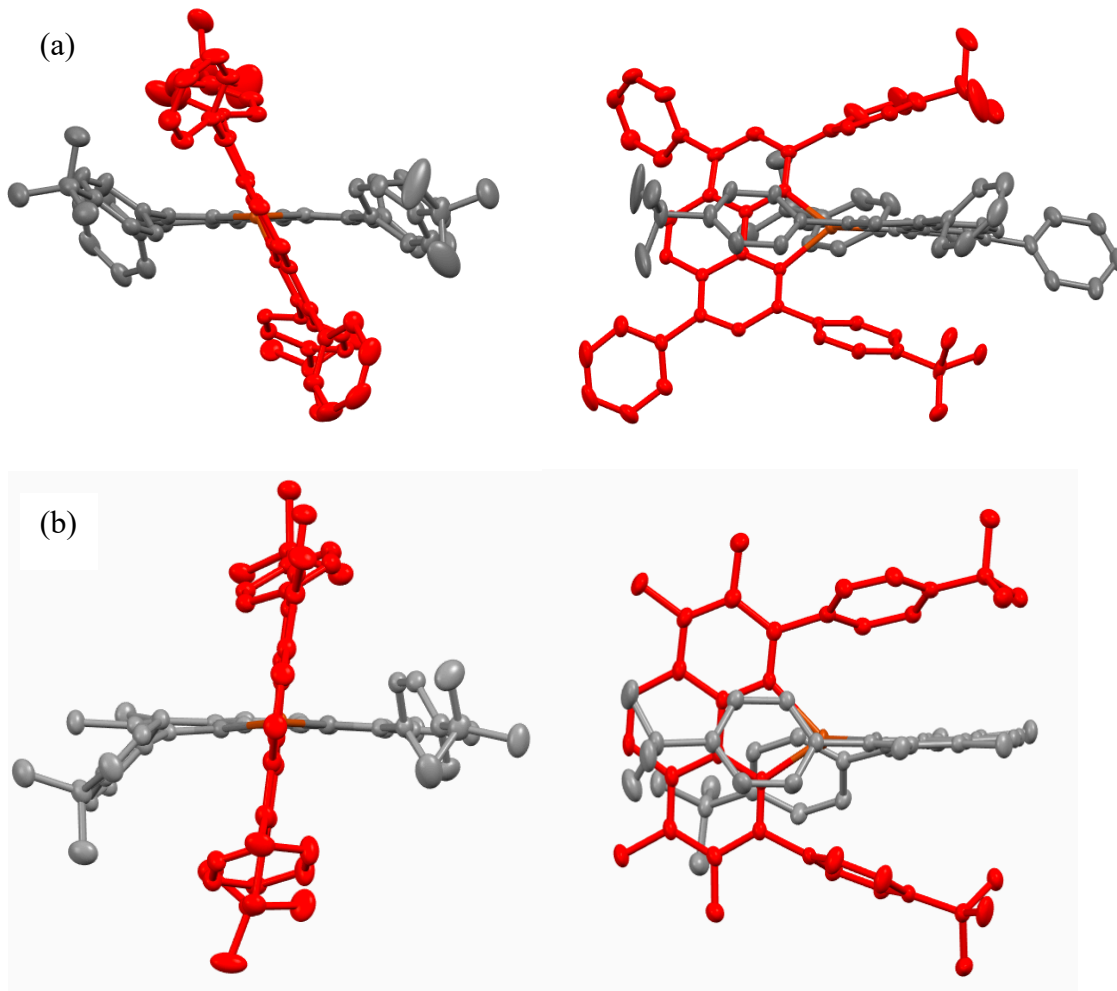


Figure 61: Crystal structures of **C12** (a) and **C13** (b)

Table 14: Geometric parameters for **C12** and **C13**

Experimental	<b>C12</b>	<b>C13</b>
Cu-N <sub>1</sub> (Å)	2.059	2.088
Cu-N <sub>2</sub> (Å)	2.062	2.009
Cu-N <sub>3</sub> (Å)	2.058	2.004
Cu-N <sub>4</sub> (Å)	2.068	2.111
X1-Cu-X2°	174	174
C1-X1-X2-C2°	66	82

Both **C12** and **C13** (Figure 61) show relatively short Cu-N bond lengths in Table 14, demonstrating that the complexes are stable. As seen in Chapter 1, steric interactions between the phenyl of the phenanthroline and the *tert*-butyl of the aryl substituent led to a near-perfect geometry for **C4** and **C5**. The addition of methyl groups for **C13** appears to be sufficient steric hindrance to block the second phenanthroline, providing a near-perfect geometry. This is apparent by the structure in Figure 61b. Surprisingly, when looking at the geometries listed in Table 14, **C13** appears to have an even more optimised geometry than **C12**. Spacefilling models of **C12** and **C13** (Figure 62) demonstrate the amount of steric hindrance present in these complexes.

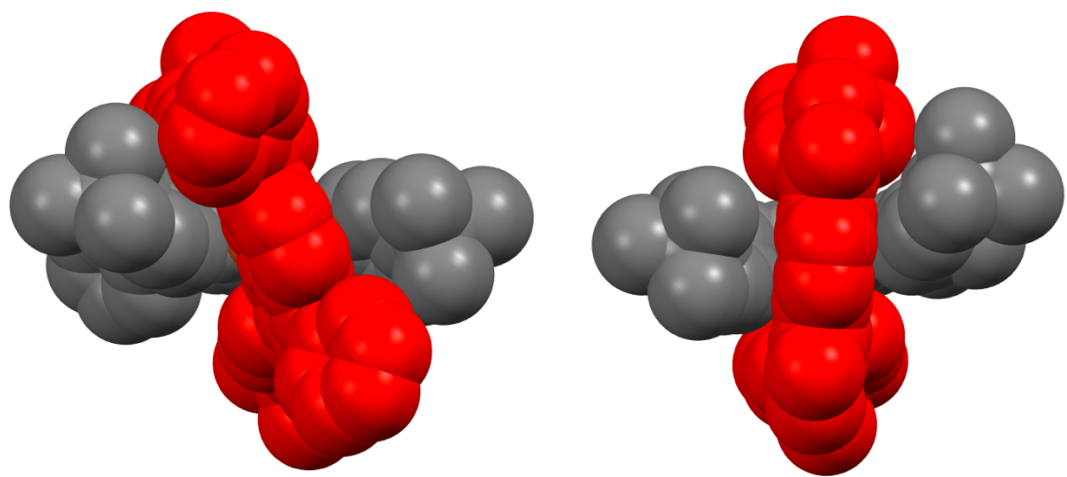


Figure 62: Spacefilling models of **C12** (left) and **C13** (right)

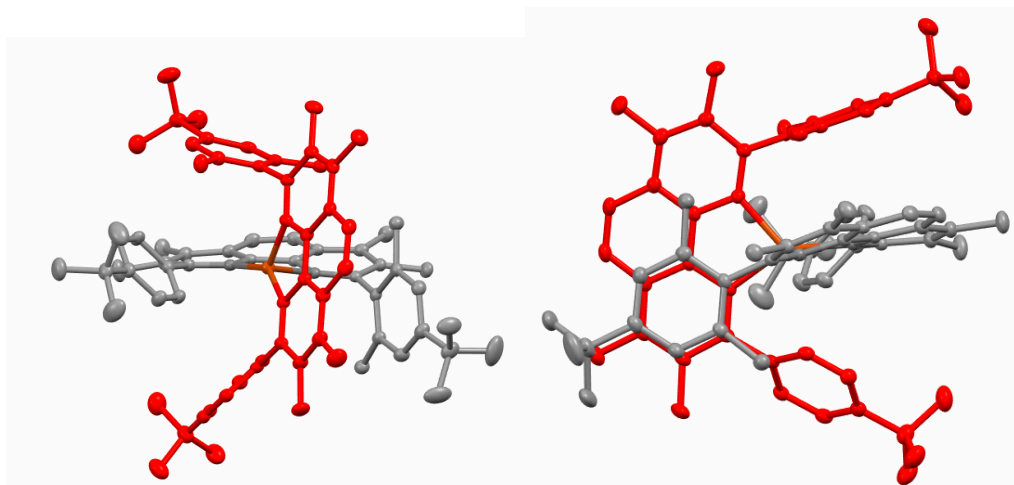


Figure 63: Crystal structure of **C16**

Table 15: Geometric parameters for **C16**

Experimental	<b>C16</b>
Cu-N <sub>1</sub> (Å)	2.028
Cu-N <sub>2</sub> (Å)	2.040
Cu-N <sub>3</sub> (Å)	2.166
Cu-N <sub>4</sub> (Å)	1.970
X1-Cu-X2°	145
C1-X1-X2-C2°	82

The X-ray crystal structure of one of the non-symmetric complexes, **C16**, was obtained (Figure 63). The complex is still stable, with only slight increases in the Cu-N bond lengths. Interestingly, there is a negative effect on the coordination geometry on addition of methyl groups on one of the aryl substituents. The complex appears to have a higher distortion than **C13** with a X1-Cu-X2 value of 145° compared to 174° for **C13** (Table 14 and 15). The reasons for this are unclear, potentially the additional methyl groups on the aryl simply cause too much distortion in the complex and the geometry is hence less favourable. This distortion is apparent in the right image of Figure 63 where the grey phenanthroline is clearly not planar. This is however good news as it demonstrates that the additional methyl groups on the aryl substituent are not necessary to obtain a near-perfect geometry and that the geometry is already optimised *cf. C13*. This is advantageous as the synthesis of symmetric ligands is clearly easier than that of their non-symmetric counter parts.

It would appear that the initial hypothesis that a methyl group would suffice to afford a near-perfect tetrahedral geometry *via* remote control is in fact correct, as **C13** and **C16** are both near-perfectly tetrahedral and show minimal distortion (Tables 14 and 15). Bizarrely the red phenanthroline in Figure 63 of **C16** appears to shift upwards, hence showing a distortion in the vertical plane.

The X-ray crystal structures of complexes **C11**, **C12**, **C13** and **C16** were optimised using DFT calculations (Table 16). The calculated results match the experimental results well demonstrating that the geometry is in its optimised form for the crystal structures obtained experimentally.

Table 16: Computed geometric parameters for **C11**, **C12**, **C13** and **C16**

Computational	<b>C11</b>	<b>C12</b>	<b>C13</b>	<b>C16</b>
Cu-N <sub>1</sub> (Å)	2.083	2.082	2.066	2.157
Cu-N <sub>2</sub> (Å)	2.070	2.077	2.103	2.086
Cu-N <sub>3</sub> (Å)	2.075	2.083	2.098	2.032
Cu-N <sub>4</sub> (Å)	2.077	2.069	2.068	2.221
X1-Cu-X2°	177	177	176	156
C1-X1-X2-C2°	65	69	85	80

### 2.2.3 Electronic properties

As for the heteroleptic complexes, the cyclic voltammetry was dominated by one oxidation and one reduction (CuI/II) (Table 17). Cyclic voltammetry was carried out in dichloromethane with tetrabutylammonium hexafluorophosphate being used as the supporting electrolyte.

Table 17: Cyclic voltammetry for **C11-C19**<sup>a</sup>

	Anodic peak potential (Volt)	Cathodic peak potential (Volt)	Potential difference (Volt)
<b>C11</b>	0.35	0.29	0.06
<b>C12</b>	0.41	0.29	0.12
<b>C13</b>	0.16	0.082	0.08
<b>C14</b>	0.55	0.48	0.07
<b>C15</b>	0.52	0.46	0.06
<b>C16</b>	0.33	0.27	0.06
<b>C17</b>	0.58	0.51	0.07
<b>C18</b>	0.55	0.48	0.07
<b>C19</b>	0.42	0.34	0.08

<sup>a</sup>  $CH_2Cl_2$ ,  $NBu_4PF_6$  (0.1M), 100 mV/s, vs.  $Fe^{+}/Fe$

The cyclic voltammetry results show that substitution with methyl groups (**C13** and **C16**) renders the complex more prone to oxidation, hence this is advantageous for applications in solar cells. The potential differences for these two complexes remain small meaning the processes are all reversible, which is surprising for certain cases: **C18** and **C19**. For **C19** the reversibility of the process could be on account of the fact that the second aryl is in the same plane as the phenanthroline, this makes distortion to a square-planar geometry more challenging due to increased rigidity and hence the small

potential difference. Addition of non-symmetry in the ligands appears to make the complex less easy to oxidise, with increases in the potentials for all the non-symmetric complexes (**C14 – C16**) *cf.* their symmetric counterparts (**C11 – C13**).

As is the case for the heteroleptic complex, there are two major features in the absorption spectrum, a  $\pi-\pi^*$  transition in the UV region and an MLCT transition in the visible region. Looking more closely at the visible part of the spectrum, information can be gained about the geometry of the molecule, with **C11** and **C12** having an additional tail up to 700 nm (Figure 64). This additional tail is much less intense for **C13**, demonstrating that there are geometrical differences between **C11**, **C12** and **C13**. Looking at the crystal structures (*vide supra*) it is apparent that **C13** is the closest to a near-perfect tetrahedral compared to **C11** and **C12**. This additional band above 550 nm demonstrates that **C11** and **C12** adopt a distorted tetrahedral geometry ( $D_2$ ). This geometry allows transitions above 550 nm whereas they are disallowed for the  $D_{2d}$  geometry of **C13**. The relative intensity of this band compared to the absorption max is also higher for **C11** than **C12** demonstrating a greater distortion in **C11** than **C12**, as is confirmed by the crystal structures above (Figures 60 and 61).

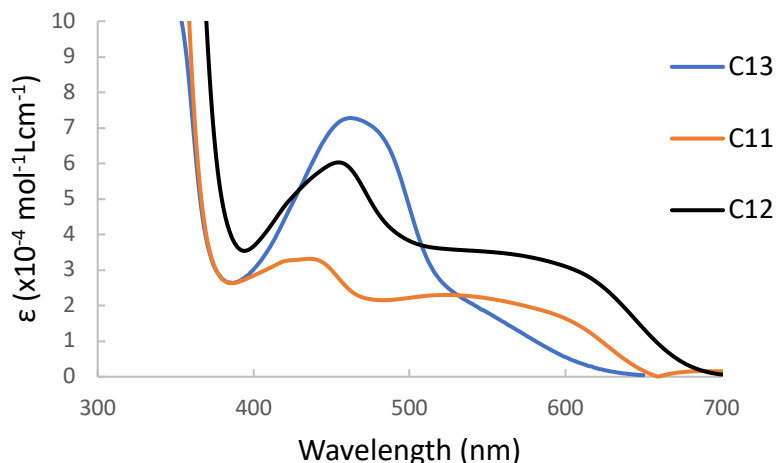


Figure 64: Absorption spectrum of the visible region for **C11**, **C12** and **C13** in dichloromethane at room temperature

Table 18: Summary of absorption properties for **C11 – C19**

	<b>C11</b>	<b>C12</b>	<b>C13</b>	<b>C14</b>	<b>C15</b>	<b>C16</b>	<b>C17</b>	<b>C18</b>	<b>C19</b>
$\lambda_{\text{max}}$ (nm)	324 445	320 464	302 475	298 457	280 477	299 458	299 458	280 452	329 450
$\epsilon \times 10^{-3}$ ( $\text{M}^{-1}\text{cm}^{-1}$ )	66 3	68 6	69 7	57 3	62 5	51 4	49 3	61 2	62 4

In terms of light absorption properties, complexes **C11-13** appear to be relatively optimal with strong visible light absorption that spreads over a wide range of the visible spectra (as seen in Figure 64).

Once again, the transitions made in these complexes can be determined by using TheoDORE analysis. The graphs below show the first 50 excitation singlet states of complexes **C11**, **C12**, **C13** and **C16**, respectively. Lower energy transitions are MLCT transitions and higher energy transitions are either LLCT or LC.

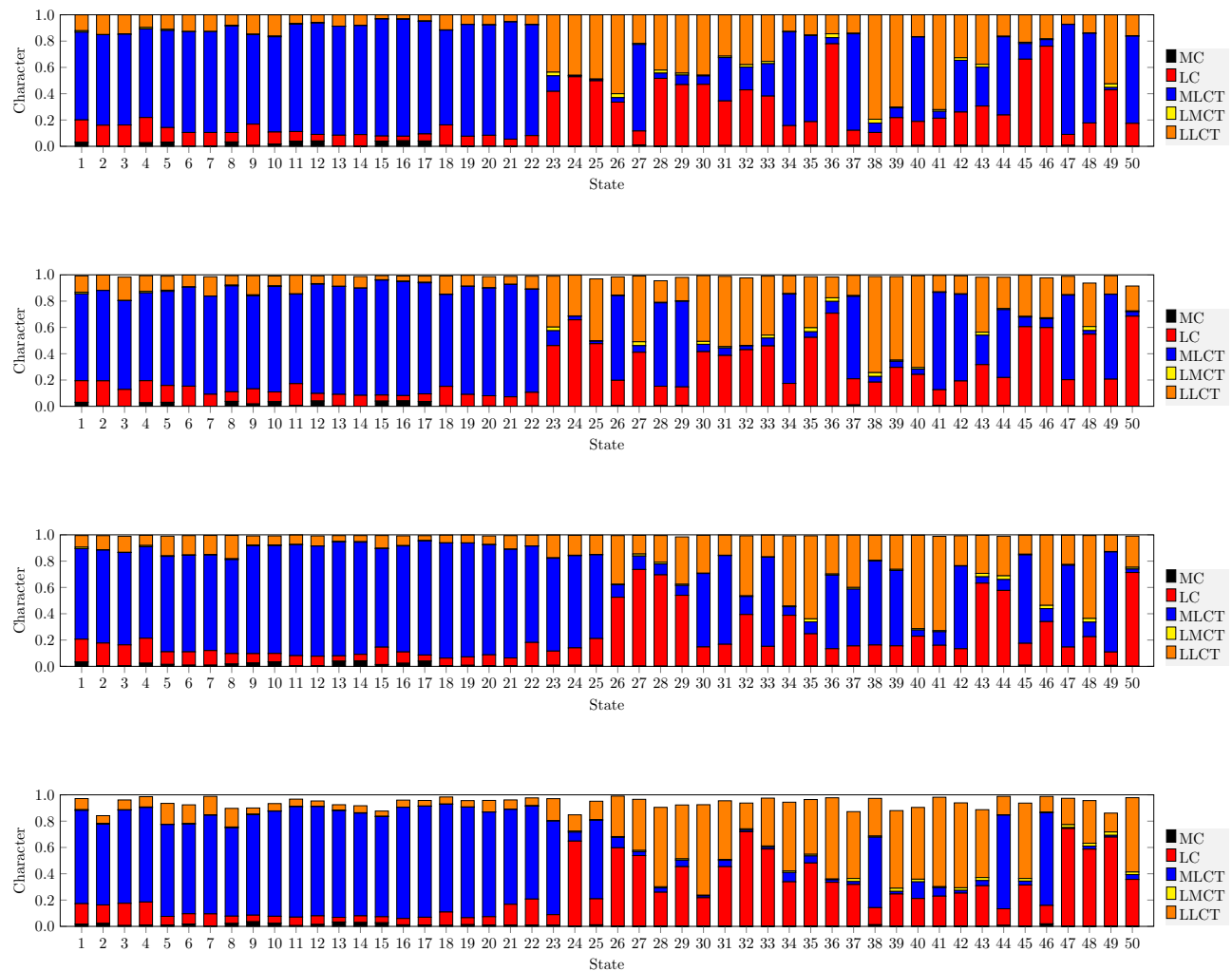


Figure 65: TheoDORE analysis of complexes **C11**, **C12**, **C13** and **C16**, respectively. Showing the nature of the first 50 transitions of the calculated absorption spectra.

## 2.2.4 Photoluminescent properties

The photoluminescent properties of the homoleptic complexes were studied once again using a fluorimeter and exciting the complexes at 456 nm in dichloromethane. The results are summarised in Table 19.

Table 19: Excited state properties for **C11 – C17**

	<b>C11</b>	<b>C12</b>	<b>C13</b>	<b>C14</b>	<b>C15</b>	<b>C16</b>	<b>C17</b>
Lifetime (ns)	219	145	326	133	92	240	163
Emission (nm)	689	714	685	679	702	678	700

The results displayed in Table 19 were compared to a standard, Cu(dpp)<sub>2</sub>, which has a lifetime of 162 ns; this complex was synthesised and used as a comparison for the other complexes. Substitution with *tert*-butyl groups had a positive effect as seen for **C11**, with the lifetime increasing to 219 ns. This is not surprising as the protection of the coordination site will be greater on addition of these bulky groups. It also shows that increasing the number of potential rotamers by adding the *tert*-butyl groups did not have a negative effect on the lifetime and that the steric bulk is more of a deciding factor than the rotamers for this complex. In contrast to this, looking at **C12** there is a decrease in the lifetime to 145 ns. This is probably due to the reasons discussed in Chapter 1, with an increased number of rotamers on substitution with phenyl groups leading to more efficient non-radiative pathways and consequently a shorter lifetime. This finding is however slightly disappointing as it means that blocking the coordination geometry by using phenyl and *tert*-butyl groups away from the coordination site is not an efficient strategy. Looking at the crystal structure in Figure 61 and 62, it is even more surprising as the complex appears quite bulky and also near-perfect tetrahedral. Hence, demonstrating that there are clearly other factors at play.

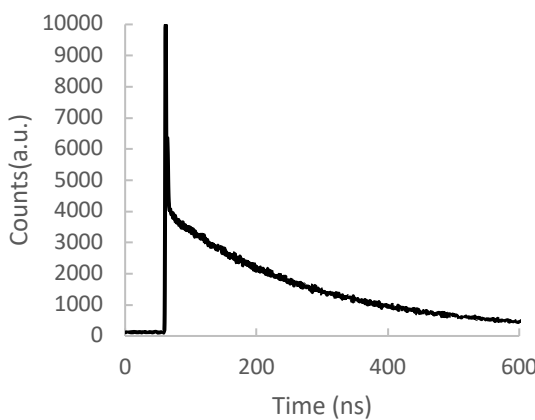


Figure 66: Lifetime decay of **C13** in dichloromethane on excitation at 456 nm

Moving on to **C13**, the longest lifetimes for this series of molecules is observed, 326 ns (Figure 66). This is a positive result as it shows that remote control of the coordination geometry using methyl groups seems to be an efficient way to prolong the excited state lifetime. The fact that the cooperative steric effect between the methyl at the 3,8-positions appears to have a minimal effect on the aryl

position, leads to the assumption that the steric interactions between the methyl groups in the 4,7-positions and the *tert*-butyl groups of the aryl is the reason for this increase in lifetime. Inductive effects could also be at play and this could also explain the difference between **C12** and **C13**.

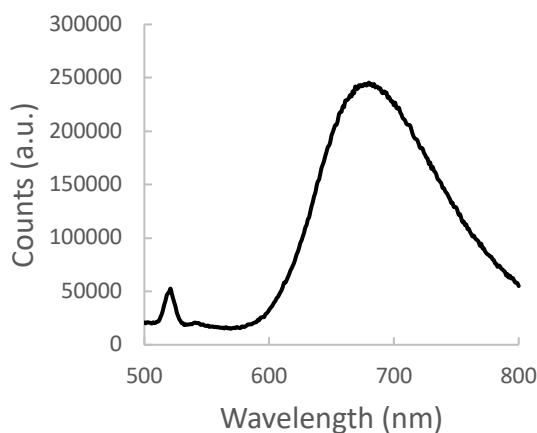


Figure 67: Emission of **C13** in dichloromethane on excitation at 456 nm. Peak at 525 nm is stray excitation light

A strong emission is present for **C13** as demonstrated in Figure 67. When comparing this to the emission of **C5** shown in Chapter 1 (Figure 44) it is apparent that this is a much more efficient process.

It was hoped that increasing the steric hindrance at the coordination site would lead to longer lifetimes, hence the series of complexes with non-symmetric ligands was synthesised (**C14** - **C16**). This was not the case and a decrease in lifetime was observed for all the non-symmetric complexes *cf.* their symmetric counterparts. Looking deeper into the literature, this is an effect that has already been observed as changing the symmetry of the complex has a negative effect on the lifetime due to an increased number of rotamers.<sup>2,3</sup> The same trend is observed for **C17** and **C18** with lower lifetimes for these two complexes. The cooperative effect between aryl and alkyl substituents in **C18** shown recently by Pellegrin<sup>4</sup> has proven to be futile in our case, once again demonstrating the necessity of the methyl groups at the 3,8-positions in order to increase the lifetimes. **C18** has many potential rotamers, with an n-butyl group this was probably a poor choice but was chosen for synthetic simplicity.

DFT calculations were carried out on certain homoleptic complexes (**C11**, **C12**, **C13** and **C16**) to see the distortion and energy levels of the excited state (Table 20).

Table 20: Computed geometric parameters for **C11**, **C12**, **C13** and **C16** in the excited state

Computational	<b>C11</b>	<b>C12</b>	<b>C13</b>	<b>C16</b>
Cu-N <sub>1</sub> (Å)	2.049	2.052	2.114	2.289
Cu-N <sub>2</sub> (Å)	2.056	2.053	2.033	2.005
Cu-N <sub>3</sub> (Å)	1.968	1.961	1.957	1.929
Cu-N <sub>4</sub> (Å)	1.974	1.965	1.964	2.064
X1-Cu-X2°	178	180	174	151
C1-X1-X2-C2°	61	68	75	88

Table 21: Comparison of computed geometric parameters for **C11**, **C12**, **C13** and **C16** between the ground and excited states

	<b>C11</b>	<b>C12</b>	<b>C13</b>	<b>C16</b>
Cu-N <sub>1</sub> (Å)	0.034	0.03	0.048	0.132
Cu-N <sub>2</sub> (Å)	0.014	0.024	0.011	0.081
Cu-N <sub>3</sub> (Å)	0.107	0.122	0.141	0.103
Cu-N <sub>4</sub> (Å)	0.103	0.104	0.104	0.157
X1-Cu-X2°	1	3	2	5
C1-X1-X2-C2°	4	1	10	8

Comparing the Cu-N bond lengths in the excited state with those in the ground state, minimal change was observed for the distance between the copper and one of the phenanthroline moieties. The larger difference observed for the second phenanthroline of the complex (**L2**), was on account of the radical anion being delocalised on one of the phenanthrolines causing it to approach the positively charged Cu(II). This small change seen in the neutral phenanthroline (**L1**) was however a positive sign as it demonstrates that the distortion in the excited state was minimal. Figure 67 shows the electron localisation on one of the phenanthroline moieties for **C12**.

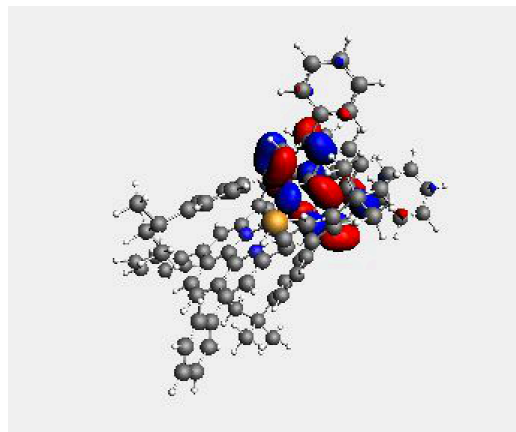


Figure 67: SOMO of **C12** in its excited state.

In terms of geometrical differences for **C12**, the X1-Cu-X2 difference in bond angles between the ground and excited state was minimal (compared to optimised complexes in the literature), demonstrating that distortion has already occurred in the ground state from the perfect-tetrahedral geometry to form the most stable motif, with  $\pi$ - $\pi$  stacking between the phenyl and the adjacent phenanthroline and hence on excitation minimal distortion occurs. This is backed up by the fact that there is minimal distortion for **C11** despite limited steric hindrance.

For the distortion in the horizontal axis C1-X1-X2-C2, minimal changes are observed for all complexes; the greatest distortion was for **C13**, 75° to 85°, which had the longest lifetime. Potentially meaning that  $\pi$ - $\pi$  interactions are not able to occur in the ground state and only occur in the excited state on account of the large steric hindrance at and away from the coordination site, meaning that this is an efficient way to block the phenanthroline. Electronic factors could also be at play as comparing **C11**, **C12** and **C13**, the complex with the longest lifetime is **C13**, with electron donating methyl groups, followed by **C11**, with no such groups, and finally the lowest being **C12**, with electron withdrawing groups, hence this could be the deciding factor.

These DFT results show that potentially the geometrical parameters of complexes have been optimised as much as possible and now the electronic properties must be ascertained and analysed.

Table 22: Calculated excited state properties for **C11**, **C12**, **C13** and **C16**

	Triplet (kcal/mol)	Singlet (kcal/mol)	$\Delta E_{ST}$ (kcal/mol)	Emission (nm)	Spin orbit coupling S1-T1 (cm <sup>-1</sup> )
<b>C11</b>	-21912.81	-21944.69	31.88	759	52.76
<b>C12</b>	-29005.09	-28998.80	6.29	808	53.85
<b>C13</b>	-25334.58	-25366.83	32.25	737	67.32
<b>C16</b>	-27043.13	-27076.41	33.28	793	42.29

As seen for the heteroleptic complexes, the relaxation pathway can be hypothesised to be thermally activated delayed fluorescence (TADF). The reasons for this conclusion are on account of the small energy difference between the singlet and triplet state ( $\Delta E_{ST}$ ) (Table 22). This small difference means that the complex will oscillate between the two states and because there is a greater coupling between the singlet and the ground state compared to the triplet and the ground state, this is the favoured pathway.<sup>5</sup> Consequently the emission that is observed experimentally is from the singlet state. The values calculated for the emission are far from those recorded experimentally. The reasons for this are summarised in Figure 68, as there are two potential oscillating states for the singlet energy level. These are difficult to distinguish between in computational studies because the two states have identical energies, as the two phenanthroline moieties are the same, yet the LUMO will be present on one or the other phenanthroline leading to differences in the emission value. The energy required to change from the  $D_2$  to  $C_2$  configuration has been calculated to be 0.028 eV, which is a very small amount of energy, meaning that interconversion between the two excited states is highly likely.

The downfall of **C12** can also potentially be explained by the  $\Delta E_{ST}$  as the two states are exceedingly close in energy with a meagre difference of 6.29 kcal/mol. This means that the interconversion between the singlet and triplet state will occur exceedingly rapidly and will lead to short excited state lifetimes. In addition to this, the large number of rotamers present for this complex with four phenyl groups will favour non-radiative decay and also decrease the excited state lifetime.

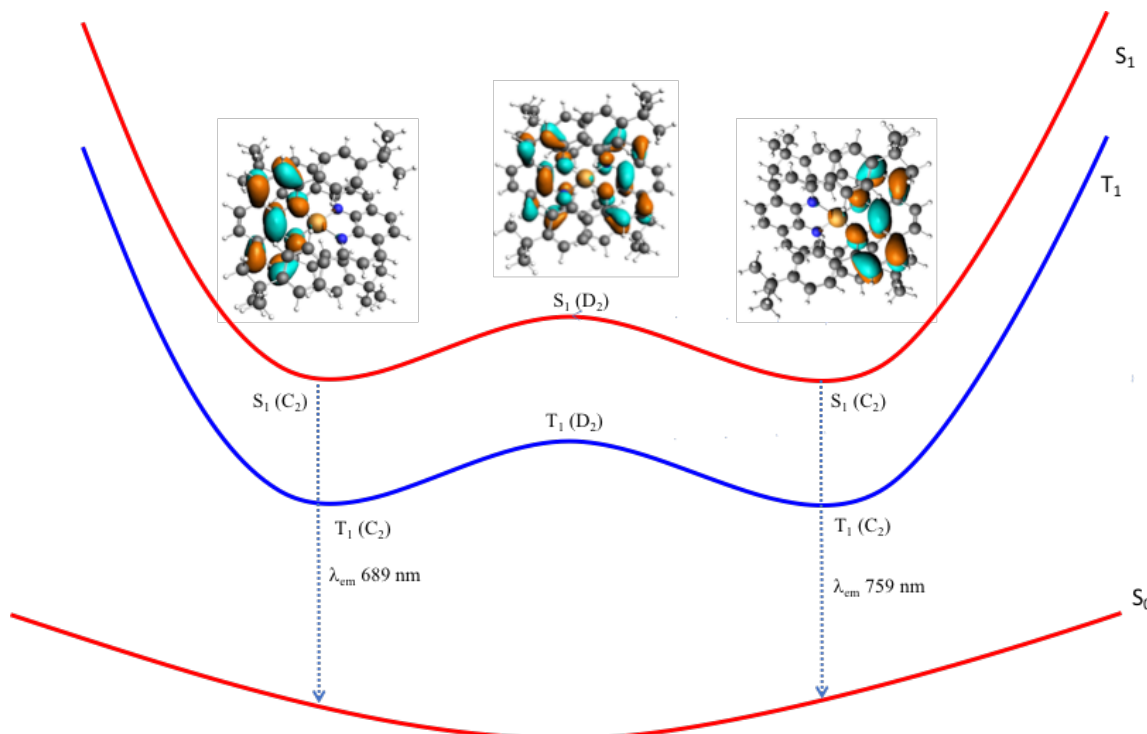


Figure 68: Two potential singlet excited states.

## 2.3 Photoluminescent Pt phenanthroline complexes

As mentioned in the introduction, phenanthroline is a very versatile ligand that can coordinate a multitude of metals ions. One of these metal ions is platinum. Platinum is very interesting as the complexes formed are likely to be highly luminescent. NNC type complexes<sup>6</sup> can be synthesised *via* an orthometallation between the Pt and the ortho position of an aryl substituent of the phenanthroline ligand. The two complexes in Figure 69 were synthesised and the photoluminescent properties were studied.

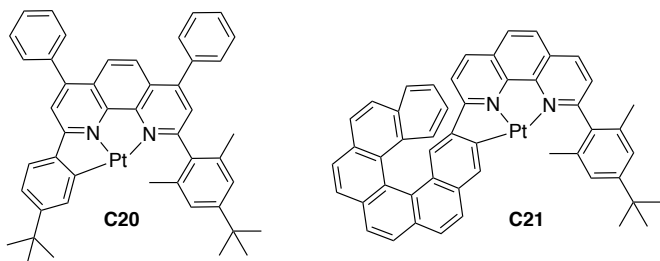


Figure 69: Pt(II)phenanthroline complexes **C20** and **C21**

The ligand synthesis for the complex **C20** is shown above (Figure 52, **L11**). For **C21** the brominated helicene was synthesised from a published procedure<sup>7</sup> and was available in the lab (synthesised by a fellow PhD student, Vincent Silber) and the helicene was added to the phenanthroline by addition of the helicene as a lithiohelicene after the halogen lithium exchange. The orthometallation occurred by simply heating the ligand in a Pt(II) source for 24 h (Figure 70).

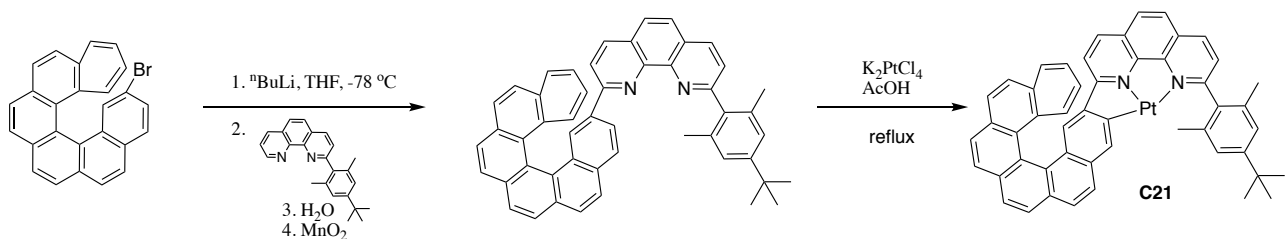


Figure 70: Synthetic route for **C21**

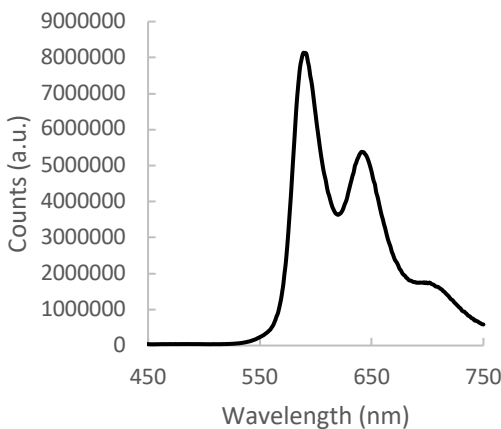


Figure 71: Emission spectrum of **C21** in dichloromethane

**C20** and **C21** were highly luminescent in solution on excitation at their respective  $\pi$ - $\pi^*$  absorption bands and presented a strong emission at 604 nm and 592 nm respectively. **C21** is presented as an example in Figure 71, with the emission at 592 nm and a shoulder just after at 650 nm.

The helicene was present as two enantiomers, orthometallation blocks the rotation of the helicene meaning that the enantiomers might be separated, and the circularly polarized luminescence (CPL) and circular dichroism (CD) properties can be determined. This is an ongoing project.

## 2.4 Conclusion

To conclude this chapter, nine homoleptic copper(I) complexes and two Pt(II) complexes have been synthesised. Once again, using lithium sources to carry out the ligand synthesis led to interesting results with surprising substitution patterns for phenanthroline ligands. The substitution of a tolyl group was already seen in Chapter 1 but has never been reported before in the literature. The cyclisation of the methyl group onto the 8 position of the phenanthroline is also unprecedented, as the substitution pattern on phenanthrolines normally occur at the 2,4,7,9-positions. The ligands were chosen based on the system design developed in Chapter 1, with the hope that remote control of the coordination site would help with the lifetime of the copper(I) phenanthroline complexes and this turned out to be the case for optimal complexes, notably **C13**. The removal of the methyl groups at the 2,6-positions of the aryl substituents meant that steric hindrance was reduced and hence homoleptic complexes could be synthesised. Yet the steric hindrance away from the coordination site was maintained, with the *tert*-butyl group of the aryl interacting sterically with either phenyl or methyl groups. In order to achieve greater steric hindrance in such homoleptic complexes, non-symmetric

phenanthrolines were synthesised. These ligands were then used to synthesise copper(I) phenanthroline complexes and the ground state and excited state properties were studied.

The ground state properties of the complexes are optimal with the complexes absorbing over a wide range of the visible region and for optimised cases, **C13** and **C16**, the oxidation of these complexes is highly facile and reversible. Looking at the excited state properties, in accordance with Chapter 1, addition of phenyl groups at the 4,7-positions of the phenanthroline has a detrimental effect on the lifetime, once again probably due to an increased number of rotamers. For the most optimised complex, **C13**, the lifetime was improved compared to the standard comparative complex ( $\text{Cu}(\text{dpp})_2$ ). The lifetime of this complex was also higher than the reference complex **C11** with no remote control. However, it is difficult to say whether it was the steric interactions away from the coordination site that were the determining factors, as electronic effects were also at play. This was however a positive finding. In order to clarify this point, a complex with phenyl groups at the 2,9-positions of 3,4,7,8-tetramethylphenanthroline should be synthesised in order to remove the remote control but retain the electronic effects of the donating methyl groups. If the lifetime for this complex remains as high as that of **C13** potentially electronic effects are the determining factor.

Thanks to calculations, the excited state geometries could be determined and there appears to be minimal changes in geometry between the ground and excited state. The excited state energies seem to be quite different from one another and this could be a contributing factor. Small  $\Delta E_{\text{ST}}$  values showed that the excited state complexes were most likely relaxing *via* TADF and that smaller  $\Delta E_{\text{ST}}$  values potentially led to shorter excited state lifetimes. Changing the symmetry of the complex by utilising non-symmetric ligands proved to be futile despite the increase in steric hindrance. This coincides with what is seen in the literature,<sup>2,3</sup> demonstrating a necessity for optimisation of the systems by not simply adding more and more steric restraint.

Moving on from this project, the remote control developed during this project may still be a useful avenue to pursue as it leads to the formation of near-perfect tetrahedral complexes. The simplicity of the functionalisation and stability of the complexes also gives phenanthroline substituted with aryl groups an advantage compared to other copper(I) complexes in the literature. Blocking the complex to prevent rotamers and geometrical deformation could be a good way to optimise the excited state properties. Hence, an interesting complex to synthesise would be one with a large amount of steric hindrance at the coordination site, yet with an additional rigid nature. Applying the synthetic design applied by Sauvage to synthesise a catenane (Figure 14) due to the preorganisation of the complex, and applied since by Fallis and Mayor (Figure 15), instead of cyclising at the aryl substituent, the

complex in Figure 72 could be synthesised. This complex has been cyclised at the 3,8-positions with an alkoxy chain. The aryl substituents at the 2,9-positions of the phenanthroline are still orthogonal to the phenanthroline and consequently are still able to protect the coordination site, unlike for Fallis and Mayor; where the cyclisation leads to a near coplanarity of the phenyl groups. The fusing of the two rings will lead to a more rigid structure and minimise distortion on excitation and also help prevent exciplex formation. This complex is clearly more challenging synthetically than those synthesised in this Chapter, but a bromination of the 3,8-position of the 2,9-di-*p*-*tert*-butylphenylphenanthroline is feasible and then on complexation, a substitution could occur between the bromine and the alkoxy with the hope that the mild preorganisation would lead to intramolecular fusion.

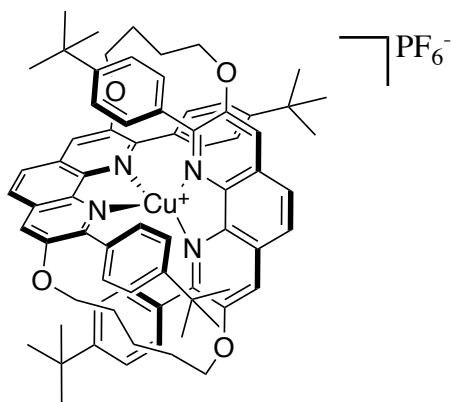


Figure 72: Perspective complex

## 2.5 General conclusions

To conclude the first part of this PhD thesis concerning the synthesis and properties of copper(I) phenanthroline properties, heteroleptic and homoleptic copper(I) phenanthroline complexes were synthesised and several crystal structures were ascertained. The ground state properties of these complexes were analysed by electronic spectroscopy and cyclic voltammetry. A new strategy has been developed in order to synthesise near-perfectly tetrahedral copper(I) complexes. The complexes that were able to undergo steric interactions between the groups at the 4,7-positions of the phenanthroline and the *tert*-butyl of the aryl of the adjacent phenanthroline possessed a near-perfect tetrahedral geometry in the ground state. It was hoped that this optimised geometry would lead to more optimal excited state properties, unfortunately for the heteroleptic complexes this proved not to be the case and the lifetimes recorded were quite short. As shown in the literature the steric hindrance around the metal coordination site was of paramount importance for optimal properties.

DFT calculations helped determine hypotheses for such short lifetimes. The large number of rotamers present for the complexes containing phenyl substituents at the 4,7-positions of the phenanthroline proved to be potentially determinantal, as this most likely leads to a more favoured non-radiative decay pathway. Information was however gained about the ground and excited state properties of these complexes. Consequently, when moving on to the homoleptic complexes a slightly different system design was developed with methyl groups at the 4,7-positions of the phenanthroline, meaning that fewer rotamers were present and it was hoped that this would prolong the lifetime for the excited state. This proved to be the case with the longest lifetime being recorded for the complex containing methyl groups at the 4,7-positions that underwent steric interactions with the *tert*-butyl groups of the aryl substituents of the adjacent phenanthroline and consequently a near-perfect tetrahedral geometry was obtained with a longer lifetime than that of the literature standard [copper(I)(2,9-diphenylphenanthroline)<sub>2</sub>]<sup>+</sup>.

The strategy with methyl groups appears to work well but the values remain considerably smaller than those obtained using alkyl groups<sup>8</sup> and phosphine groups.<sup>9</sup> Mixed phenyl and alkyl systems also do not seem as optimal.<sup>4</sup> Fully blocking the complex by linking the substituents of one phenanthroline with the substituents of the adjacent phenanthroline, in order to prevent rotation, exciplex formation and to minimise the number of rotamers, is a possible avenue to pursue. Once again phenyl group proved to be detrimental to the excited state lifetime. Non-symmetrical complexes were also synthesised with a larger amount of steric hindrance at the coordination site however the change in symmetry meant that these complexes had a lower lifetime when compared to their symmetric counterparts. The combined experimental-computational approach of this project led to an increased knowledge of the system.

## 2.6 References

- 1 C. O. Dietrich-Buchecker, P. A. Marnot and J. P. Sauvage, *Tetrahedron Lett.*, 1982, **23**, 5291–5294.
- 2 D. Felder, J. F. Nierengarten, F. Barigelli, B. Ventura and N. Armaroli, *J. Am. Chem. Soc.*, 2001, **123**, 6291–6299.
- 3 M. T. Miller, *Inorg. Chem.*, 1999, **38**, 3414–3422.
- 4 L. Gimeno, E. Blart, J. N. Rebilly, M. Coupeau, M. Allain, T. Roisnel, A. Quarré de Verneuil, C. Gourlaouen, C. Daniel and Y. Pellegrin, *Chem. Eur. J.*, 2020, **26**, 11887–11899.
- 5 P. K. Samanta, D. Kim, V. Coropceanu and J. L. Brédas, *J. Am. Chem. Soc.*, 2017, **139**, 4042–4051.
- 6 X. G. Liu and W. Sun, *Eur. J. Inorg. Chem.*, 2013, 4732–4742.
- 7 M. Jakubec, T. Beránek, P. Jakubík, J. Sýkora, J. Žádný, V. Církva and J. Storch, *J. Org. Chem.*, 2018, **83**, 3607–3616.
- 8 S. Garakyanaghi, P. D. Crapps, C. E. McCusker and F. N. Castellano, *Inorg. Chem.*, 2016, **55**, 10628–10636.
- 9 D. G. Cuttell, S. M. Kuang, P. E. Fanwick, D. R. McMillin and R. A. Walton, *J. Am. Chem. Soc.*, 2002, **124**, 6–7.

# INTRODUCTION 2

## Porphyrins

### The properties of dimers, oligomers and more

I2.1 Porphyrins	94
I2.1.1 Optical properties	95
I2.1.2 Electronic properties	95
I2.1.3 Magnetic properties	96
I2.2 Assembling porphyrins	98
I2.2.1 Changing the position of the linking unit	100
I2.2.2 Changing the linking unit	101
I2.2.3 Fused porphyrins	104
I2.2.4 Metal ion linked porphyrins	105
I2.3 To trimers, tetramers, oligomers and supramolecular assemblies	110
I2.3.1 Self-assembly of porphyrins at the solid-liquid interface	112
I2.4 Conclusions and project plan	114
I2.5 References	115

## I2.1 Porphyrins

A Porphyrin is a macrocycle consisting of four pyrrole units that are linked by methine bridges (Figure 73). Tetrapyrrolic macrocycles are the molecules that make our blood red and the grass green and are consequently widely present in Nature. These pigments of life have been used in Nature for billions of years for good reason, with their aromatic character leading to an accessible HOMO-LUMO (highest occupied molecular orbital and lowest unoccupied molecular orbital, respectively) gap that can be exploited for energy and/or electron transfer processes as seen in chlorophyll and cytochrome. Porphyrin derivatives are also used for the transportation and storage of oxygen in our body as seen in haemoglobin and myoglobin. The large planar macrocycles are abundant in Nature, not only because of their electronic properties, but also on account of their ability to self-assemble into large well-organised motifs. This parameter facilitates energy transfer processes, as described by Marcus,<sup>1</sup> Dexter<sup>2</sup> and Förster.<sup>3</sup>

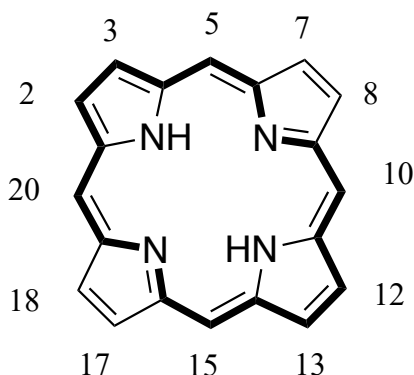


Figure 73: Structure and nomenclature of a porphyrin

The  $\pi$  system of the aromatic macrocycle is composed of  $22\pi$  electrons, 18 of which contribute to the aromaticity of the porphyrin (these are highlighted in bold in Figure 73). The positions  $\beta$  to the nitrogen of the pyrrole (2, 3, 7, 8, 12, 13, 17 and 18) are known as the  $\beta$ -pyrrolic positions of the porphyrin. The methine bridges of the pyrrole units (5, 10, 15 and 20) are known as the *meso* positions. Porphyrins functionalised at the  $\beta$  and the *meso* positions exist both in Nature and synthetically. The ring effect in NMR can confirm the aromaticity of the porphyrin unit with the exterior protons being deshielded and the protons of the internal nitrogens being strongly shielded. Coordination chemistry can be carried out in the cavity of the porphyrin and a metal ion with varying degrees of oxidation can be coordinated. This leads to a metallated porphyrin that can be obtained from the free-base (non-metallated) porphyrin. A multitude of metal ions can be placed at the centre of the macrocyclic ligand and the cations used could lead to a deformation of the planar nature of the aromatic ligand. There are three types of distortions: ruffled, saddle-shaped and domed.<sup>4</sup> The *meso*

and  $\beta$  substituents and intermolecular interactions with the metal ion could also lead to deformations. Auxiliary ligands can also lead to displacement of non-square planar metal ions out of the porphyrin cavity.

### I2.1.1 Optical properties

The absorption bands for porphyrins are in the visible and near-UV region of the electromagnetic spectrum. The origin of their electronic properties comes from  $\pi-\pi^*$  transitions between the ground state ( $S_0$ ) and the first ( $S_1$ ) and second ( $S_2$ ) excited state. These two transitions are known as the Q-band and the Soret band respectively.

Looking at an electronic spectrum of a porphyrin, the Soret band ( $S_0$  to  $S_2$ ) is found at around 400 nm with a molar extinction coefficient on the order of magnitude of  $10^5 \text{ M}^{-1}\text{cm}^{-1}$  and the Q-band is situated at around 600 nm with an order of magnitude of  $10^4 \text{ M}^{-1}\text{cm}^{-1}$ . The position of the two of these bands will depend on the substituents present at both the  $\beta$  and *meso* positions. In general, the number of Q-bands present in the spectra will depend on the symmetry and hence dipole moment of the porphyrin, the most notable differences being between the free-base and the metallated porphyrin. For a symmetric porphyrin, once metallated, by a metal in a square-planar geometry, the symmetry of the porphyrin changes from  $D_{2h}$  to  $D_{4h}$  and this leads to two bands for the metallated porphyrin, as opposed to four for the free-base. This number will vary depending on the symmetry of the porphyrin. Despite the intensity of the Q-bands being one order of magnitude smaller than that of the Soret band, it is the Q-bands that give the intense colour of the porphyrin in the visible region of the electromagnetic spectrum. Such observations are corroborated by the four-orbital model proposed by Gouterman,<sup>5,6</sup> where transitions from the HOMO ( $a_{1u}$ ) and the HOMO-1 ( $a_{2u}$ ) to the two degenerate LUMOs  $e_g(x)$  and  $e_g(y)$  are responsible for the absorption bands. The metal centre and the substituents will affect the relative energies of these orbitals and consequently of the transitions between them.

### I2.1.2 Electronic properties

Thanks to the large aromatic nature of a porphyrin, redox processes are able to occur to form relatively stable organic radicals. This fact leads to reversible oxidation and reduction processes on the organic macrocycle. The position of such transitions, that can be observed by cyclic voltammetry, will depend on the  $\beta$  and *meso* positions, but the type of transitions remains the same for most porphyrins. Two monoelectronic oxidations and two reductions are able to occur with either the depopulation of the HOMO or the population of the LUMO, respectively, leading to such transitions. If the metal is not

electroactive, the fact that the redox chemistry occurs on the macrocycle means that the HOMO-LUMO gap can be measured by cyclic voltammetry. There are numerous examples of both electroactive and non-electroactive metal porphyrins.

### I2.1.3 Magnetic properties

The first electron paramagnetic resonance (EPR) spectrum was carried out by Zavoisky in 1945 on a Mn(II)/Cu(II) sample.<sup>7</sup> Where nuclear magnetic resonance (NMR) measures the interaction between the magnetic moment of nuclei and electromagnetic radiation, EPR measures the interaction between the magnetic moment of electrons and electromagnetic radiation. On placing an electron into a magnetic field ( $B$ ), the previously degenerate two states of the electron now have a difference in energy. This interaction with a magnetic field is known as the Zeeman effect and it is summarised in Figure 74, with a simple  $S = 1/2$  example. The interaction of the magnetic moment with the magnetic field will lead to  $2S+1$  possible energy levels, therefore there are two energy levels for a  $S = 1/2$  system and the separation of the two levels is written as follows:

$$\Delta E = g\beta B \quad (\text{Eq. 1})$$

where  $g$  is the  $g$ -factor,  $\beta$  the bohr magneton constant and  $B$  is the magnetic field.

This equation can also be described as  $h\nu$  ( $h\nu = g\beta B$ ). The magnetic field used is around 0.3 T, as a microwave in the range of 9 GHz for X-band EPR spectroscopy. The energy of this transition then translates into an absorption, but for technical reasons the first derivative is detected and this gives an EPR spectrum.

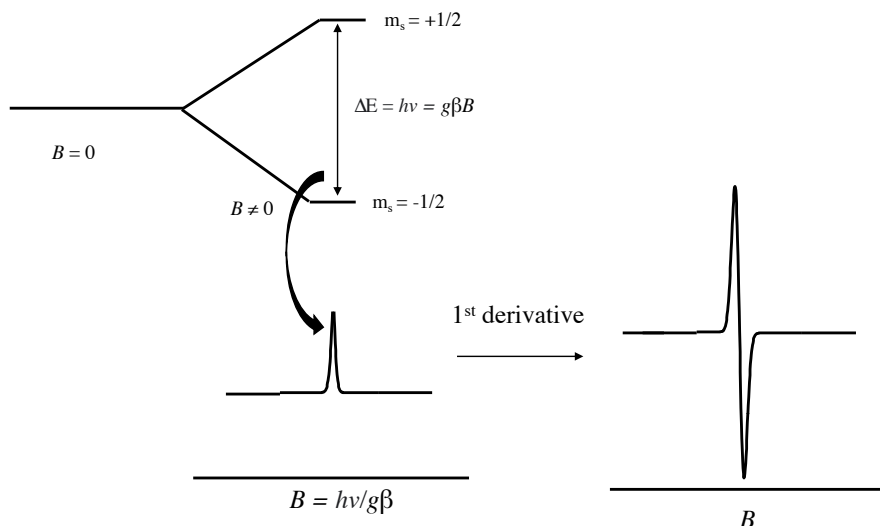


Figure 74: Zeeman splitting that leads to the signal observed in EPR spectroscopy

For a free electron, the  $g$  value is 2.0023. However, several parameters will lead to variations in this value. The main parameter that affects this value is orbital angular momentum which is observed as a spin-orbit coupling. Variation from the free electron ( $g = g_e + \Delta g$ ) will be larger or smaller depending on the spin-orbit constant. This means that organic radicals will be quite close to the free electron value and the introduction of metal radicals will lead to larger variations in the  $\Delta g$  value. The value will vary more and more substantially when moving down the periodic table, on account of an increased spin-orbit coupling.

Another parameter that will affect the observed EPR spectrum is coupling between the electronic spin ( $S$ ) and the nuclear spin ( $I$ ), known as hyperfine coupling ( $A$ ). This coupling is similar to  $J$ -coupling in NMR with the difference being that  $J$ -coupling is coupling between two nuclei and hyperfine coupling is between a nucleus and an electron. This coupling leads to new possible transitions in the spectrum and hence more lines. The number of lines can be determined by the  $I$  value for example an  $I$  value of  $3/2$  would lead to 4 lines ( $2I+1$ ) for one nucleus. Such transitions are summarised in Figure 75; the selection rules determine that transitions only occur for  $\Delta m_s \pm 1$  and  $\Delta m_I \pm 0$ .

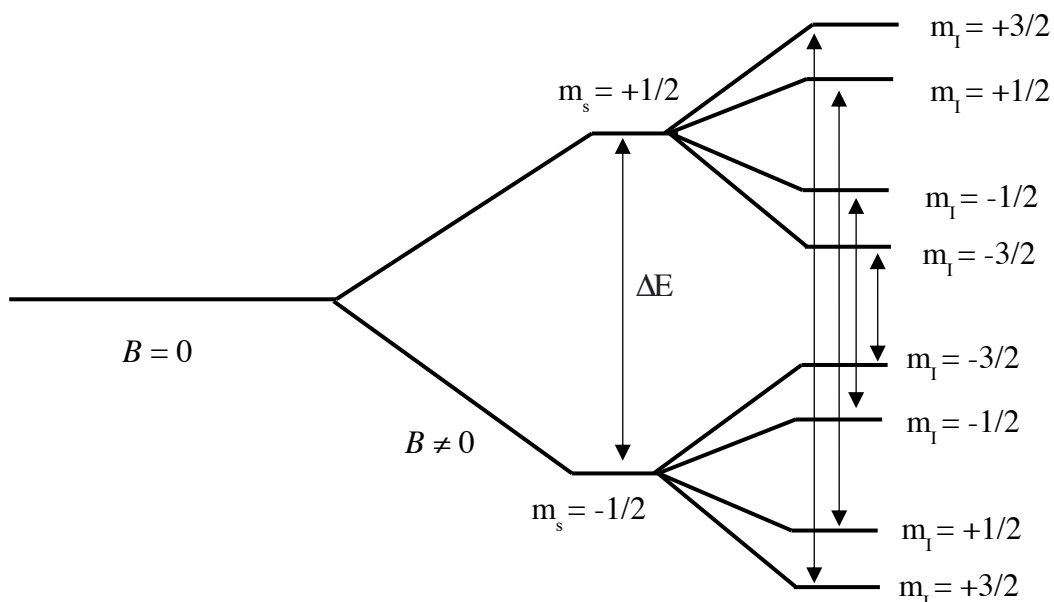


Figure 75: EPR transitions for a spin  $S=1/2$  coupled to a nucleus with  $I=3/2$  in the presence of a magnetic field.

The  $g$  factors for the three principle axes x, y and z are different, depending on the molecule being measured. Orbital angular momentum has an orientation in a molecule and consequently the magnitude of spin-orbit coupling will be direction dependent, otherwise known as anisotropic.<sup>8</sup> If the spectrum is recorded in solution, this anisotropy will average out. However, this is not the case for single crystal, powder or frozen solution. Figure 76 shows the effect of anisotropy on the spectrum:

(a)  $g_x = g_y = g_z$  meaning the  $g$  factor is isotropic and therefore there is no variation in the principle axes; (b)  $g_x = g_y = "g_{\perp}" \neq g_z = "g_{\parallel}"$  the perpendicular ( $g_{\perp}$ ) and the parallel ( $g_{\parallel}$ )  $g$  factors are different, this is called an axial spectrum; (c)  $g_x \neq g_y \neq g_z$  all of the  $g$  factors are non-equivalent, known as a rhombic spectrum.

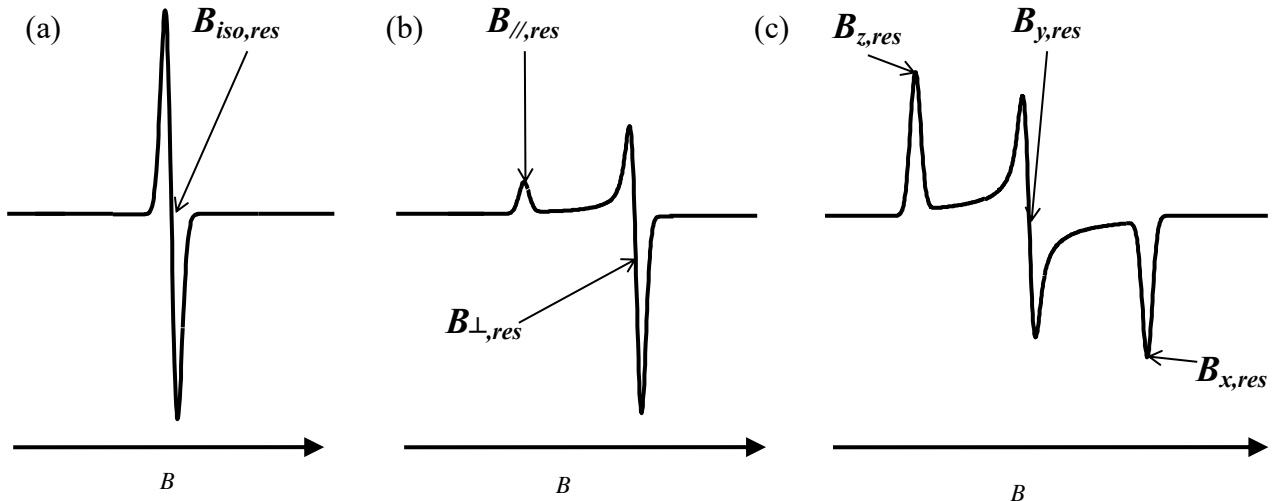


Figure 76: Three EPR spectra (a) isotropic (b) axial (where  $g_{\parallel} > g_{\perp}$ ) and (c) rhombic

Both the magnetic and the electronic properties of porphyrins can be tuned by changing the linking units between two porphyrins. This can be done in a number of different ways, be it covalently or non-covalently. The rest of this introduction will describe different porphyrin assemblies in the literature and the optimisation of their electronic and magnetic properties.

## I2.2 Assembling porphyrins

The publication of the structure of the bacterial photosynthetic reaction centre in 1985,<sup>9</sup> led to porphyrin oligomers being more and more abundant in the literature. Since this time, an attempt to study and replicate such optimised systems, that have passed through evolution for billions of years, was attempted by synthetic chemists. An attempt to replicate this kinked nature of the reactive site was achieved by Sauvage<sup>10</sup> and Sessler<sup>11</sup> (Figure 77). Sauvage also extended the synthesis and formed a catenane with such precursors.<sup>12</sup>

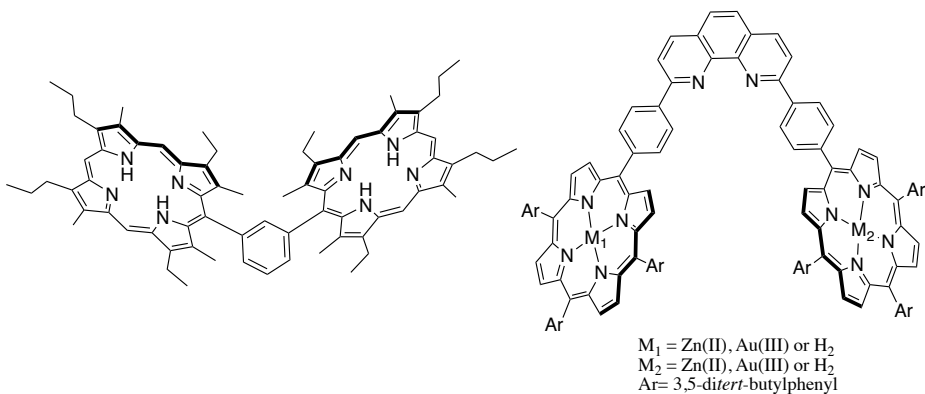


Figure 77: Two porphyrin systems developed by Sessler (left) and Sauvage (right) attempting to mimic Nature

Nine years after the reaction centre was first published, the circular structure of the light harvesting antenna in plants was published by Fuiyoshi,<sup>13</sup> and the energy transport carried out so majestically in Nature was studied, and is still trying to be replicated to this day. The arrangement of porphyrins in Nature allows for good orbital overlap between porphyrin moieties on account of their close proximity, this is defined as a J-aggregate shown in Figure 78. In order to replicate the models demonstrated in Nature, many porphyrins with organic linkers were synthesised, which allows for the porphyrins to be in close proximity as observed in Nature.

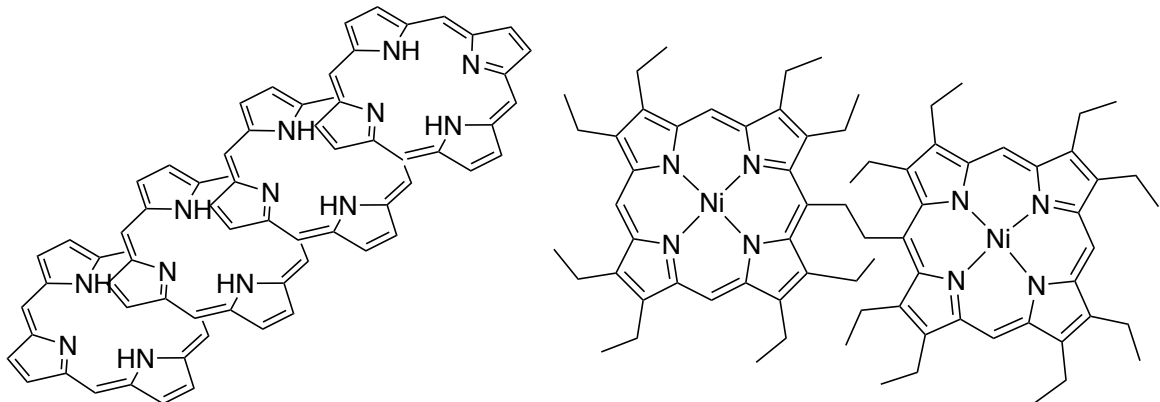


Figure 78: J-aggregate of porphyrins (left) and an attempt to replicate this close proximity synthetically (right)

For the dimer shown on the right of Figure 78,<sup>14</sup> no electronic communication was observed between the two porphyrin moieties. In 1978, Arnold and Johnson came up with an alternative way to allow for two porphyrin moieties to communicate. In their system design, Arnold and Johnson's ethylene bridge (Figure 78, right), that linked the two porphyrins at the *meso* position, was replaced by a butadiene bridge<sup>15</sup> (Figure 79, left). A bathochromic shift was observed in the electronic spectrum when comparing the monomer and the dimer. This bathochromic shift was deemed to be on account of an orbital overlap between the porphyrin and the organic linker's  $\pi$  orbitals, acting as a bridge for

electronic communication between the two porphyrin moieties. The close proximity of the two porphyrins led to an excitonic coupling, however the orbital overlap was deemed to be the pertinent property, which explains why Arnold and Johnson observed electronic communication for the butadiene bridged porphyrin dimer and no electronic communication for the ethylene bridged porphyrin dimer. This phenomenon of linking porphyrins in order to expand the electronic properties has since been done in many ways.

### 12.2.1 Changing the position of the linking unit

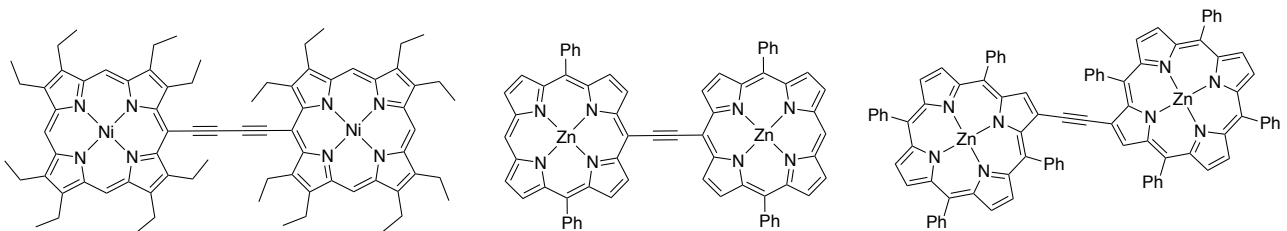


Figure 79: Different ways to link porphyrin moieties

A few examples of the first linked porphyrin dimers is shown in Figure 79. This work has been considerably developed by Osuka,<sup>16</sup> Therien<sup>17</sup> and Anderson.<sup>18</sup> Linking the porphyrins *via* the *meso* position of the porphyrin was deemed of paramount importance in order to maintain the orbital overlap between porphyrin moieties. When the porphyrins were linked at the  $\beta$  position, considerably less electronic communication was observed, once again demonstrating the importance of orbital overlap as opposed to excitonic coupling as seen for the ethane linked porphyrins. A dimer linked at the  $\beta$ -*meso* position was also synthesised and whilst the communication was higher than the  $\beta$ - $\beta$  linked porphyrin, the *meso*-*meso* linked porphyrin remained the most effective for good electronic communication. The position of the linker had an effect on both the electronic<sup>19</sup> and magnetic<sup>20</sup> properties.

This can be explained in a number of ways:

- Structurally by considering the fact that a *meso*-*meso* linked porphyrin will be more planar than the corresponding  $\beta$ - $\beta$  linked and  $\beta$ -*meso* linked porphyrins.
- Electronically with a smaller HOMO-LUMO gap for the *meso*-*meso* linked porphyrin compared to the  $\beta$ - $\beta$  linked and  $\beta$ -*meso* linked porphyrins, demonstrating a more conjugated aromatic system granted by the increased orbital overlap and hence increased electronic communication.
- Experimentally for the absorption spectrum of an ethyne linked porphyrin linked at the *meso*-*meso* position being 683 nm compared to 611 and 641 for the  $\beta$ - $\beta$  and  $\beta$ -*meso* linked porphyrins respectively.

- The reason for the maintained electronic interaction, despite minimal overlap, can be explained by applying a model proposed by Kasha,<sup>21</sup> where the electrostatic interactions between the two porphyrins led to slight stabilisation of the molecular orbitals through dipolar interactions/excitonic coupling. This stabilisation effect will be increased when orbital interaction is able to occur as demonstrated in Figure 80.<sup>22</sup>

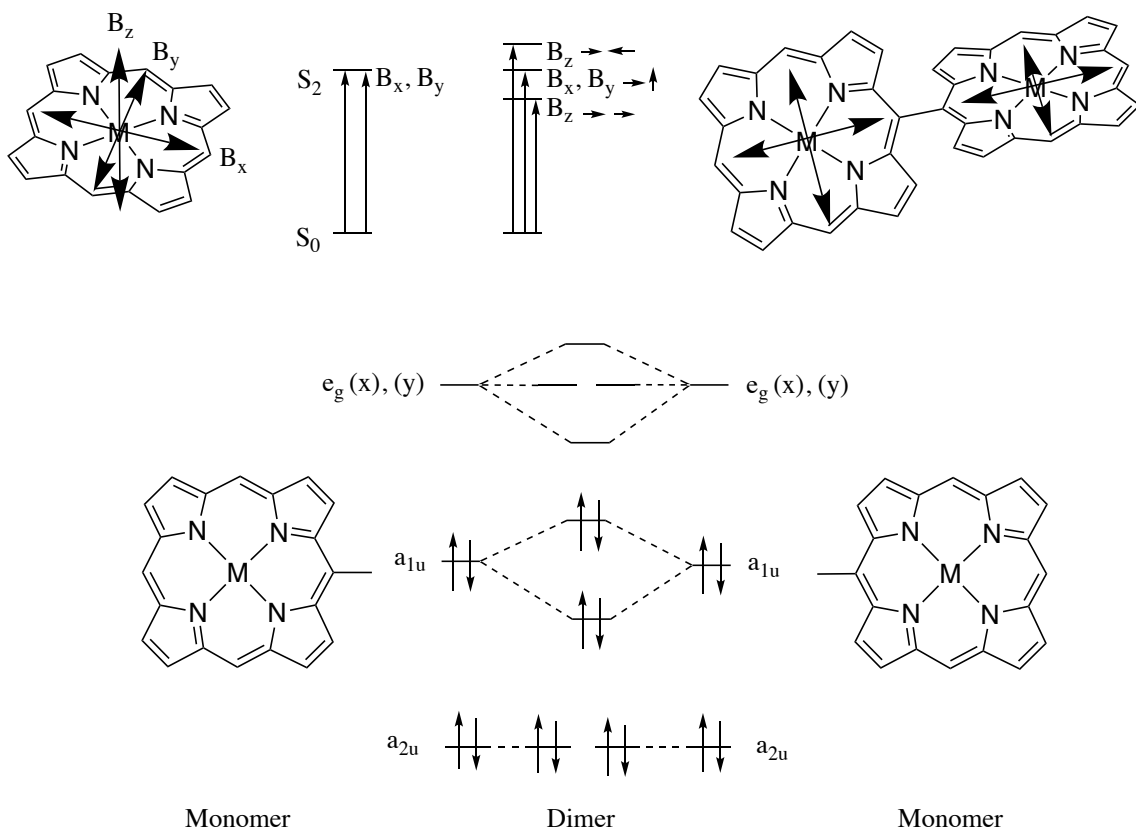


Figure 80: Electronic interactions between porphyrin moieties by excitonic coupling (top) and orbital interactions (bottom)

The greater the electronic communication, the greater the bathochromic shift that can be observed in electronic spectroscopy. Consequently, only small bathochromic shifts are observed for excitonic coupling and larger bathochromic shifts are observed for orbital overlap. The extent of the bathochromic shift will depend on the efficiency of the orbital overlap and hence the stabilisation of the molecular orbitals. The above comments mean that the porphyrin dimers (or oligomers) most prominent in the literature are those that are linked at the *meso* position.

### I2.2.2 Changing the linking unit

Many linking moieties are possible at both the  $\beta$  and the *meso* position, many of which have been summarised by Osuka in a recent review.<sup>23</sup>

Now that the best position for the linking unit has been determined (I2.2.1), a consideration of the linking unit itself can be discussed. Increasing the size of the linker from ethyne to butadiene leads to a decreased electronic communication with the absorption maxima being 683 and 676 nm respectively. The increased distance between the two porphyrins led to weaker excitonic coupling.

The optoelectronic properties seemed to be on account of the resonance form of the quinoidal/cumulenic structure. A new series of porphyrin linkers was then developed in order to favour the quinoidal form. Initially simple systems were developed by Anderson where adding dicyanomethylene groups at the *meso* position of porphyrin monomers<sup>24</sup> helped stabilise the quinoidal structure (Figure 81, left). This progressed onto Osuka's *meso-meso* fused porphyrins (Figure 81, right).

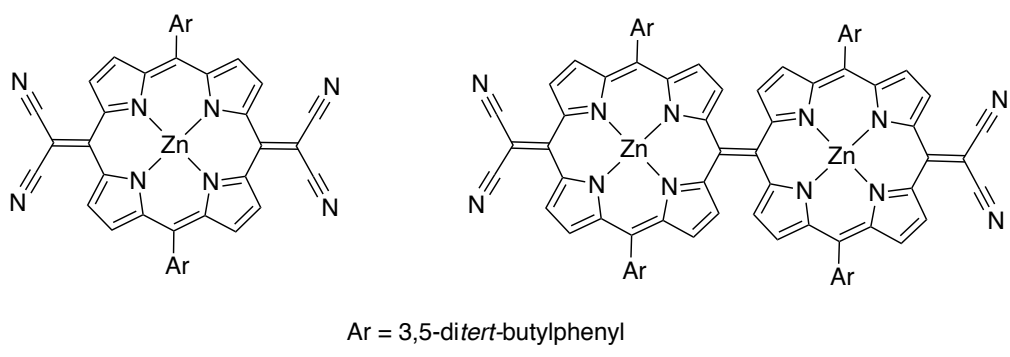


Figure 81: Cumulenic quinoidal porphyrin monomer (left) and dimer (right)

Anderson (Figure 82, left) then advanced to using the cumulenic structure as a linking moiety for porphyrin dimers.<sup>25</sup> Morisue<sup>26</sup> studied in more detail the effect of adding different linking moieties to increase electronic delocalisation between the two porphyrin moieties, one of which is shown below with an anthracene moiety (Figure 82, right).

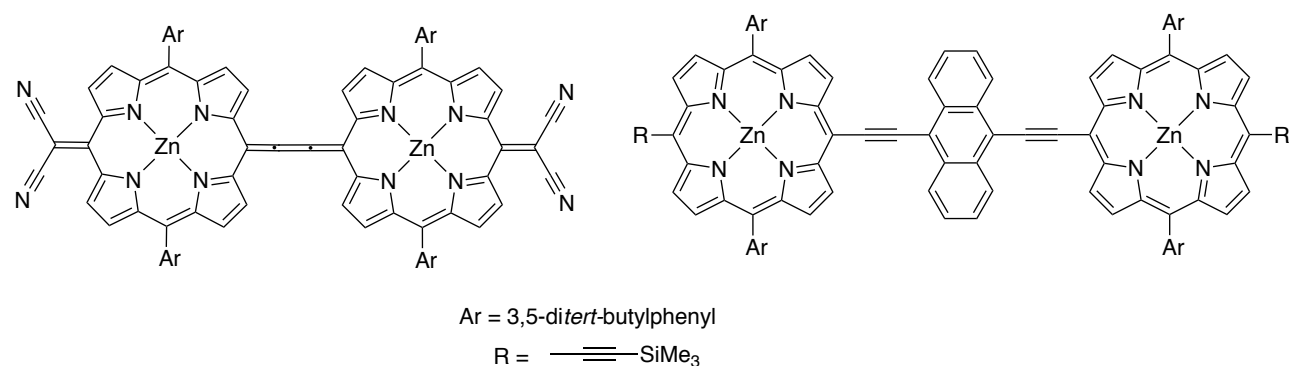


Figure 82: Two porphyrins synthesised in an attempt to favour the quinoidal structure

One experimental evidence for electronic communication is the bathochromic shift and splitting of the Soret band in absorption spectroscopy. Osuka and Therien<sup>17</sup> provided a second experimental evidence for electronic communication, electrochemistry. They demonstrated the fact that good

electronic overlap led to splitting in the first oxidation and first reduction wave of the cyclic voltammograms. This was due to a contribution of the HOMO and the LUMO of the organic linking moiety. This splitting is on account of electronic communication between the two porphyrins which means that the two porphyrins no longer behave independently. This interaction can occur, as  $\pi$  conjugation is present in the linking unit and consequently the porphyrin behaves as one large chromophore. The better the communication, the larger the splitting. As seen for the size of the bathochromic shift, this splitting will be larger or smaller depending on the efficiency of the linking unit for electronic communication.

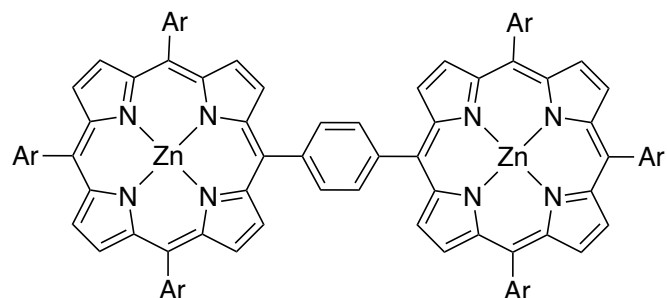


Figure 83: Phenyl linked porphyrin dimer developed by Osuka

Changing the linker to a phenyl group (Figure 83)<sup>27</sup> leads to decreased electronic communication as the phenyl group and the porphyrin are orthogonal to one another, hence minimising orbital overlap.

EPR techniques have been used to observe the spin delocalisation in paramagnetic porphyrin systems. This can either be when the metal is paramagnetic or when an organic radical has been formed on the porphyrin moiety. Changing the linking unit was also shown by Therien to have an effect on the magnetic properties of the porphyrin dimer. The systems studied had a paramagnetic metal bound to the internal cavity of the porphyrin (Cu(II)) and two different linking units, either ethyne or butadiene. A decreased through-bond magnetic communication was observed for the butadiene linker, compared to the ethyne, due to an increased distance between the two paramagnetic metals and a decreased dipolar interaction and also the butadiene decreased efficiency for communication, led to a decreased magnetic interaction by through-bond interactions.<sup>28</sup>

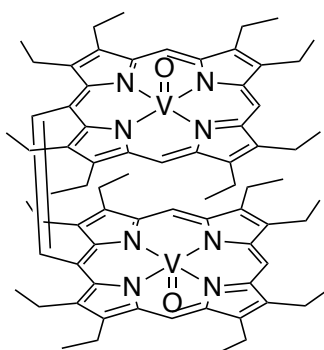


Figure 84: Porphyrin dimer developed by Rath to study the magnetic communication in porphyrin dimers

Magnetic communication is also able to occur when porphyrins are stacked. Rath<sup>29</sup> described the variation in interactions for a vanadyl porphyrin dimer with an ethene bridge (Figure 84); the interaction varied whether the linking ethene bridge was in a *cis* or *trans* configuration. Oxidation was also carried out on the porphyrin and varying the radical cation or cations formed also had an effect on the coupling. DFT calculations showed minimal electron density on the linking unit. No metal-metal interactions occurred for the *trans* dimer and a weak interaction was observed for the *cis* dimer, as the proximity of the porphyrin moieties allowed for  $\pi$ - $\pi$  interactions and this led to communication between the two paramagnetic metals as a result of this  $\pi$ - $\pi$  orbital overlap. Switching the metal ion from vanadyl to silver led to the same observations with variations in the coupling constants. On changing the linker from ethene to ethylene,<sup>30</sup> the distance between the two porphyrins increased and hence a lesser  $\pi$ - $\pi$  stacking was observed leading to a loss of the mild coupling between the paramagnetic metals mentioned previously. The same phenomenon of stacked porphyrin leading to a coupling between the two paramagnetic metals was carried out by Eaton as early as 1985 for two copper porphyrins with a *J* coupling  $>0.3\text{ cm}^{-1}$ .<sup>31</sup>

### 12.2.3 Fused porphyrins

Another way to link porphyrins is by fusing them together, namely Osuka, Diederich and Anderson have progressed this field. On fusing porphyrins together, their proximity is increased and also a greater orbital interaction is observed. This therefore leads to augmented properties in terms of electronic communication and consequently the best electronically communicating porphyrin dimer is observed for this series of porphyrins, which is Osuka's triply fused porphyrin (Figure 85, bottom left).<sup>32</sup>

Osuka studied the effect of singly, doubly and triply fusing porphyrins to form porphyrin dimers and singly and doubly fused corroles.<sup>33</sup> A triply fused porphyrin has also been studied by Diederich.<sup>34</sup> For the triply-fused porphyrin, the lack of free rotation, close proximity and orbital overlap all contributed to this increased electronic communication. The electronic communication was determined by the splitting in the first oxidation wave of the cyclic voltammetry, and the largest splitting is present for this triply fused dimer, 440 mV. Anderson<sup>35</sup> also developed a way to fuse porphyrins together (Figure 85, bottom right), yet a lesser splitting was observed here than for that of Osuka's fused porphyrins, most likely on account of a lesser orbital interaction and a larger separation between the porphyrin moieties.

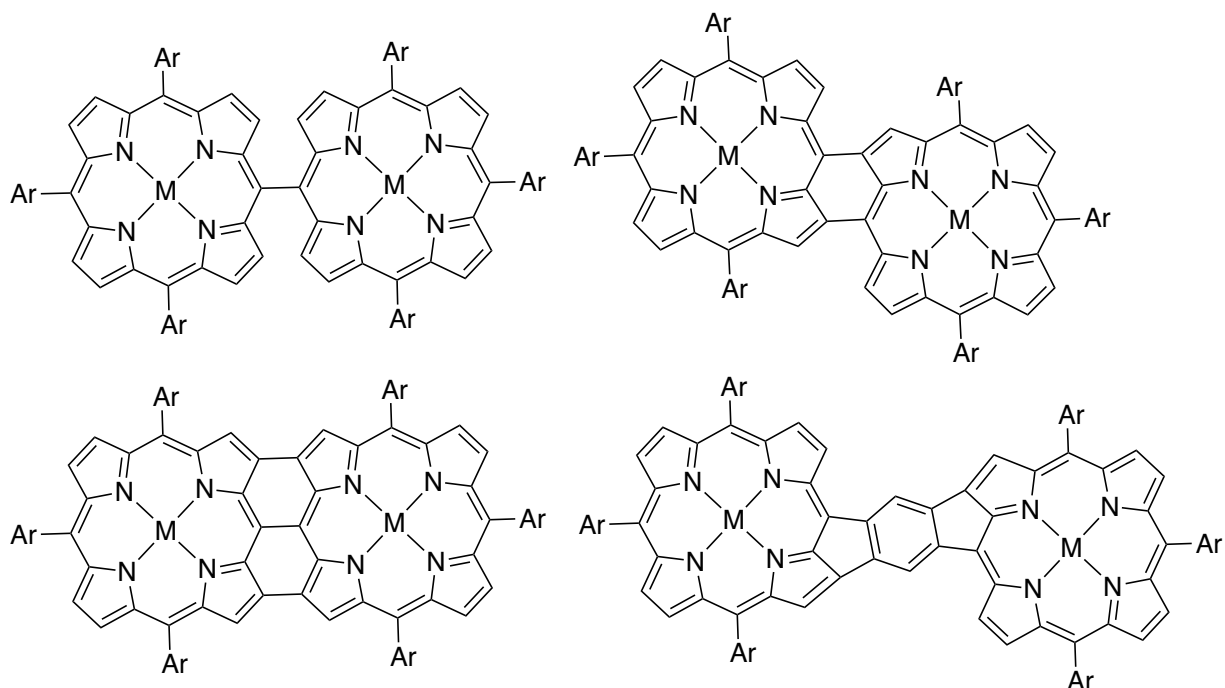


Figure 85: Linked and fused porphyrins developed by Osuka and Anderson.

Osuka studied the effect of varying the position of the linker and also the effect of fusing the porphyrins together on the magnetic properties (Figure 85).<sup>20</sup> The triply fused porphyrins (Figure 85, bottom left) led to a coupling between two Ag(II) metal ions, a coupling that was not present for the linked (Figure 85, top left) and the doubly fused (Figure 85, top right) porphyrins. The coupling was deduced by variations in the EPR spectra and SQUID measurements, with weak antiferromagnetic coupling being in accordance with Curie's law where the magnetisation was inversely proportional to the temperature. The triply fused dimer of Osuka led to an antiferromagnetic coupling when the internal metals were either Cu(II) or Ag(II). This coupling was able to occur over a long range as the distance between the two metal sites was 8.42 Å; the  $J$  coupling for the Cu(II) and Ag(II) was  $-1.43\text{ cm}^{-1}$  and  $-1.73\text{ cm}^{-1}$ , respectively.

#### I2.2.4 Metal ion linked porphyrins

As well as linking porphyrins *via* an organic linker, it can also be envisaged to link porphyrins with a metal ion;<sup>36</sup> clearly this means that an external metal coordination site is required. Porphyrins were hence functionalised at the *meso* positions with potential coordination sites for a metal ion.

Three pertinent examples are shown in Figure 86, one of the first being developed by Lehn and Drain (larger assemblies were also assembled), the second by Sanders<sup>37</sup> and expanded to trimers by Harvey<sup>38</sup> and the third by Sauvage.<sup>39</sup> In the first example presented by Lehn and Drain, the electronic

interactions between the two porphyrin dimers are exceedingly small. This can be explained by the fact that the pyridine groups are orthogonal to the plane of the porphyrin hence diminishing interaction; this was also seen above with the phenyl linker at the *meso* position (Figure 83). The same results were observed for the two other examples shown in Figure 86. In our group as well, non-coplanarity of the organometallic linking units led to small electronic communication.<sup>40,41</sup>

For the system developed by Sauvage and co-workers (Figure 86, bottom), the photophysical properties of this set of dimers was studied and the Ru(II) linker was not only able to act as a template for the assembling process but also as an aid for the electron transfer processes. The robustness of the system allowed for minimal reorganisation energies as seen in photosynthetic processes.

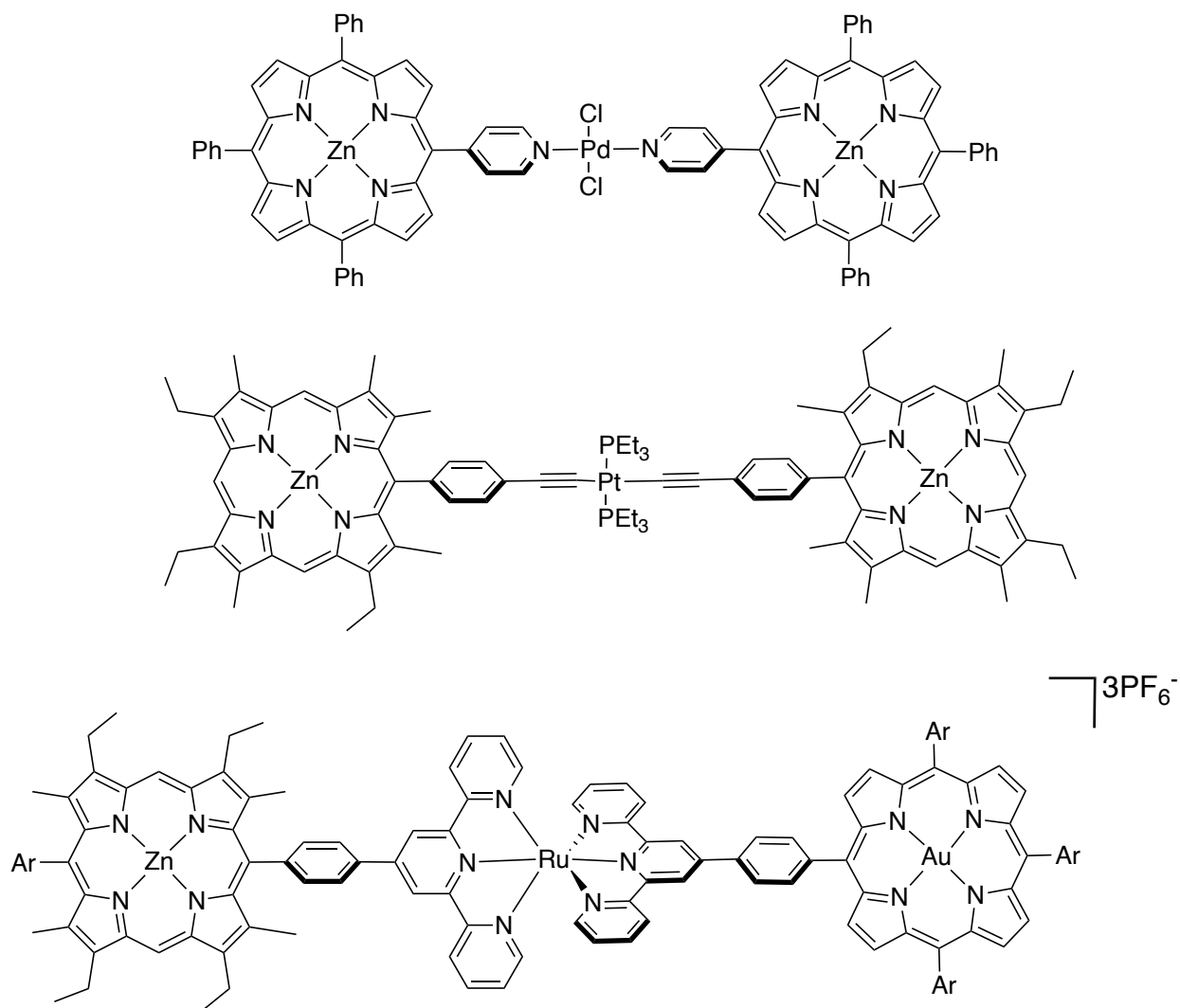


Figure 86: Examples of metal linked porphyrin dimers

An increase in the electronic communication was observed when a Pt(II) ion was linked directly to the *meso* position of a porphyrin. Osuka and co-workers<sup>42</sup> synthesised such Ni porphyrin dimers with a Pt(II) bridge and a larger bathochromic shift was observed for these dimers on account of an orbital

interaction between the  $\pi$ -orbitals of the porphyrin and the d-orbitals of the Pt(II) ion. Osuka and Torres adapted slightly the linking moiety and also used phthalocyanines as well as porphyrins.<sup>43</sup> Electronic communication was also observed by Chen and co-workers<sup>44</sup> when the phenyl groups of Figure 86, middle, were removed leading to an organometallic bridging unit. Electronic communication was confirmed by electronic spectroscopy and electrochemistry. However, the interaction is less than that of the porphyrin linked by a butadiene.<sup>19</sup>

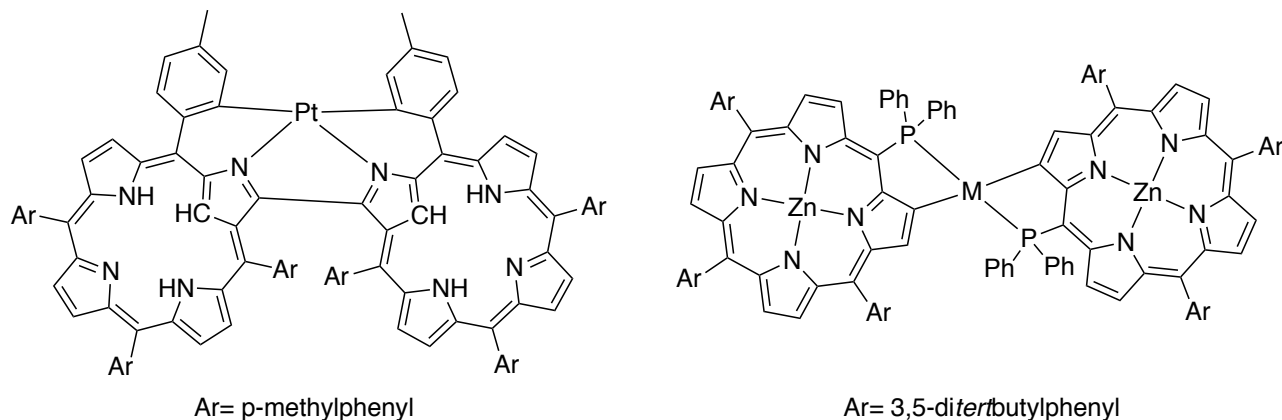


Figure 87: Metal linked porphyrin dimers with an N-confused porphyrin (left) and with a phosphine linker (right)

Furuta<sup>45</sup> and Latos-Grażyński<sup>46</sup> simultaneously developed a series of porphyrins that were described as an N-confused porphyrin (NCP), where one of the pyrrole units was inverted to the exterior of the macrocycle. This work was extended in later years by Chmielewski,<sup>47</sup> to use the inverted pyrrole of the NCP as a coordination site for a Pt(II) ion, the other two sites were occupied by an orthometallation with a carbon of the aryl *meso* substituent (Figure 87, left). Orthometallation directly at the  $\beta$  position of the porphyrin has also been noted in the literature by Matano<sup>48</sup> (Figure 87, right).

One of the first examples of using a metal ion to link porphyrins/porphyrazines using the metal periphery was developed by Barrett and Hoffman who synthesised a porphyrazine with thiolate groups at the  $\beta$ -positions of the pyrrole units that were used to coordinate a Ni(II) ion and hence link the two porphyrin moieties (Figure 88).

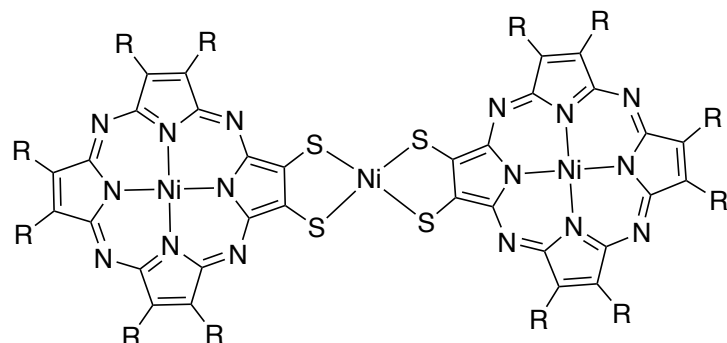


Figure 88: Metal linked porphyrazine dimer developed by Barrett and Hoffman

Barrett and Hoffman also developed a metalloporphyrazine with a linking group for a metal ion in close proximity in order to observe coupling between the two metal ions (Figure 89). Various metals, R groups and spacers were used for these systems.<sup>49,50,51</sup> The effect of the coupling was dependent on the metal employed. It was deemed that sigma delocalisation and the novel symmetries of the metallic orbitals led to the exchange coupling between Cu and VO ions ( $M_1$  and  $M_2$ , respectively). The Cu-Mn coupling was 3-fold higher than that of the VO-Mn coupling. Hence, the orbital interactions are of paramount importance for the exchange coupling interactions.

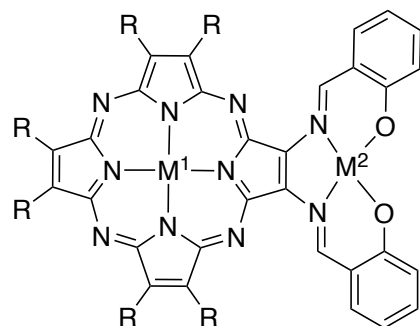


Figure 89: Metalloporphyrazine with an external coordination site for a metal ion  $M_1 = Cu$  or  $VO$ ,  $M_2 = VO$  or  $Mn$

A new synthetic pathway developed by Callot<sup>52</sup> paved the way for the system design developed in our group over the years. On addition of trifluoroacetic acid to an aldehyde substituted at the  $\beta$ -position of the porphyrin, a cyclised ketoporphyrin was obtained. This synthesis has since been optimised and will be discussed further in Chapter 3. A ketone could then be aminated *via* a Michael addition and this formed a porphyrin with an external coordination site at its periphery. Since the 2000s, this external coordination site has been exploited by our group to form porphyrin dimers<sup>53</sup> that are able to communicate electronically by good  $\pi/d$ -orbital interactions that are present due to the planar nature of the linking metal site. Two external coordination sites have been developed in our group, one of them being the enaminoketone<sup>54</sup> (Figure 90, left) and the second being the enaminoaldehyde<sup>55</sup> (Figure 90, right)

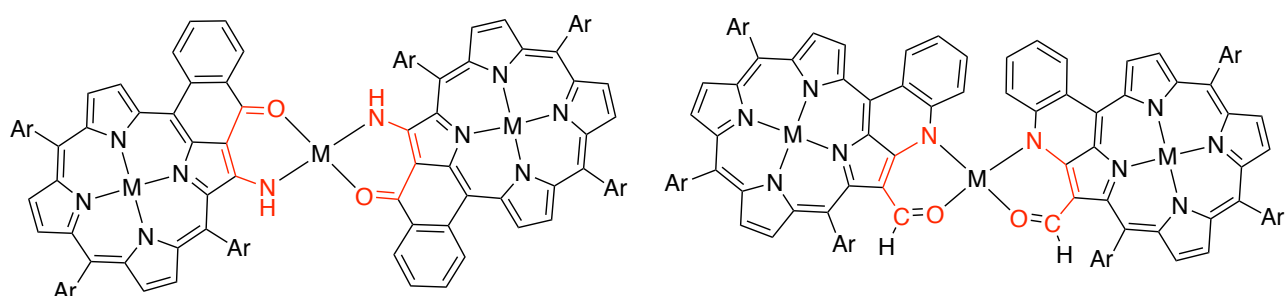


Figure 90: Two porphyrin dimers with an external coordination site for a metal ion shown in red

Good electronic communication between the two porphyrin moieties can be determined by a splitting in the Soret band and a bathochromic shift of both the Soret and the Q-bands in the electronic absorption spectrum. The electronic communication can also be assessed by cyclic voltammetry (Figure 91), with a splitting in the first oxidation wave on account of good  $\pi/d$ -orbital interactions, whereas the first reduction wave did not show any splitting.<sup>54</sup> This analysis was confirmed by DFT calculations (Figure 92) where the d-orbitals were present on the HOMO and not on the LUMO. Consequently no good  $\pi/d$ -orbital interactions were able to occur for the LUMO contrary to the HOMO where this communication is present.<sup>56</sup>

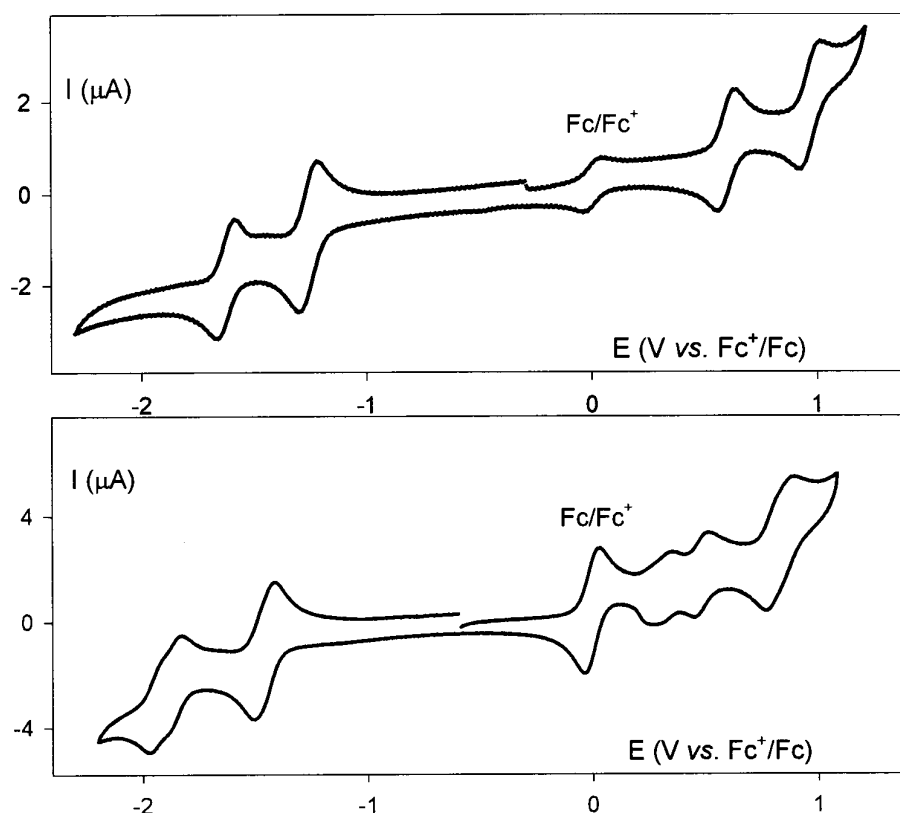


Figure 91: Cyclic voltammetry of the porphyrin monomer (top) and the corresponding porphyrin dimer in Figure 90, left

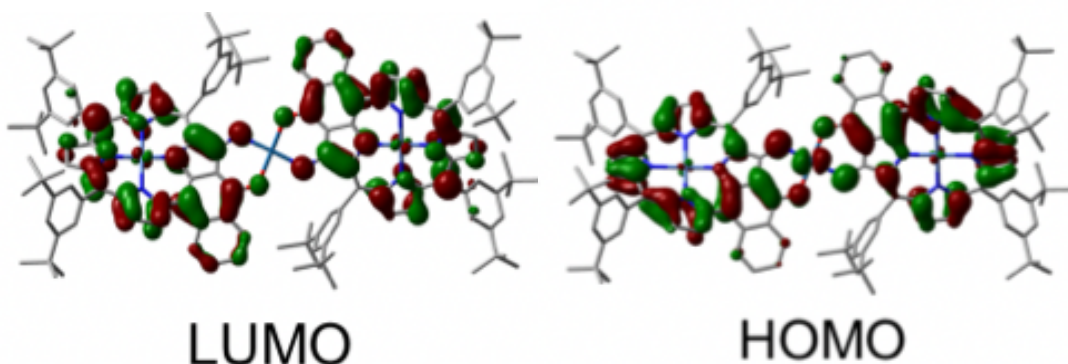


Figure 92: DFT calculated HOMO and LUMO for the porphyrin dimer in Figure 90, left

## 12.3 To trimers, tetramers, oligomers and supramolecular assemblies

This work has been extended in our group by synthesising an A<sub>2</sub>B<sub>2</sub> porphyrin that has two external enaminoketone groups<sup>57</sup> so that trimers (Figure 93, top) and tetramers could be analysed in solution. This large extended porphyrin system led to good electronic communication between all four of the porphyrin moieties and large splitting in the Soret band of the electronic absorption spectrum. Larger porphyrin assemblies have also been synthesised by other research groups notably the triply fused porphyrin by Osuka (Figure 93, bottom right),<sup>32</sup> the ethyne linked porphyrins by Therien (Figure 93, bottom left)<sup>58</sup> and Anderson who has studied both systems.<sup>59</sup>

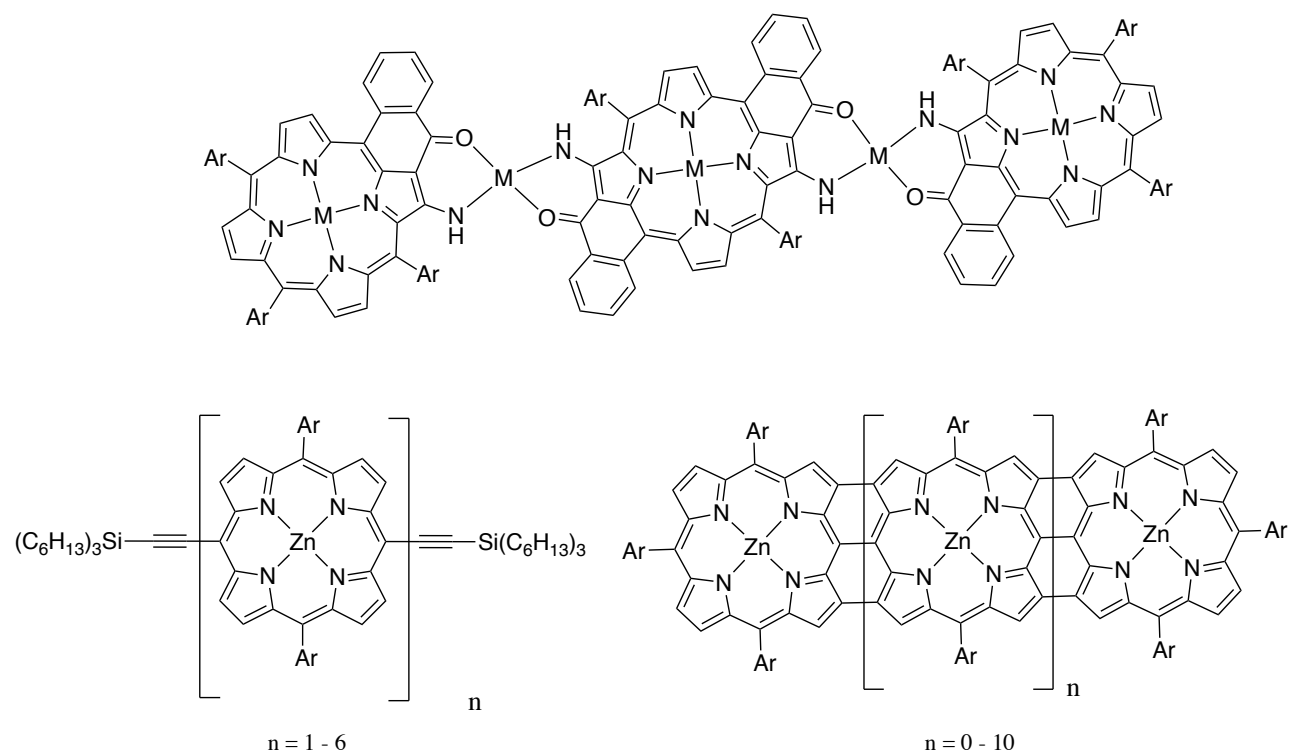


Figure 93: Porphyrin trimers and oligomers developed by Ruppert (top), Anderson (bottom left) and Osuka (bottom right)

The electronic and, in certain cases, magnetic delocalisation in such porphyrin assemblies have been assessed. Taking Anderson's system as an example (Figure 93, bottom left) because both the electronic and magnetic communication were evaluated<sup>60</sup> a radical cation was generated in solution by chemical or electrochemical oxidation. The electronic absorption spectrum showed NIR bands, demonstrating the delocalisation of the radical cation over 2 or 3 porphyrin units. After this point ( $n > 3$ ) there was minimal communication between porphyrin moieties and it was only the central porphyrins that were able to undergo electronic communication. This communication was verified by electron-nuclear double resonance (ENDOR) and continuous wave EPR where discrepancies in the

<sup>14</sup>N hyperfine coupling showed the distribution of the spin over 2 or 3 porphyrin units coinciding with the electronic communication. Anderson applied theory from Norris and co-workers,<sup>61</sup> where the line width varied depending on the number of monomeric units of which the radical cation was delocalised.<sup>62</sup> If the spin density was completely delocalised, the width of the spectra should be inversely proportional to the square root of the number of monomers, according to Norris. Norris' theory was also applied by Osuka for similar systems.<sup>27</sup> As for the electronic communication, the magnetic communication was also dependent on the position of the linking unit, be it at the  $\beta$  or the *meso* position.<sup>20</sup>

As well as linear assemblies of porphyrins, Anderson has also designed porphyrin nanorings (Figure 94)<sup>63</sup> by using a supramolecular approach with the fifth coordination site of a zinc porphyrin leading to the self-assembly of such systems. For this porphyrin nanoring, the spin was spread over 4-6 porphyrins on account of a decreased conformational disorder.<sup>62</sup> Osuka<sup>27</sup> has also designed a porphyrin nanotube, with phenyl linking units. The increased rigidity when in a ring structure allows for communication between the porphyrin moieties, unlike what is seen for the dimer with this linker.

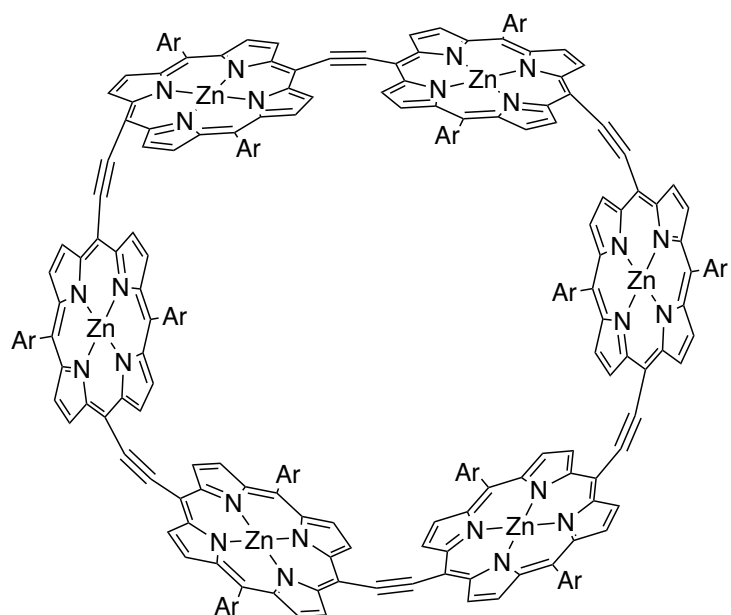


Figure 94: Porphyrin nanoring developed by Anderson

Anderson has also studied the electronic properties of the triply fused porphyrin trimer (Figure 95) by studying the charge transport, hence starting to progress onto molecular electronic devices.<sup>64</sup> The periphery groups of the porphyrin trimer (pyrene) act as electron rich anchoring groups onto the graphene source. Electron-electron interactions are deemed of paramount importance for the efficiency of electronic devices with electronic communication between porphyrins allowing for

vibrationally coupled electronic transition states that allow for charge transport. The porphyrin trimer was weakly coupled to the graphene source and the anchor groups acted as a drain for electrons.

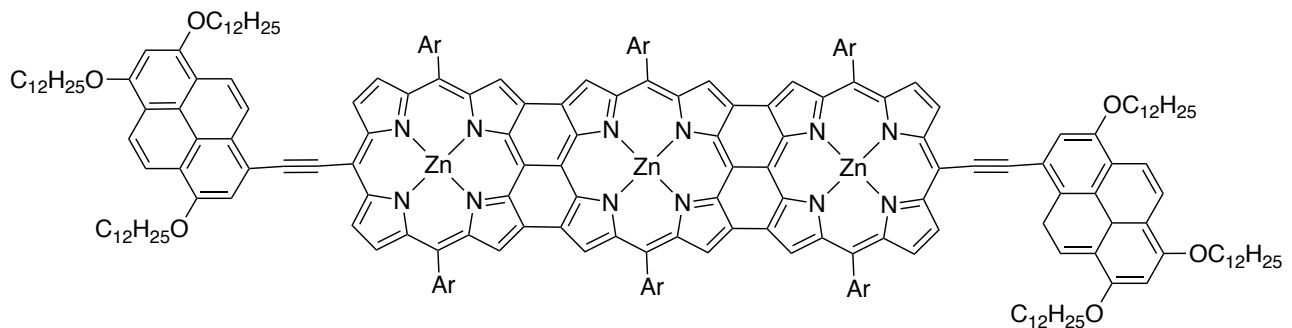


Figure 95: Porphyrin trimer that has had its electronic properties studied

### 12.3.1 Self-assembly of porphyrins at the solid-liquid interface

Increasing the number of porphyrins in these planar porphyrin systems leads to a decrease in their solubility and more complicated characterisation, which is not surprising. A way around this is to assemble porphyrins at a solid-liquid interface. On doing so, the issue of solubility can be removed and large porphyrin oligomers can be assembled and then visualised using scanning tunnelling microscopy (STM) in high definition. In our group, the A<sub>2</sub>B<sub>2</sub> porphyrin similar to the one shown in Figure 93, top was deposited onto a highly ordered pyrolytic graphite (HOPG) surface with and without a Ni(II) source. The enaminoketone was used as an external coordination site for this metal ion and motifs assembled at the solid-liquid interface (Figure 96).<sup>65</sup> The porphyrin self-assembled onto the surface to form nano-ribbons with a size of around 20 nm.

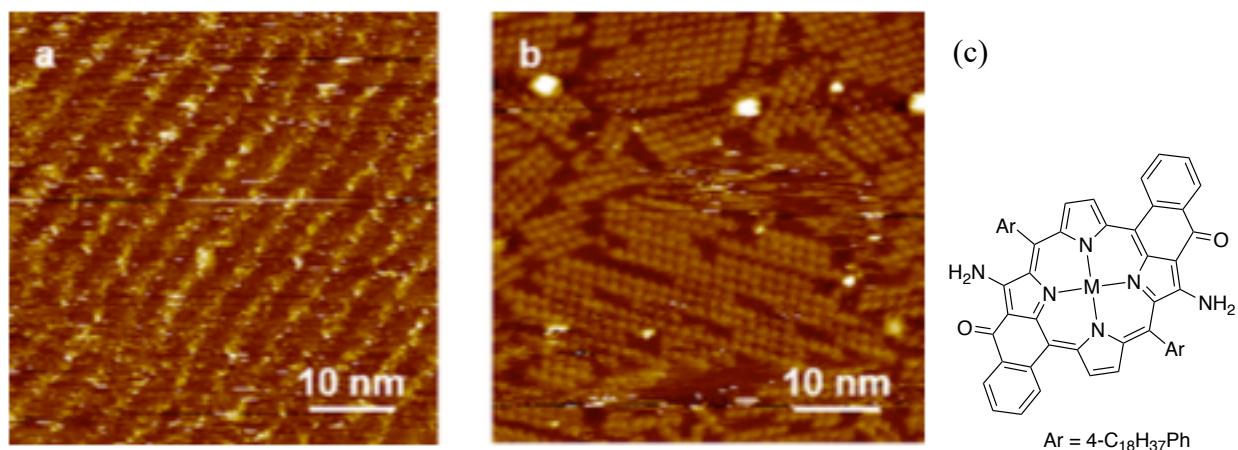


Figure 96: STM height images of porphyrin synthesised by Ruppert and co-workers<sup>65</sup> (1 mM phenyloctane solution): (a) before and (b) after addition of Ni(acac)<sub>2</sub> (1 eq.). Tunnelling conditions: (a)  $I = 2.0 \text{ pA}$ ,  $V = -515 \text{ mV}$ , (b)  $I = 1.3 \text{ pA}$ ,  $V = -405 \text{ mV}$  (c) porphyrin used for self-assembly at the solid-liquid interface

Weiss and co-workers (Figure 97)<sup>66</sup> also used non-covalent interactions in order to form oligomers, and visualised them using atomic force microscopy (AFM), the oligomers were described by the authors as daisy chains. A triazole moiety attached at the *meso* position of the porphyrin was able to undergo hydrogen bonding with the phenanthroline of an adjacent strapped porphyrin and the zinc metal ion at the coordination site of the porphyrin.

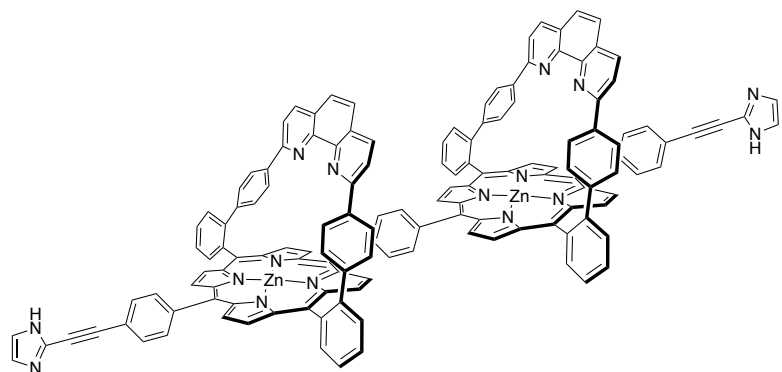


Figure 97: Porphyrin system used to assemble daisy chains at an AFM surface

Metal organic frameworks (MOFs) (Figure 98) using porphyrins have also been assembled at the solid-liquid interface by Hosseini and Samori. This approach is similar to the one employed in our group with the lability of the linking metal unit allowing for correction to occur on the surface. This means that the most thermodynamic product can be self-assembled onto the surface.<sup>67</sup>

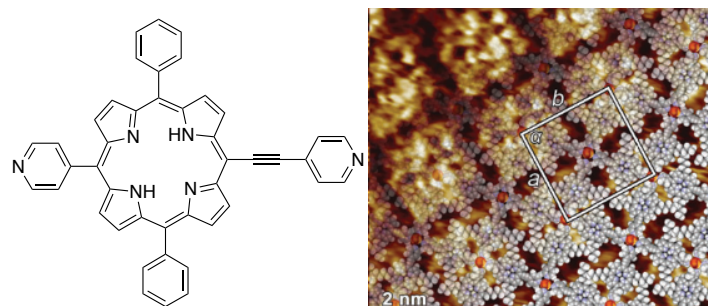


Figure 98: Porphyrin used to assemble MOFs (left) that were visualised by STM techniques (right)

Anderson<sup>68</sup> also assembled the butadiene linked porphyrin system onto a HOPG surface. This is different to the system shown above as there is no dynamic nature to the self-assembly onto the surface and the porphyrin will assemble as a tetramer and not an infinite number of porphyrin monomers as is potentially the case for the above systems.

## I2.4 Conclusions and project plan

The literature demonstrates the importance of the linking moiety in order to increase communication between porphyrin moieties. Co-planarity and good orbital overlap are recurring parameters that are deemed to be important in order for good electronic and magnetic communication to occur. Porphyrins present good electronic properties on account of their large planar aromatic nature and the communication between the porphyrins can be observed for larger systems as well, with the facile functionalisation of porphyrins allowing for these larger motifs to be synthesised.

Our group has also been able to develop a porphyrin system where moieties are able to communicate as a result of orbital interactions between the  $\pi$  orbitals of the porphyrin and the d orbitals of the linking metal ion. The electronic properties of these porphyrins have been widely studied in our group. However, the magnetic properties have been less widely studied and consequently this project will describe the effect of varying both the internal and external metal ion on the electronic and magnetic properties. Porphyrins are ideal candidates to study the magnetic properties as they are co-planar and rigid. This is advantageous as liberty of movement is highly reduced compared to other ligands hence decreasing the number of potential conformers. The distances between metal sites found in crystal structures is also more definite and can be used to guide simulated spectrum in EPR. The large aromatic planar nature of these porphyrins will also be exploited to assemble porphyrin dimers at a solid-liquid interface and the assembled structures will be observed using STM.

## I2.5 References

- 1 R. A. Marcus, *J. Chem. Phys.*, 1965, **43**, 679–701.
- 2 D. L. Dexter, *J. Chem. Phys.*, 1953, **21**, 836–850.
- 3 T. Förster, *Ann. Phys.*, 1948, **28**, 5829–5932.
- 4 W. R. Scheidt and Y. J. Lee, *Struct. Bond.* Springer-Verlag, New-York, 1987, **64**, 1–70.
- 5 M. Gouterman, *J. Mol. Spectrosc.*, 1961, **6**, 138–163.
- 6 M. Gouterman, G. H. Wagnière and L. C. Snyder, *J. Mol. Spectrosc.*, 1963, **11**, 108–127.
- 7 E. Zavoisky, *J. Physics*, 1945, **IX:3**, 211–216.
- 8 A. Van Der Est, *eMagRes*, 2016, **5**, 1411–1422.
- 9 J. Deisenhofer, O. Epp, K. Miki, R. Huber and H. Michel, *Nature*, 1985, **318**, 618–624.
- 10 S. Noblat, C. O. Dietrich-Buchecker and J. P. Sauvage, *Tetrahedron Lett.*, 1987, **28**, 5829–5832.
- 11 J. L. Sessler, J. Hugdahl and M. R. Johnson, 1986, **51**, 2838–2840.
- 12 A. Harriman and J. P. Sauvage, *Chem. Soc. Rev.*, 1996, **25**, 41–48.
- 13 V. S. Y. Lin, S. G. DiMagno and M. J. Therien, *Nature*, 1994, **264**, 1105–1111.
- 14 D. P. Arnold, A. W. Johnson and M. Winter, *J.C.S. Chem. Comm.*, 1976, 797–798.
- 15 D. P. Arnold, A. W. Johnson and M. Winter, *J. Chem. Soc., Perkins Trans. 1*, 1978, 366–370.
- 16 T. Ogawa, Y. Nishimoto, N. Yoshida, N. Ono and A. Osuka, *Angew. Chem. Int. Ed.*, 1999, **38**, 176–179.
- 17 V. S. Y. Lin, S. G. DiMagno and M. J. Therien, *Science*, 1994, **264**, 1105–1111.
- 18 H. L. Anderson, C. J. Walter, A. Vidal-Ferran, R. A. Hay, P. A. Lowden and J. K. M. Sanders, *J. Chem. Soc. Perkin Trans. 1*, 1995, 2275–2279.
- 19 V. S. Y. Lin and M. J. Therien, *Chem. Eur. J.*, 1995, **1**, 645–651.
- 20 T. Ikeue, K. Furukawa, H. Hata, N. Aratani, H. Shinokubo, T. Kato and A. Osuka, *Angew. Chem. Int. Ed.*, 2005, **44**, 6899–6901.
- 21 M. Kasha, H. R. Rawls and M. A. El-Bayoumi, *Pure Appl. Chem.*, 1965, **11**, 371–392.
- 22 S. Ohira and J.-L. Brédas, *J. Mater. Chem.*, 2009, **19**, 7545–7550.
- 23 T. Tanaka and A. Osuka, *Chem. Soc. Rev.*, 2015, **44**, 943–969.
- 24 I. M. Blake, H. L. Anderson, D. Beljonne, J.-L. Bredas and W. Clegg, *J. Am. Chem. Soc.*, 1998, **120**, 10764–10765.
- 25 I. M. Blake, L. H. Rees, T. D. W. Claridge and H. L. Anderson, *Angew. Chem. Int. Ed.*, 2000, **39**, 1818–1821.
- 26 M. Morisue, Y. Hoshino, M. Nakamura, T. Yumura, S. Machida, Y. Ooyama, M. Shimizu

and J. Ohshita, *Inorg. Chem.*, 2016, **55**, 7432–7441.

27 T. M. Wilson, T. Hori, M. C. Yoon, N. Aratani, A. Osuka, D. Kim and M. R. Wasielewski, *J. Am. Chem. Soc.*, 2010, **132**, 1383–1388.

28 R. Wang, A. M. Brugh, J. Rawson, M. J. Therien and M. D. E. Forbes, *J. Am. Chem. Soc.*, 2017, **139**, 9759–9762.

29 A. K. Singh, M. Usman, S. Sarkar, G. Sciortino, D. Kumar, E. Garribba and S. P. Rath, *Inorg. Chem.*, 2021, **60**, 16492–16506.

30 A. K. Singh, M. Usman, G. Sciortino, E. Garribba and S. P. Rath, *Chem. Eur. J.*, 2019, **25**, 10098–10110.

31 S. S. Eaton, G. R. Eaton and C. K. Chang, *J. Am. Chem. Soc.*, 1985, **107**, 3177–3184.

32 A. Tsuda, H. Furuta and A. Osuka, *J. Am. Chem. Soc.*, 2001, **123**, 10304–10321.

33 S. Hiroto, K. Furukawa, H. Shinokubo and A. Osuka, *J. Am. Chem. Soc.*, 2006, **128**, 12380–12381.

34 F. Cheng, S. Zhang, A. Adronov, L. Echegoyen and F. Diederich, *Chem. Eur. J.*, 2006, **12**, 6062–6070.

35 M. Pawlicki, M. Morisue, N. K. S. Davis, D. G. McLean, J. E. Haley, E. Beuerman, M. Drobizhev, A. Rebane, A. L. Thompson, S. I. Pascu, G. Accorsi, N. Armaroli and H. L. Anderson, *Chem. Sci.*, 2012, **3**, 1541–1547.

36 J. F. Longevial, S. Clément, J. A. Wytko, R. Ruppert, J. Weiss and S. Richeter, *Chem. Eur. J.*, 2018, **24**, 15442–15460.

37 L. G. Mackay, H. L. Anderson and J. K. M. Sanders, *J. Chem. Soc. Perkin Trans. 1*, 1995, 2269–2273.

38 D. Bellows, S. M. Aly, C. P. Gros, M. El Ojaimi, J. M. Barbe, R. Guillard and P. D. Harvey, *Inorg. Chem.*, 2009, **48**, 7613–7629.

39 A. Harriman, F. Odobel and J. P. Sauvage, *J. Am. Chem. Soc.*, 1995, **117**, 9461–9472.

40 J. Haumesser, J.-P. Gisselbrecht, J. Weiss and R. Ruppert, *Chem. Commun.*, 2012, **48**, 11653–11655.

41 J. F. Longevial, A. Langlois, A. Buisson, C. H. Devillers, S. Clément, A. Van Der Lee, P. D. Harvey and S. Richeter, *Organometallics*, 2016, **35**, 663–672.

42 N. Fukui, H.-W. Jiang and A. Osuka, *Org. Chem. Front.*, 2017, **4**, 767–772.

43 G. Lavarda, D. Shimizu, T. Torres and A. Osuka, *Angew. Chem. Int. Ed.*, 2020, **59**, 3127–3130.

44 Y. J. Chen, S. S. Chen, S. S. Lo, T. H. Huang, C. C. Wu, G. H. Lee, S. M. Peng and C. Y. Yen, *Chem. Commun.*, 2006, **5**, 1015–1017.

45 H. Furuta, T. Asano and T. Ogawa, *J. Am. Chem. Soc.*, 1994, 767–768.

46 P. J. Chmielewski, L. Latos-Grażyński, K. Rachlewicz and T. Glowiak, *Angew. Chem. Int. Ed.*, 1994, **33**, 779–781.

47 P. J. Chmielewski, B. Durlej, M. Siczek and L. Szterenberg, *Angew. Chem. Int. Ed.*, 2009, **48**, 8736–8739.

48 Y. Matano, K. Matsumoto, Y. Nakao, H. Uno, S. Sakaki and H. Imahori, *J. Am. Chem. Soc.*, 2008, **130**, 4588–4589.

49 M. Zhao, C. Zhong, C. Stern, A. G. M. Barrett and B. M. Hoffman, *J. Am. Chem. Soc.*, 2005, **127**, 9769–9775.

50 C. Zhong, M. Zhao, C. Stern, A. G. M. Barrett and B. M. Hoffman, *Inorg. Chem.*, 2005, **44**, 8272–8276.

51 C. Zhong, M. Zhao, T. Goslinski, C. Stern, A. G. M. Barrett and B. M. Hoffman, *Inorg. Chem.*, 2006, **45**, 3983–3989.

52 H. J. Callot, E. Schaeffer, R. Cromer and F. Metz, *Tetrahedron*, 1990, **46**, 5253–5262.

53 S. Richeter, C. Jeandon, R. Ruppert and H. J. Callot, *Chem. Commun.*, 2001, **2**, 91–92.

54 S. Richeter, C. Jeandon, J. P. Gisselbrecht, R. Ruppert and H. J. Callot, *J. Am. Chem. Soc.*, 2002, **124**, 6168–6179.

55 S. Richeter, C. Jeandon, J. P. Gisselbrecht, R. Graff, R. Ruppert and H. J. Callot, *Inorg. Chem.*, 2004, **43**, 251–263.

56 H. Dekkiche, A. Buisson, A. Langlois, P. L. Karsenti, L. Ruhlmann, R. Ruppert and P. Harvey, *Chem. Eur. J.*, 2016, **22**, 10484–10493.

57 S. Richeter, C. Jeandon, J. P. Gisselbrecht, R. Ruppert and H. J. Callot, *Inorg. Chem.*, 2007, **46**, 10241–10251.

58 G. Bullard, F. Tassinari, C. H. Ko, A. K. Mondal, R. Wang, S. Mishra, R. Naaman and M. J. Therien, *J. Am. Chem. Soc.*, 2019, **141**, 14707–14711.

59 E. Leary, B. Limburg, A. Alanazy, S. Sangtarash, I. Grace, K. Swada, L. J. Esdaile, M. Noori, M. T. González, G. Rubio-Bollinger, H. Sadeghi, A. Hodgson, N. Agralt, S. J. Higgins, C. J. Lambert, H. L. Anderson and R. J. Nichols, *J. Am. Chem. Soc.*, 2018, **140**, 12877–12883.

60 G. Moise, L. Tejerina, M. Rickhaus, H. L. Anderson and C. R. Timmel, *J. Phys. Chem. Lett.*, 2019, **10**, 5708–5712.

61 J. R. Norris, R. A. Uphaus, H. L. Crespi and J. J. Katz, *Proc. Natl. Acad. Sci. USA.*, 1971, **68**, 625–628.

62 M. D. Peeks, C. E. Tait, P. Neuhaus, G. M. Fischer, M. Hoffmann, R. Haver, A. Cnossen, J. R. Harmer, C. R. Timmel and H. L. Anderson, *J. Am. Chem. Soc.*, 2017, **139**, 10461–10471.

63 M. Rickhaus, A. Vargas Jentzsch, L. Tejerina, I. Grübner, M. Jirasek, T. D. W. Claridge and

H. L. Anderson, *J. Am. Chem. Soc.*, 2017, **139**, 16502–16505.

64 J. O. Thomas, J. K. Sowa, B. Limburg, X. Bian, C. Evangelı, J. L. Swett, S. Tewari, J. Baugh, G. C. Schatz, G. A. D. Briggs, H. L. Anderson and J. A. Mol, *Chem. Sci.*, 2021, **12**, 11121–11129.

65 M. A. Carvalho, H. Dekkiche, M. Nagasaki, Y. Kikkawa and R. Ruppert, *J. Am. Chem. Soc.*, 2019, **141**, 10137–10141.

66 C. Kahlfuss, Y. Kikkawa, J. A. Wytko and J. Weiss, *Helv. Chim. Acta*, 2019, **102**, 1900058.

67 M. El Garah, A. Ciesielski, N. Marets, V. Bulach, M. W. Hosseini and P. Samorì, *Chem. Commun.*, 2014, **50**, 12250–12253.

68 A. Bellamy-Carter, C. Roche, H. L. Anderson and A. Saywell, *Sci. Rep.*, 2021, **11**, 20388.

# Chapter 3

## Synthesis of porphyrin dimers and the study of their magnetic and electronic properties

3.1 Introduction	120
3.2 Porphyrin synthesis	120
3.3 Electronic properties	126
3.3.1 Vanadyl porphyrins	126
3.3.2 Copper porphyrins	131
3.4 Magnetic properties	133
3.4.1 Vanadyl porphyrins	140
3.4.2 Copper porphyrins	
3.5 Enaminothioketone Porphyrins	144
3.5.1 Synthesis	145
3.5.2 Electronic properties	147
3.5.3 Magnetic properties	
3.6 Qubits for quantum computing	149
3.6.1 Hahn echo	150
3.6.2 Saturation recovery	151
3.6.3 Vanadyl monomer M4	152
3.6.4 2-Qubit systems	156
3.7 Conclusions and perspectives	159
3.8 References	161

### 3.1 Introduction

Porphyrins are ubiquitous in Nature and their exceptional properties have been exploited by synthetic chemists for decades. Our group is no exception to this, with an optimised porphyrin moiety possessing an internal and external coordination site for the formation of high light absorbing,<sup>1</sup> good electronic communicating<sup>2</sup> and magnetically coupled porphyrin dimers.<sup>3</sup> The enhanced properties of these porphyrin dimers are aided by the coplanarity of the two porphyrin moieties, as the linking metal ion has a square-planar geometry. This allows for orbital interactions between the porphyrin and the d-orbitals of the metal ion and consequently electronic and magnetic communication can be observed between the two porphyrin moieties. These effects can be enhanced by fine-tuning the interactions between the porphyrins and the linking metal ion.

The synthesis and properties of such porphyrins will be discussed in this chapter. Paramagnetic metals were chosen at the internal and/or external metal coordination site, in order for the magnetic communication between the porphyrin moieties to be evaluated by electron paramagnetic resonance (EPR) spectroscopy. The electronic communication will be evaluated by electronic absorption spectroscopy and cyclic voltammetry.

### 3.2 Porphyrin synthesis

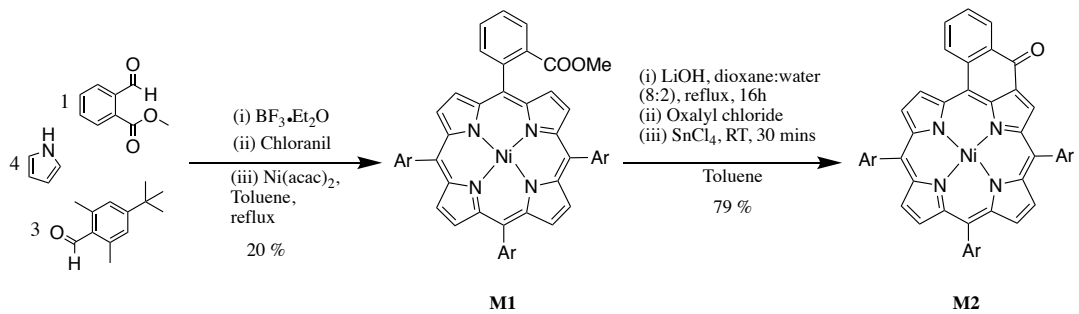


Figure 99: Synthesis of the Ni(II) ketoporphyrin, M2

The porphyrin was synthesised using classical Lindsey conditions<sup>4</sup> in a stoichiometric manner (Figure 99). The free base porphyrin was then metallated with a Ni(II) source in order to form the so-called A<sub>3</sub>B porphyrin, M1, in a 20% yield, with A being the three 2,6-dimethyl-*para*-*tert*-butylphenyl substituents (represented as Ar in Figure 99) and B being the phenylester at the fourth *meso* position. After hydrolysis of the M1 ester using lithium hydroxide, an acid chloride was formed on addition of oxalyl chloride and an intramolecular Friedel-Crafts reaction occurred on addition of  $\text{SnCl}_4$ . This process was high yielding (79%).

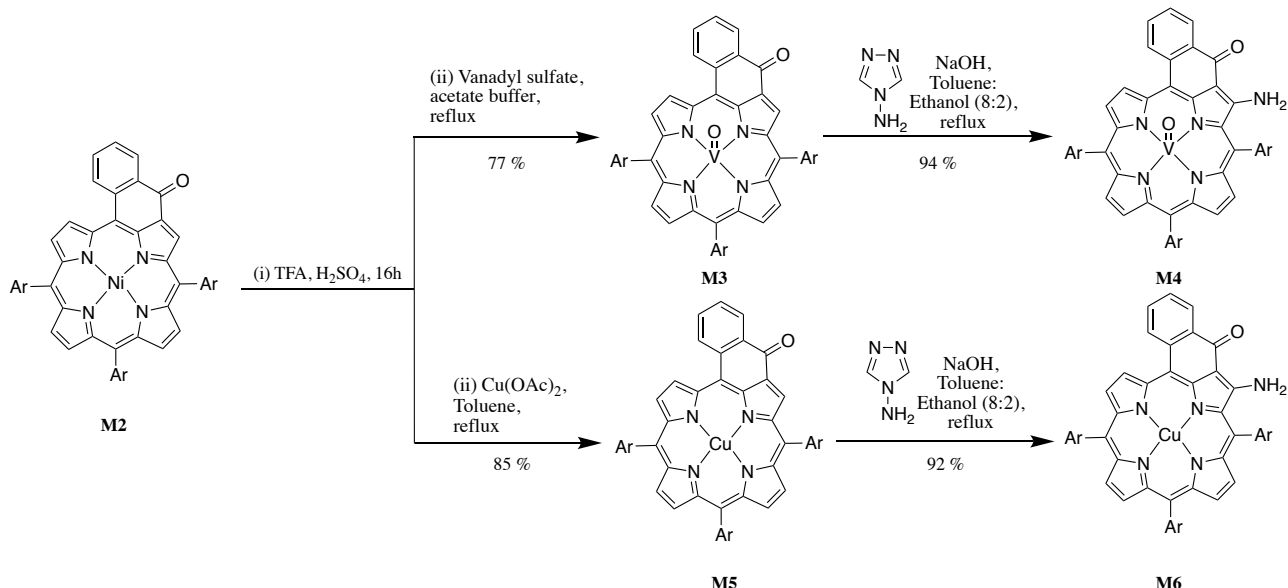


Figure 100: Synthesis of the metallated enaminoketone porphyrins

The nickel ketoporphyrin, **M2**, was then demetallated in a TFA/H<sub>2</sub>SO<sub>4</sub> solution (Figure 100). The demetallated porphyrin was then metallated with one of two paramagnetic metal ions chosen. The two paramagnetic metal ions that were introduced at the internal coordination site of the porphyrin were copper(II) and vanadyl(IV); this was done by heating the appropriate metal ion source with the free-base in an appropriate solvent. Once metallated, an amination was then carried out on the porphyrin *via* a Michael addition onto the ketone of the porphyrin using Katritzky's reagent.<sup>5</sup> This led to the synthesis of two porphyrin monomers, **M4** and **M6**, with an internal coordination site used to coordinate either vanadyl or copper respectively and an external coordination site (enaminoketone) available for the formation of dimers.

A crystal structure was obtained for the vanadyl monomer, **M4**. The vanadyl sat slightly out of the plane of the porphyrin with a square pyramidal geometry and the *meso* substituents were perpendicular to the porphyrin plane. There was also a mild distortion in the aromatic macrocyclic ring on account of steric interactions between one proton of the cyclised phenyl and the proton of the neighbouring pyrrole (Figure 101, right, H shown in white).

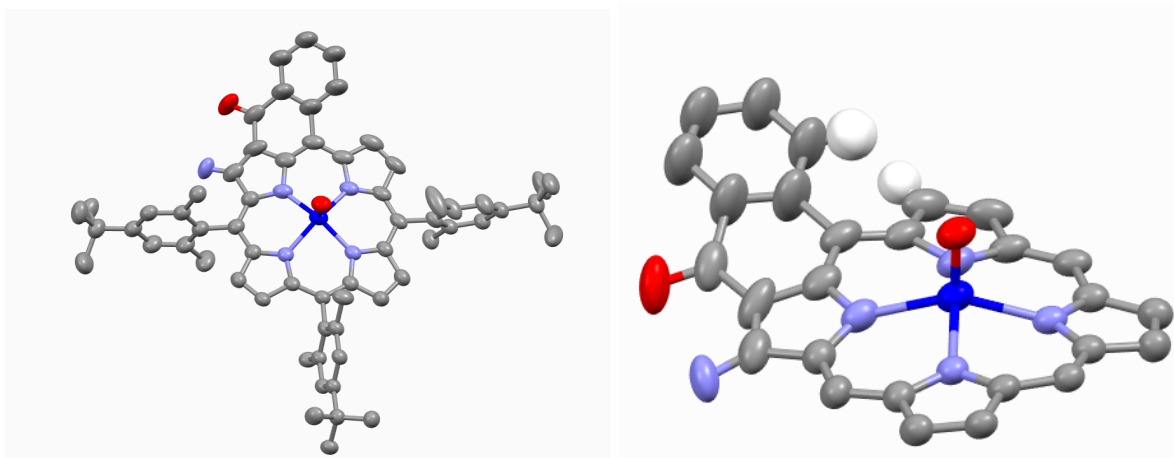


Figure 101: Two visual representations of the crystal structure of **M4**. V blue; C grey; O red; N light blue; H white. For the structure on the left the hydrogen atoms have been omitted, and on the right the meso substituents and the hydrogen atoms have been omitted for clarity.

This set of porphyrins proved challenging to recrystallise as the *meso* aryl groups led to a highly soluble porphyrin. In order to facilitate recrystallisation, the same porphyrins were synthesised with phenyl groups at the *meso* positions, instead of 2,6-dimethyl-4-*tert*-butylphenyl. A crystal structure was obtained for the vanadyl monomer with phenyl groups at the *meso* position (Figure 102) and the same steric distortion was present as seen for **M4**. The vanadyl monomer with phenyl *meso* groups showed an interesting dimeric assembly in the crystal structure, as a result of a methanol molecule being coordinated to the vanadium. Hydrogen bonding was able to occur between the hydrogen of the methanol and the ketone of an adjacent porphyrin and  $\pi$ - $\pi$  interactions occurred between the two aromatics. To our knowledge, a sixth coordination site for a V(IV) with a methanol *trans* to the oxo has never been reported in the literature for vanadyl porphyrins and this supramolecular assembly of porphyrins is quite a novel and interesting find; there are however examples in the literatures of the coordination of methanol *trans* to the oxo known for other complexes.<sup>6</sup> Looking at the crystal structure it is apparent that steric hindrance would impede such interactions for the porphyrin with 2,6-dimethyl-4-*tert*-butylphenyl substituents, as the second porphyrin comes into close proximity to the first. The distance between the oxygen of the methanol and the oxygen of the ketone is 2.670 Å and between the oxygen of the methanol and the vanadium is 2.323 Å.

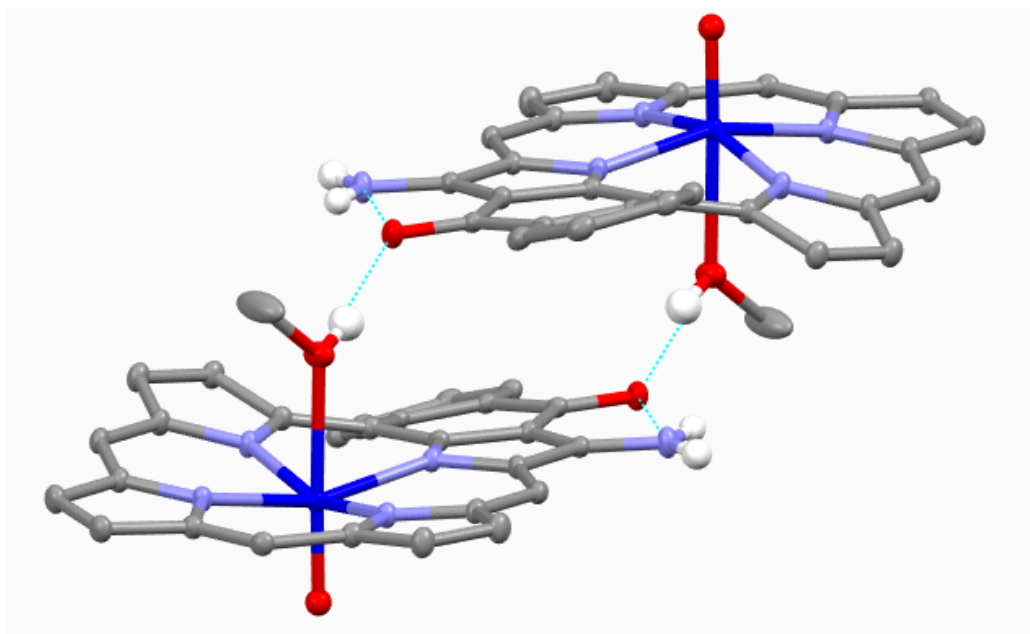


Figure 102: Crystal structure of vanadyl monomer with phenyl substituents at the meso-positions, demonstrating the formation of a dimeric assembly. V blue; C grey; O red; N light blue; H white. Hydrogen bonding shown as blue dotted line. Hydrogen atoms and meso phenyl groups were omitted for clarity.

The external coordination site, enaminoketone, could then be exploited to form the porphyrin dimers, **D1-D7**, on addition of half an equivalent of an appropriate metal ion source (Figure 103). The yields and reaction conditions for this process varied substantially depending on the linking metal ion.

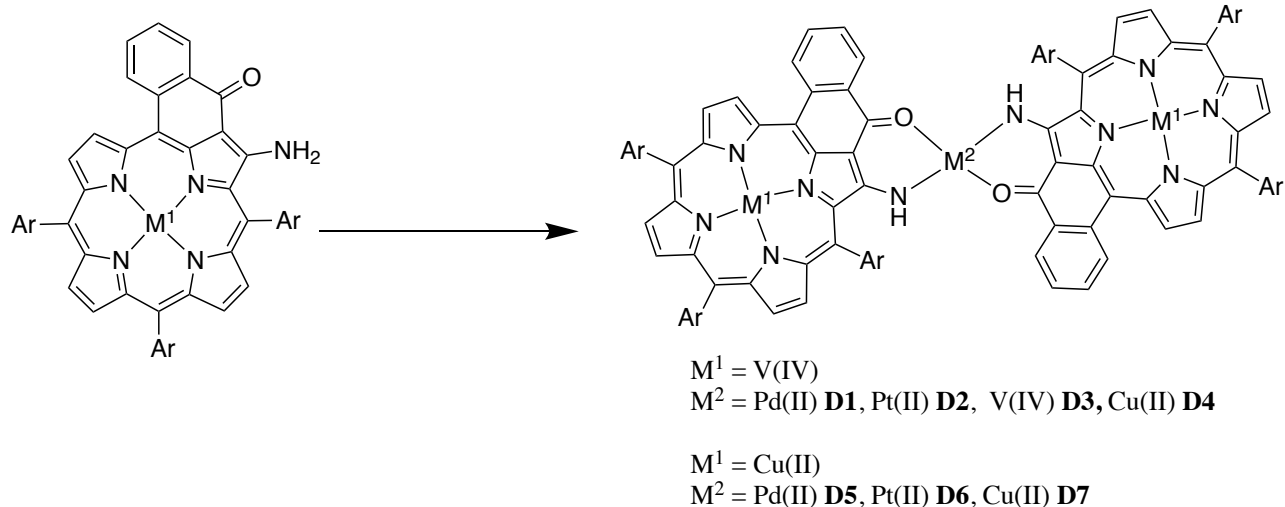


Figure 103: Synthesis of porphyrin dimers

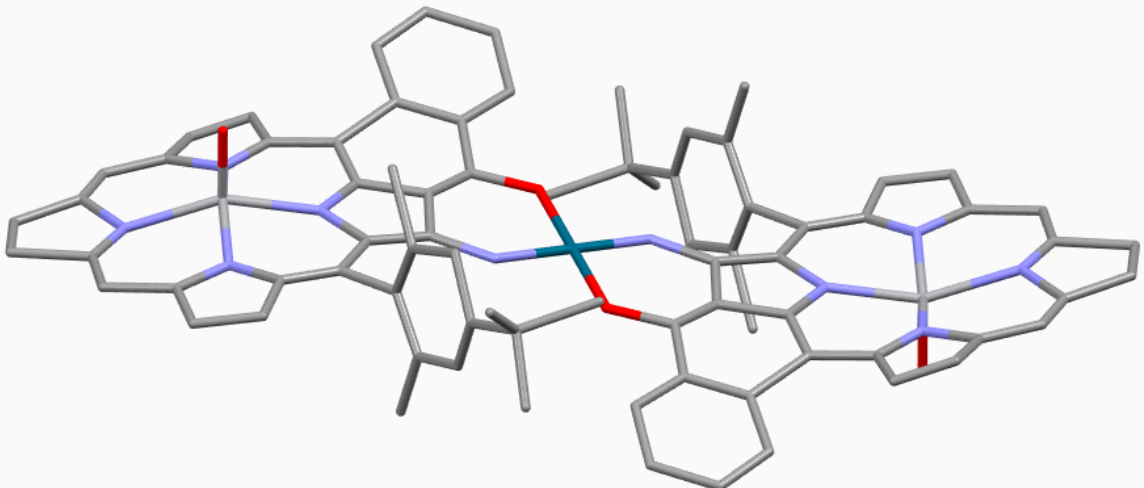


Figure 104: Crystal structure of **D1**. V light grey; C dark grey; O red; N light blue; Pd emerald. Hydrogen atoms and meso-substituents omitted for clarity. Two meso groups were kept to explain why the *trans* dimer forms

A crystal structure was also obtained for VPdV dimer, **D1** (Figure 104). The two porphyrins are co-planar with a square planar Pd(II) metal ion linking the two porphyrins together. The co-planarity will help increase electronic communication between the two porphyrin moieties along with other electronic factors. The geometry around the Pd(II) coordination site is *trans* and only the *trans* form was observed. This is on account of the steric hindrance provided from the aryl groups, (shown in Figure 104) making the *cis* isomer impossible.

The paramagnetic metal sites are quite far away from each other, 14.32 Å and there is 7.16 Å between the vanadyl(IV) and the palladium(II) ions. The  $\alpha,\beta$  isomer of the dimer was also the only one observed, with one of the vanadyl metal ions pointing up ( $\alpha$ ) and the other pointing down ( $\beta$ ). The  $\alpha,\beta$  isomer was most likely the thermodynamic product due to the increased symmetry gained in this configuration with a centre of inversion at the palladium(II) metal ion. Crystals suitable for X-ray diffraction were also obtained for the VPdV dimer with phenyl substituents and minimal differences were observed between these two crystal structures in terms of distortions and distances with the vanadyl-vanadyl distance now being equal to 14.34 Å (Figure 105).

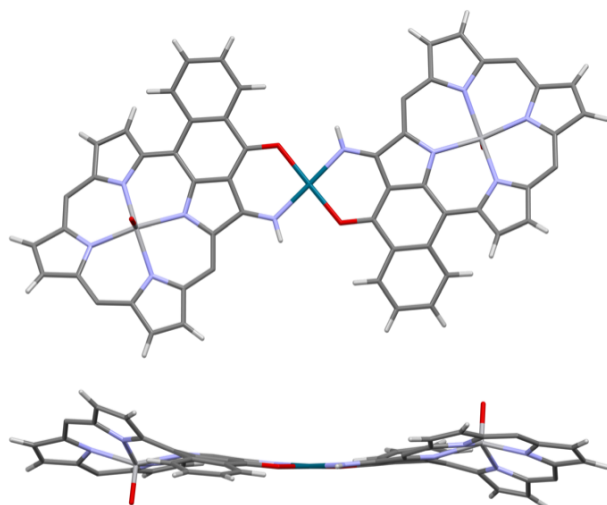


Figure 105: Two representations of the crystal structure of VPdV with meso phenyl groups. V light grey; C dark grey; O red; N light blue; Pd emerald. Hydrogen atoms and meso-substituents omitted for clarity.

The vanadyl Pt vanadyl dimer, **D2** proved more challenging to synthesise and no product was formed even after heating **M4** with half an equivalent of a Pt(II) source for 4 days at reflux in 1,2-dichlorobenzene. This issue was resolved by using the microwave. After 5 hours in the microwave at 200 °C, the colour of the solution had turned brown and **D2** had formed. Interestingly, two products were isolated by column chromatography. The hypothesis is that these two dimers were the  $\alpha,\alpha$  and the  $\alpha,\beta$  isomers with the vanadyl either pointing up both times ( $\alpha,\alpha$ ) or once up and once down ( $\alpha,\beta$ ). These two dimers were able to be separated by column chromatography as the  $\alpha,\alpha$  dimer is more polar than the  $\alpha,\beta$  dimer. Two dimers were not observed for the **D1**, as this dimer required less harsh conditions (heating at reflux in toluene for 16 h), demonstrating that the coordination bond was more labile and consequently ligand exchange would most likely be able to occur. Hence, the thermodynamic product was able to form due to the lability of the bond. Whereas for the case of **D2**, the coordination bond with platinum is more inert and consequently after formation of the dimer, ligand exchange is less possible and hence the two dimers ( $\alpha,\alpha$  and  $\alpha,\beta$ ) are most likely formed.

The synthesis of **D3** proved challenging on account of an instability of the dimer, most likely due to the oxyphilic nature of the vanadyl(IV) ion.

### 3.3 Electronic properties

Having synthesised the two porphyrin monomers and the seven porphyrin dimers, their electronic properties were evaluated by electronic absorption spectroscopy and cyclic voltammetry. Both of these analyses were carried out in the solvent dichloromethane.

#### 3.3.1 Vanadyl porphyrins

The electronic spectra of porphyrins are dominated by two main bands: one of these is named the Soret band ( $S_0$  to  $S_2$ ) and the other is known as the Q-band ( $S_0$  to  $S_1$ ). The position of these bands depends on the nature of the porphyrin. Looking at the vanadyl monomer **M4**, the Soret band is located at 470 nm and the lowest energy Q-band is found at 672 nm.

Our porphyrin monomer has a slight bathochromic shift compared to other porphyrins in the literature.<sup>7</sup> This is on account of the expanded porphyrin gained by the fused phenyl ring. On formation of a porphyrin dimer, there was a large bathochromic shift; the size of this bathochromic shift depended on the linking metal ion (Figure 106 and Table 23). Going down the periodic table from Pd to Pt, there is a progression from 4d to 5d orbitals and hence a more efficient orbital interaction with the enaminoketone binding site. Consequently, there was an increased electronic delocalisation between the two porphyrins and hence a larger bathochromic shift, 46 nm, between **M4** and **D1**. There was also an increase in the intensity of the Q-band with increased electronic communication and a further splitting of the Soret band was also observed.

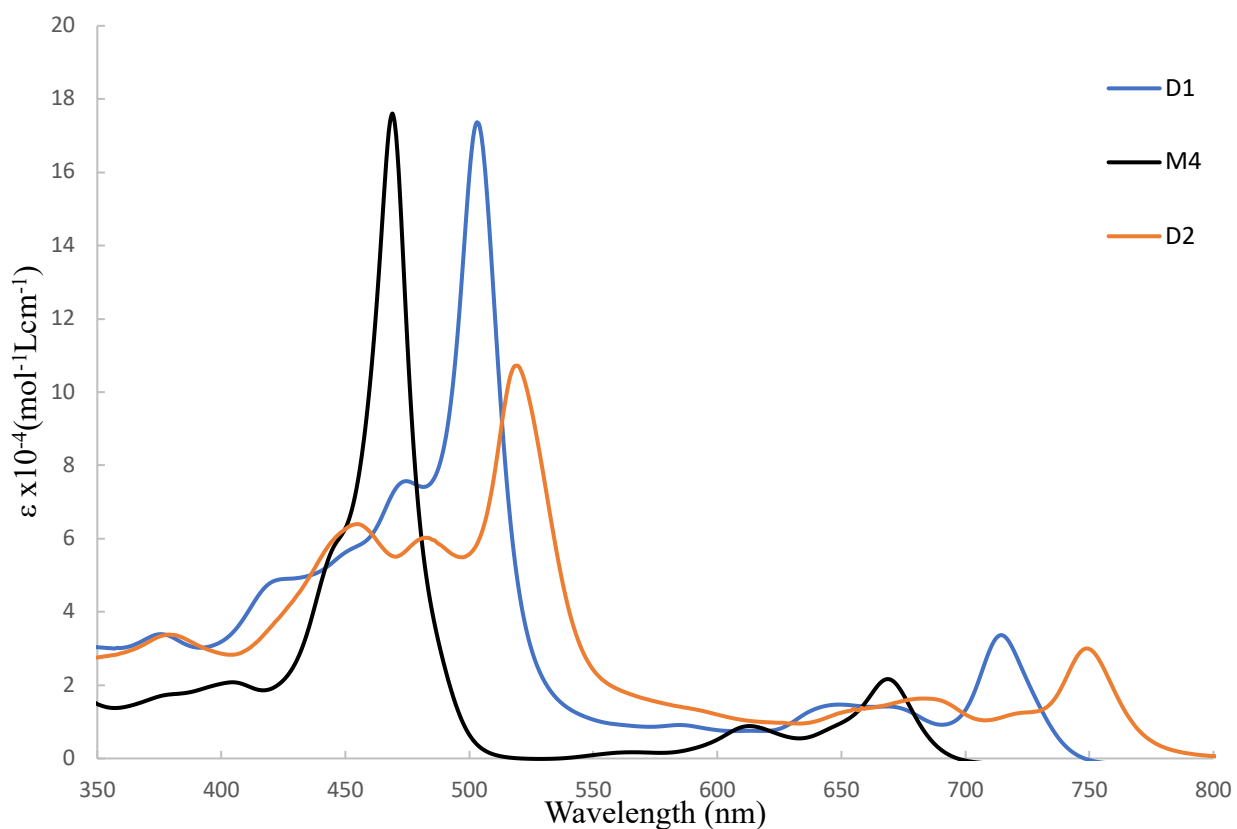


Figure 106: Electronic spectra of selected porphyrins **M4**, **D1** and **D2** in dichloromethane at room temperature

Table 23: Absorption maximum of the vanadyl porphyrin series

	Soret $\lambda_{\max}$ (nm) ( $\epsilon$ , ( $M^{-1}cm^{-1}$ ))	Q-band $\lambda_{\max}$ (nm) ( $\epsilon$ , ( $M^{-1}cm^{-1}$ ))	Bathochromic shift vs. <b>M4</b> (nm)
<b>M4</b> (V)	470 (173 000)	672 (20 000)	-
<b>D1</b> (VPdV)	505 (169 000)	718 (31 000)	46
<b>D2</b> (VPtV)	522 (130 000)	785 (20 000)	113
<b>D3</b> (VVV)	494 (100 000)	703 (17 000)	31
<b>D4</b> (VCuV)	472 (86 000)	675 (20 000)	3

Cyclic voltammetry was carried out on the vanadyl porphyrins in dichloromethane with tetrabutylammonium hexafluorophosphate (0.1 M) as the supporting electrolyte. The voltammograms show two reversible oxidation and two reversible reduction monoelectronic waves (Figure 107). It is known that the redox chemistry occurs solely on the porphyrin and the vanadyl remains formally at

the oxidation state IV, meaning that the radicals observed experimentally are ligand-centred radical cations on oxidation and ligand centred-radical anions on reduction. The potential difference between the first oxidation and the first reduction was equal to 1.83 V, which is very similar to Ni(II) porphyrins already reported in our group<sup>2</sup> but was a lot smaller than other porphyrins in the literature which are not functionalised, where the value is closer to 2.10 - 2.40 V.<sup>8</sup>

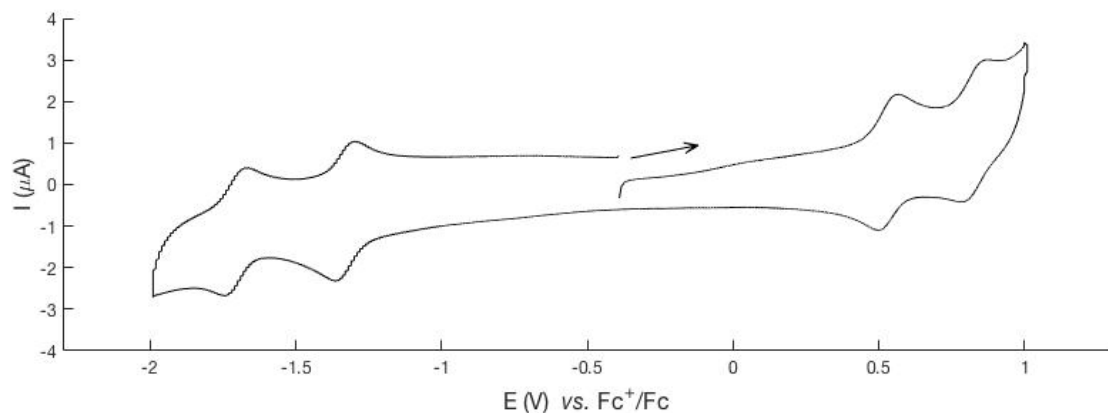


Figure 107: Cyclic voltammetry of **M5** in dichloromethane with tetrabutylammonium hexafluorophosphate (0.1 M) at a scan rate of 100 mV/s. Arrow shows direction of the measurement

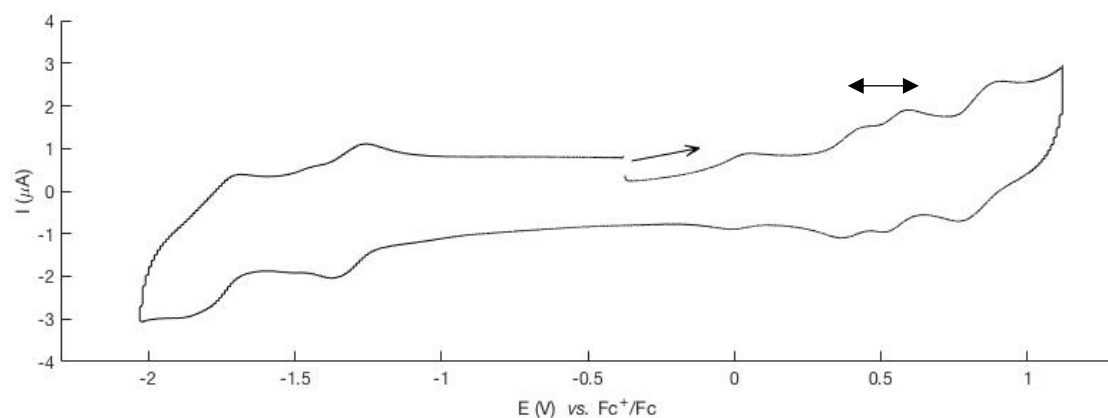


Figure 108: Cyclic voltammetry of VPdV, **D1** in dichloromethane with tetrabutylammonium hexafluorophosphate (0.1 M) at a scan rate of 100 mV/s. Arrow shows direction of the measurement and the doubly headed arrow shows the splitting of the first oxidation wave

The cyclic voltammetry for **D1** (Figure 108) was the same as that of the monomer, apart from an additional splitting of the first oxidation wave of the porphyrin. This was on account of additional communication between the two porphyrin moieties. This splitting is a way of establishing electronic communication between porphyrin moieties, as stated by Therien.<sup>9</sup> The linker will dictate whether communication is able to occur or not, for example it is known that a 1,4-butadiynylene bridge will lead to communication between porphyrin moieties on account of efficient  $\pi$ -overlap and the splitting for this porphyrin dimer with a 1,4-butadiynylene bridge is 110 mV. Without this efficient  $\pi$ -overlap, only electrostatic interactions are able to occur between the porphyrins; this can be seen for phenylene

bridged porphyrins.<sup>10</sup> These porphyrins communicate less efficiently as the porphyrin and the phenyl are perpendicular to one another, meaning that orbital overlap is minimal (see Introduction 2). Generally, the values in the literature vary from 0 to 440 mV for covalently linked porphyrin dimers, the splitting being maximal for the triply fused porphyrins of Osuka.<sup>11</sup>

Table 24: Oxidations potentials measured for the vanadyl porphyrin <sup>a</sup>

	E <sub>ox1</sub> (Volt)	E <sub>ox2</sub> (Volt)	Splitting E <sub>ox2-ox1</sub> (mV)	E <sub>ox3</sub> (Volt)
<b>M4</b> (V)	0.56	0.85	-	-
<b>D1</b> (VPdV)	0.42	0.58	164	0.88
<b>D2</b> (VPtV)	0.46	0.68	228	0.90

<sup>a</sup>  $CH_2Cl_2$ ,  $NBu_4PF_6$  (0.1M), 100 mV/s, vs.  $Fe^{+}/Fe$

In our metal ion linked systems, the splitting occurred, showing that there was good electronic communication between the porphyrin moieties. This was because the porphyrins were in the same plane and there was good orbital overlap between the porphyrin and the d-orbitals of the metal ion. The increased electronic communication led to a slight decrease in the first oxidation potential compared to **M4**. This confirms increased electronic communication as this coincides with a decreased HOMO-LUMO gap. The HOMO-LUMO gap will also decrease, as on formation of the dimer, a six-membered ring has essentially been formed at the coordination site.

The additional communication between the two moieties leads to a difference in the oxidation potentials on oxidising the first and second porphyrin of the dimer and the fact that the second oxidation occurs on a charged species will also slightly increase the oxidation potential. This splitting phenomenon was not observed for the reduction as there was no communication between the porphyrin moieties on reduction. This was corroborated using DFT calculations (B3LYP) (Figure 109). The calculations showed that the HOMO was  $d\pi/\pi$ -type in character with a metallic contribution from the linking metal ion that led to delocalisation, and consequently communication, over the two porphyrin moieties. The LUMO does not have this metallic contribution and consequently there was no communication between the two porphyrins.

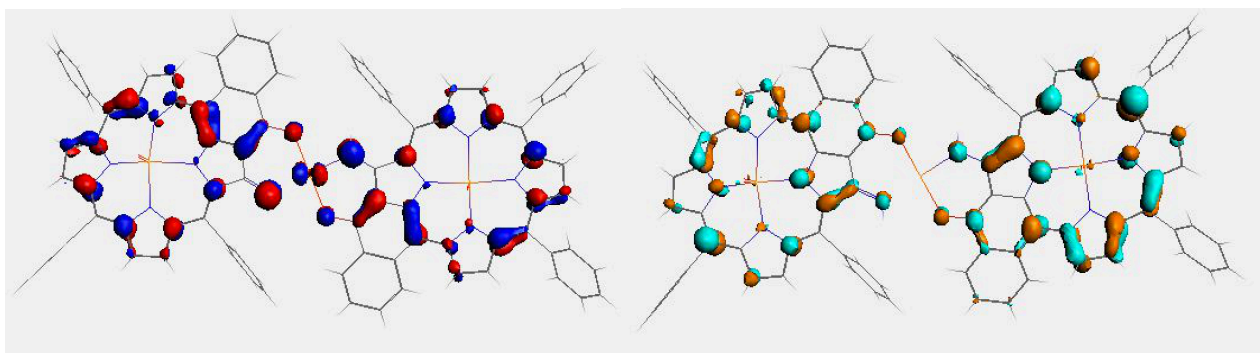


Figure 109: Frontier molecular orbitals, the HOMO (left) and LUMO (right) of **D1** calculated by DFT calculations (B3LYP)

**D2** also showed the same splitting of the first oxidation peak of the cyclic voltammetry (Table 24). The splitting was however greater for **D2** than **D1**, (229 mV and 164 mV, respectively) on passing from 4d to 5d orbitals, due to an increased orbital delocalisation. These values were as high on account of the planarity of the porphyrin dimer, which allowed for good electronic communication. The splitting was decreased when a first row transition metal was used as the linking metal ion, with a smaller splitting value for **D3**. The reduction was also not reversible for **D4** as the reduction of the linking Cu(II) ion to Cu(I) led to a breakdown of the porphyrin dimer.

The two forms of **D2** ( $\alpha,\alpha$  and  $\alpha,\beta$ ) presented identical absorption spectroscopy and cyclic voltammetry, consequently **D2** was only represented once in Tables 23 and 24. This result was not surprising as the interactions discussed here are ligand based and it was the linking metal ion that determined the communication. Consequently, varying the distance between the vanadyl metal ions would have a minimal effect on the electronic properties, especially when the difference was minimal, less than 0.4 Å.

### 3.3.2 Copper porphyrins

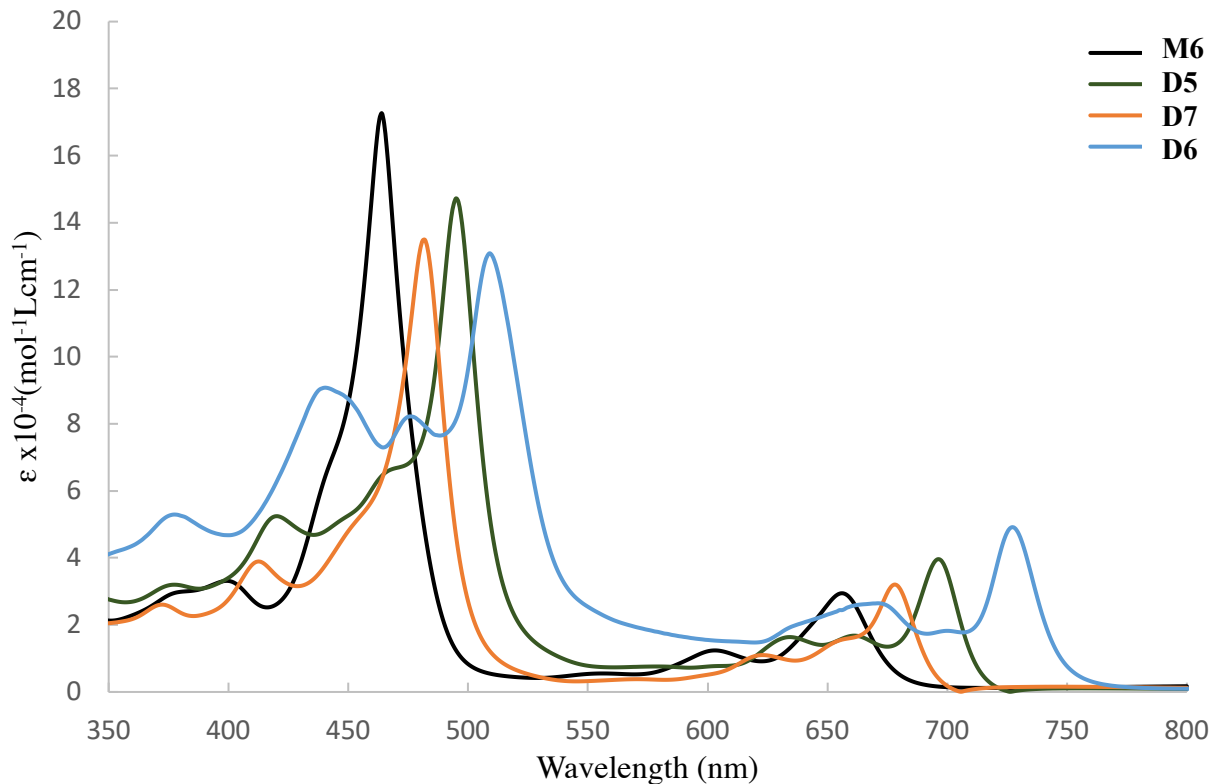


Figure 110: Electronic spectra for the copper porphyrin series in dichloromethane at room temperature

As seen for the vanadyl series, moving from 3d to 4d to 5d will lead to greater electronic communication and hence a larger bathochromic shift (Figure 110 and Table 25). This was seen by the larger bathochromic shift when Pd(II) was the linking metal ion compared to Cu(II), 14 nm and 33 nm respectively.

Table 25: Absorption maximum of the copper porphyrin series

	Soret $\lambda_{\max}$ (nm) ( $\epsilon(M^{-1}cm^{-1})$ )	Q-band $\lambda_{\max}$ (nm) ( $\epsilon(M^{-1}cm^{-1})$ )	Bathochromic shift vs. <b>M6</b> (nm)
<b>M6</b> (Cu)	465 (169 000)	660 (25 000)	-
<b>D5</b> (CuPdCu)	496 (142 000)	699 (36 000)	33
<b>D6</b> (CuPtCu)	512 (128 000)	731 (45 000)	71
<b>D7</b> (CuCuCu)	480 (133 000)	674 (30 000)	14

Table 26: Oxidation potentials measured for the copper porphyrin series<sup>a</sup>

	E <sub>ox1</sub> (Volt)	E <sub>ox2</sub> (Volt)	Splitting E <sub>ox2-ox1</sub> (mV)	E <sub>ox3</sub> (Volt)
<b>M6</b> (Cu)	0.42	0.77	-	-
<b>D5</b> (CuPdCu)	0.27	0.44	173	0.77
<b>D7</b> (CuCuCu)	0.34	0.47	129	0.80

<sup>a</sup>  $CH_2Cl_2$ ,  $NBu_4PF_6$  (0.1M), 100 mV/s, vs.  $Fe^{+}/Fe$

Cyclic voltammetry was carried out on the copper monomer, **M6**, **D5** and **D7** (Table 26). The same trend observed for the vanadyl dimers was also observed for the copper dimers, with increased electronic communication as the linking metal ion becomes softer. The values for E<sub>ox3</sub> varied minimally between **D5** and **D7**, also the value was very close to that of E<sub>ox2</sub> for **M6**. This demonstrated that the electronic communication was only occurring in the HOMO and not in the HOMO-1. Consequently, varying the linking metal ion had minimal effect and explains why E<sub>ox3</sub> varied minimally between the dimers.

There are notable discrepancies between the copper porphyrins and vanadyl porphyrins, demonstrating that even though the electronic interactions are mainly ligand based, the metal still had an effect on the electronic communication. The porphyrin geometry could have an effect here, with a copper porphyrin being ruffled and a vanadyl porphyrin being more planar. This slight discrepancy could lead to the minor increase in electronic communication for the vanadyl porphyrins compared to the copper porphyrins.

### 3.4 Magnetic properties

The magnetic properties of the porphyrins were analysed by electron paramagnetic resonance (EPR) spectroscopy. Continuous wave EPR was carried out on the porphyrin monomers and dimers, with varying linking metal ions, in order to ascertain the differences between the spectra and hence gain knowledge about the magnetic communication occurring between porphyrin moieties. The spectra were carried out at a concentration of  $10^{-4}$  M in order to avoid intermolecular interactions, such intermolecular interactions were observed for the  $10^{-3}$  M solution. The EPR studies were carried out in a frozen  $CH_2Cl_2:CHCl_3$  (8:2) solution; this combination of solvents was chosen in order to form a homogeneous glass on freezing. The solutions were frozen in order to facilitate comparison between porphyrin monomers and dimers. If the analysis was carried out in fluid solution, the tumbling effect would lead to loss of information in the spectra for the dimers.<sup>12</sup> Varying the temperature also allowed

for greater knowledge of the system, as this undoubtably led to varying energy state occupancy. Simulations of most of the spectra were carried out using the MATLAB toolbox Easyspin,<sup>13</sup> in order to gain a greater understanding of these systems.

### 3.4.1 Vanadyl porphyrins

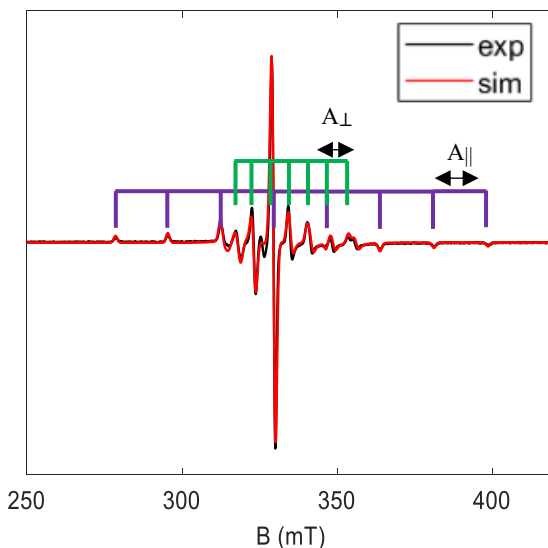


Figure 111: X-band experimental (black) and simulated (red) EPR spectra of **M4** ( $10^{-4}$  M; 80:20;  $\text{CH}_2\text{Cl}_2:\text{CHCl}_3$ ) at 15 K recorded with a microwave power of 0.1 mW and a modulation amplitude of 0.5 mT. Lines in purple and green indicate the  $A$  values along the parallel ( $z$ ) and perpendicular ( $x,y$ ) orientations respectively

The continuous wave EPR spectrum of **M4** in a frozen solution (Figure 111) exhibited a typical frozen line shape of vanadyl complex comparable with other vanadyl porphyrins in the literature.<sup>14</sup> The characteristic features result from the hyperfine interaction of the unpaired electron spin  $S = 1/2$  of  $\text{V}^{4+}$  ( $3\text{d}^1$ ) with the  $I = 7/2$  nuclear spin  $^{51}\text{V}$  isotope (99.75 % abundant). The planar structure of the vanadyl porphyrin leads to  $\mathbf{g}$  and  $\mathbf{A}$  tensors with approximatively an axial symmetry. Consequently, the EPR spectrum is composed of 16 partially overlapped components of hyperfine structure, with 8 lines in parallel and 8 in the perpendicular direction coming from  $I = 7/2$ . Figure 111 shows 8 peaks in both the parallel (purple) and perpendicular (green) orientations. The middle point of the 8 lines, between lines 4 and 5, allowed for the determination of the  $g$  values for this porphyrin, which were used as starting values for spectral simulation. In the same way, the distance between two lines in the spectrum allowed for the hyperfine coupling constants,  $A_V$ , to be determined for the paramagnetic species. The  $A$  values for the main orientations ( $x$ ,  $y$ , and  $z$ , respectively) were as follows: 170; 152; 472 MHz; matching with the almost axial symmetry of the spectrum. No hyperfine coupling between the vanadium and the four nitrogen atoms of the porphyrin was observed. This can be explained as

the lone electron was in a non-bonding orbital ( $d_{xy}$ ),<sup>15</sup> and hence it underwent minimal interactions with the surrounding porphyrin due to limited orbital overlap between the  $d_{xy}$  orbital and the nitrogen orbital.

Taking into account the local symmetry at the porphyrin site ( $\mathbf{g}$  and  $\mathbf{A}$  tensors were assumed axial and colinear), the spectrum is simulated very satisfactorily using an axial spin-Hamiltonian with the set of spectroscopic parameters given in Table 27 (page 139).

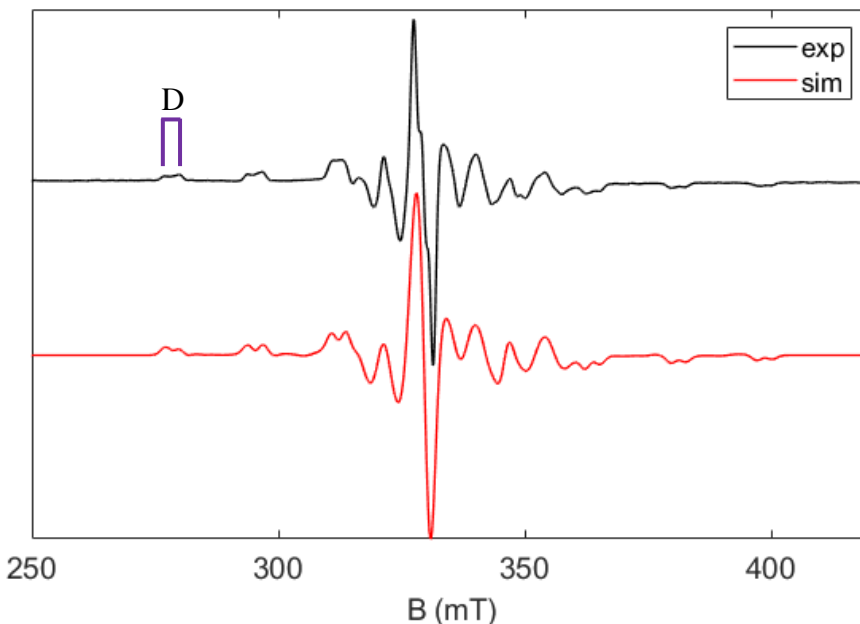


Figure 112: X-band experimental (black) and simulated (red) EPR spectra of **D1** ( $10^{-4}$  M; 80:20;  $\text{CH}_2\text{Cl}_2:\text{CHCl}_3$ ) at 0.1 mW, 0.4 mT and 15 K. D is the dipolar interaction between the two vanadyl metal ions

The EPR spectrum of **D1** (Figure 112) was recorded in the same conditions as **M4** and appeared to be very similar to that of the vanadyl monomer with one pertinent difference. The two spectra superimpose onto each other with similar  $g$  factors but a closer comparison shows a mild splitting in each peak of the spectrum, indicating the presence of magnetic interactions between the two VO units. This well-resolved interaction was able to occur despite the fact that the crystal structure showed that the two metal sites were quite far apart (14.3 Å). To simulate the EPR spectrum, we added a term to the spin Hamiltonian to account for the electron spin-spin interaction. The singlet ( $S = 0$ ) and triplet ( $S = 1$ ) states arising from the interaction of two VO porphyrin units were separated by the magnitude of the isotropic exchange interaction, whereas the levels within the triplet state were separated by the magnetic dipole-dipole interaction and anisotropic exchange terms. As the distance between the two vanadyl metal ions was quite large, the isotropic exchange coupling is considered small and less than the microwave quantum of energy ( $\sim 0.33 \text{ cm}^{-1}$  for X-band) and consequently the triplet and singlet states are mixed, complicating the EPR spectrum. With this assumption, for **D1** the

major contribution arises mainly from a through-space dipolar interaction ( $D$ ) with a small effect from exchange terms and the distance,  $r$ , between the two VO units can be evaluated with the following equation:<sup>16</sup>

$$D = \frac{3g\beta}{2r^3} = 1.39 \times 10^4 \frac{g}{r^3} \quad (\text{eq.2})$$

Where  $\beta$  is the Bohr magneton and  $r$  is the distance in Å and  $D$  in Gauss.

This equation is applied assuming the point dipole approximation. With a  $D$  value of 40 MHz measured from the spectrum, an  $r$  value of 13 Å was calculated. This value was close to that obtained by X-ray crystallography. The spectrum was fitted using the esfit function in Easyspin<sup>13</sup> with the following Hamiltonian that encompasses the  $\mathbf{g}$  tensor, hyperfine tensor  $\mathbf{A}$  for both VO porphyrin units and the electron-electron interaction matrix  $\mathbf{J}$ :

$$\hat{H} = \mu_B \mathbf{B} \mathbf{g}^V \hat{S}^V + \hat{S}^V \mathbf{A}^V \hat{I}^V + \hat{S}^V \mathbf{J} \hat{S}^V \quad (\text{eq.3})$$

Where  $\mathbf{J}$  can be rewritten:

$$\mathbf{J} = JS_1S_2 + \mathbf{d}_{12}S_1 \times S_2 + S_1\mathbf{D}S_2 \quad (\text{eq.4})$$

$J$  is the isotropic exchange,  $\mathbf{d}_{12}$  is a polar vector an antisymmetric term,  $S_1$  and  $S_2$  are the two spins of the vanadyl and  $\mathbf{D}$  is a symmetric traceless tensor including the anisotropic dipolar coupling and anisotropic exchange arising from  $g$  anisotropy.

The obtained values  $\mathbf{g}$  and  $\mathbf{A}$  tensors for the monomer were kept the same for the simulation of **D5** with the through-space dipolar interaction extracted from the EPR spectrum, then the isotropic exchange coupling  $J$  was calculated by varying its values from 1 to 10 MHz. The best simulated EPR spectrum assessed to the magnitude of  $|J|$  of around  $6 \pm 2$  MHz, this is a weak coupling regime. The distance between the two vanadyls allows for a simplification of the above equation, as the anisotropic exchange and the antisymmetric are assumed to be near zero when the two paramagnetic metals are as far apart as 14 Å.

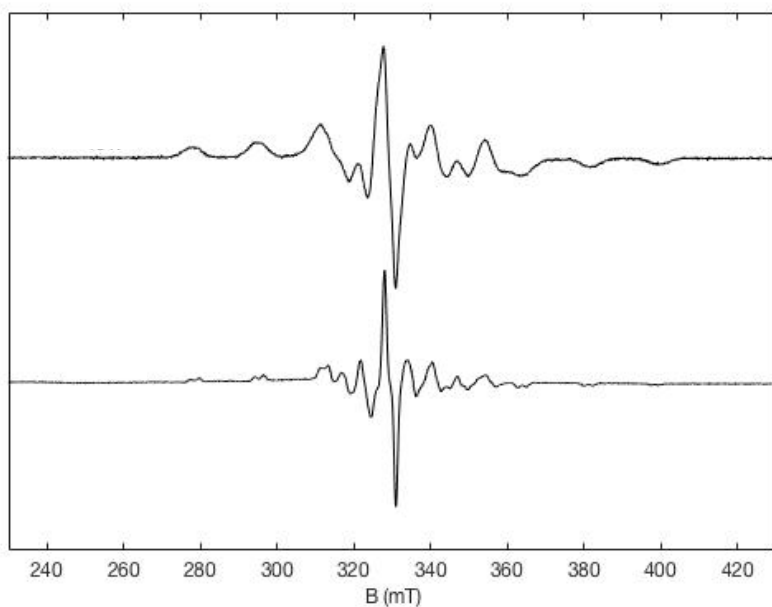


Figure 113: X-band experimental EPR spectra of the two forms of **D2** ( $10^{-4}$  M; 80:20;  $CH_2Cl_2:CHCl_3$ ), thought to be the  $\alpha,\alpha$  (top) and the  $\alpha,\beta$  (bottom), recorded at 15 K with a microwave power of 0.1 mW and a modulation amplitude of 0.4 mT

CW EPR was also carried out on the two VPtV dimers, **D2**  $\alpha,\alpha$  and  $\alpha,\beta$  (Figure 113). These two dimers were able to be separated by column chromatography as the  $\alpha,\alpha$  dimer is more polar than the  $\alpha,\beta$  dimer. Despite the two molecules having identical electronic properties, the magnetic properties of these two dimers were different. As seen by the crystal structure, there was a slight difference in the distance between the  $\alpha,\alpha$  and the  $\alpha,\beta$  dimers because the vanadyl was slightly out of the plane of the porphyrin. However, the change in distance still remains small,  $< 0.4$  Å, and consequently the dipolar interactions ( $D$ ) will be basically identical for the  $\alpha,\alpha$  and the  $\alpha,\beta$  dimers. Differences between the spectra shown in Figure 113 are hence assumed to be on account of an increase in isotropic exchange,  $J$ . With the two vanadyls being in the same direction for the  $\alpha,\alpha$  dimer, this would lead to a more favourable electronic pathway between two porphyrin dimers and consequently lead to a more pronounced  $J$  coupling. Another hypothesis could be that a sandwich type stacking could potentially be envisaged, as one of the dimers could be inverted and would lead to the vanadyl sites being in close proximity. However, this hypothesis is less likely, and a more pronounced  $J$  coupling is more likely.

The bottom spectrum of Figure 113 was thought to be the  $\alpha,\beta$  dimer on account of its similarity to the VPdV dimer, **D1**, which was also  $\alpha,\beta$  and also had a mild splitting in all the peaks. **D2** and **D1** superimposed onto one another almost perfectly. This was to be expected as the interaction was dipolar, meaning that it was a through-space interaction, consequently the linking metal ion of the

two porphyrins should not have an impact on the interactions. This point helps confirm the hypothesis that a mild dipolar coupling interaction was able to occur between the two vanadyl sites, despite the large distances between them.

The top spectrum of Figure 113 has a stronger interaction compared to the bottom spectrum of Figure 113, evident by the increase in line broadening compared to the monomer and the bottom spectrum. This spectrum was thought to be the  $\alpha, \alpha$  as the results of the EPR simulation for **D2** leads to a similar  $D$  but with a more important  $J$  value (see Table 27, page 139) indicating a better through-bond interaction on the structure that is responsible for the spectral broadening observed. This simulation matches with the experimental results (Figure 114).

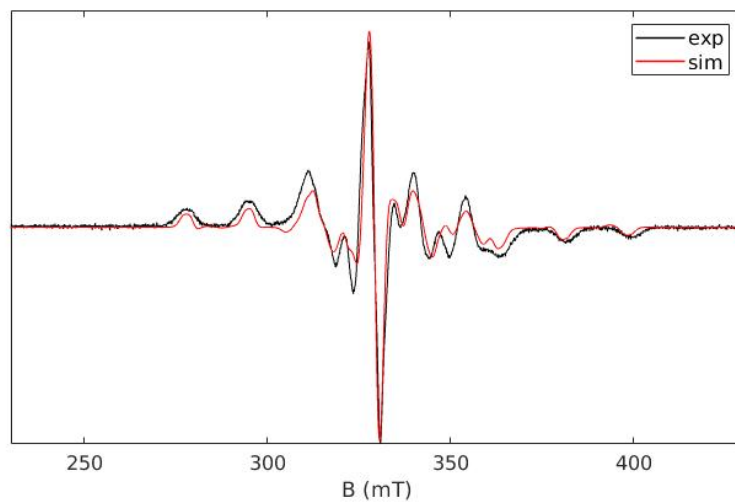


Figure 114: X-band experimental (black) and simulated (red) EPR spectra of **D2** ( $\alpha, \alpha$ ) recorded at 15 K with a microwave power of 0.1 mW and a modulation amplitude of 0.4 mT

For the VVV dimer **D3**, the linking metal ion is paramagnetic and consequently it was able to act as a relay for communication between the two paramagnetic sites. The synthesis of this dimer was not obvious due to its instability. The spin Hamiltonian used to describe the isotropic exchange interaction in a linear symmetric trimer is defined by:

$$H = J(S_1S_2 + S_2S_3) + J'S_1S_3 \quad (\text{eq.5})$$

where  $J$  refers to  $S_1S_2$  coupling and  $J'$  refers to  $S_1S_3$  coupling and  $S_1$  and  $S_2$  are the two spins of the vanadyl.

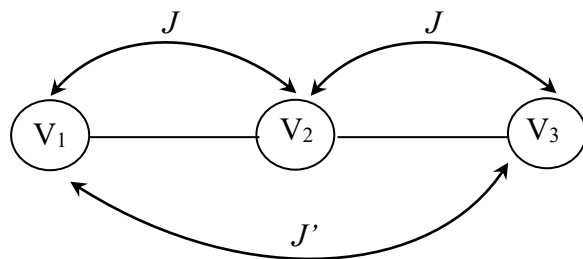


Figure 115: Visual demonstration of possible isotropic exchange interactions occurring for **D3**

As seen above for **D1** and **D2**, the system is linear and a negligible interaction between the two external vanadyl ions is measured ( $J'$ ). This means that the  $J'$  value is negligible compared to  $J$  (Figure 115) and the resulting spin multiplets are two doublets and one quartet,  $S = 1/2$  ions and  $S = 3/2$  respectively. The distribution of the relative energies of these various spin states depends on the  $J$  value. If  $J$  is negative, the ground state is  $E(1/2, I)$  and if  $J$  is positive, the ground state is  $E(3/2, I)$ .<sup>17</sup>

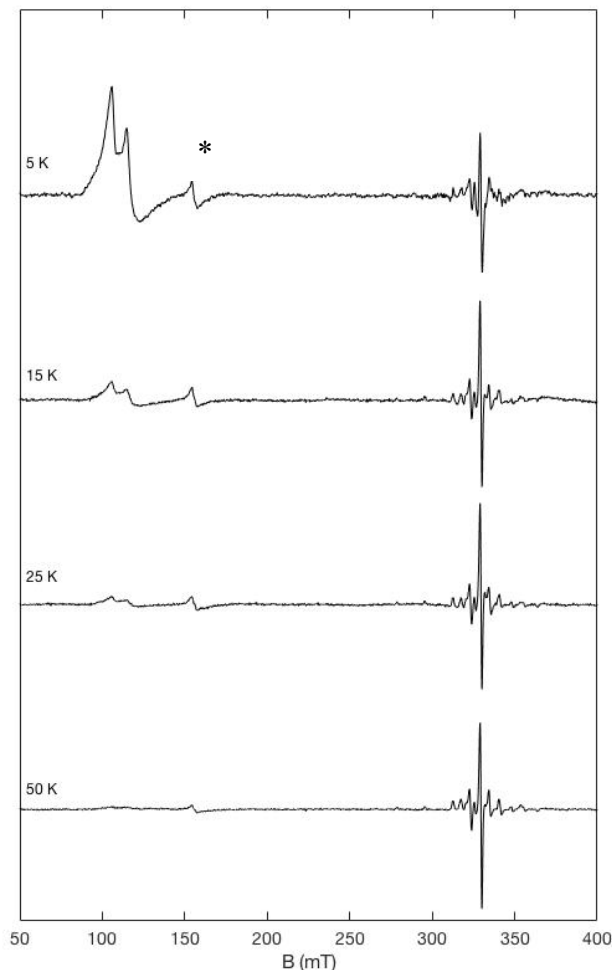


Figure 116: EPR spectra recorded at temperatures between 5 and 50 K of **D3** ( $10^{-4}$  M; 80:20;  $\text{CH}_2\text{Cl}_2:\text{CHCl}_3$ ) with a microwave power of 0.1 mW and a modulation amplitude 0.4 mT. Baseline correction was done with a spline. \* is an impurity in the EPR cavity

The EPR spectrum (Figure 116), shows at  $\sim 330$  mT a spectrum exceedingly close to that of the porphyrin monomer **M4**, however there is an additional peak at  $\sim 100$  mT. The peak at  $\sim 150$  mT is an impurity in the cavity. On varying the temperature of the EPR sample (Figure 116), information was gained about the nature of the two peaks at 100 and 330 mT, as differences in their population were observed as the temperature varied. At low temperature, 5 K, there was an intense peak at 100 mT. This well-populated state was deemed to be the  $S = 3/2$  peak, with the three  $S = 1/2$  vanadyl sites undergoing ferromagnetic coupling. On increasing the temperature there was a depopulation of the quartet state ( $S = 3/2$ ) and a population of the doublet state at 340 mT ( $S = 1/2$ ). Consequently, a decrease in the intensity of the peak at 100 mT was observed and an increase in intensity of the peak at 340 mT was respectively observed and led to the population of higher lying energy states. The EPR parameters of **D3** are summarised in Table 27.

*Table 27: Best fit EPR parameters obtained for the simulation of the EPR spectra of **M4**, **D1**, **D2** ( $\alpha, \alpha$ ) and **D3**. \*Values were estimated by treating the system as an effective  $S = 1/2$*

	<b>M4</b>	<b>D1</b>	<b>D2</b> ( $\alpha, \alpha$ )	<b>D3</b>
$g_x$ ( <i>g strain</i> )	1.9823 (0.0087)	1.9827 (0.0017)	1.9827 (0.0017)	6.4* (0.1)
$g_y$ ( <i>g strain</i> )	1.9845 (0.0087)	1.9838 (0.0017)	1.9838 (0.0017)	5.7* (0.1)
$g_z$ ( <i>g strain</i> )	1.9636 (0.0075)	1.9634 (0.0013)	1.9634 (0.0013)	2.5* (0.1)
$A_V$ (MHz)	[170; 152; 472]	[170; 152; 472]	[170; 152; 472]	-
$ J $ (MHz)	-	<6	35	-
$D$ (MHz)	-	42	42	-

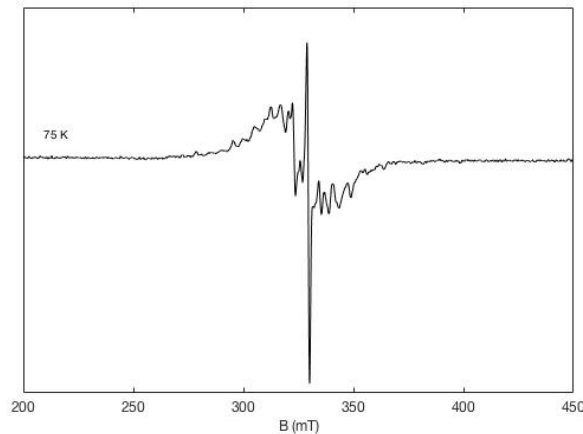


Figure 117: X-band experimental EPR spectrum of **D4** ( $10^{-4}$  M; 80:20;  $\text{CH}_2\text{Cl}_2:\text{CHCl}_3$ ) at 75 K recorded with a microwave power of 0.1 mW and a modulation amplitude of 0.4 mT

A dimer with two different paramagnetic metals, **D4**, was also assembled with vanadyl at the internal coordination of the porphyrin and copper at the external coordination site, serving as the linking metal ion. The EPR spectra, of **D4** (Figure 117) shows that unlike **D3**, no other peaks were observed at low temperatures. The observed hyperfine pattern is not consistent with two identical non interacting  $\text{Cu}^{2+}$  and  $\text{V}^{4+}$  and is complicated by hyperfine splitting from exchange-coupled  $^{51}\text{V}$  and  $^{63,65}\text{Cu}$  centres. Further analysis needs to be carried out on this dimer in order to determine the magnitude and the nature of the coupling (antiferromagnetic or ferromagnetic). This will be done by recording double integrated  $\Delta m_s=1$  transition *versus* temperature.

### 3.4.2 Copper porphyrins

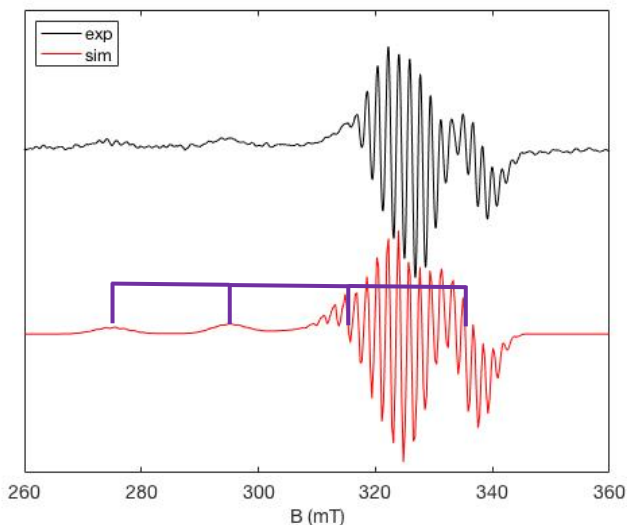


Figure 118: X-band experimental (black) and simulated (red) EPR spectra of **M6** ( $10^{-4}$  M; 80:20;  $\text{CH}_2\text{Cl}_2:\text{CHCl}_3$ ) at 100 K, recorded with a microwave power of 0.5 mW and a modulation amplitude of 0.2 mT.

The EPR spectrum of **M6** (Figure 118) is characteristic of a copper porphyrin with the expected four line arising from the interaction of the  $S = 1/2$  and the nuclear spin  $I = 3/2$  ( $^{63,65}\text{Cu}$ ). However, the spectrum appears to be considerably more complicated than four lines. This was on account of superhyperfine coupling between the unpaired electron and the nitrogen isotope ( $^{14}\text{N}$ ,  $I = 1$ ). This interaction was able to occur as the unpaired electron of the copper metal ion was in a bonding orbital ( $d_{x^2-y^2}$ ) with the nitrogen atoms, leading to good orbital overlap and consequently a superhyperfine coupling interaction was able to occur. The calculated  $g$  values were higher than that of the vanadyl porphyrin,  $g_x = 2.061$ ;  $g_y = 2.051$ ;  $g_z = 2.180$ , which was also to be expected with a  $d^9$  configuration. The  $\Delta g$  is 0.13, demonstrating a slightly greater anisotropy than that of **M4**. The values coincide with those found in the literature.<sup>18</sup>

Along the parallel axis, the four lines expected in this spectrum can be visualised in Figure 118, starting at 280 mT and the third and fourth peak were hidden by the signals from the perpendicular region. The hyperfine interactions are similar for **M4** and **M6**, with slightly larger hyperfine coupling constants ( $A$ ) observed for **M6**,  $A_{\text{Cu}}(\text{MHz}) = [135; 125; 600]$ . The distance between two peaks is 17 G, which is around the expected value for hyperfine coupling with nitrogen atoms. This value was incorporated into the simulated spectra as an  $A$  value for the nitrogen atoms of 49 MHz. This led to a simulated spectrum that matched well with the experimental result (Figure 118).

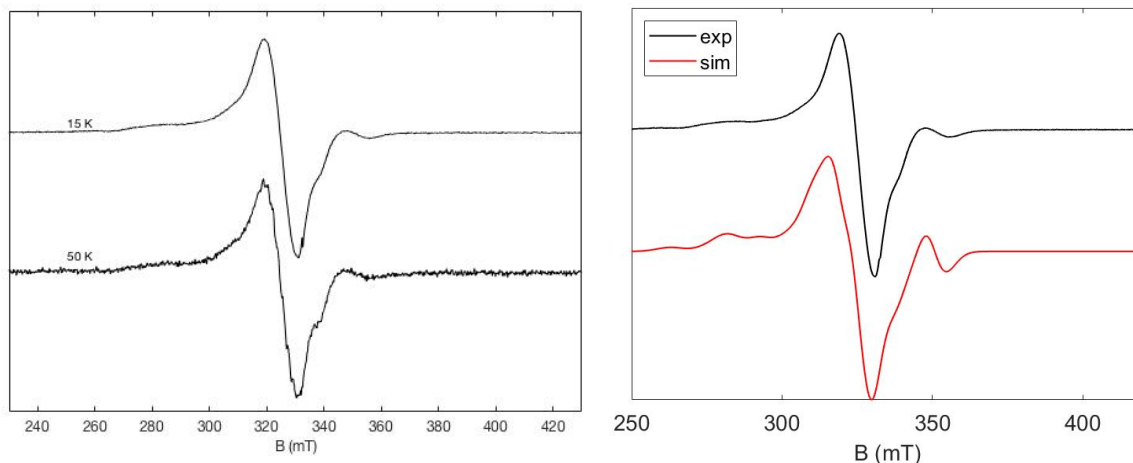


Figure 119: Left: X-band experimental EPR spectrum of **D5** ( $10^{-4} \text{ M}$ ; 80:20;  $\text{CH}_2\text{Cl}_2:\text{CHCl}_3$ ) at 15 K and 50 K, recorded with a microwave power of 0.1 mW and a modulation amplitude of 0.4 mT. Right: experimental (black) and simulation (red) of **D5** at 15 K.

The spectra of **D5** at 15 K and 50 K are represented in Figure 119, left. The distance between the two paramagnetic sites is similar for **D1** and **D5**, hence the dipolar interactions for **D1** and **D5** will be essentially the same (40 MHz). The EPR spectrum of **D5** suggests there was a weak magnetic interaction between the two paramagnetic metals. This can be visualised by comparing the EPR

spectra of **M6** with **D5**, where the line broadening in the spectrum led to a loss of the hyperfine coupling and an intricate spectral pattern. The temperature variation also showed no spectral changes. A stronger magnetic interaction was not able to occur as the paramagnetic sites were far from each other ( $\sim 14$  Å) and the linking metal ion was diamagnetic. The EPR spectrum can be analysed in the same way as **D1**, where  $|J| < h\nu$  and the Hamiltonian described in eq. (3) can be used for the simulation of **D5** as well. Line broadening and the large number of parameters that could be adjusted hindered better matched simulations for **D5**, hence Q-band experiments are ongoing. The spectrum from the best fit parameters is shown in Figure 119, right. The same  $\mathbf{g}$  and  $\mathbf{A}$  tensors as **M6** were assumed for **D5** and the  $D$  value was fixed around 40 MHz, which corresponds to the value estimated from the point dipole approximation, and the  $J$  value was varied from 100 to 1000 MHz. The best values are shown in Table 28.

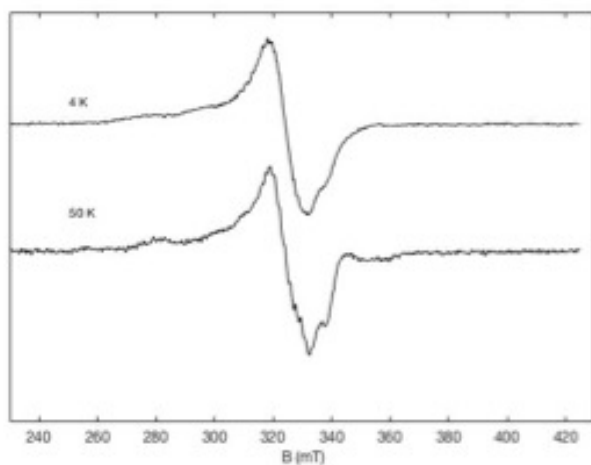


Figure 120: X-band experimental EPR spectra of **D6** ( $10^{-4}$  M; 80:20;  $\text{CH}_2\text{Cl}_2:\text{CHCl}_3$ ) at 4 K and 50 K recorded with a microwave power of 0.1 mW and a modulation amplitude of 0.4 mT

The experimental EPR spectrum of **D6** (Figure 120) was similar to that of **D5**, which was to be expected as they are both diamagnetic linkers and there are few discrepancies between the two spectra. Superimposing the two spectra shows that the line width was exactly the same and consequently, it can be assumed that the coupling in both the dimers was similar. The EPR parameters for the simulation of the EPR spectrum of **D6** are given in Table 28 and they are quite similar to the **D5** simulated parameters, demonstrating that the linking metal ion was not the determining point for the isotropic exchange coupling path. This means that changing the diamagnetic linking metal ion has a weak effect on the magnetic properties. Nevertheless, the value of the isotropic coupling is much more important for **D5** and **D6** compared to **D1** and **D2** and demonstrates a different orbital overlap.

Table 28: Best fit EPR parameters obtained for the simulation of the EPR spectra of **M7**, **D5** and **D6**

	<b>M7</b>	<b>D5</b>	<b>D6</b>
$g_x$ ( <i>g</i> strain)	2.061 (0.003)	2.061 (0.04)	2.061 (0.04)
$g_y$ ( <i>g</i> strain)	2.051 (0.0075)	2.061 (0.04)	2.061 (0.04)
$g_z$ ( <i>g</i> strain)	2.180 (0.001)	2.180 (0.07)	2.180 (0.07)
$A_{Cu}$ (MHz)	[135; 125; 600]	[130 130 600]	[130 130 600]
$A_N$ (MHz)	49	-	-
$ J $ (MHz)	-	700±50	700±50
$D$ (MHz)	-	42±5	42±5

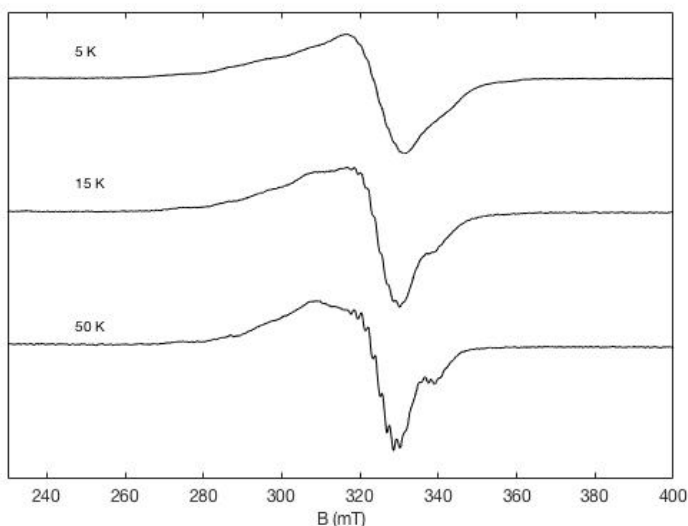


Figure 121: X-band experimental EPR spectra of **D7** ( $10^{-4}$  M; 80:20;  $CH_2Cl_2:CHCl_3$ ) at 5 K, 15 K and 50 K recorded with a microwave power of 0.1 mW and a modulation amplitude of 0.4 mT.

At lower temperatures (Figure 121, top), **D7** appears to be similar to the copper monomer **M7**, as only the fundamental spin state was observed up to 100 K. A similar porphyrin dimer has already been synthesised by our group.<sup>3</sup> For that porphyrin the lowest spin state was determined to be  $S = 1/2$  by SQUID measurements with an antiferromagnetic coupling of  $-25.2$  cm<sup>-1</sup>. On increasing the temperature, the  $S = 3/2$  state was occupied and led to the changes in the spectrum at 15 K (Figure 121, middle). At 50 K (Figure 121, bottom) the spectrum was still broadening, this may be due to the superposition of signals from both the doublet and quartet levels. The superhyperfine coupling between the unpaired electron and the nitrogen once again becomes visible in the perpendicular region of the spectrum at 50 K, this is apparent as the peak separation was equal to 17 G.

## 3.5 Enaminothioketone Porphyrins

The results for the electronic properties of the porphyrin dimers all point to the fact that a softer metal ion leads to an increased electronic communication. Another way to increase the electronic communication is by not only using a softer metal ion, but also a softer metal coordination site. Hence, a series of porphyrins was synthesised with an enaminothioketone as the coordinating moiety, as opposed to an enaminoketone moiety. It was hypothesised that changing the ketone to a thioketone would lead to a softer coordination site and hence increase electronic properties.

### 3.5.1 Synthesis

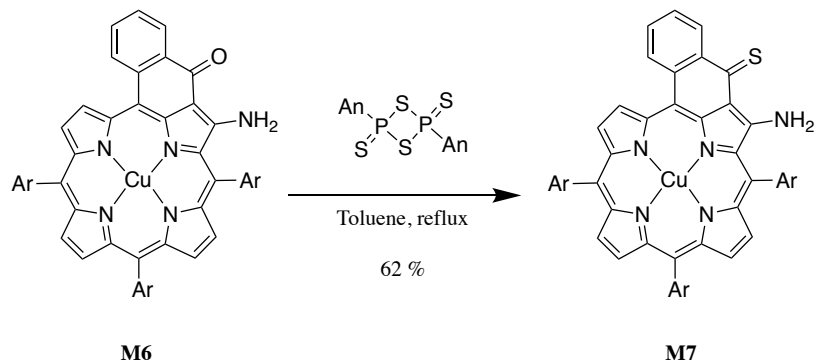


Figure 122: Synthesis of M7

The enaminoketone was converted to an enaminothioketone (Figure 122) using Lawesson's reagent.<sup>19</sup> Conversion from the enaminoketone to a enaminothioketone rendered the external coordination site softer and consequently formation of dimers (Figure 123) required considerably less harsh conditions, on account of the hard-soft acid base (HSAB) principle. This meant that instead of heating the porphyrin for 4 days with a Pt(II) source at 200 °C to form a dimer, simply 2 h at reflux in toluene sufficed. To form a dimer with either copper(II) or palladium(II) as the linking metal ion, 1h heating in toluene led to the desired product. As well as facilitating the synthesis, there were also advantageous properties on softening the external coordination site.

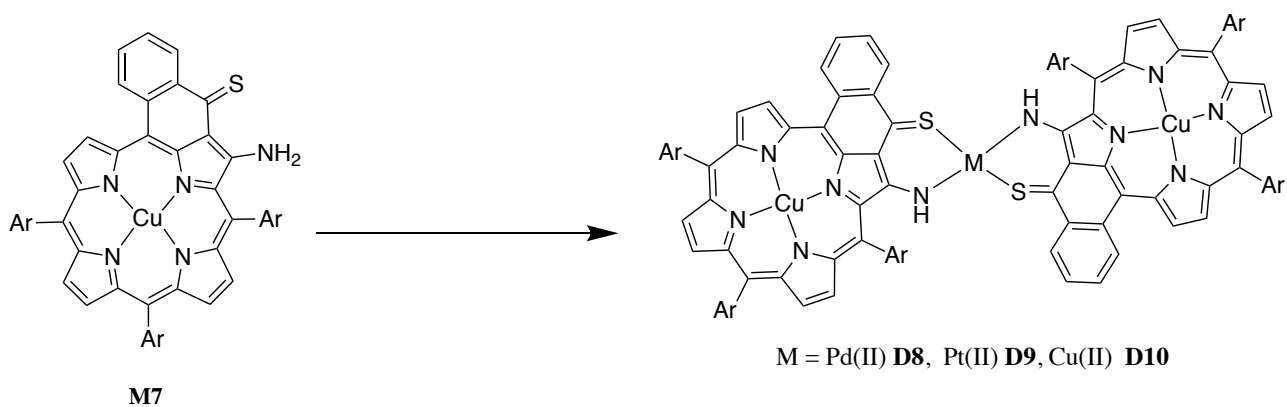


Figure 123: Formation of dimers **D8-D10**

### 3.5.2 Electronic properties

The formation of a softer external coordination site had drastic effects on the electronic properties of the porphyrin dimers **D8-D10**, with better electronic communication being able to occur on account of an increased orbital interaction. As seen for the enaminoketone series, moving to softer metal ions led to greater electronic interactions, consequently the complex with the greatest electronic interactions of this series was **D9**, with platinum(II) as the linking metal ion. The extent of the electronic interaction between the porphyrin moieties for **D9** is evident in the electronic absorption spectrum (Figure 124). This complex presented immense splitting in the Soret band, demonstrating a strongly electronically communicating porphyrin dimer. The Q-band even shifts as high as 797 nm for **D9**. This is an exceedingly large bathochromic shift of 80 nm, compared to the monomer **M8**. Comparing the bathochromic shifts to the enaminoketone porphyrin series, **D5-D7**, larger bathochromic shifts were observed (Table 29) due to the increased orbital interaction from the enaminothioketone, compared to the enaminoketone.

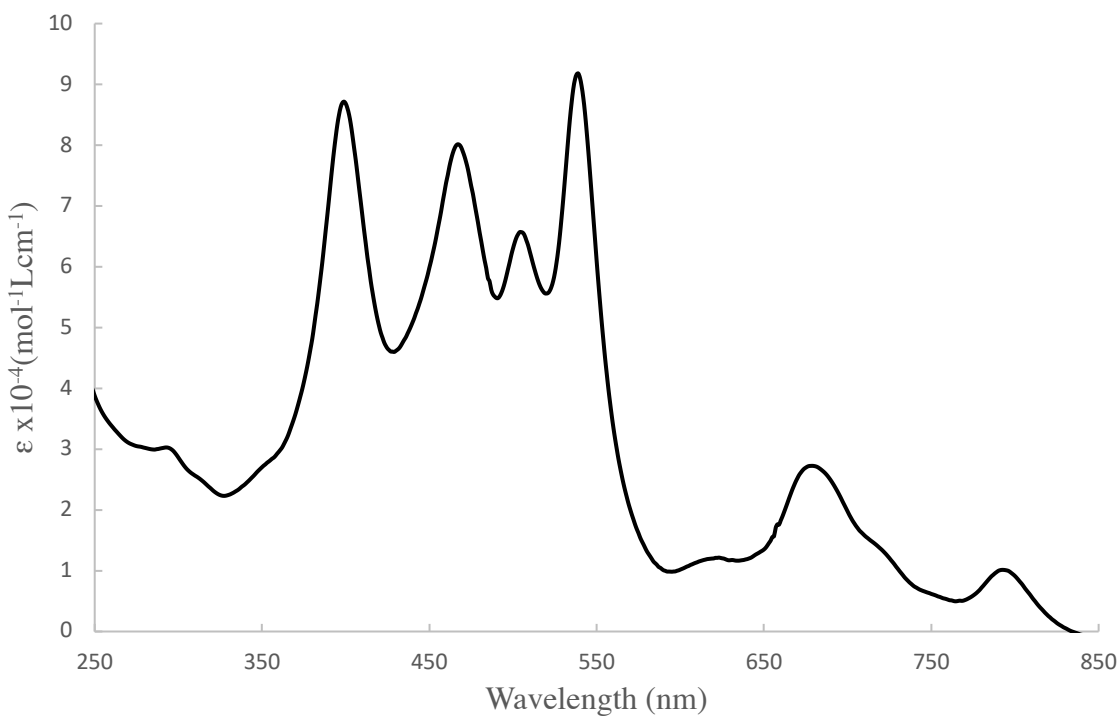


Figure 124: Electronic absorption spectrum of **D9** in dichloromethane at room temperature

Table 29: Absorption maximum of the enaminothioketone porphyrin series

	Soret $\lambda_{\max}$ (nm) ( $\epsilon$ (M <sup>-1</sup> cm <sup>-1</sup> ))	Q-band $\lambda_{\max}$ (nm) ( $\epsilon$ (M <sup>-1</sup> cm <sup>-1</sup> ))	Bathochromic shift vs. <b>M7</b> (nm)
<b>M7</b>	491 (89 000)	717 (13 000)	-
<b>D8</b> (CuPdCu)	519 (91 000)	737 (17 000)	20
<b>D9</b> (CuPtCu)	540 (90 000)	797 (12 000)	80
<b>D10</b> (CuCuCu)	503 (73 000)	702 (27 000)	12

Coinciding with the electronic spectra, the cyclic voltammetry (Table 30) also shows stronger electronic communication for **D8-D10** cf. **D5-D7**, once again on account of the HSAB theory. The splitting between  $E_{ox2}$  and  $E_{ox1}$  was exceedingly large and is comparable to that of Osuka's triply fused porphyrin dimers,<sup>11</sup> the highest reported splitting in the literature. Hence demonstrating the efficiency of this system, with a planar metal linking ion being just as efficient as an organically conjugated system.

The largest  $E_{ox2-ox1}$  splitting was observed for **D9**, with a splitting of 345 mV. This was the largest splitting recorded in our group. Comparing **D5** and **D8**, the effect of simply changing the oxygen to a sulphur at the external coordination site becomes exceedingly apparent, with an increase in the splitting of the first oxidation wave from 173 mV to 237 mV.

Table 30: Oxidations potentials measured for the enaminothioketone porphyrin series<sup>a</sup>

Dimer	$E_{ox1}$ (Volt)	$E_{ox2}$ (Volt)	Splitting $E_{ox2-ox1}$ (mV)	$E_{ox3}$ (Volt)
<b>D8</b>	0.26	0.50	237	0.86
<b>D9</b>	0.23	0.57	345	0.90
<b>D10</b>	0.30	0.58	273	0.95

<sup>a</sup>  $CH_2Cl_2$ ,  $NBu_4PF_6$  (0.1M), 100 mV/s, vs.  $Fe^{+}/Fe$

### 3.5.3 Magnetic properties

Increased magnetic properties for the enaminothioketone porphyrin dimers, compared to the ketoporphyrin dimers, were also observed. Superimposing **D6** and **D9** showed differences (Figure 125) with an additional transition at high field (~350 mT) for **D6**. This transition was not present for **D9**, indicating differences in magnetic coupling on changing the external paramagnetic metal sites.

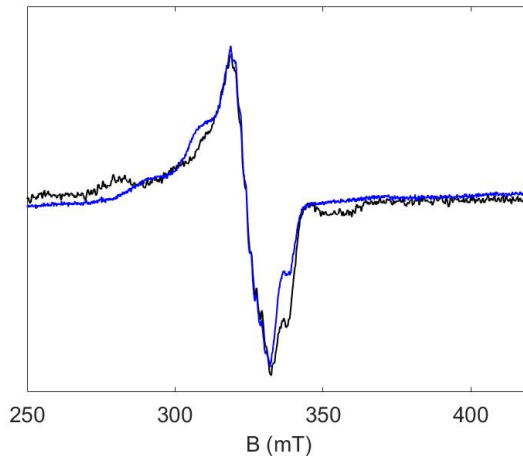


Figure 125: Superimposition of **D6** (black) and **D9** (blue) EPR spectra at 15K.

In contrast, superimposing **D8** and **D9** spectra (Figure 126) shows that the transitions and line width were exactly the same, as seen for **D5** and **D6**. This demonstrates that varying the external metal ion from Pd(II) to Pt(II) has minimal effect on the magnetic properties, yet varying the external coordination site from a enaminoketone to an enaminothioketone appears to increase the coupling between the two paramagnetic metal ions on account of a more efficient through-bond interaction.

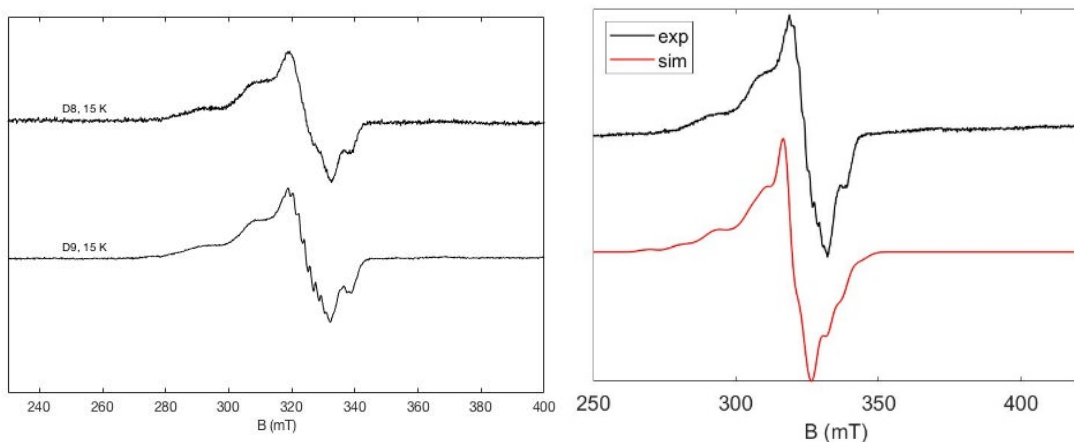


Figure 126: Left: X-band experimental EPR spectrum of **D8** (top) and **D9** (bottom) ( $10^{-4}$  M; 80:20;  $\text{CH}_2\text{Cl}_2:\text{CHCl}_3$ ) at 15 K recorded with a microwave power of 0.1 mW and a modulation amplitude of 0.4 mT. Right: experimental EPR spectrum of **D9** under the same conditions (black) and the corresponding simulation (red).

EPR simulation parameters (Table 31) for **D8** and **D9** are the same as that of **D5** and **D6** with the coupling between the paramagnetic metal ions varying for the two systems (enaminoketone and enaminothioketone). The  $J$  values obtained for **D6** and **D9** reinforced the idea that it was indeed an enhancement of the isotropic exchange coupling and consequently an enhancement of the anisotropic exchange that led to increased interactions between the two paramagnetic metal ion sites. The increased  $D$  value for the enaminothioketone simulated spectra compared to the enaminoketone spectra showed that an anisotropic exchange coupling was also occurring.

Table 31: Best fit EPR parameters obtained for the simulation of the EPR spectra of **D5**, **D6**, **D8** and **D9**

	<b>D5</b>	<b>D6</b>	<b>D8</b>	<b>D9</b>
$g_x$ ( <i>g strain</i> )	2.061 (0.04)	2.061 (0.04)	2.061 (0.03)	2.061 (0.03)
$g_y$ ( <i>g strain</i> )	2.061 (0.04)	2.061 (0.04)	2.061 (0.03)	2.061 (0.03)
$g_z$ ( <i>g strain</i> )	2.180 (0.07)	2.180 (0.07)	2.180 (0.05)	2.180 (0.05)
$A_{Cu}$ (MHz)	[130 130 600]	[130 130 600]	[130 130 600]	[130 130 600]
$A_N$ (MHz)	-	-	-	-
$ J $ (MHz)	$700 \pm 50$	$700 \pm 50$	$4400 \pm 500$	$4400 \pm 500$
$D$ (MHz)	$42 \pm 5$	$42 \pm 5$	$130 \pm 10$	$130 \pm 10$

### 3.6 Qubits for quantum computing

The rigid planar nature of porphyrins means that they have potential applications in quantum computing as a quantum bit/qubit. One of the main goals of current physics research is the development of a digital quantum computer (QC), a device that uses real quantum phenomena like superposition states or entanglement to outperform classical computers in some specific tasks ranging from structural biology to quantum physics.<sup>20</sup> Quantum bits, or qubits, are the fundamental component of quantum computational devices, used to define a superposition state in which the information is encoded. Various approaches for implementing them are being investigated, including ionic traps, quantum dots in semiconductors, photons, and superconducting nanostructures.<sup>21</sup> Spins, whether nuclear or electronic, are among the most efficiently addressable objects for the construction of these logical units, since their initialisation and read-out may be accomplished using well-established magnetic resonance techniques.

Pulsed EPR techniques allow for the analysis of how paramagnetic systems evolve through time. This is done by sending a series of EPR pulses and hence exciting electronic transitions in the static magnetic field. The relaxation times can then be determined for these states, and this provides information about the quantum coherence properties of the molecule studied. To develop systems for quantum information, qubits with long spin-spin and spin-lattice relaxation times,  $T_2$  and  $T_1$ , are required. These parameters arise in the Bloch equation which describe the time evolution of the net magnetisation of an ensemble of spins in a magnetic field.  $T_2$  denotes the lifetime of information in quantum computing, whereas  $T_1$  indicates the highest potential memory storage time and the shortest feasible time period between each computational cycle. Longer relaxation times means more robust quantum coherence properties. The relaxation time is the time taken for the system to return to equilibrium after it is manipulated by the spin pulses. Two relaxation processes are analysed to assess the quantum coherence properties:

- $T_1$  is defined as the relaxation time along the  $z$  axis and is dependent on spin-lattice interactions
- $T_2$  is defined as the relaxation time along the  $xy$  plane and is dependent on spin-spin interactions

In solid-state systems, electron spins are promising candidates for quantum bits due to their relative decoupling from their surroundings and their integration in a solid matrix, but the electron spin-based molecular qubits approach constitute a different strategy. Modifying the chemical structure of

molecules allows for the control of the specific lattice vibrations, resulting in changes to  $T_1$ . Numerous research on potential qubit molecular design has focused on prolonging  $T_1$  and  $T_2$  and strengthening their persistence to higher temperatures and the impact of phonons and local vibrational modes in influencing the spin dynamics of electronic spin qubits is particularly important. Despite the identification of several potential molecular qubits, the use of one-qubit operations, quantum computer applications require the capacity to perform two-qubit gates. This provides a significant challenge in using magnetic molecules as qubits, since they require switchable qubit-qubit interactions.

Prior studies on  $^{IV}\text{VO}$  metal complexes demonstrated good coherence times  $T_m^{22,23}$  and recently vanadyl dimers in fused porphyrins allowed for the benefit of a large planar conjugated  $\pi$ -system that provides significant advantages for vanadyl(IV) ions communication to be explored.<sup>24,25</sup>

For reasons described in the previous section, **D1** and **D2** are expected to be good candidates for a two-qubit gate. Compared to the other studies, our system has an isotropic exchange coupling close to zero, with the magnetic exchange driven by only a weak through-space dipolar interaction. Thus, the potential performance of the vanadyl monomer **M4**, the VPdV dimer **D1** and a new dimer, VPdCu, **D11** as qubit quantum gate has been studied by pulsed EPR spectroscopy.

### 3.6.1 Hahn echo

The echo of the spin relaxation is recorded in pulsed EPR, as the actual relaxation occurs during what is known as the ‘dead time’ when measurements cannot be recorded for technical reasons. The Hahn echo decay avoids this problem and allows for information to be obtained. This works by sending a  $\pi/2$  pulse along the x axis which rotates the magnetisation by  $90^\circ$ , from the z direction to the y direction. Then, after a period of time  $\tau$ , during which the magnetisations of the spin packets decohere, a  $\pi$  pulse reverses the magnetisation of all the spin packets. The magnetisation refocuses, after a time  $\tau$ , leading to the echo observed on the spectrometer. The sequence is summarised in Figure 127. When the echo intensity is recorded as function of the time  $\tau$ , an exponential decay that depends on the relaxation time,  $T_2$ , is recorded. This relaxation time is dependent on spin-spin interactions. Since additional processes are involved (spin diffusion, spectral diffusion), the characteristic time obtained through these experiments is a sum of all these processes and this is referred to as the phase-memory time,  $T_m$ .

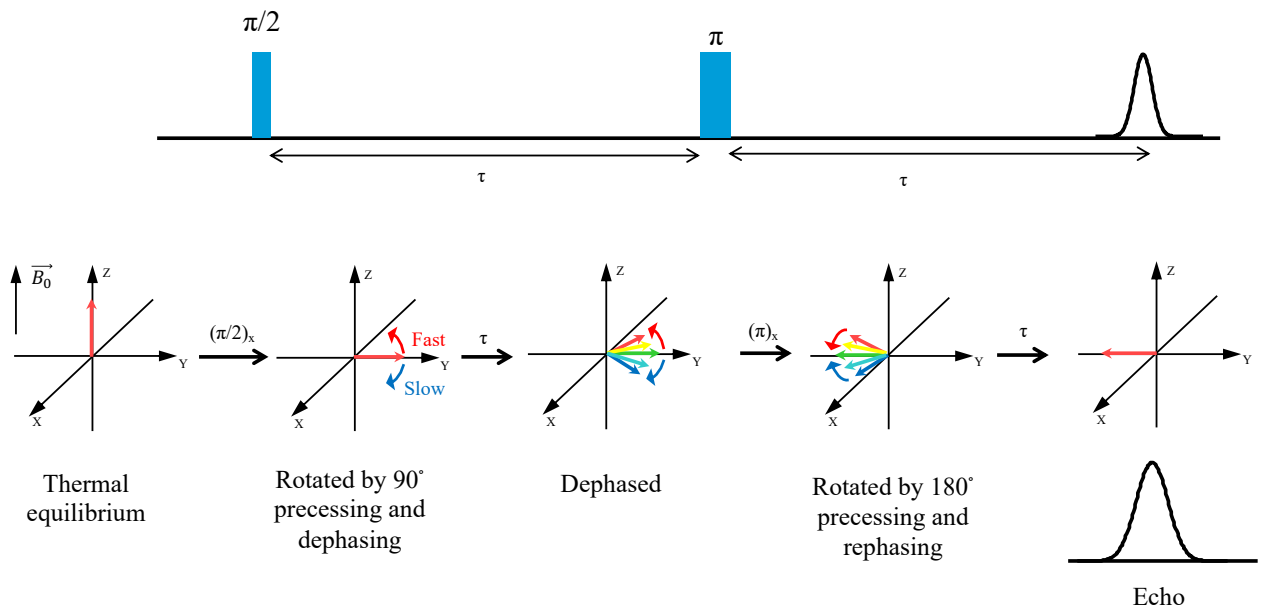


Figure 127: Hahn echo sequence and the evolution of the magnetisation during the Hahn echo sequence

### 3.6.2 Saturation recovery

The simplest implementation of measuring spin-lattice relaxations is the inversion recovery sequence (Figure 128). The sequence starts with a  $\pi$  pulse which flips the spin along the  $z$  axis. A certain time  $t$  is then allowed for the system to evolve, and then an echo sequence is employed as described above (3.6.1) to measure the magnetisation. When the echo is recorded as function of the time  $t$ , an exponential growth with a time constant is recorded.

However, since spectral and spin diffusion are usually observed, this prevents a full excitation of the spins, so instead a saturation recovery sequence was used. This starts with a series of  $\pi$  pulses that saturate the magnetisation (a “picket fence” sequence). After a waiting time  $t$ , the recording of a Hahn echo reveals an exponential recovery characterised by the same time  $T_1$ .

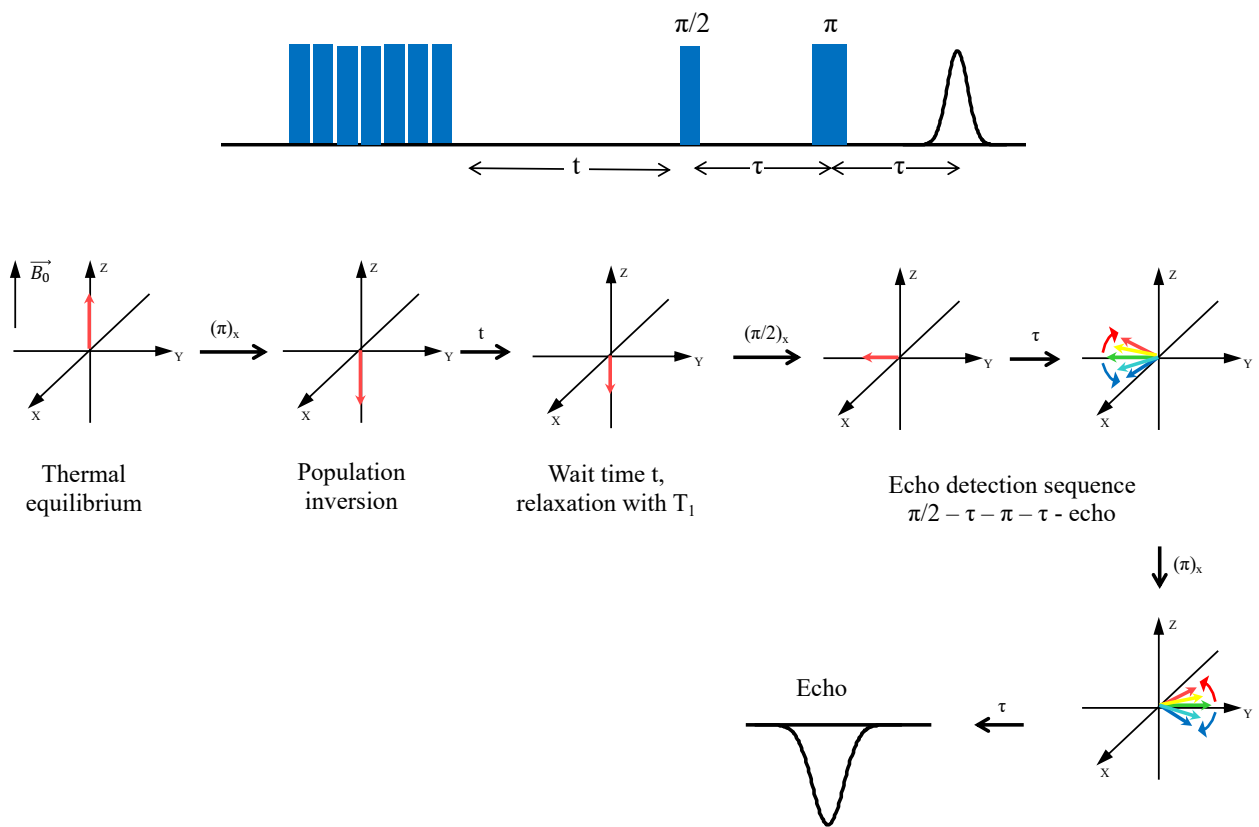


Figure 128: Inversion recovery sequence and evolution of the magnetisation during the inversion recovery sequence

### 3.6.3 Vanadyl monomer M4

The vanadyl monomer **M4** was analysed using pulsed EPR techniques. The measurements were carried out on powder samples to allow room-temperature studies, which are generally hampered in liquid solutions. The vanadyl monomer was diluted in a diamagnetic matrix in an attempt to decrease spin-spin interactions by distancing the paramagnetic species. The matrix chosen was a Ni porphyrin exactly the same as that of the vanadyl porphyrin **M4**, except for the metal at the internal coordination site. Three dilutions were carried out for the V:Ni porphyrin matrix: 1:10, 1:100 and 1:1000. The best results were clearly found for the 1:1000 dilution, as these had the lowest spin-spin interactions and these results will be shown first and then compared to their less diluted counterparts.

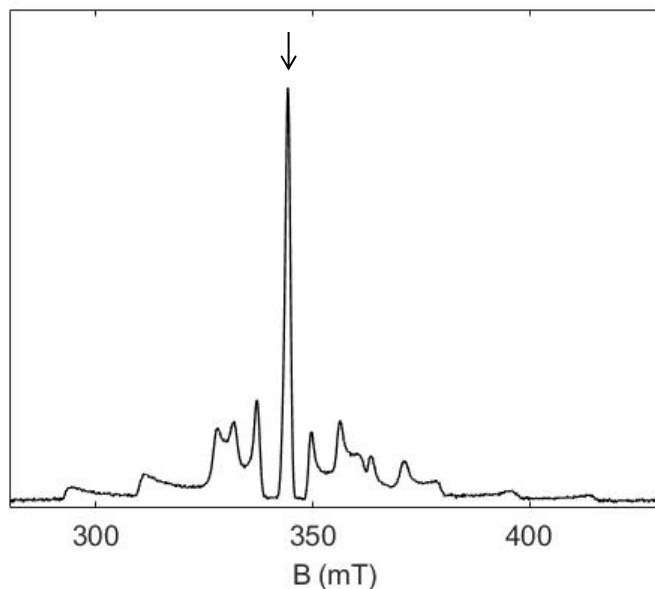


Figure 129: EDFS of **M4**. Arrow indicates field position chosen to determine quantum coherence properties

An echo detected field sweep (EDFS) was first carried out on the vanadyl monomer (Figure 129). The presence of a spin-echo means that quantum coherence properties are expected for **M4**, hence saturation recovery experiments at varying temperatures were carried out for **M4**. The arrow on Figure 129 is the field position chosen for the pulsed EPR experiments which was used to obtain the  $T_1$  and  $T_m$  values.

The  $T_m$  value is dependent on spin-spin interactions. Hence, if the molecule exhibits stronger magnetic interactions, this value will decrease considerably. The echo decay at different temperatures is shown in Figure 130. Oscillations can clearly be seen on the echo decay traces. These modulations are due to weakly coupled nuclei. This effect is called ESEEM (electron spin echo envelope modulation). A  $T_m$  value at room temperature as large as the one observed, 0.7  $\mu$ s for the vanadyl monomer is exceedingly sought after. Values found in the literature are similar for vanadyl systems, for example 0.83  $\mu$ s for a vanadyl phthalocyanine system at room temperature.<sup>26</sup> The system is also comparable to deuterated systems, a  $(PPh_3)_2[Cu(mnt)_2]$  diluted 1000 times in a  $(PPh_3)_2[Ni(mnt)_2]$  has a  $T_m$  value of 0.6  $\mu$ s at room temperature.<sup>27</sup> Both of these systems from the literature are already considerably higher than values found for other systems and a lot of systems reported do not present quantum coherence properties at room temperature. The system of van Slageren<sup>27</sup> minimises superhyperfine coupling by choosing thiolate ligands as this coupling decreases the quantum coherence time. This is the reason why the vanadyl porphyrin (**M4**) was chosen over the copper porphyrin (**M6**). This is backed up by other work in the literature.<sup>28,29</sup>

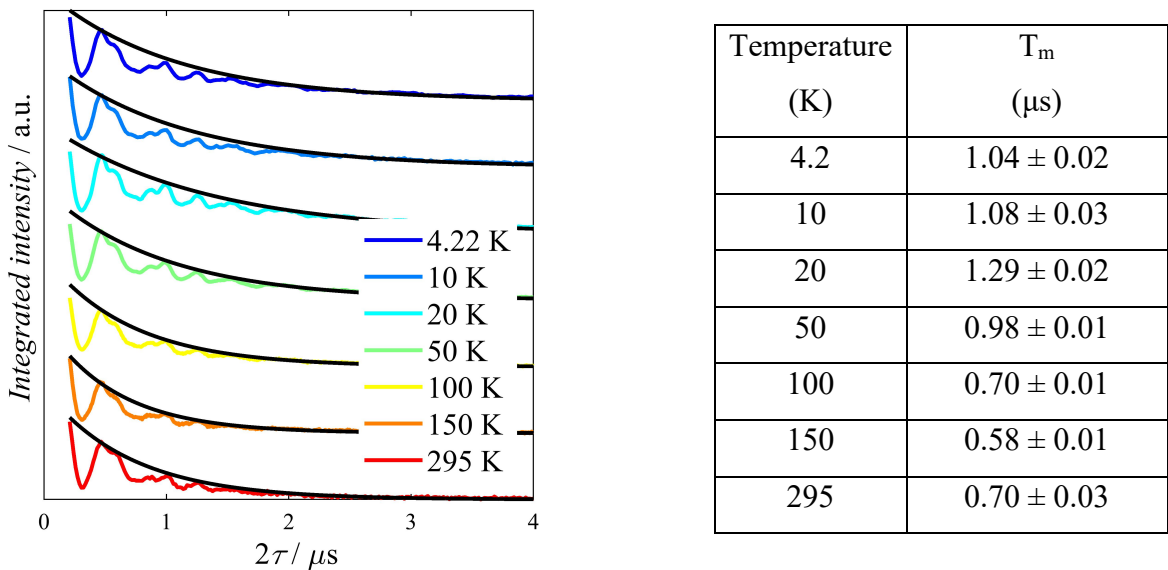


Figure 130: Echo decay traces (in varying colours) and fit (in black) with a mono-exponential decay at varying temperatures (left) and table of the  $T_m$  values (right)

Comparing the  $T_m$  and  $T_1$  values at 50 K, it is apparent that the dilution had a large effect on the quantum coherence, with longer  $T_m$  values obtained when the porphyrin was diluted in the diamagnetic matrix. This is most apparent by comparing the dark blue and yellow oscillations in Figure 131, left as the oscillation is clearly quenched earlier for the yellow line (1:10) compared to that of the dark blue line (1:1000). Longer  $T_1$  values are also observed for diluted samples.

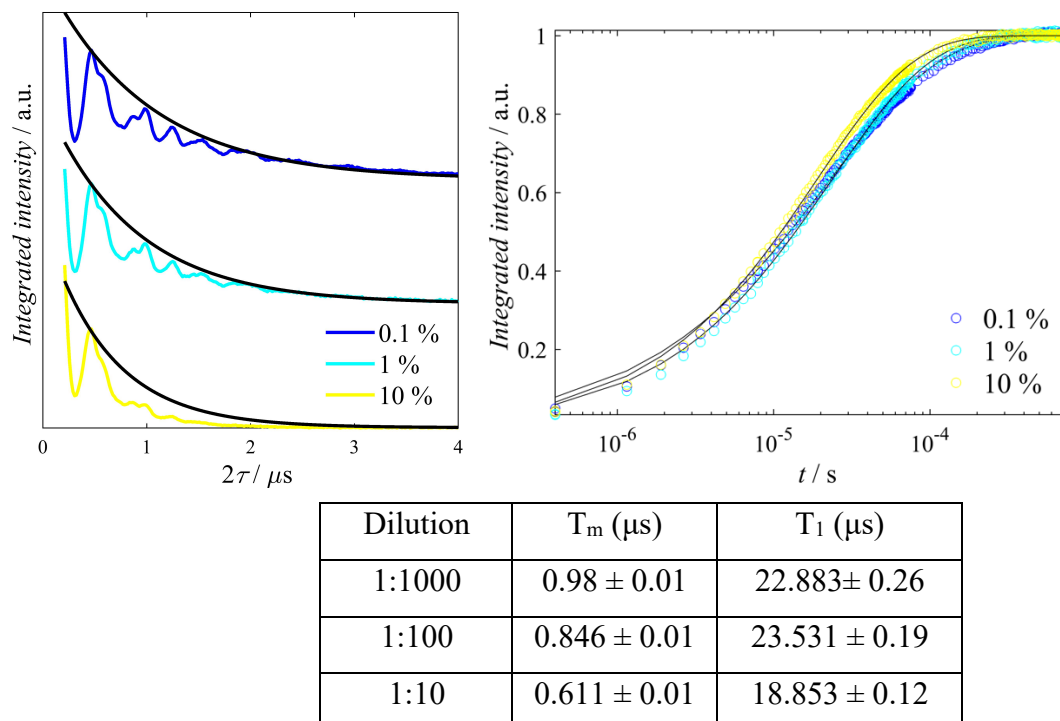


Figure 131: Echo decay traces (in varying colours) and fit (in black) with a mono-exponential decay at varying magnetic dilutions (left) and table of the relaxation time  $T_m$

The picket fence saturation recovery traces and  $T_1$  values are shown in Figure 132. This is the time taken for the magnetisation to relax to its ground state. A value for  $T_1$  was able to be obtained at 295 K demonstrating that the upper limit for the coherence times are high. Quantum coherence properties at room temperature is still quite a rarity in the literature. The  $T_1$  values found are comparable with some of the best values found in the literature.<sup>23</sup> On increasing the temperature, the  $T_1$  values will decrease on account of increased vibrational energy.

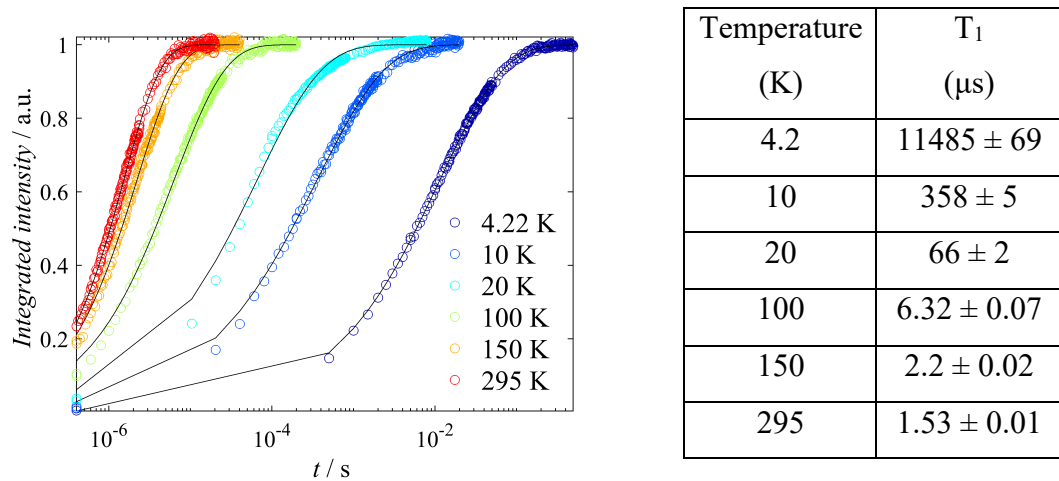


Figure 132: Picket fence saturation recovery traces (in varying colours) recorded at varying temperatures and fit with a mono exponential stretched curve (black) (left). Values of  $T_1$  used to fit the picket fence saturation recovery traces (right)

In order to verify that spin manipulation was feasible, nutation measurements at different microwave powers were carried out. The field chosen was always the same at the most intense part of the peak of the EDFS spectrum of the vanadyl monomer. The nutation for the vanadyl monomer was carried out from 4 K to room temperature at varying powers. The nutation at room temperature was chosen as an example, Figure 133, as this was the most impressive result. The nutation frequency should be proportional to the square root of the power. This was indeed the case as demonstrated by the straight line of Figure 133. On changing the power, the frequency of the nutation will change as is seen in Figure 133, right. This confirmed that the main oscillations observed in the spectra were indeed due to a nutation and not hyperfine interactions, as hyperfine coupling does not change frequency on varying the power. Observing a nutation at room temperature is an exceedingly important point demonstrating the robustness of the quantum coherence properties. This is potentially on account of the rigidity of the porphyrin system.

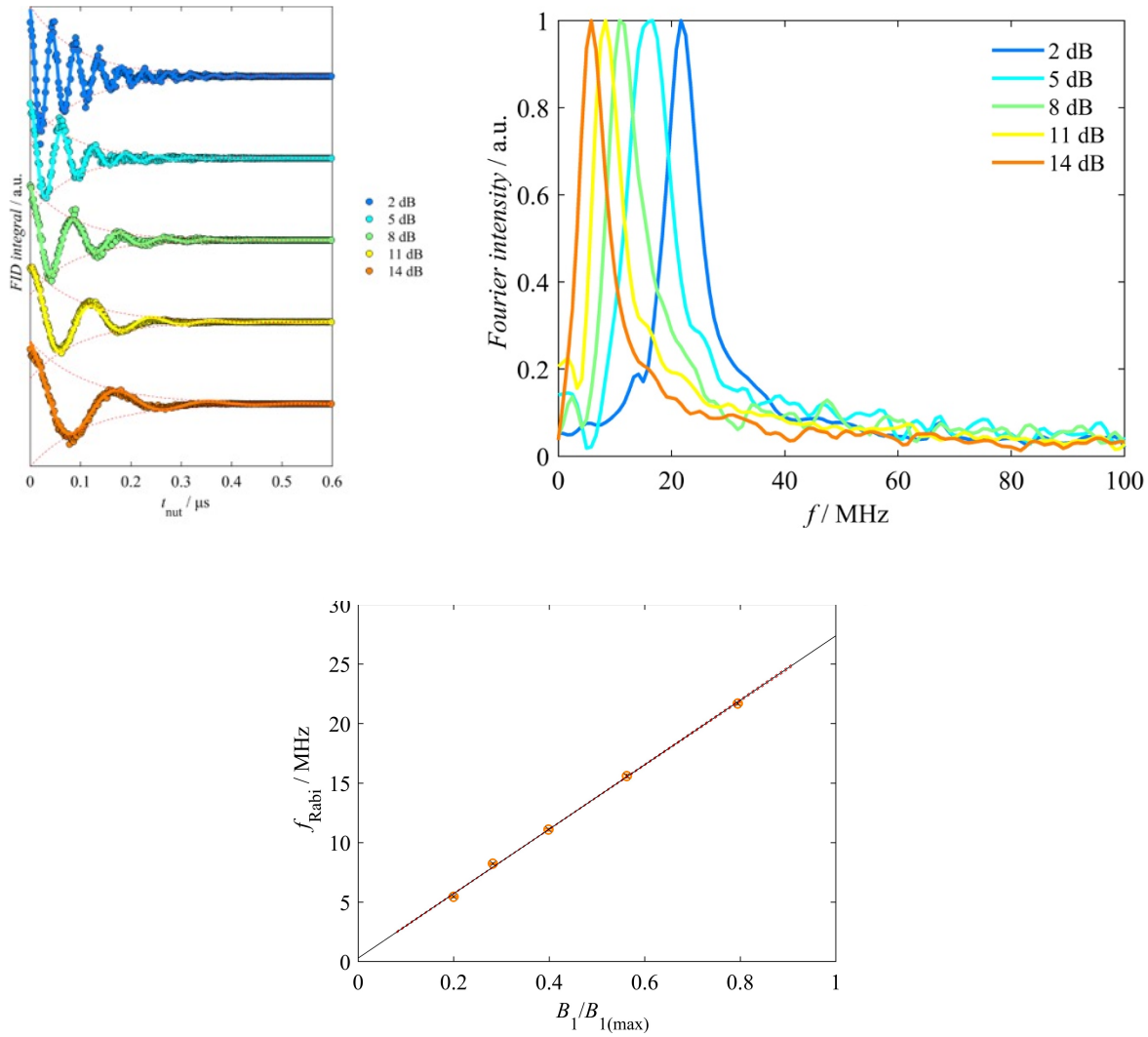


Figure 133: Nutation traces of **M4** at varying powers (top left), Fourier transform of the nutation at varying powers (top right), correlation between varying the power and the nutation frequencies transform (bottom)

### 3.6.4 2-Qubit systems

The results obtained for the vanadyl monomer led to the progression on to 2-qubit systems. Two porphyrin dimers were chosen to be analysed by pulsed EPR. They were the VPdV dimer **D1** and a VPdCu dimer, **D11**. The hope for the VPdCu dimer was that by using two different spin systems, this would lead to decreased spin-spin interactions, as the two spins resonated at slightly different fields. This also allows for increased tunability of the spin system as one of the spins could be manipulated whilst the other remained unaffected. This asymmetric system (VPdCu) was hence designed so that selective addressing of each of the two qubits could be possible. This allows for the spins to be manipulated independently and allows for implementation in multi-qubit gates.<sup>30</sup> These two dimers were once again diluted in a diamagnetic matrix, independently. A NiPdNi dimer was chosen in order to keep the matrix identical and vary only the internal metal centre from paramagnetic to diamagnetic.

The fact that the 1:1000 dilution gave the best results means that only this series will be presented, with the 1:10 and 1:100 presenting shorter  $T_1$  and  $T_m$  values.

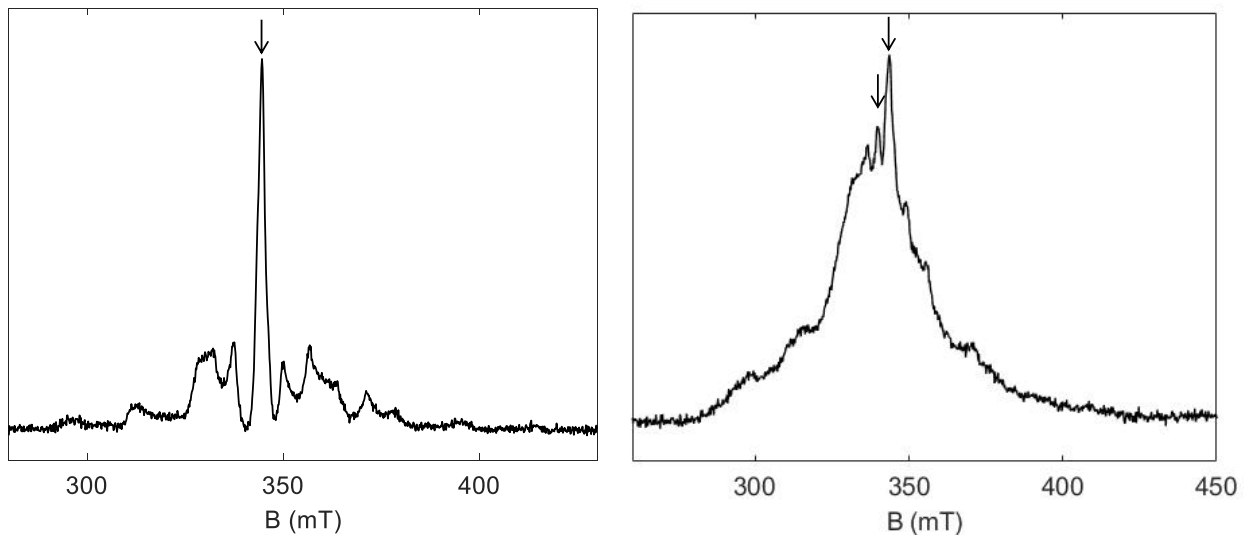


Figure 134: EDDFS of VPdV (**D1**) at room temperature (left) and VPdCu (**D11**) at 150K (right). Arrows indicate field position chosen to determine quantum coherence properties

The EDDFS of **D1** at room temperature and VPdCu at 150 K are shown in Figure 134. Unfortunately, the separation of the two spins for the VPdCu dimer was not particularly optimal (Figure 134, right). No echo was detected at room temperature for the VPdCu dimer, as the relaxation time  $T_m$  was too short. The  $T_1$  and  $T_m$  values were once again assessed using pulsed EPR techniques.

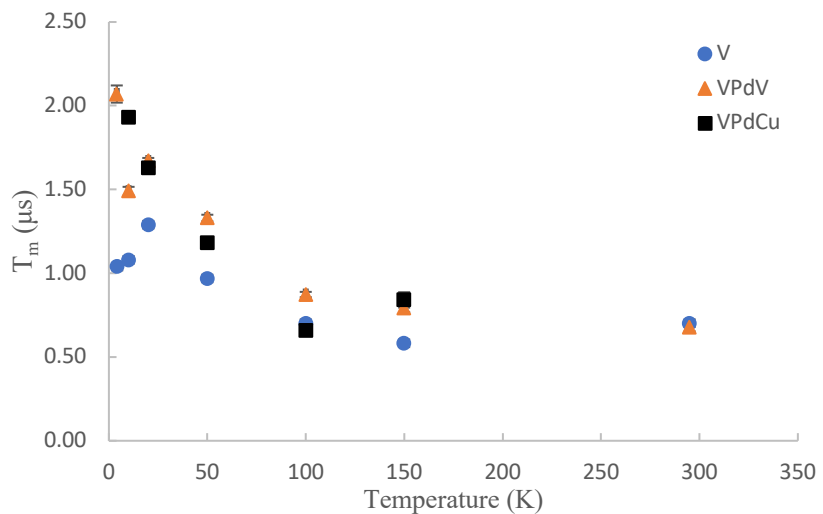


Figure 135:  $T_m$  values for Vanadyl monomer, VPdV (**D1**) and VPdCu (**D11**) dimers with error bars (error bars are occasionally hidden by the marker)

The  $T_m$  values for **M4**, **D1** and **D11** are summarised in Figure 135. Comparing the values for the vanadyl monomer and the VPdV dimer, minimal differences can be observed. This is not surprising for the  $T_1$  values as this is defined by interactions between the spin and the lattice, parameters that

were not altered on changing from the monomer to the dimer. Despite this, the values remain large, taking the room temperature measurement as an example, the difference between the monomer and the dimer is a meagre 0.002  $\mu$ s. Hence a large value is still able to be obtained for a 2-qubit system, even at room temperature, with a nutation being present at room temperature. To our knowledge, this is the first 2-qubit system showing quantum coherence at room temperature.

Moving on to the VPdCu dimer, the values for this dimer are lower than that of the VPdV dimer. This is hence most likely on account of the addition of the copper which leads to a decreased quantum coherence than that of the vanadyl metal. Yet, the results remain reasonable for a 2-qubit system. However, unfortunately a nutation was no longer observed at room temperature.

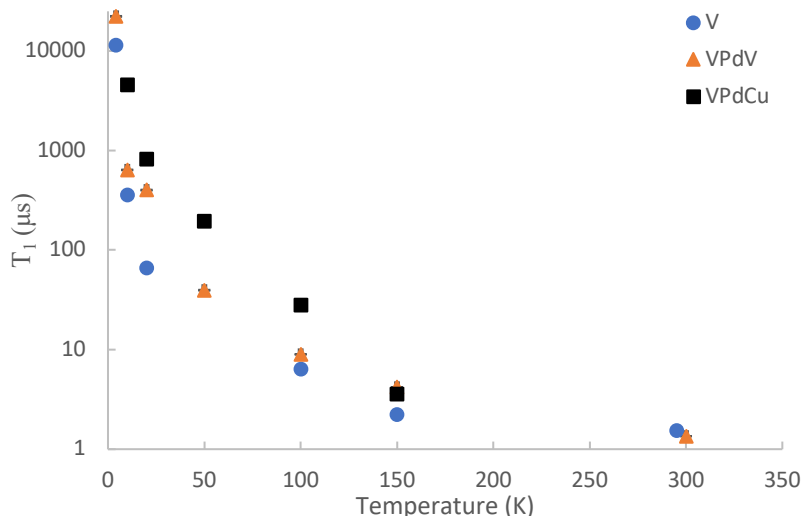


Figure 136:  $T_1$  values as a logarithmic scale for Vanadyl monomer, VPdV (**D1**) and VPdCu (**D11**) dimers with error bars (error bars are occasionally hidden by the marker)

The  $T_1$  values for **M4**, **D1** and **D11** are summarised in Figure 136. There are few differences between the monomer and the VPdV dimer at higher temperature ( $> 50$  K); discrepancies are only apparent at lower temperatures. These results are once again impressive and show that the addition of a second spin for the dimer does not hinder the systems quantum coherence properties. The values obtained for VPdCu remain comparative with those found in the literature, however the lack of a nutation higher than 150 K shows that the system is less robust than the VPdV dimer.

The nutation at room temperature for VPdV is shown in Figure 137. Once again demonstrating that this dimer could be useful for applications as a two-qubit system.

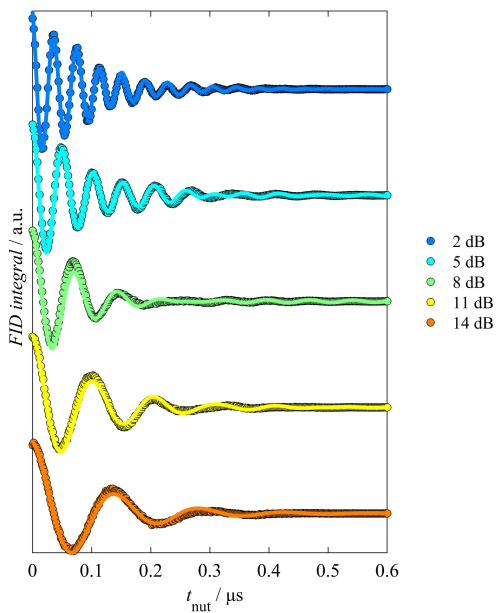


Figure 137: Nutation traces of VPdV at varying powers

### 3.7 Conclusions and perspectives

To summarise this chapter, two porphyrin monomers and eleven porphyrin dimers have been synthesised with varying metals at the internal and external coordination sites. The electronic and magnetic properties varied massively depending on the metal ion at the internal and external coordination sites and the type of external coordination site used. Softer metal ions led to increased electronic communication and the splitting in the first oxidation of the cyclic voltammetry was comparable to the best results present in the literature, hence demonstrating the efficiency of these porphyrin moieties to undergo electronic communication on account of their coplanarity and good orbital overlap.

CW EPR spectroscopy allowed for the analysis of the magnetic properties of these porphyrin dimers. A weak dipolar interaction was able to occur between the two vanadyl ions at the internal metal coordination sites when the metal ion at the external coordination site was diamagnetic. This interaction was increased for the VPtV ( $\alpha,\alpha$ ) dimer which had a larger  $J$  coupling than the VPtV ( $\alpha,\beta$ ) dimer. The magnetic coupling for copper porphyrin dimers proved to be different to that of vanadyl dimers as a slightly more significant isotropic exchange was detected. This isotropic exchange was enhanced when the external coordination site was changed from an enaminoketone to an enaminothioketone.

Switching the metal at the external coordination site to a paramagnetic metal ion led to increased magnetic interactions, as the metal ion was able to act as a relay for communication and led to a ferromagnetic ground state for **D3** and to an antiferromagnetic ground state for **D7**. Such coupling constants should now be quantified, this can be done by either carrying out recording double integrated  $\Delta m_s=1$  transition *versus* temperature or by using SQUID measurements. SQUID measurements were attempted during the course of this PhD, however there were issues on account of trace metal impurities in the starting metal ion. The purity of the metal ion was 99.9% and trace metals were still observed when the SQUID measurements were carried out.

To summarise the pulsed EPR project, **M4**, **D1**, and **D11** were analysed for potential applications as qubits for quantum computing. Three different paramagnetic porphyrin systems were diluted in a diamagnetic matrix in an attempt to minimise spin-spin interactions and their  $T_1$  and  $T_m$  values were determined using pulsed EPR techniques. Measurements were carried out in powder in order to prevent solvent interactions and also to allow for higher temperature studies to be carried out. Were the experiments to be carried out in solution, the tumbling effect would also have prevented  $T_m$  measurements for the porphyrin dimers. The preliminary results obtained are exceedingly promising with long  $T_1$  and  $T_m$  values being obtained for the porphyrin monomer. Passing to a porphyrin dimer (**D1**), and hence adding an extra spin to the system, surprisingly had minimal detrimental effects on the quantum coherence lifetimes. Long quantum coherence was observed for the porphyrin dimer, these values were almost as long as that of the porphyrin monomer. In an attempt, to facilitate the tuning of the quantum coherence, a second porphyrin dimer was also analysed, VPdCu. This dimer had shorter quantum coherence values than that of the monomer and the VPdV dimer.

The results obtained are exceedingly promising for applications in quantum computing, with quantum coherence being observed at room temperature for both the vanadyl monomer and the VPdV dimer. Further analysis of these preliminary results is currently underway.

### 3.8 References

- 1 S. Richeter, C. Jeandon, R. Ruppert and H. J. Callot, *Chem. Commun.*, 2001, **2**, 91–92.
- 2 S. Richeter, C. Jeandon, J. P. Gisselbrecht, R. Ruppert and H. J. Callot, *J. Am. Chem. Soc.*, 2002, **124**, 6168–6179.
- 3 M. A. Carvalho, H. Dekkiche, S. Richeter, C. Bailly, L. Karmazin, D. McKearney, D. B. Leznoff, G. Rogez, B. Vileno, S. Choua and R. Ruppert, *J. Porphyrins Phthalocyanines*, 2019, **23**, 238–246.
- 4 J. S. Lindsey, I. C. Schreiman, H. C. Hsu, P. C. Kearney and A. M. Marguerettaz, *J. Org. Chem.*, 1987, **52**, 827–836.
- 5 A. R. Katritzky and K. S. Laurenzo, *J. Org. Chem.*, 1986, **51**, 5039–5040.
- 6 A. J. Tasiopoulos, A. N. Troganis, A. Evangelou, C. P. Raptopoulou, A. Terzis, Y. Deligiannakis and T. A. Kabanos, *Chem. Eur. J.*, 1999, **5**, 910–921.
- 7 R. Bonnett, P. Brewer, K. Noro and T. Noro, *Tetrahedron*, 1978, **34**, 379–385.
- 8 K. M. Kadish and E. Van Caemelbecke, *J. Solid State Electrochem.*, 2003, **7**, 254–258.
- 9 V. S. Y. Lin, S. G. DiMagno and M. J. Therien, *Science*, 1994, **264**, 1105–1111.
- 10 J. J. Piet, P. N. Taylor, H. L. Anderson, A. Osuka and J. M. Warman, *J. Am. Chem. Soc.*, 2000, **122**, 1749–1757.
- 11 A. Tsuda, H. Furuta and A. Osuka, *J. Am. Chem. Soc.*, 2001, **123**, 10304–10321.
- 12 S. S. Eaton and G. R. Eaton, *eMagRes*, 2016, **5**, 1543–1556.
- 13 S. Stoll and A. Schweiger, *J. Magn. Reson.*, 2006, **178**, 42–55.
- 14 M. P. Espinosa, A. Campero and R. Salcedo, *Inorg. Chem.*, 2001, **40**, 4543–4549.
- 15 Y. Deligiannakis, M. Louloudi and N. Hadjiliadis, *Coord. Chem. Rev.*, 2000, **204**, 1–112.
- 16 S. S. Eaton and G. R. Eaton, *Biomed. EPR, Part B Methodol. Instrumentation, Dyn.*, 2005, **Chapter 8**, 223–236.
- 17 O. Kahn, *VCH Publ. Inc.*
- 18 M. Akbar Ali, P. V. Bernhardt, M. A. H. Brax, J. England, A. J. Farlow, G. R. Hanson, L. L. Yeng, A. H. Mirza and K. Wieghardt, *Inorg. Chem.*, 2013, **52**, 1650–1657.
- 19 B. S. Pedersen, S. Scheibye, N. H. Nilsson and S.-O. Lawesson, *Bull. Soc. Chim. Belg.*, 1978, **87**, 223–228.
- 20 S. Barnett, *Quantum Information*, Oxford Univ. Press. Oxford.
- 21 T. D. Ladd, F. Jelezko, R. Laflamme, Y. Nakamura, C. Monroe and J. L. O'Brien, *Nature*, 2010, **464**, 45–53.
- 22 C. J. Yu, M. J. Graham, J. M. Zadrozny, J. Niklas, M. D. Krzyaniak, M. R. Wasielewski, O. G. Poluektov and D. E. Freedman, *J. Am. Chem. Soc.*, 2016, **138**, 14678–14685.

23 J. M. Zadrozny, J. Niklas, O. G. Poluektov and D. E. Freedman, *ACS Cent. Sci.*, 2015, **1**, 488–492.

24 I. Pozo, F. Lombardi, D. Alexandropoulos, F. Kong, J-R. Deng, P. Horton, S. Coles, W. Myers, L. Bogani, H. Anderson, *ChemRxiv*.

25 D. Ranieri, F. Santanni, A. Privitera, A. Albino, E. Salvadori, M. Chiesa, F. Totti, L. Sorace and R. Sessoli, *ChemRxiv*.

26 M. Atzori, L. Tesi, E. Morra, M. Chiesa, L. Sorace and R. Sessoli, *J. Am. Chem. Soc.*, 2016, **138**, 2154–2157.

27 K. Bader, D. Dengler, S. Lenz, B. Endeward, S. Da Jiang, P. Neugebauer and J. Van Slageren, *Nat. Commun.*, 2014, **5**, 5304.

28 A. Ardavan, O. Rival, J. J. L. Morton, S. J. Blundell, A. M. Tyryshkin, G. A. Timco and R. E. P. Winpenny, *Phys. Rev. Lett.*, 2007, **98**, 057201.

29 A. Urtizberea, E. Natividad, P. J. Alonso, L. Pérez-Martínez, M. A. Andrés, I. Gascón, I. Gimeno, F. Luis and O. Roubeau, *Mater. Horizons*, 2020, **7**, 885–897.

30 J. N. Nelson, J. Zhang, J. Zhou, B. K. Rugg, M. D. Krzyaniak and M. R. Wasielewski, *J. Chem. Phys.*, 2020, **152**, 014503.

# Chapter 4

## Self-assembly of porphyrin dimers at a solid-liquid interface

4.1 Introduction	164
4.2 Porphyrin synthesis	165
4.3 Surface studies	166
4.3.1 Ni monomer	166
4.3.2 Ni dimer	169
4.3.2.1 2D surface chirality	170
4.3.3 Pd monomer	172
4.3.4 Pd dimer	174
4.3.4.1 Pd cis dimer	175
4.4 Towards porphyrin nano-ribbons	177
4.5 Conclusions and perspectives	181
4.6 General conclusions	183
4.7 References	185

## 4.1 Introduction

A molecule can assemble at an interface through hydrogen bonding, Van der Waals interactions, dipole-dipole interactions and  $\pi$ - $\pi$  interactions. The physisorption of the molecule at the solid-liquid interface is a dynamic process<sup>1</sup> through the aforementioned weak interactions, hence the molecules are not fixed at the surface (as is the case for chemisorption) and consequently rearrangements can occur. This can be seen as corrections in order to obtain the most thermodynamically stable motif, as is seen with self-assembly in solution.<sup>2</sup>

The unique optical and electronic properties of porphyrins mean that they are quite well suited to such applications, with large planar aromatics that can interact well with the surface and the ability to substitute the *meso* positions with long alkyl chains, aids the interactions with the surface. The self-assembly of porphyrins at a solid-liquid interface leads to a 2D assembly of porphyrins in a repeating fashion, a motif. Once assembled, the motifs can be visualised by scanning tunnelling microscopy (STM),<sup>3</sup> where current is passed through a tip and the tunnelling effect allows for the visualisation of the motifs that assemble at the solid-liquid interface. The parts of the images with a higher light intensity are areas with high electronic density. The large aromatic system of a porphyrin is hence perfect for imaging. The solid chosen was highly-oriented pyrolytic graphite (HOPG) as this surface would help minimise defaults in the self-assembly and the liquid chosen was phenyloctane. The choice to substitute the *meso* position with long alkyl chains aids physisorption of the porphyrin onto the surface. A porphyrin is ideally suited for adsorption as its large planar aromatic macrocycle is rich in  $\pi$  electrons and therefore interactions are able to occur between the porphyrin and the surface. A porphyrin with an enaminoketone moiety has the added advantage of being able to undergo hydrogen bonding which will strongly influence the arrangement on adsorption. These advantageous properties mean that a well-ordered motif should assemble at the solid-liquid interface; the well-ordered nature could allow for applications in microelectronics.<sup>4</sup>

Assembling porphyrins at a solid-liquid interface is a topic that has already been researched by our group, with the synthesis of porphyrins with 4-alkyl or 4-alkoxy phenyl groups at the *meso* positions of the porphyrin.<sup>5</sup> The issue with this system design was the fact that the phenyl groups were perpendicular to the porphyrin plane and consequently hindered the interaction with the surface. Additionally, the phenyl groups meant that the first two CH<sub>2</sub> groups of the alkyl chains were not able to undergo Van der Waals interactions with the surface as they were too far away. Hence, a new design was developed with alkyl groups substituted directly to the *meso* position of the porphyrin. The hypothesis was that this would lead to greater interactions with the surface as there were no

phenyl groups impeding interactions and additionally all of the alkyl groups would be able to interact with the HOPG surface. This work was carried out in a collaboration with Nicholas Turetta from the laboratory of Pr. Paolo Samori (ISIS, Université de Strasbourg).

## 4.2 Porphyrin synthesis

The porphyrins **M11** and **M13** (Figure 138) were synthesised using the same synthetic method employed for the synthesis of the porphyrins in Chapter 3, with the *meso* aryl groups of the porphyrin being replaced by C<sub>12</sub>H<sub>25</sub> chains (Figure 138). The only difference was that a dipyrromethane (DPM) was used to synthesise the porphyrin as opposed to classical Lindsey conditions with pyrrole. An additional discrepancy was that two equivalents of DPM and one equivalent of the aldehyde ester was used, the scrambling phenomenon then led also to formation of the A<sub>3</sub>B porphyrin in addition to the expected A<sub>2</sub>B<sub>2</sub> porphyrin. The yields for the synthesis were slightly lower than for the porphyrins shown in Chapter 3 (**M4** and **M6**), potentially on account of a decreased thermal stability for the porphyrins with alkyl *meso* substituents. This meant that benzene was sometimes used as the solvent for the cyclisation step, meaning that less heat was required for the Dean-Stark process. Ni(II) and Pd(II) were the internal metal ions used.

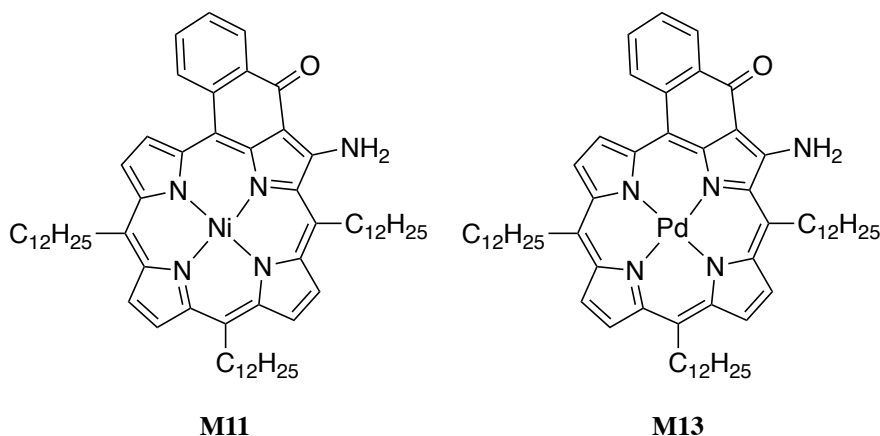


Figure 138: Ni porphyrin, **M11** and Pd porphyrin **M13**, used for STM studies

## 4.3 Surface studies

### 4.3.1 Ni monomer

The monomer **M11** was deposited as a 1 mM solution in phenyloctane onto a HOPG surface. The self-assembly of an exceedingly large motif was then observed by STM at the solid-liquid/HOPG-phenyloctane interface.

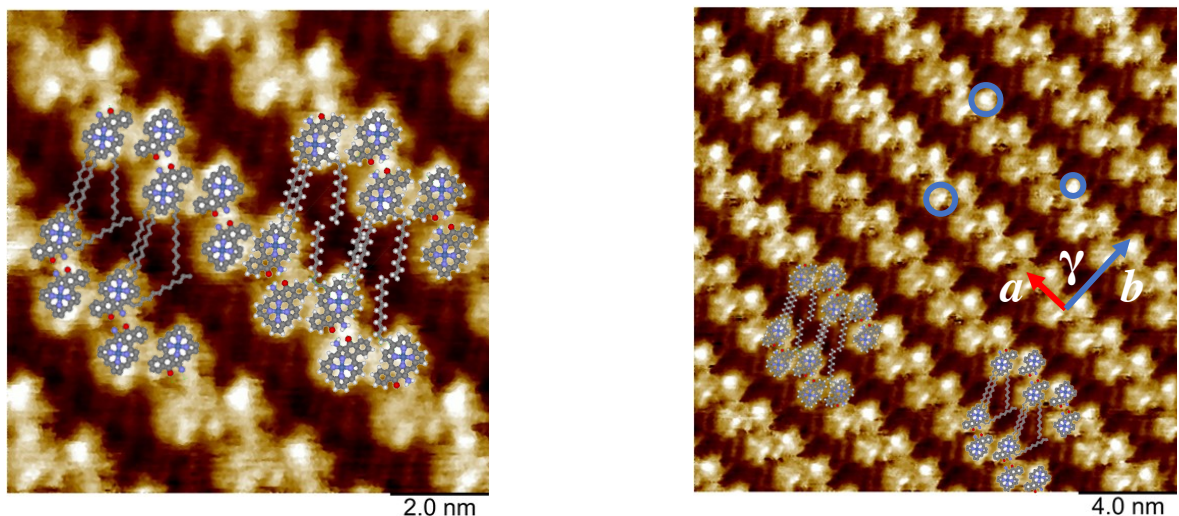


Figure 139: STM images of the Ni monomer **M11** at 10 nm (left) and 20 nm (right) at the HOPG-phenyloctane interface.  $I = 2 \text{ pA}$ ,  $V = -650 \text{ mV}$ . Prediction of assembly shown by porphyrins also shown over the STM images. Lines show direction of  $a$ ,  $b$  and the angle  $\gamma$ . Blue circles show places of higher light intensity, showing the non-planar nature of the porphyrin

Table 32: Unit cell parameters for the Ni monomer **M11**

	$a$ (nm)	$b$ (nm)	$\gamma$ (°)
STM	$1.90 \pm 0.08$	$3.39 \pm 0.08$	$91.0 \pm 3.7$

The porphyrin self-assembled onto the surface as a well-ordered single motif, where one porphyrin was in close proximity to a second porphyrin as the two porphyrins were able to undergo intermolecular interactions on account of the enaminoketone groups (Figure 139). This arrangement led to the formation of parallel rows of porphyrin monomers, with gaps between the rows allowing for the alkyl chains to undergo interactions with the surface; only two out of the three chains interacted with the surface, the third was most likely orientated towards the liquid phase.

The unit cell parameters for the porphyrin monomer are summarised in Table 32. The  $a$  value represents the distance between two porphyrin pairs, the  $b$  value represents the distance between two rows and the  $\gamma$  is the angle between the vector of  $a$  and the vector of  $b$  (shown in Figure 139, right).

Comparison of the unit cell parameters allows for discrepancies between different systems to be assessed more easily. The fact that the luminosity between rows of porphyrins was the same and that there was no difference in luminosity between each porphyrin pair, demonstrated that the porphyrin assembled in a highly homogeneous manner with no issues of stacking or different motifs for this porphyrin.

Comparing these unit cell values to those found for the 4-alkylphenyl substituents at the *meso* position, the *a* value had increased to 1.90 nm for **M11** compared to 1.16 nm for the 4-alkylphenyl porphyrin. An *a* value of 1.90 nm is much closer to the expected distance between two porphyrins *cf.* crystal structures, 1.7 nm. This demonstrated that this porphyrin was more planar than the 4-alkylphenyl porphyrin, as the smaller value hints at the fact that the porphyrin was ruffled. Hence the hypothesis was correct and the addition of alkyl groups directly at the *meso* position had led to a more planar porphyrin arrangement. The porphyrin was still not completely planar. This is apparent as parts of the porphyrin appear brighter than other parts. This effect occurs when the tip is closer to the porphyrin, hinting at the fact that the Ni porphyrin is distorted on the surface to a ruffled geometry as seen in solution. This is highlighted by the blue circles in Figure 139. If part of the porphyrin is not undergoing interactions with the surface, this is potentially a disadvantage and a parameter that could be improved upon. The amount of brightness is however less when the alkyl chains are directly attached to the *meso* position as opposed to the 4-alkylphenyl system, once again hinting at the fact that this porphyrin design had led to a more planar self-assembly than the previous system design.

There were two potential arrangements for the chains as shown in the two crystal structures of a Ni monomer in Figure 140. This is potentially caused by the lack of symmetry of the porphyrin core. Varying the angle of the STM tip from 0° to 90° hinted at which conformer was most likely to be observed at the solid-liquid interface. As the configuration on the left of Figure 140 led to a distortion in the porphyrin core adjacent to the hydrogen bonding site, this was deemed unfavourable, which means that the conformer in the middle is potentially more thermodynamically favourable. The configuration in the middle of Figure 140 will also have increased Van der Waals interactions between the porphyrin chains as they are in closer proximity in this orientation; this would also be favourable. The energy gained from such interactions between methylene groups is estimated to be -1.48 kcal/mol.<sup>6</sup>

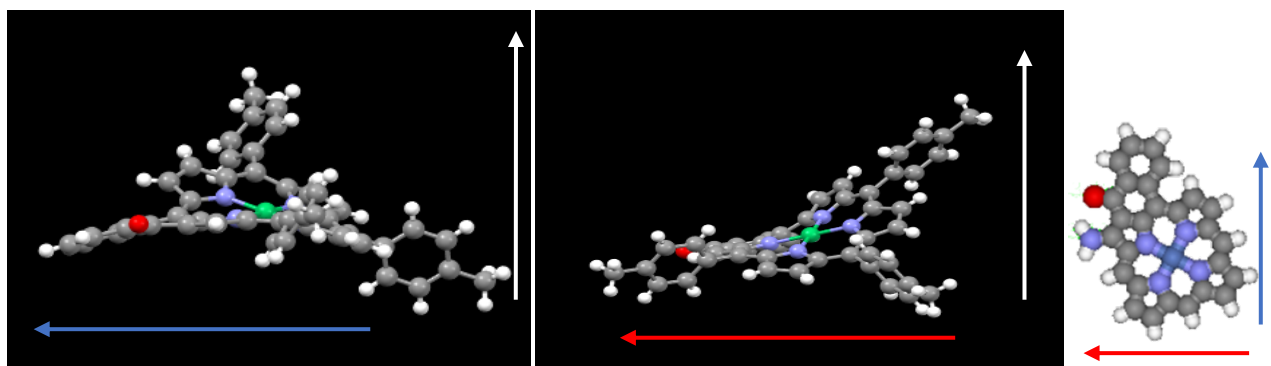


Figure 140: Crystal structures showing two potential arrangements of the Ni porphyrin (left and middle), with the orientation explained by the blue and red arrows (right)

Despite the ruffled porphyrin geometry, the monomer was exceedingly stable on the HOPG surface and formed a single motif over hundreds of nanometers. A single motif over a 480 nm range (the maximum of the STM machine) is an exceedingly rare find, demonstrating a stable dynamic self-assembly (Figure 141). This is advantageous for potential applications in electronics as there are minimal faults in the repeating motif and consequently charge transfer properties could potentially be optimal in these systems.

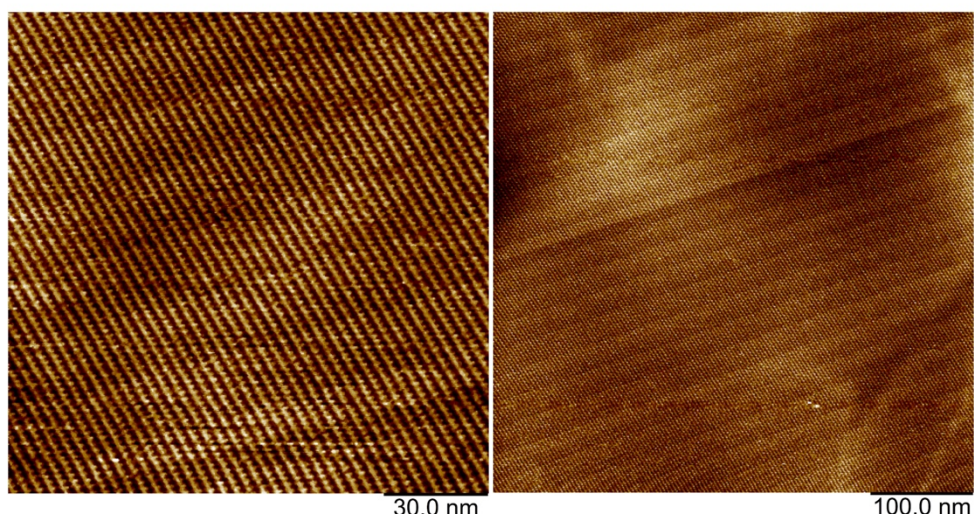


Figure 141: STM images of the Ni monomer, M11, at 140 nm (left) and 480 nm (right) at the HOPG-phenyloctane interface

### 4.3.2 Ni dimer

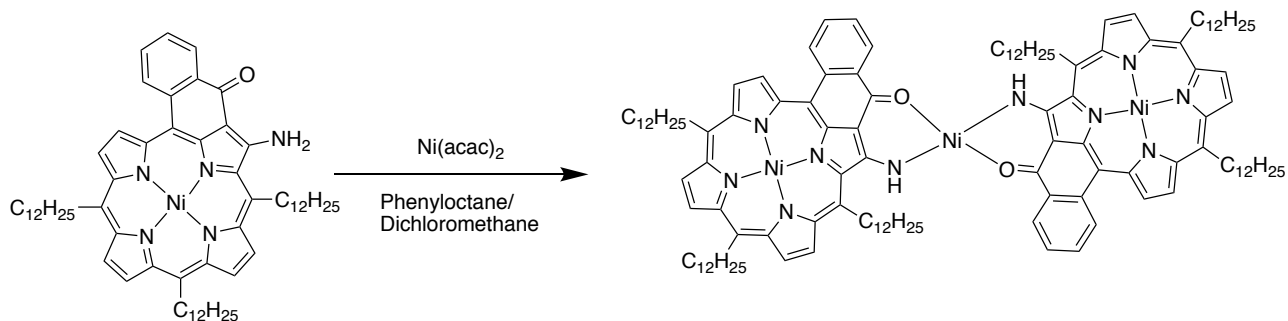


Figure 142: Formation of porphyrin dimers

Dimers were formed by adding half an equivalent of  $\text{Ni}(\text{acac})_2$  in dichloromethane to the porphyrin monomer dissolved in phenyloctane (Figure 142). After 1 hour, the dichloromethane was evaporated using a flow of argon and the brown solution was deposited onto the HOPG surface. The concentration of the dimer was assumed to be 0.5 mM, with full evaporation of the dichloromethane and complete conversion from monomer to dimer. The evaporation of the dichloromethane proved to be of paramount importance for the stability of the self-assembled structure, as presence of dichloromethane led to scrambling.  $\text{Ni}(\text{II})$  was chosen as a linking metal ion as it is relatively labile and consequently would help the self-assembly, as larger motifs could be formed on correction using this metal ion.

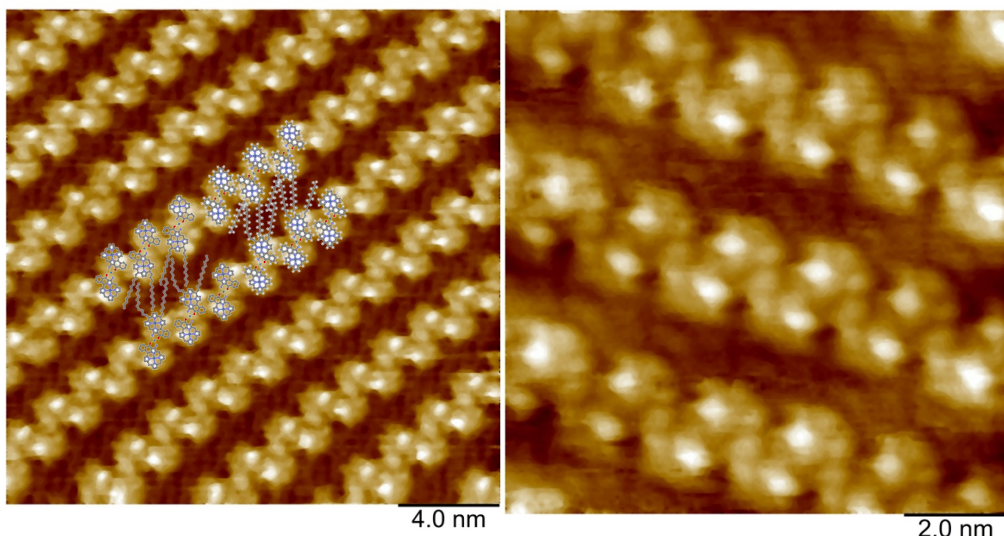


Figure 143: STM images of the Ni dimer at 20 nm (left) and 10 nm (right) at the HOPG-phenyloctane interface.  
 $I = 2 \text{ pA}$ ,  $V = -500 \text{ mV}$

Table 33: Unit cell parameters for the Ni dimer

	$a$ (nm)	$b$ (nm)	$\gamma$ (°)
STM	$1.76 \pm 0.04$	$3.43 \pm 0.11$	$92.6 \pm 2.7$

The Ni dimer self-assembled at the solid-liquid interface (Figure 143) in a manner exceedingly similar to that of the Ni monomer. This was evident by the images themselves (Figure 143) and the unit cell parameters (Table 33), with the distance between two porphyrin pairs decreasing slightly and the rows of porphyrins becoming a little closer. This minor change is expected. As in previously reported crystal structures,<sup>7</sup> the distance between two porphyrins before and after adding a metal linking ion varied minimally as the porphyrins were already in close proximity due to the hydrogen bonding. As seen for the monomer, there were brighter spots demonstrating the ruffled nature of the porphyrin. There were once again two potential arrangements of the alkyl chains; the same arguments discussed above are applied here and therefore the arrangement on the right of Figure 140, left is assumed to be the favourable one.

#### 4.3.2.1 2D surface chirality

The dimer presented so-called 2D chirality when assembled onto the surface, with two possible enantiomers, named S and Z for their directionality (Figure 144). It was the arrangement on the surface which led to the chirality observed; meaning that the chirality was not observed in solution. The additional chirality means that two potential motifs were now possible. The small-scale images of Figure 143 show only one of the motifs and the larger scale images of Figure 145 show the two motifs (S and Z) in the same image. The molecular orientation also led to 2D chirality for other systems in the literature.<sup>8</sup>

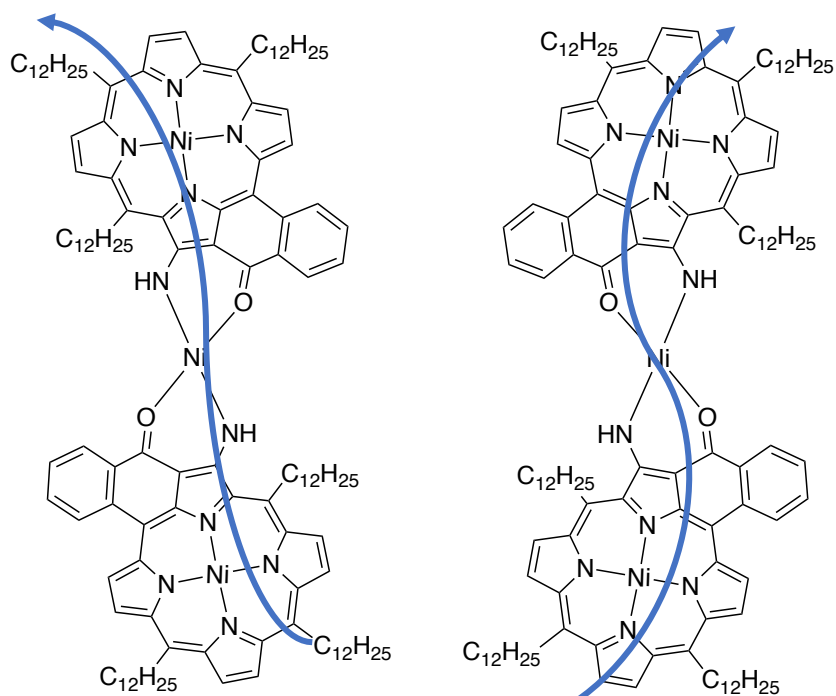


Figure 144: Two enantiomers present on the surface Z (left) and S (right)

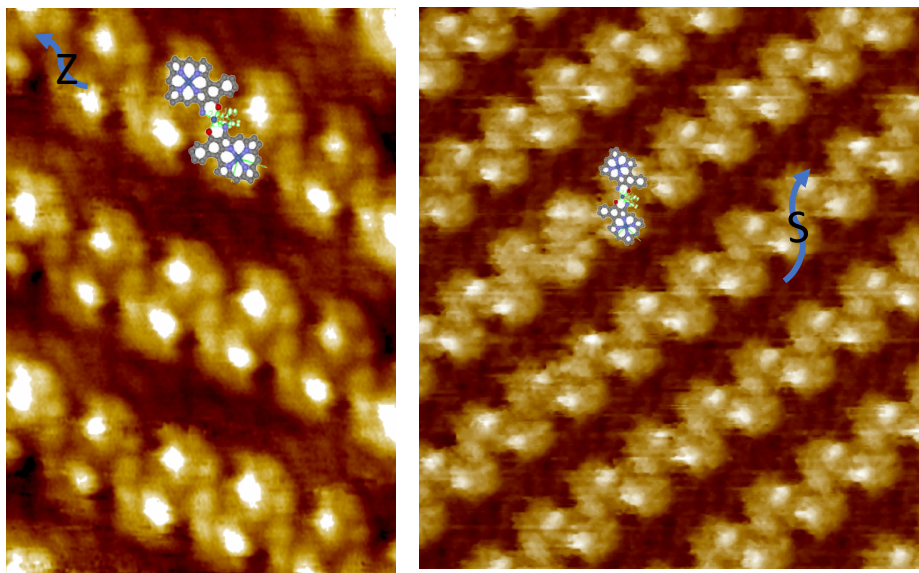


Figure 145: STM images of the two enantiomers of Ni dimer: the Z enantiomer at 10 nm (left) and the S enantiomer at 20 nm (right) at the HOPG-phenyloctane interface.  $I = 2 \text{ pA}$ ,  $V = -500 \text{ mV}$

This chirality can be seen more clearly on a larger scale. Figure 146 shows the chirality change in the red box from S to Z. The additional chirality led to the formation of smaller motifs compared to the monomer counterparts. The size of the domains was typically around 50 nm. There appears to be no preferential formation of one motif over another meaning that the S and Z form are probably exceedingly close in energy which means that there will be equal probability of both enantiomers assembling onto the surface; which is what was observed, with the sizes of the two motifs being of similar size on the surface.

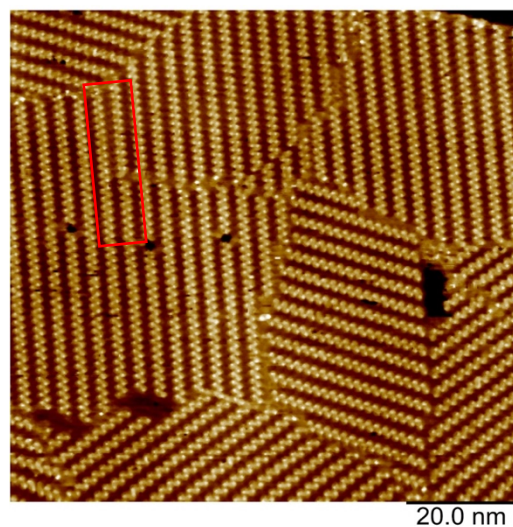


Figure 146: STM images of the two enantiomers of Ni dimer S and Z at 95 nm, at the HOPG-phenyloctane interface. The red box demonstrates the change in chirality.  $I = 2 \text{ pA}$ ,  $V = -500 \text{ mV}$

### 4.3.3 Pd monomer

In order to increase the interactions with the surface, a planar porphyrin was chosen as opposed to a ruffled one. It was hoped that this would lead to greater interactions with the surface. The two X-ray structures below of a ruffled Ni tetraphenyl porphyrin<sup>9</sup> (Figure 147, left) and a planar Pd tetraphenyl porphyrin<sup>10</sup> (Figure 147, right) demonstrate this distortion. Looking at the crystal structures, the structure on the right is more optimal for assembly onto a surface as the interactions with the surface will be more homogeneous throughout the entire porphyrin core, as opposed to the Ni porphyrin.

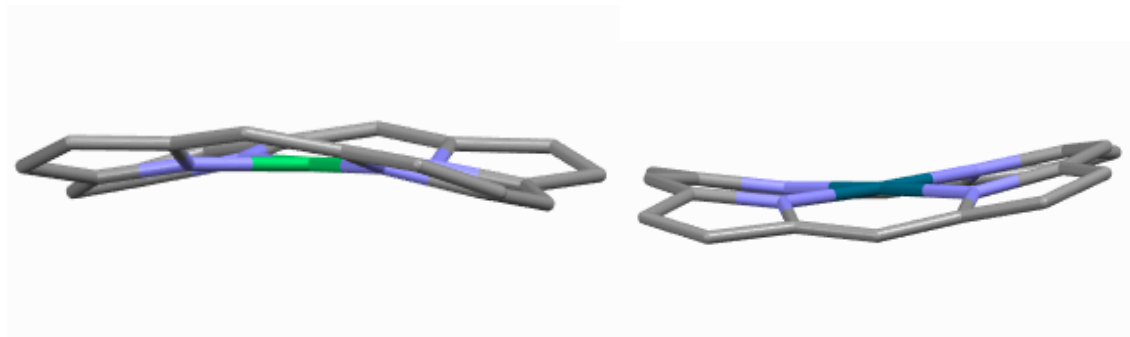


Figure 147: Two crystal structures of Ni (left) and Pd (right) tetraphenyl porphyrin. Hydrogen atoms and aryl substituents omitted for clarity

The Pd monomer, **M13**, was deposited as a 1 mM solution in phenyloctane onto a HOPG surface in the same way as **M11**.

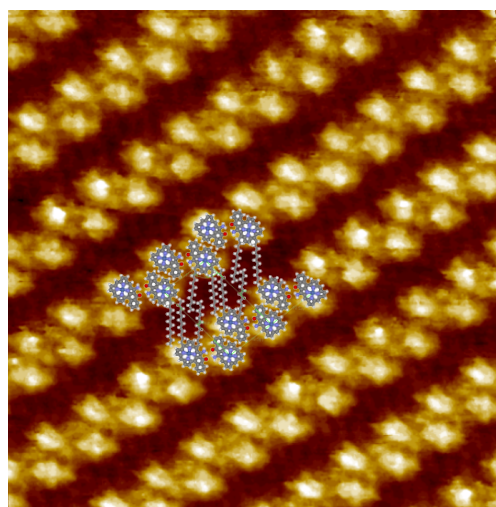


Figure 148: STM images of Pd monomer **M13** at 15 nm.  $I = 4 \text{ pA}$ ,  $V = -600 \text{ mV}$

Table 34: Unit cell parameters for the Pd monomer **M13**

	$a \text{ (nm)}$	$b \text{ (nm)}$	$\gamma \text{ (°)}$
STM	$1.86 \pm 0.14$	$3.28 \pm 0.12$	$99.5 \pm 3.4$

Once again, the porphyrin self-assembled at the solid-liquid interface to form large motifs in close proximity to a second porphyrin due to favourable hydrogen bonding interactions (Figure 148). The Pd(II) porphyrin was also more planar than the Ni(II) porphyrin, meaning that the images obtained have equal luminosity throughout the entire porphyrin. The unit cell parameters for the Ni and Pd monomer are similar (Table 34).

Looking at the large-scale images shown in Figure 149, multiple motifs appear to have formed with the S and Z enantiomers being present. There is also a central region in Figure 149 left, where the porphyrin was more tightly packed. The domains appear to be around 100 nm in size which is still very large.

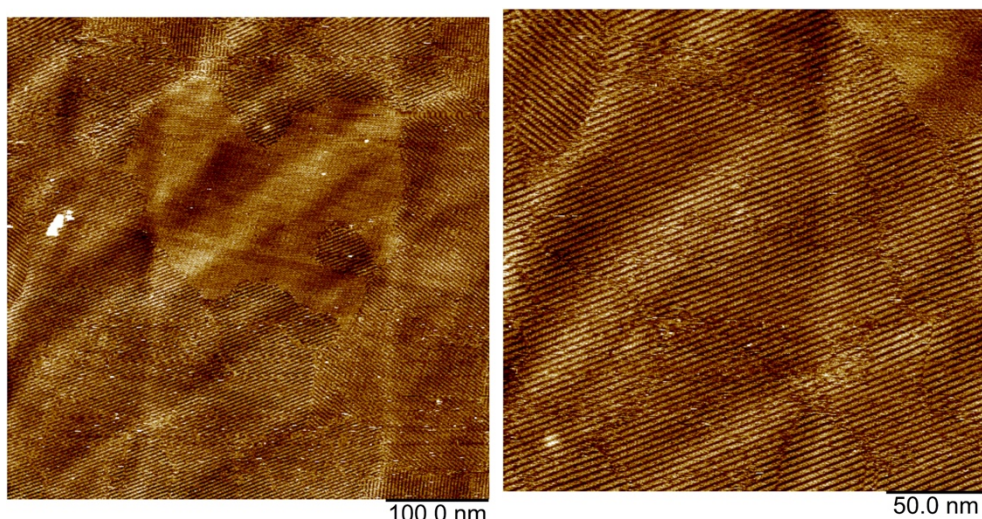


Figure 149: Large scale STM images of Pd monomer M13 at 480 nm (left) and 250 nm (right).  $I = 4 \text{ pA}$ ,  $V = -600 \text{ mV}$

In addition to the S and Z surface chirality, two different cell arrangements were also present on the surface for this monomer: the monoclinic cell and the rectangular cell. The blue line in Figure 150 right demonstrates the division between these two cells and the fact that the yellow and red lines are not straight, demonstrates that a change in the cell orientation has occurred. All four of the potential motifs are present in Figure 150 left, with the top part of the image being Z, rectangular and monoclinic and the bottom part of the image showing a monoclinic S structure.

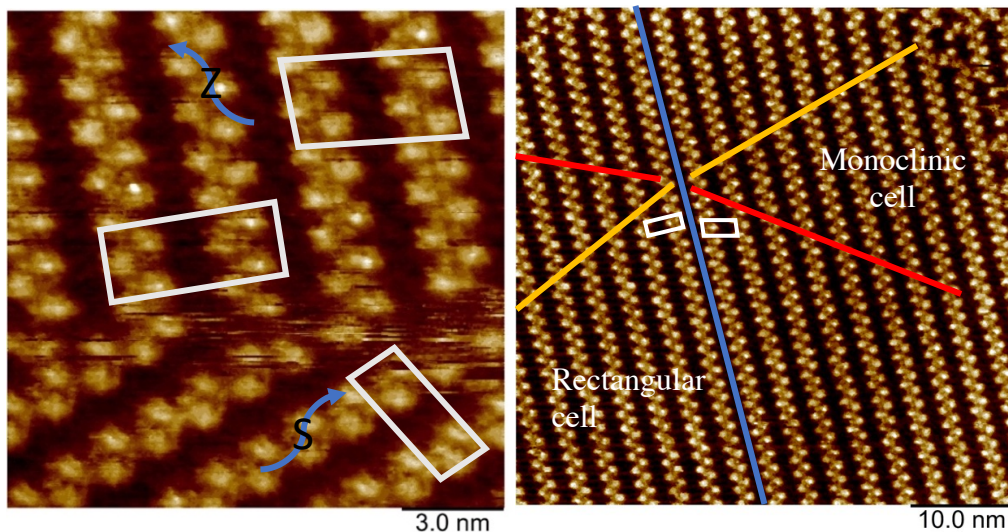


Figure 150: STM images showing the two enantiomers (S and Z) and the two unit cells (rectangular and monoclinic cell) present for M13. Blue line on the right image shows the change in unit cell.

#### 4.3.4 Pd dimer

Pd(II) porphyrin dimers were assembled at the solid-liquid interface, with Ni(II) as the linking metal ion (Figure 151). The same technique was used as for the Ni dimer for the dimerisation process. The Pd dimers produced optimal images with even the ability to clearly see the alkyl chains, which is unusual as there is very limited electron density here and hence tunnelling is minimal at these positions. The fact that the chains can be seen, demonstrates that these dimers are exceedingly planar and good interactions are able to occur with the surface in this system. The unit cell parameters shown in Table 35 are very similar to that of the Ni dimer, demonstrating that the assembly on the surface is very similar. The discrepancies between the two dimer assemblies can be seen by looking at the STM images themselves, with the Pd porphyrin being more planar than the Ni dimer as the luminosity is homogeneous for the entire porphyrin moiety.

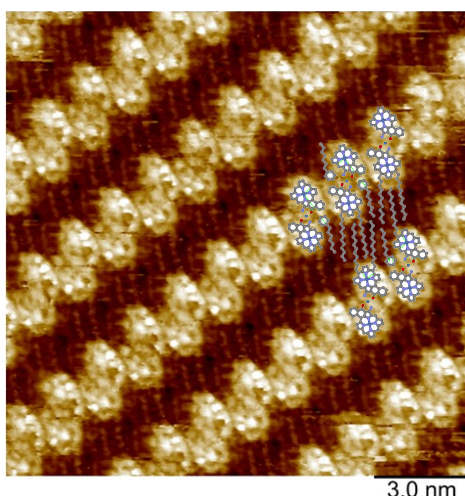


Figure 151: STM images showing the Pd dimer at 15 nm.  $I = 6 \text{ pA}$ ,  $V = -650 \text{ mV}$

Table 35: Unit cell parameters for the Pd dimer

	$a$ (nm)	$b$ (nm)	$\gamma$ (°)
STM	$1.77 \pm 0.02$	$3.48 \pm 0.06$	$96.3 \pm 0.7$

#### 4.3.4.1 Pd cis dimer

Interestingly the *cis* dimer was also observed at the solid-liquid interface (Figure 152, left). As discussed in Chapter 3, normally only the *trans* dimer is observed due to the bulky phenyl groups preventing the formation of the *cis* dimer (Figure 104). In this case, with alkyl chains, the dimerisation can also lead to the *cis* product as there is limited steric hindrance provided by alkyl chains; this is demonstrated by the schematic in Figure 152, right. An attempt was made to visualise the *cis* dimers in solution however, sizable  $\pi$ - $\pi$  stacking brought about by the lack of *meso* phenyl groups made interpretation of NMR spectra exceedingly challenging, even when the NMR sample was heated; meaning that no conclusions were able to be drawn. It is hence difficult to say whether in solution there is a dynamic issue between the *cis* and *trans* isomer or between the monomer and  $\pi$ - $\pi$  stacked oligomers.

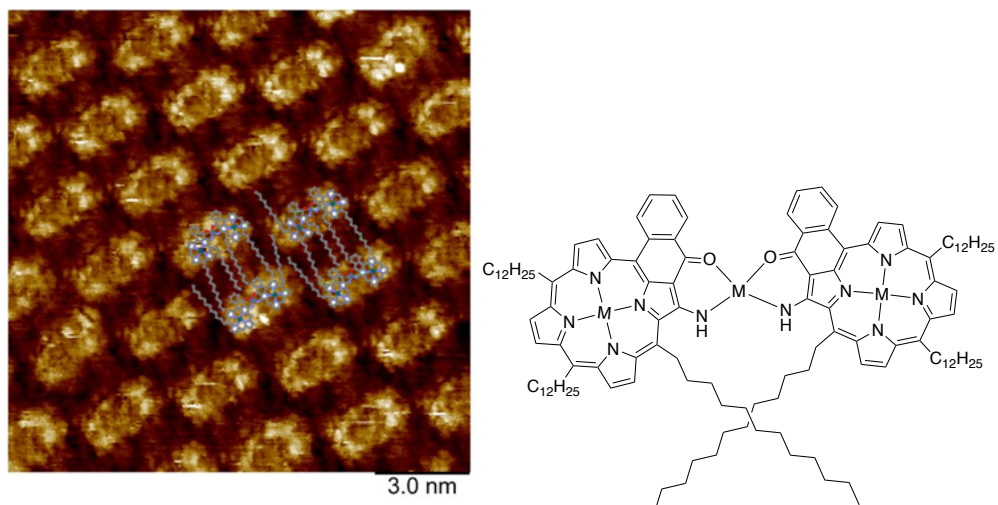


Figure 152: STM images showing the Pd *cis* dimer at 15 nm I: 5 pA, V: -200 mV (left) and schematic representation of the *cis* dimer demonstrating that it would be possible to form the *cis* dimer in solution (right).

Table 36: Unit cell parameters for the Pd *cis* dimer

	$a$ (nm)	$b$ (nm)	$\gamma$ (°)
STM	$2.42 \pm 0.03$	$3.14 \pm 0.07$	$107.1 \pm 2.7$

The cell parameters for the *cis* dimer (Table 36) were quite different to the *trans* dimer in terms of cell parameters, with a larger distance between pairs of dimers ( $a$  value). This is apparent by looking

at Figure 152, left. The images were still homogeneous in terms of luminosity demonstrating that the dimers assembled in a planar fashion on the surface and that stacking was not an issue. There were once again two possible arrangements of the chains.

Large scale images allow for the visualisation of both the *cis* and the *trans* form (Figure 153). The two forms have been highlighted in Figure 153 with different coloured circles: blue for *cis* and green for *trans*. The size of the motifs was around 40 nm and surprisingly a large proportion of the image (Figure 153, right) was the *cis* dimer. The *cis* dimer has never been observed in our group for surface chemistry, yet porphyrins with such little steric bulk at the *meso* positions have also never been synthesised. The *cis* form is potentially slightly more stable than the *trans*, judging by the proportion of *cis* to *trans* on the surface.

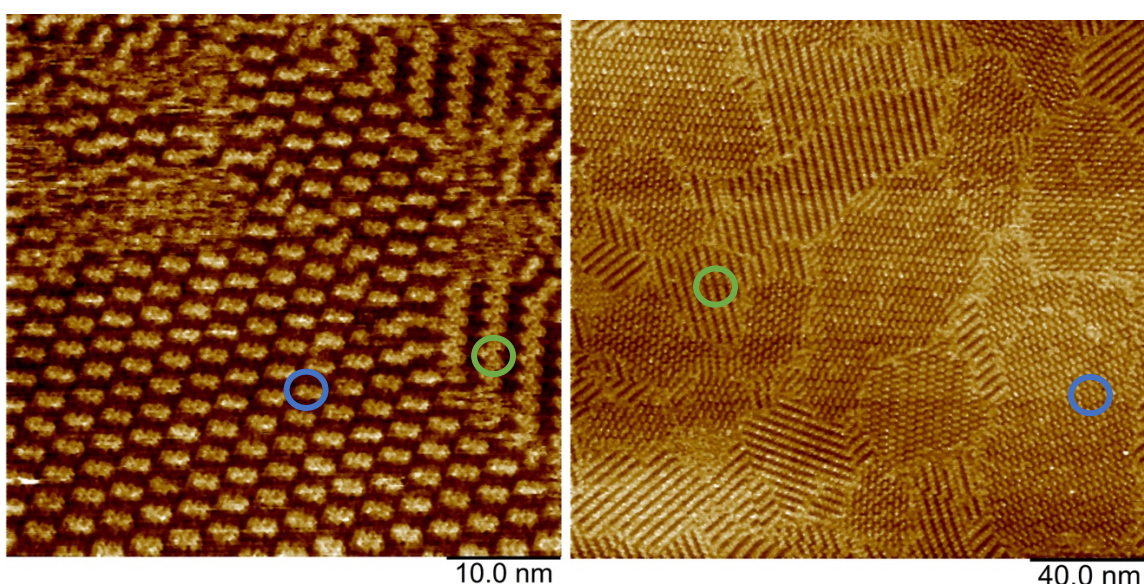


Figure 153: STM images showing the Pd dimer at 50 nm (left) and 200 nm (right). The *cis* form is highlighted in blue and the *trans* form in green.

To summarise, the assembly of porphyrin dimers onto the surface was highly efficient with large single motifs observed for the porphyrin monomers, especially Ni. On formation of the dimer, the porphyrin also assembled in a homogeneous fashion with a smaller motif being observed for the dimers on account of the two types of unit cells that could assemble onto the surface (monoclinic and rectangular). A more planar porphyrin was observed when Pd(II) was placed at the internal coordination site. This was evident by the homogenous light distribution and the observation of the chains on the surface. *Cis* and *trans* dimers were observed for the Pd dimer. This is a new find in our group and demonstrated a new assembly of porphyrin dimers. The system has hence been optimised by changing the substitution at the *meso* positions from 4-alkylphenyl to alkyl substituents. This

optimisation can be justified as the alkyl groups will be directly in contact with the surface and there is no orthogonal phenyl group, consequently a maximum  $\pi$ - $\pi$  interaction can occur between the porphyrin and the HOPG surface.

#### 4.4 Towards porphyrin nano-ribbons

Having successfully assembled porphyrin monomers and dimers at the solid-liquid interface, the next step was to assemble oligomers or so-called nano-ribbons. This could be done by synthesising a porphyrin with two external coordination sites for a metal ion. The synthesis is exactly the same as for the porphyrin with one external coordination site, with minor nuances to synthesise the  $A_2B_2$  porphyrins (Figure 154).<sup>11</sup>

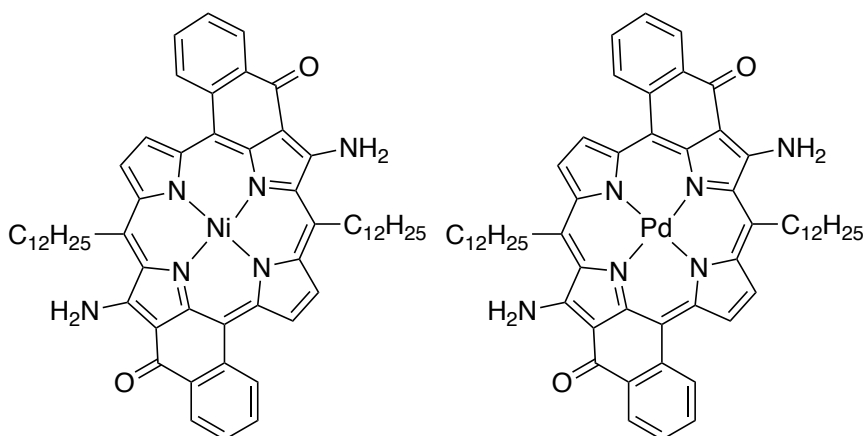


Figure 154: Two monomers with two external coordination sites for the assembly of porphyrin nano-ribbons at the solid-liquid interface

The two above  $A_2B_2$  porphyrins were synthesised with the hope of self-assembling porphyrin nano-ribbons onto the HOPG surface. Unfortunately, after multiple attempts to assemble both the monomer and the supposed oligomer onto the surface, no images were able to be collected. It is hypothesised that it is more favourable for the porphyrin to undergo  $\pi$ - $\pi$  stacking with itself rather than self-assembling onto the surface. The subtraction of one alkyl chain would diminish the potential interactions with the surface and may hinder the above porphyrin's ability to self-assemble onto a HOPG surface; additionally, two enaminoketone sites would favour  $\pi$ - $\pi$  stacking. The additional alkyl chain present in the  $A_3B$  porphyrin most likely prevented such substantial  $\pi$ - $\pi$  stacking. This result is however disappointing as porphyrin nano-ribbons have already been self-assembled onto the surface in our group.<sup>12</sup> This porphyrin had phenyl groups and  $C_{18}$  chains which would have disfavoured  $\pi$ - $\pi$  stacking and the longer alkyl chain will have led to increased interaction with the surface. This is most likely the reason why self-assembly was able to occur for these porphyrins and not for those shown in Figure 154.

Consequently, a new system design was developed in order to assemble nano-ribbons. The new system design (shown in Figure 155) had two external coordination sites for a metal ion, yet three alkyl chains still remained for potential interactions with the surface. This therefore should overcome the factors that impeded the self-assembly of the porphyrins in Figure 154.

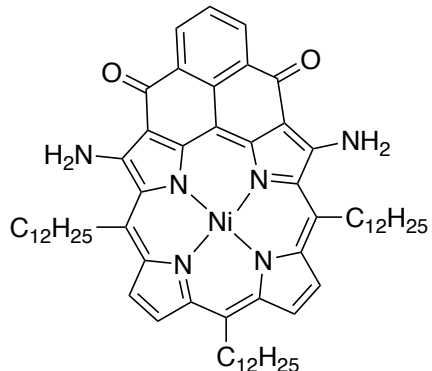


Figure 155: New design for the assembly of porphyrin nano-ribbons

The porphyrin in Figure 155 has not yet been synthesised, as it was decided that the properties would be studied in solution before moving onto surface studies. The A<sub>2</sub>BC porphyrin in Figure 156 was synthesised to study the solution chemistry. Four R groups were tested for this synthesis, only 3,5-di-*tert*-butylphenyl led to the desired product. The <sup>n</sup>Bu and 2,6-dimethyl-4-*tert*-butyl R groups led solely to the monocyclised product and the cyclisation with the paraethoxy group failed to cyclise at all. The dicyclisation of an A<sub>3</sub>B porphyrin has already been described in our group<sup>13</sup> and this was the basis for the synthetic procedure employed, yet with this being an A<sub>2</sub>BC porphyrin, changes had to be made to the published procedure.

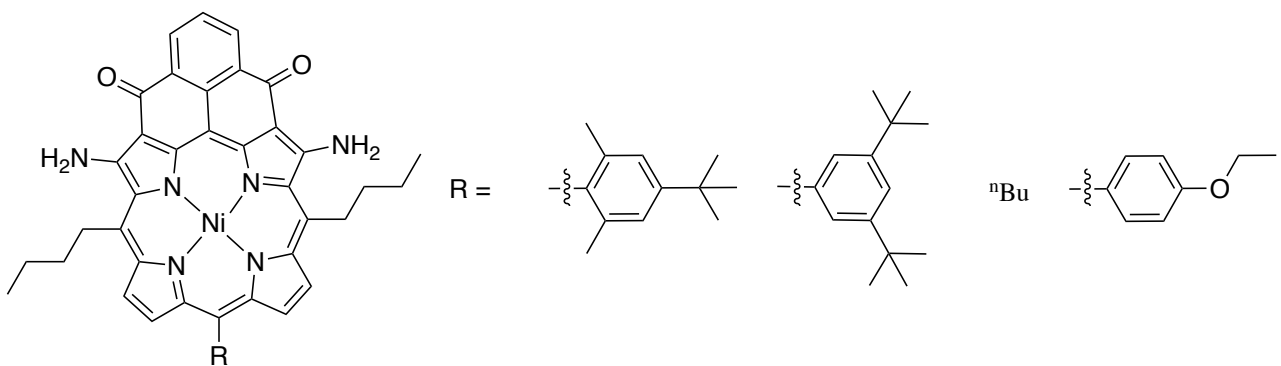


Figure 156: A<sub>2</sub>BC porphyrin for solution studies

The synthesis of **M14** (Figure 157) was carried out in a statistical manner from the n-butyl DPM and the two appropriate aldehydes. Only the synthesis with 3,5-di-*tert*-butyl aldehyde will be discussed in detail as this was the only one that led to the final product. The synthesis of this porphyrin was not obvious and different synthetic pathways were tested in order to optimise this process.

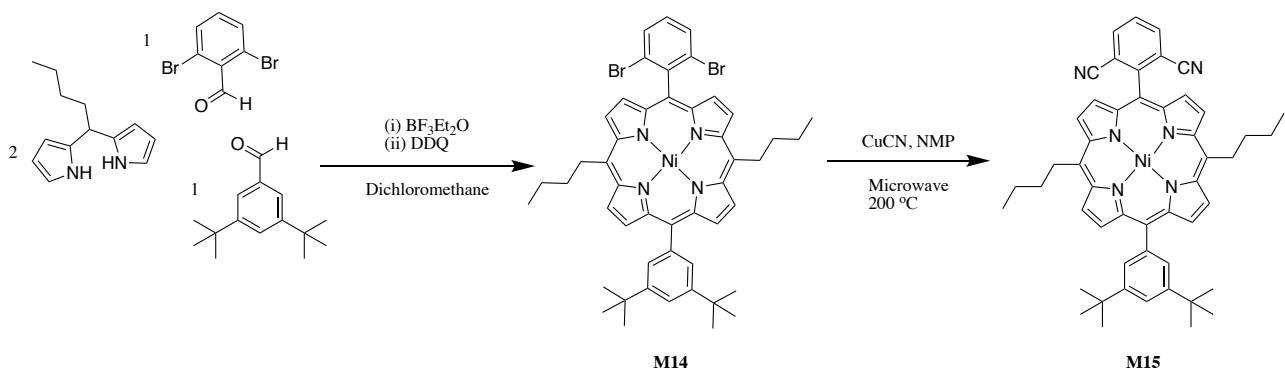


Figure 157:  $\text{A}_2\text{BC}$  porphyrin synthesis of **M14** and **M15**

The complexity of an  $\text{A}_2\text{BC}$  porphyrin synthesis meant that DPM was used instead of pyrrole, in an attempt to favour the formation of the desired product. The synthesis of the DPM was optimised by using trifluoroacetic acid (TFA).<sup>14</sup> Alternative Lewis acid sources were also attempted but led to lower yields;  $\text{InCl}_3$  for example. TFA led to the formation of the dipyrromethene in a 44% yield. The porphyrin synthesis, **M14**, was optimised to 4% yield, which for an  $\text{A}_2\text{BC}$  porphyrin is an acceptable yield, considering all the possible arrangements of meso groups:  $\text{A}_2\text{B}_2$ ,  $\text{A}_2\text{C}_2$ ,  $\text{A}_3\text{B}$ , etc.; without optimising reaction parameters, the yield was 1%.

The Rosenmund-von Braun reaction,<sup>15,16</sup> used to convert the Br to a CN and form **M15**, in Figure 157, was also optimised. The reaction was initially attempted using the free-base porphyrin instead of the Ni porphyrin. The porphyrin was instantaneously metallated with Cu(II), (apparent from a notable colour change) but this did not improve the yield of the reaction and simply led to a more tedious purification with paramagnetic porphyrins. Chlorine was used instead of bromine, (as 2,6-dichlorobenzaldehyde is considerably cheaper than the 2,6-dibromobenzaldehyde) however this led to a mixture of monocyanated and dicyanated products. Bromine proved to be a suitable alternative with only the formation of the dicyanated product in a much higher yield. The initial reaction parameters were to heat the porphyrin in  $\text{N}$ -methyl-2-pyrrolidone (NMP) for 4 days at  $200\text{ }^\circ\text{C}$ ; the high temperature and duration of heating led to decomposition of the porphyrin. A microwave proved to be a better choice, and simply heating the porphyrin in NMP at  $200\text{ }^\circ\text{C}$  for 5 and a half hours led to a higher yielding and an easier work-up process.

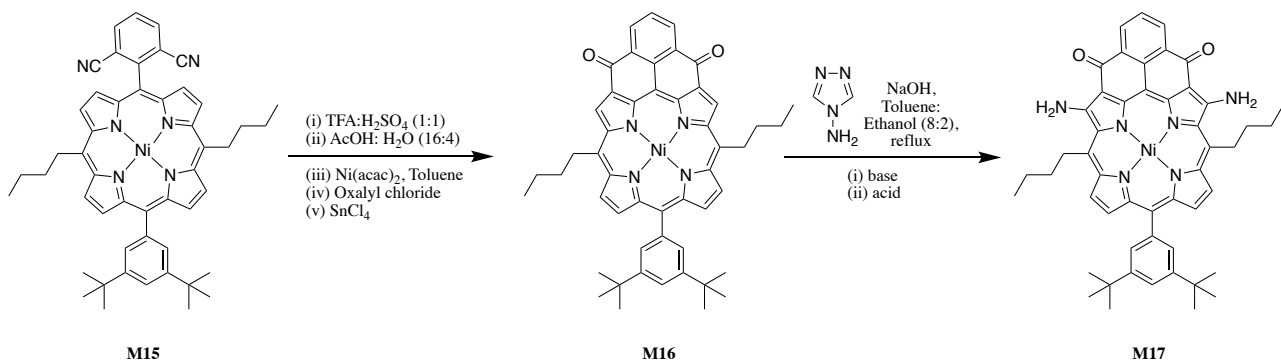


Figure 158: *A<sub>2</sub>BC* porphyrin synthesis of **M16** and **M17**

The cyano groups of **M16** (Figure 158) were then hydrolysed in harsh conditions (TFA/H<sub>2</sub>SO<sub>4</sub>); these acidic conditions also led to the demetallation of the porphyrin. The carboxylic acid groups of the remetallated Ni porphyrin were converted into acyl chloride groups and addition of SnCl<sub>4</sub> led to the cyclised product *via* an intramolecular Friedel-Craft reaction. It was this step that proved the most problematic, with the three other R groups failing at this step. The other three R groups had fundamental issues at the cyclisation step and led to a mixture of non-cyclised and monocyclised products. The n-butyl group most likely had issues due to  $\pi$ - $\pi$  interactions and the paraethoxyphenyl had solubility issues when two carboxylic acids were present. The reasons for the failure to cyclise with the 2,6-dimethyl-4-*tert*-butyl substituent is less apparent, but with the only difference between this group and 3,5-di-*tert*-butylphenyl being additional steric bulk at the porphyrin core, potentially this was the issue for this specific case. The diketo porphyrin **M16** could then be diaminated leading to the final product **M17**. A crystal structure of the ketoporphyrin was obtained from slow diffusion of methanol into a solution of the porphyrin in chlorobenzene (Figure 159).

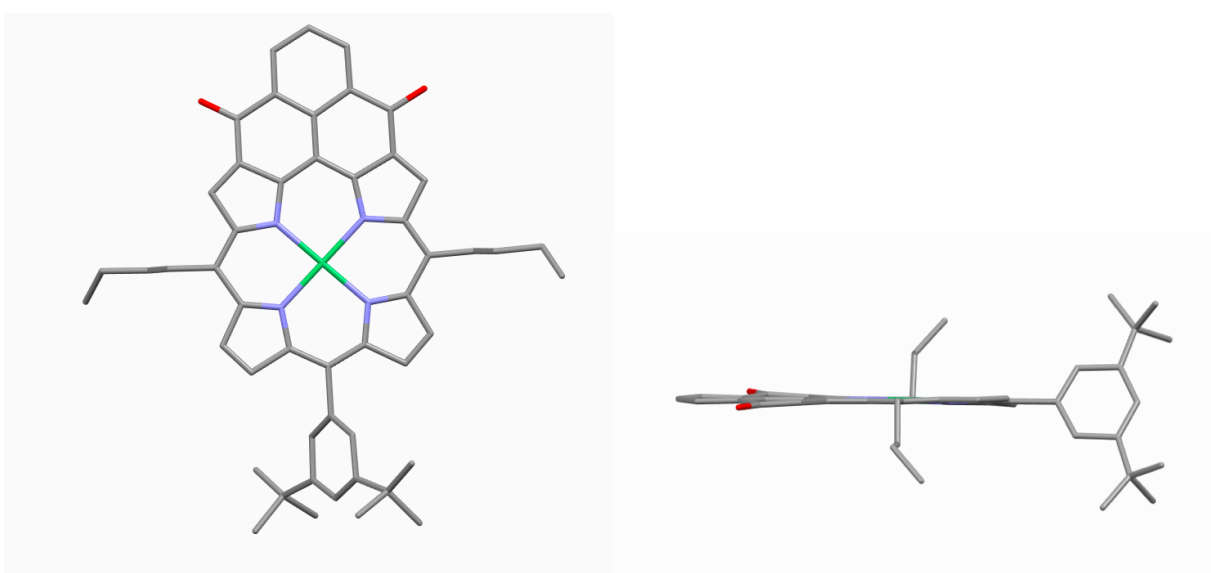


Figure 159: Two representations of the crystal structure of **M16**

The crystal structure shows an exceedingly planar porphyrin with the phenyl groups perpendicular to the plane of the porphyrin. It is rare to find planar nickel(II) porphyrins, as normally they are ruffled; the rigidity imposed by the double cyclisation most likely led to this planar porphyrin. Looking at the unit cell for the porphyrin (Figure 160), an alternate arrangement of the porphyrins was observed in order for  $\pi$ - $\pi$  stacking to occur with minimal steric interactions between the phenyl groups, with a 3.4 Å distance between two porphyrins.

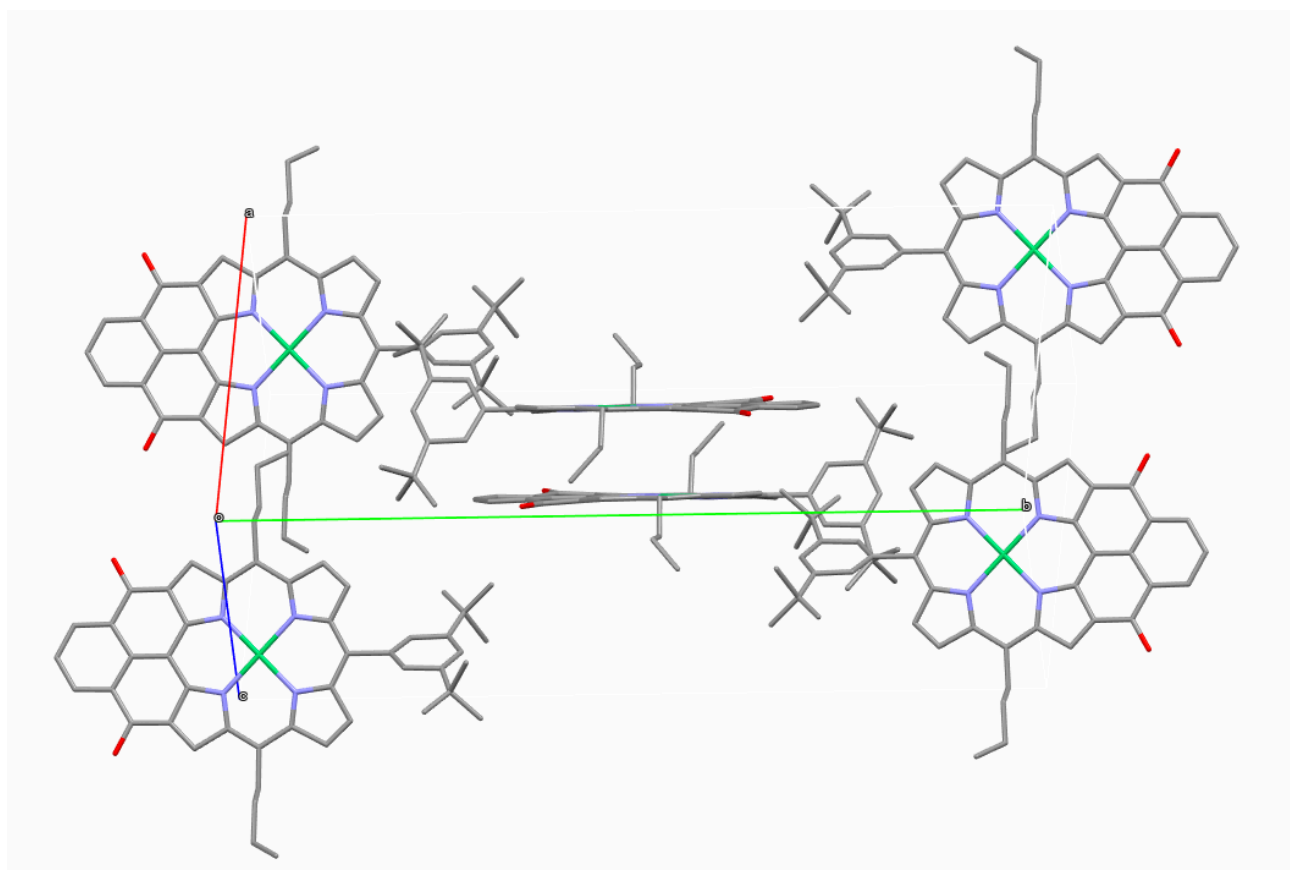


Figure 160: Unit cell of M16

#### 4.5 Conclusions and perspectives

After the optimisation of the synthesis of the A<sub>2</sub>BC porphyrin, this is where this project ends, for the time being. However, the synthesis is now a lot more feasible on optimisation. The next steps would be to study the coordination geometry in solution and the assembly of dimers and trimers and then to progress onto surface studies. Another interesting point about the above molecule is the fact that *cis* and *trans* configuration can be formed on addition of a linking metal ion. The addition of n-butyl at the *meso* positions was a choice made in order to favour the *cis* formation, as the coordination geometry could potentially lead to an interesting supramolecular architecture as shown in Figure 161. The internal metal would most likely be Ni, the external metal would be palladium and

enaminothioketone would be chosen for the external coordination site as this would make the coordination bond more inert and help favour the *cis* form. On formation of the supramolecular complex in Figure 161, the electronic and magnetic properties could then be determined by forming a radical cation. With the d-orbitals leading to communication between the porphyrin moieties, the radical cation should be delocalised around the ring. This phenomenon has already been elegantly shown by Anderson's group with his supramolecular porphyrin ring<sup>17</sup> and the ring has been assembled on the surface and the core of the ring has been used for Ullmann reactions.<sup>18</sup> Osuka also synthesised a nanotube with a phenyl linking moiety where the porphyrins were able to communicate.

The synthesis unfortunately could not be carried out in the timeframe of the PhD, especially when the project was envisaged in the latter stages of the PhD. This project came about as the A<sub>2</sub>B<sub>2</sub> porphyrins (Figure 154) failed to form nano-ribbons during surface studies, most likely on account of more preferential  $\pi$ - $\pi$  interactions. This led to a new system design of the A<sub>2</sub>BC porphyrin.

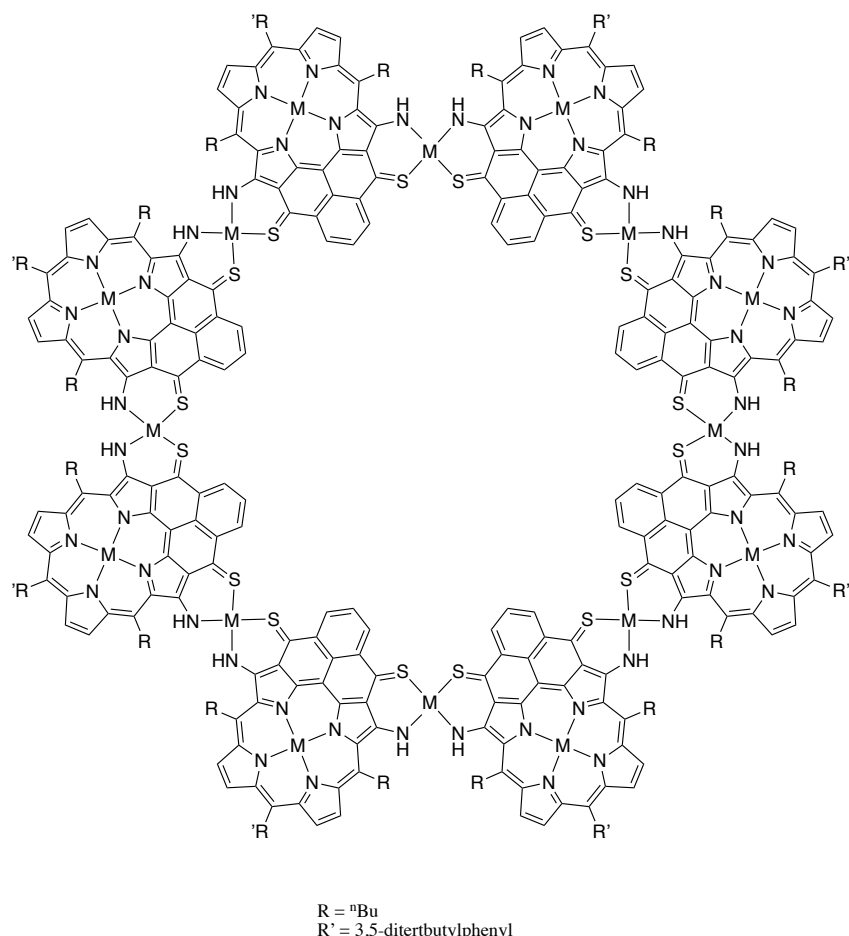


Figure 161: Proposed supramolecular porphyrin circle

## 4.6 General conclusions

To conclude the second part of this PhD, the synthesis of porphyrin dimers and the study of their electronic and magnetic properties and their assembly at the solid-liquid interface has been carried out. Porphyrins were synthesised with an internal and external coordination site for coordination of a metal ion. Good electronic communication was observed between the porphyrin moieties and this communication was amplified on passing from 3d to 4d to 5d linking metal ions and when softer coordination sites were employed, switching from a ketone to a thioketone. The electronic communication was evaluated by electronic studies (electronic spectroscopy and cyclic voltammetry). A larger bathochromic shift was observed as the electronic communication increased by the aforementioned methods and the splitting in the first oxidation wave of the cyclic voltammograms was the largest observed in our group and comparable to the largest splitting found in the literature. This demonstrates that a linking metal ion is just as efficient as an organic linker in order to achieve good communication between porphyrin moieties. DFT calculations were used to confirm this electronic communication and it was found that the HOMO was able to have an electronic communication on account of the  $d\pi/\pi$  nature of this orbital. The application of coordination chemistry to synthesise porphyrin dimers led to a simplified synthesis compared to the coupling reaction necessary to link porphyrins with carbon-carbon bonds. The synthesis is also usually higher yielding and leads to easier purification processes *via* column chromatography, with larger differences in  $R_f$  values between the starting materials and the final product, for the majority of cases, *cf.* their organic counterparts.

The metal ions chosen were both diamagnetic and paramagnetic and consequently the magnetic communication between paramagnetic sites was determined. Strong communication was observed between the paramagnetic sites when all three of the metal ions were paramagnetic. A weak yet significant communication was observed when the linking metal ion was diamagnetic. This weak communication led to the pursuit of applications for qubits in quantum computing. Initial findings for this project appear to show that these porphyrins could be used for such applications with a nutation being observed at room temperature. This is not a common property for paramagnetic species for qubits and demonstrates that the vanadyl porphyrin series could be optimal for use as qubits. The availability of an  $A_2B_2$  porphyrin could be used to synthesise porphyrin trimers with vanadyl(IV) at the internal metal coordination site and Pd(II) at the external metal coordination site. The magnetic communication for the trimer could be determined and potentially a 3-qubit system could be developed. The ability to increase the size of the porphyrin is an exceedingly sought-after property and demonstrates the efficiency of the system design developed in our group.

Finally, a slightly different porphyrin system with long alkyl chains at the *meso* positions was self-assembled at a solid-liquid interface and the motifs were observed by STM. Monomers were able to be assembled and they produced large single motifs demonstrating the efficiency of the self-assembly in such porphyrin systems. Motifs as large as 480 nm were even observed demonstrating that these porphyrins present the necessary properties for optimal surface studies. The external coordination site was once again exploited to form dimers, this time at the solid-liquid interface, which displayed smaller motifs on account of the different conformers that could form at the solid-liquid interface. The conformers were exceedingly planar and the images obtained were of high quality demonstrating the efficiency of the porphyrin to undergo self-assembly. A new project to pursue, could be to replace the Ni(II) with Cu(II) and see how changing the linking metal ion affected the self-assembly at the solid-liquid interface.

As the A<sub>2</sub>B<sub>2</sub> porphyrins failed to self-assemble at the HOPG-phenyloctane interface, the A<sub>2</sub>BC porphyrin was developed and the synthesis of this porphyrin monomer was optimised. Now that the porphyrin monomer is relatively accessible, this paves the way for solution studies of this large aromatic motif. It would be expected that porphyrin moieties would be able to communicate electronically and magnetically (as seen in Chapter 3) and this should be the next objective for this project. Once a greater understanding of the solutions chemistry has been ascertained, surface studies should then be carried out in the hope that supramolecular arrays would also be able to form.

On a personal note, this PhD has been exceedingly multi-disciplinary and I have been able to gain knowledge in a vast area of different fields of Chemistry and I am forever grateful to my PhD supervisors for having granted me the freedom to be able to perform all the analysis (DFT calculations, EPR studies and STM studies) myself.

## 4.7 References

- 1 R. Gutzler, L. Cardenas and F. Rosei, *Chem. Sci.*, 2011, **2**, 2290–2300.
- 2 G. M. Whitesides and B. Grzybowski, *Science*, 2002, **295**, 2418–2421.
- 3 G. Binning, H. Rohrer, C. Gerber and E. Weibel, *Phys. Rev. Lett.*, 1982, **49**, 57–61.
- 4 J. V Barth, G. Costantini and K. Kern, *Nature*, 2005, **437**, 671–679.
- 5 M. A. Carvalho, H. Dekkiche, L. Karmazin, F. Sanchez, B. Vincent, M. Kanesato, Y. Kikkawa and R. Ruppert, *Inorg. Chem.*, 2017, **56**, 15081–15090.
- 6 A. J. Gellman and K. R. Paserba, *J. Phys. Chem. B*, 2002, **106**, 13231–13241.
- 7 F. Lachaud, C. Jeandon, A. Monari, X. Assfeld, M. Beley, R. Ruppert and P. C. Gros, *Dalton Trans.*, 2012, **41**, 12865–12871.
- 8 Y. Wei, K. Kannappan, G. W. Flynn and M. B. Zimmt, *J. Am. Chem. Soc.*, 2004, **126**, 5318–5322.
- 9 A. L. Maclean, G. J. Foran, B. J. Kennedy, P. Turner and T. W. Hambley, *Australian J. Chem.*, 1996, **49**, 1273–1278.
- 10 E. B. Fleischer, C. K. Miller and L. E. Webb, *J. Am. Chem. Soc.*, 1964, **86**, 2342–2347.
- 11 S. Richeter, C. Jeandon, R. Ruppert and H. J. Callot, *Chem. Commun.*, 2002, **2**, 266–267.
- 12 M. A. Carvalho, H. Dekkiche, M. Nagasaki, Y. Kikkawa and R. Ruppert, *J. Am. Chem. Soc.*, 2019, **141**, 10137–10141.
- 13 S. Richeter, C. Jeandon, N. Kyritsakas, R. Ruppert and H. J. Callot, *J. Org. Chem.*, 2003, **68**, 9200–9208.
- 14 C. H. Lee and J. S. Lindsey, *Tetrahedron*, 1994, **50**, 11427–11440.
- 15 K. W. Rosenmund and E. Struck, *Ber. Dtsch. Chem. Ges.*, 1919, **52**, 1749.
- 16 J. von Braun and G. Manz, *Liebigs Ann. Chem.*, 1931, **488**, 111–126.
- 17 M. D. Peeks, C. E. Tait, P. Neuhaus, G. M. Fischer, M. Hoffmann, R. Haver, A. Cnossen, J. R. Harmer, C. R. Timmel and H. L. Anderson, *J. Am. Chem. Soc.*, 2017, **139**, 10461–10471.
- 18 C. J. Judd, D. V. Kondratuk, H. L. Anderson and A. Saywell, *Sci. Rep.*, 2019, 11676–11688.

## Résumé en français.

Cette thèse a été co-dirigée par Sylvie CHOUA et Romain RUPPERT, dans le cadre d'une collaboration entre les équipes POMAM et CLAC de l'UMR 7177 du CNRS. Cette thèse a été financée par une bourse de l'Ecole Doctorale 182 (Physique et Chimie-Physique). Les aspects multidisciplinaires développés au cours de cette thèse recouvrent des domaines variés en chimie et chimie-physique.

Deux grandes thématiques ont été abordées au cours de cette thèse.

Dans le premier projet, la synthèse de ligands phénanthroline et de complexes de cuivre(I) stables a été réalisée. Les synthèses de nouveaux ligands phénanthroline très encombrés sur les positions proches du site de coordination ont permis d'obtenir des complexes homo- et hétéro-leptiques de cuivre(I). Dans cette approche, l'importance de la géométrie de coordination de l'état fondamental sur les propriétés photophysiques de ces photosensibilisateurs a été évaluée. Différentes approches ont été utilisées pour déterminer les propriétés optiques de ces photosensibilisateurs : l'électrochimie, la spectroscopie électronique, la fluorescence, la diffraction des rayons X et les calculs DFT.

Dans le second projet, la synthèse de nouveaux dimères de porphyrines reliées par des cations métalliques a été réalisée. Les propriétés électroniques et magnétiques de ces dimères ont été comparées aux propriétés des porphyrines monomères. Des études électrochimiques, de spectroscopie électronique et de résonance paramagnétique électronique (RPE) ont permis de mettre en évidence les facteurs influençant l'ampleur de la communication électronique et/ou magnétique entre les sous-unités dans ces dimères. Dans le but de démontrer les possibles applications de ces nouvelles molécules dans le domaine des qubits, des études RPE plus poussées ont été réalisées en RPE pulsé. Finalement, plusieurs porphyrines monomères et dimères comportant des chaînes alkyles ont été auto-assemblées à l'interface solide/liquide et ont conduit à des structures régulières de très grandes dimensions qui ont été visualisées à l'aide de techniques STM (Scanning Tunneling Microscopy – microscope à effet tunnel).

## Projet 1 : Complexes de cuivre(I)

La chimie de fonctionnalisation des ligands phénanthroline et notamment sur les positions adjacentes aux atomes d'azote a été très étudiée depuis les années 1980.<sup>1</sup> En introduisant des groupements aromatiques sur ce ligand phénanthroline, il a été possible de préparer des complexes homoleptiques de cuivre(I) qui présentaient des durées de vie de l'état excité très longues.<sup>2</sup> L'importance de l'encombrement stérique autour du cation cuivre(I), notamment pour atteindre une géométrie de coordination parfaitement tétraédrique, a permis d'obtenir des durées de vie supérieures à la microseconde. Cependant, ces complexes très encombrés se sont avérés peu stables en présence de solvants polaires.<sup>3</sup> En augmentant encore l'encombrement stérique, seuls les complexes hétéroleptiques ont pu être préparés.<sup>4</sup>

En variant les conditions expérimentales lors de l'introduction de groupements aryles très encombrés sur les positions 2 ou 9 du ligand phénanthroline par addition d'aryllithiens, trois nouveaux ligands ont pu être isolés (cf Figure RésFr 1). Alors que les ligands **L1** et **L2** sont des produits classiques de telles réactions, le ligand **L3**, isolé avec 56% de rendement et présentant une fonctionnalisation sur les positions 2 et 7, n'était pas attendu. La structure du ligand a été confirmée en préparant le complexe de cuivre(I) comportant deux ligands **L3**.<sup>5</sup> Dans la maille cristalline de ce complexe chiral de cuivre(I), un seul des deux énantiomères était présent (cf Figure RésFr 2). Cette résolution spontanée d'un complexe de cuivre(I) n'avait été observée que pour une seule structure, celle du fameux noeud trifolié préparé par C.O. Dietrich-Buchecker et J.-P. Sauvage.<sup>6</sup>

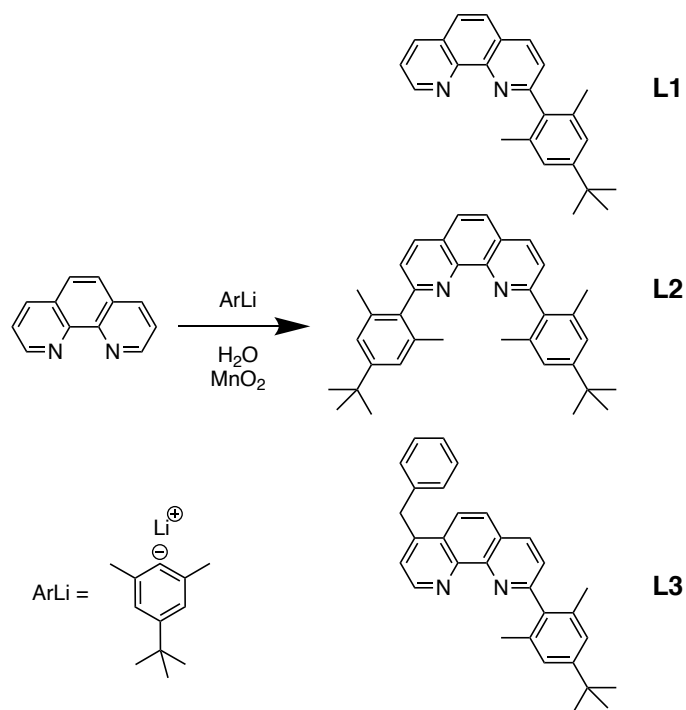


Figure RésFr 1 : Préparation des ligands **L1**, **L2** et **L3**

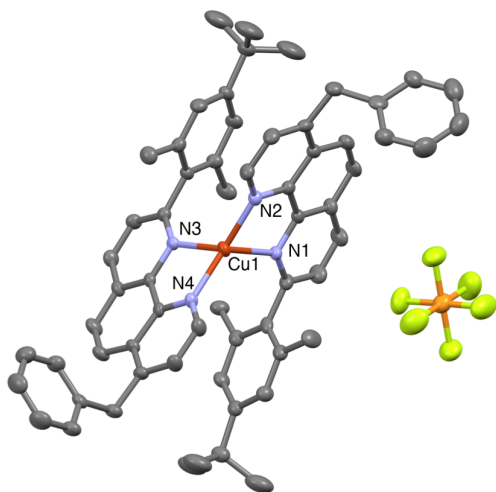


Figure RésFr 2 : Structure aux rayons X du complexe  $\text{Cu}(\text{L3})_2\text{PF}_6$  (les atomes d'hydrogène sont omis)

La synthèse de complexes hétéroleptiques de cuivre(I) possédant une géométrie de coordination tétraédrique quasi-parfaite (*cf.* Figure RésFr 3, à gauche) a été rendu possible par l'introduction de groupements encombrés éloignés du site de coordination qui bloquent les deux ligands lors de la formation du complexe. Cette stratégie a permis l'obtention d'une série de complexes hétéroleptiques de cuivre(I) qui s'avèrent stables en milieux polaires et qui possèdent une géométrie de coordination tétraédrique quasi-parfaite. De nombreuses structures aux rayons X de ces complexes ont permis de rationaliser l'importance d'un encombrement stérique éloigné du site de coordination.

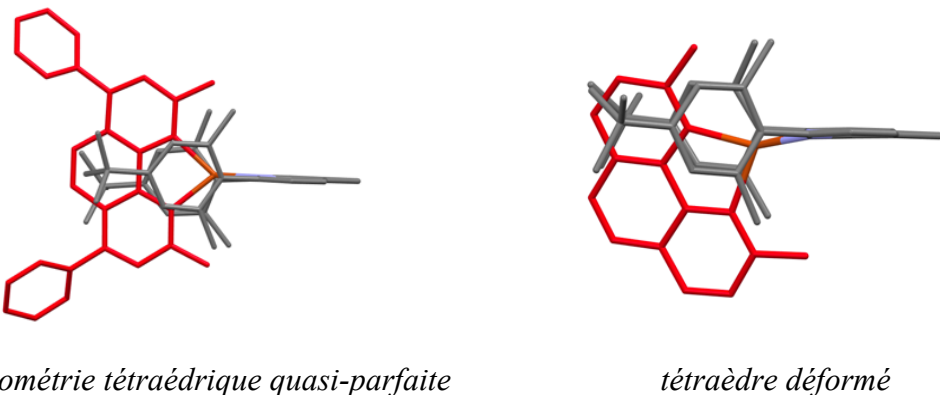


Figure RésFr 3 : Structures aux rayons X de complexes hétéroleptiques de cuivre(I) comportant deux ligands phénanthroline (un ligand **L2** en gris et une autre phénanthroline en rouge). Différences structurales induites par la présence (ou non) de deux groupements aryles sur les positions 4 et 7 d'un des ligands phénanthroline.

Des calculs DFT ont corroboré cette approche et des optimisations de géométrie ont fourni des structures très proches des structures expérimentales. Cependant, ces calculs DFT ont également montré qu'à l'état excité la présence de groupements encombrés proches du site de coordination restait

indispensable pour obtenir des propriétés de fluorescence acceptables. Ceci a été confirmé par la mesure des temps de vie de ces nouveaux complexes de cuivre(I).

Ayant pu démontrer qu'un encombrement stérique éloigné du cuivre(I) permettait d'obtenir des géométries tétraédriques presque parfaites, des complexes homoleptiques de cuivre(I) ont été préparés en utilisant cette approche "remote control". Pour permettre la formation de complexes comportant deux ligands identiques, il a bien évidemment fallu diminuer l'encombrement à proximité du cuivre(I). Deux approches ont été envisagées et sont décrites ci-dessous (Figure RésFR 4). Il faut noter la présence du groupement tertiobutyle sur la position *para* de l'aryle qui devait permettre d'optimiser la géométrie de coordination.

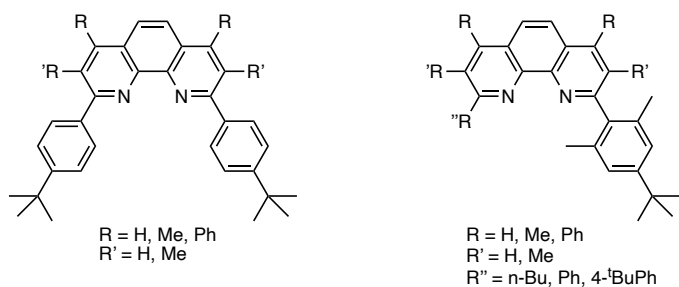


Figure RésFr 4 : Structures des différents ligands phénanthroline préparés pour obtenir des complexes homoleptiques de cuivre(I)

En utilisant ces ligands, des complexes homoleptiques de cuivre(I) symétriques et non-symétriques ont été préparés. Plusieurs structures aux rayons X ont été obtenues et comme précédemment pour les complexes hétéroleptiques, l'encombrement stérique loin du cation central a permis de générer des géométries tétraédriques quasi-parfaites pour les ligands possédant des substituants sur les positions 4 et 7 et des groupements *t*-butylphényle en *ortho* des atomes d'azote. Deux exemples de complexes de cuivre(I) sont représentés ci-après. Dans le premier cas, le ligand symétrique ne comporte aucun substituant sur les positions 3, 4, 7 et 8 (cf Figure RésFr5,  $R = R' = H$ ). Par contre, dans le deuxième exemple présenté, le ligand comporte quatre groupements méthyle sur les positions 3, 4, 7 et 8 (cf Figure RésFr 6,  $R = R' = Me$ ). On remarque que le deuxième complexe présente une géométrie tétraédrique quasi-parfaite contrairement au premier qui est déformé.

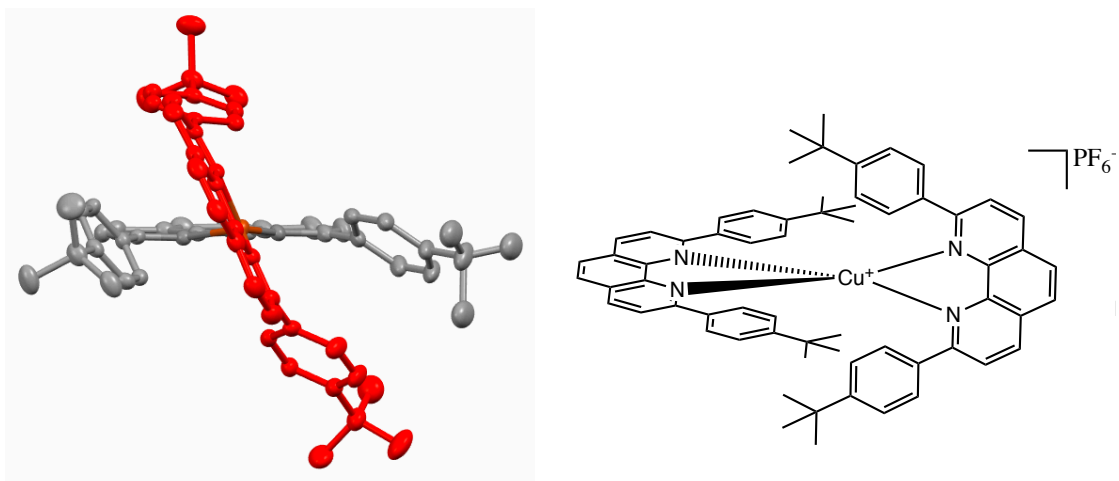


Figure RésFr 5 : Structure aux rayons X d'un complexe de cuivre(I) **C11** sans encombrement à l'arrière des ligands phénanthroline

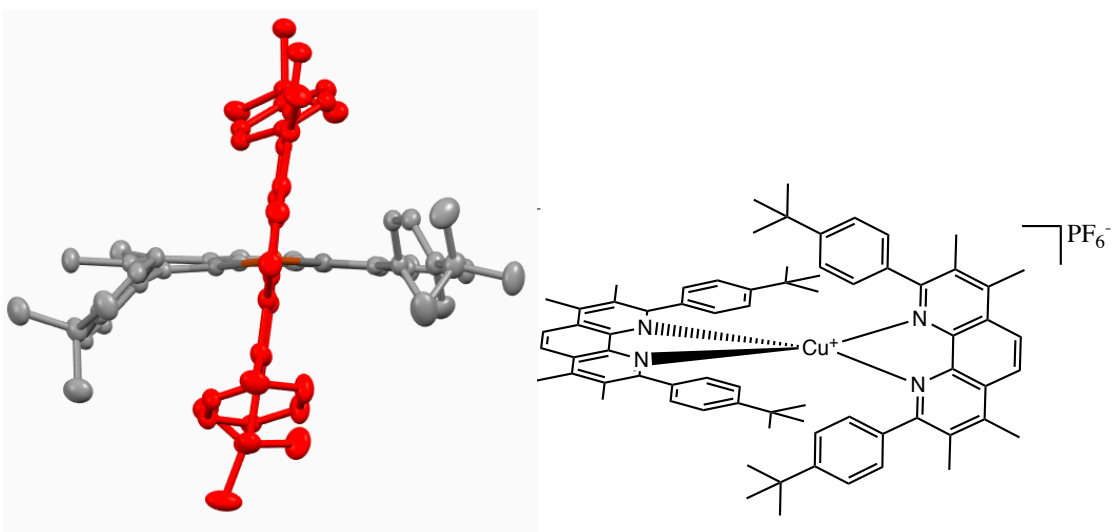


Figure RésFr 6 : Structure aux rayons X d'un complexe de cuivre(I) **C13** préparé avec des ligands phénanthroline comportant quatre substituants méthyle sur les positions 3, 4, 7 et 8

Les propriétés de ces complexes ont été étudiées par électrochimie, spectroscopie électronique d'absorption et d'émission et ces résultats expérimentaux corroborés par des calculs DFT. Les durées de vie de la plupart de ces complexes se sont avérées relativement faibles, à l'exception d'un ou deux complexes symétriques, dont les durées de vie de l'état excité étaient supérieures à celle d'un complexe de cuivre(I) de référence ( $\text{Cu}(\text{diphenylphenanthroline})_2\text{PF}_6$ ). Ces données sont résumées ci-après (Tableau RésFr1).

Tableau RésFr1 : Sommaire des durées de vie des complexes de  $Cu(dpp)_2PF_6$ , **C11** et **C12**

Complexe	Temps de vie (ns)	Emission
$Cu(dpp)_2PF_6$	162 ns	
<b>C11</b>	219 ns	689
<b>C13</b>	326 ns	685

En conclusion, cette étude a permis de mettre en évidence un facteur stérique qui influence très fortement la géométrie de coordination de complexes de cuivre(I). Contrairement aux études décrites essayant de modifier et d'optimiser l'encombrement à proximité du site de coordination, cette approche qu'on pourrait qualifier de "remote steric control" permet d'obtenir des géométries de coordination tétraédriques quasi-parfaites. Cependant il s'avère que les durées de vie mesurées pour ces complexes sont restés modestes.

## Projet 2 : Etude de dimères porphyriniques

### Etude RPE

Les porphyrines sont présentes dans les systèmes naturels et leurs propriétés exceptionnelles ont été exploitées par les chimistes depuis des décennies. Dans notre équipe, des porphyrines comportant un site de coordination interne et externe (cf. Figure RésFr 7) ont été préparées et permettant d'obtenir des dimères (ou des oligomères) connectés par des ions métalliques.<sup>7</sup> Des interactions électroniques et magnétiques entre les sous-unités ont été mis en évidence.<sup>8,9</sup> Des auto-assemblages de ces porphyrines à l'interface solide/liquide ont également été décrits.<sup>10</sup>

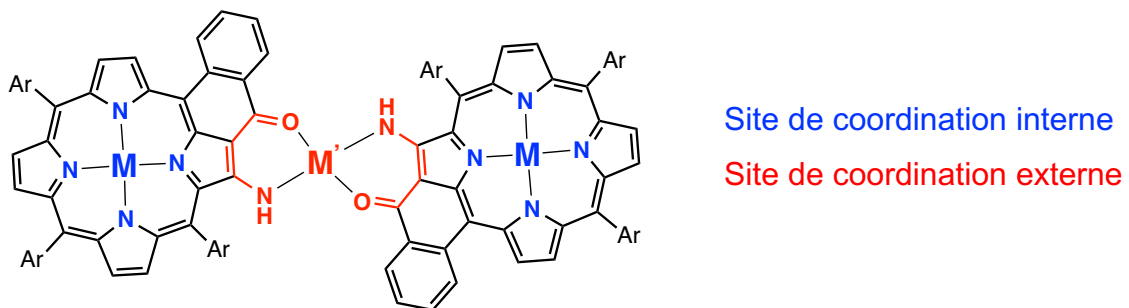


Figure RésFr 7 : Porphyrines comportant deux sites de coordination (interne et externe) et dimères assemblés à l'aide de cations métalliques

La plupart des dimères et/ou oligomères de porphyrines préparés précédemment au laboratoire comportait des cations métalliques diamagnétiques. Dans cette étude, des vanadylporphyrines ont été préparées et étudiées par spectroscopie électronique, électrochimie et résonance paramagnétique électronique (RPE). La synthèse de ces composés est décrite ci-après (cf Figure RésFr 8).

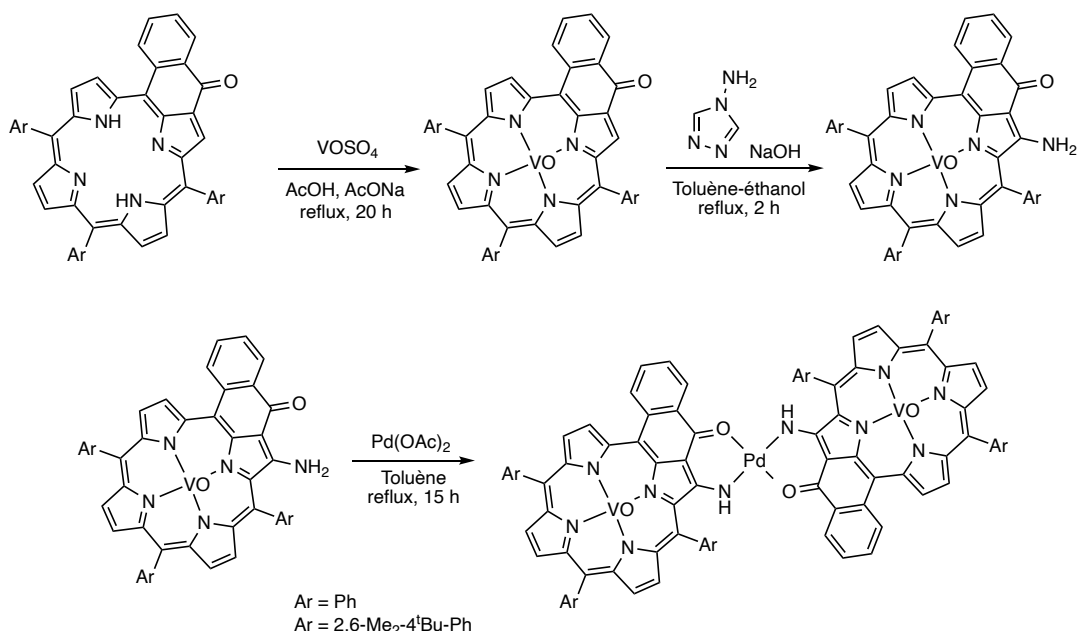


Figure RésFr 8 : Synthèse de dimères de vanadylporphyrines.

Ces nouveaux composés ont pu être caractérisés par des structures aux rayons X, ce qui donne accès à des paramètres géométriques très précis, utiles pour des simulations de spectres RPE. Ci-dessous sont représentés les structures RX d'une vanadylporphyrine et d'un dimère comportant deux vanadylporphyrines connectées par un ion palladium(II) (cf. Figure RésFr 9 et 10).

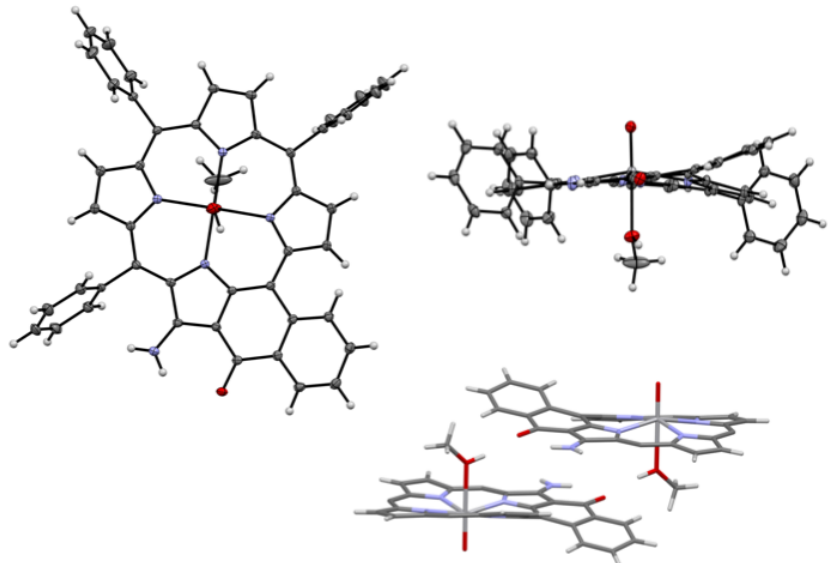


Figure RésFr 9 : Structure aux rayons X d'une vanadylporphyrine. Il faut noter la présence d'un ligand apical méthanol supplémentaire (seul exemple connu de vanadylporphyrine hexacoordinée) et la formation de paires assemblées par liaison hydrogène à l'état solide.

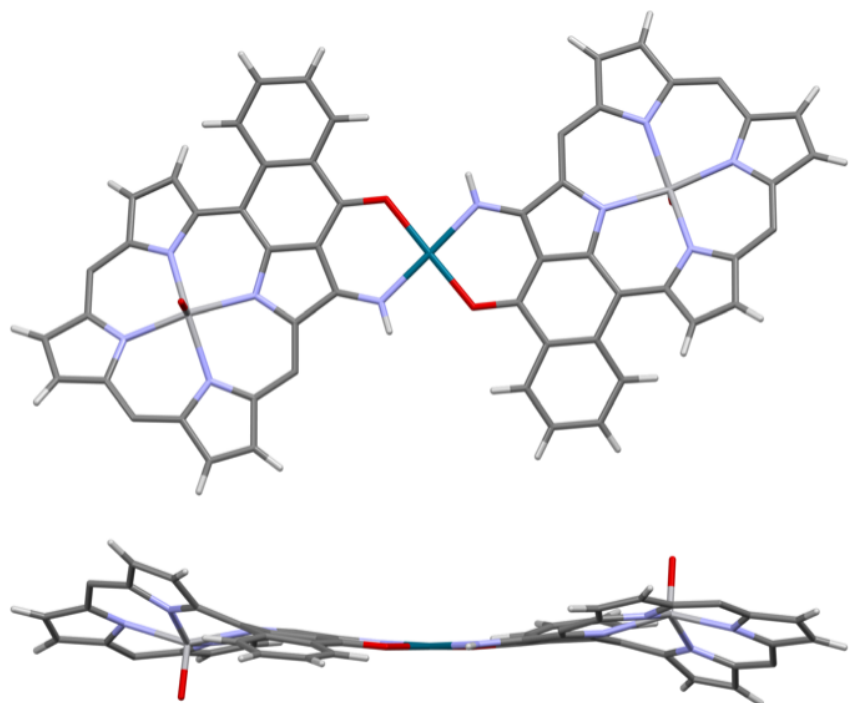


Figure RésFr 10 : Structure aux rayons X d'un dimère de vanadylporphyrines connectées par un ion palladium(II). Trois substituants phényle meso sont omis. Le produit majoritaire isolé lors de la synthèse est l'isomère trans (autour du palladium(II)) et  $\alpha, \beta$  pour l'orientation des deux vanadyles.

La communication électronique entre les deux porphyrines des dimères a été démontrée par spectroscopie électronique et la présence d'interactions faibles entre les sites paramagnétiques par des études RPE (*cf.* Figure RésFr 11 et 12). La nature de l'ion métallique connecteur influe fortement sur le degré de communication électronique, avec un effet plus important en descendant une colonne du tableau périodique ( $5d > 4d > 3d$ , Pt > Pd > Ni). Des ions paramagnétiques connecteurs auront un rôle additionnel de relais et ceci conduit à des couplages antiferromagnétiques importants.

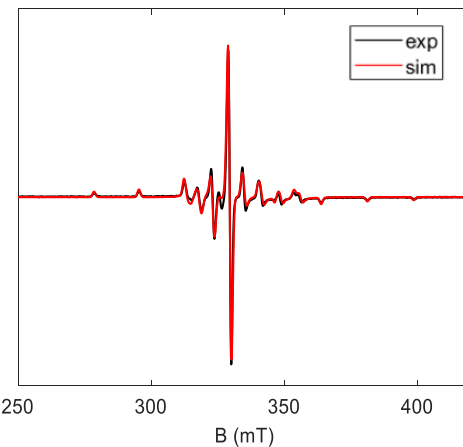


Figure RésFr 11 : Spectre RPE de la vanadylporphyrine à 16 K

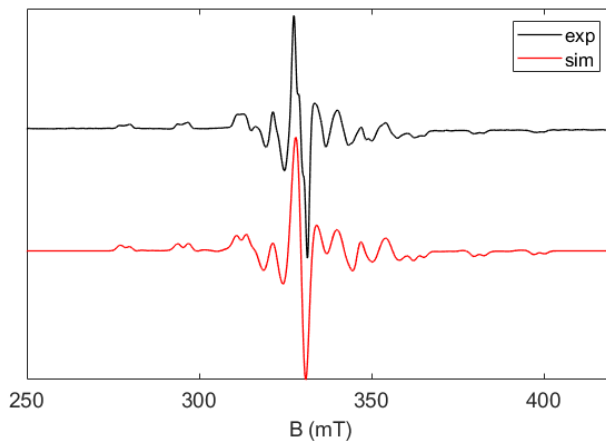


Figure RésFr 12 : Spectre RPE du dimère  $O=VPdV=O$  (deux vanadylporphyrines liées par un ion palladium(II)) à 15 K

Dans le cas du dimère  $O=VPdV=O$ , une interaction dipolaire très faible est observée entre les deux sites paramagnétiques, malgré la distance importante (14,3 Å) entre les deux ions vanadium(IV). Ceci nous a conduit à étudier ces porphyrines par RPE pulsée pour d'éventuelles applications dans le domaine des qubits. Le spin de l'ion paramagnétique vanadium(IV) est centré sur l'ion et interagit très peu avec son environnement. Dans le dimère un couplage très faible est présent ce qui est optimal

pour des systèmes à deux qubits. Des oscillations de Rabi ont été détectées à température ambiante laissant présager une bonne robustesse de la cohérence quantique.

#### *Auto-assemblage de porphyrines à l'interface solide/liquide*

De nouvelles porphyrines et les dimères correspondants ont également été auto-assemblés à l'interface solide/liquide et visualisés par des techniques STM. Ces assemblages ont été réalisés sur des aires importantes et les résolutions des images sont parfois excellentes. Ceci est dû au fait que ces porphyrines de nickel(II) et de palladium(II) comportant des chaînes alkyles sur les positions *meso* sont des molécules aromatiques étendues et très planes conduisant à de très bonnes interactions avec le support solide HOPG (Highly oriented pyrolytic graphite). L'étude a été réalisée en utilisant principalement les deux porphyrines, représentées ci-après (*cf.* Figure RésFr 13).

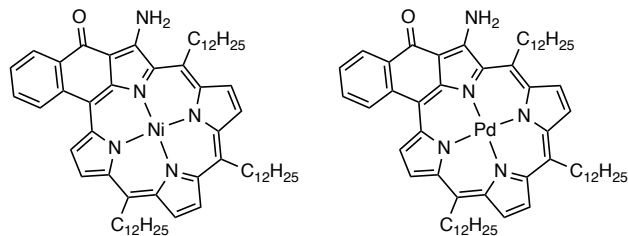


Figure RésFr 13 : Porphyrines de nickel(II) et de palladium(II) utilisées

A titre d'exemple, la porphyrine de nickel(II) présentée ci-dessus a permis de générer des assemblages réguliers et extrêmement bien ordonnés à l'interface HOPG/phényloctane sur des surfaces très importantes (*cf.* Figure RésFr 14, NB carré de 480 nm de côté).



Figure RésFr 14 : Porphyrines de nickel(II) à l'interface HOPG/phényloctane

Ces porphyrines comportant un site de coordination externe ont pu être assemblées sur la surface à l'aide d'un cation métallique. Dans cette étude, le nickel(II) a été choisi comme cation connecteur. Par rapport au palladium(II) utilisé lors des études RPE, le nickel(II) est cinétiquement moins inerte et permet d'assembler les sous-unités porphyriniques plus rapidement et à température ambiante. Ci-dessous, les images obtenues en utilisant une porphyrine de palladium(II) et l'image STM après assemblage avec l'ion nickel(II) (*cf.* Figure RésFr 15).

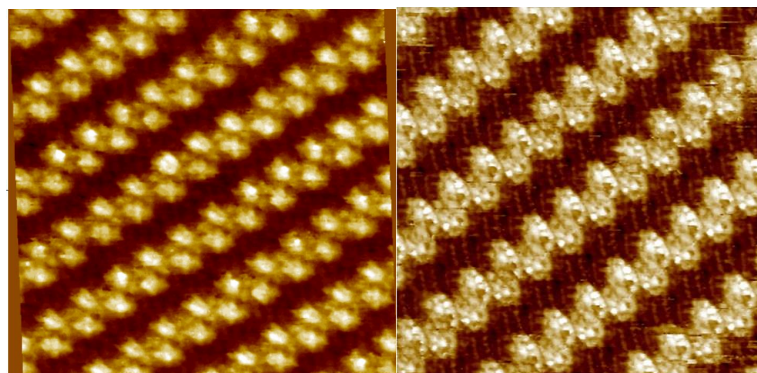


Figure RésFr 15 : Images STM d'une Pd(II) porphyrine (à gauche) et d'un dimère (à droite) à l'interface HOPG/phényloctane

## Conclusion

En conclusion, cette thèse qui comportait essentiellement deux projets a permis d'aborder de nombreux aspects théoriques et expérimentaux en chimie et en chimie-physique. De nouveaux complexes luminescents de cuivre(I) ont été préparés et leurs géométries de coordination optimisées afin d'essayer de comprendre les relations géométrie de coordination/propriétés de fluorescence de ces entités. Par ailleurs, de nouveaux dimères de porphyrines ont été obtenus et l'étude de leurs propriétés électroniques et magnétiques permet d'envisager des applications dans le domaine des qubits. D'autres porphyrines ont pu être auto-assemblées à l'interface HOPG/phényloctane de façon très efficace.

REFERENCES :

- [1] C. O. Dietrich-Buchecker, P. A. Marnot, J.-P. Sauvage, *Tetrahedron Lett.* **1982**, *23*, 5291-5294.
- [2] C. O. Dietrich-Buchecker, P. A. Marnot, J.-P. Sauvage, J. Kirchhoff and D. McMillin, *J. Chem. Soc., Chem. Commun.*, **1983**, 513-515.
- [3] O. Green, B. A. Gandhi and J. N. Burstyn, *Inorg. Chem.*, **2009**, *48*, 5704–5714.
- [4] M. Schmittel, U. Lüning, M. Meder, A. Ganz, C. Michel and M. Herderich, *Heterocycl. Commun.*, **1997**, *3*, 493–498.
- [5] J. L. Appleton, V. Silber, L. Karmazin, C. Bailly, J.-C. Chambron, J. Weiss and R. Ruppert, *Eur. J. Org. Chem.*, **2020**, *47*, 7320–7326.
- [6] C. O. Dietrich-Buchecker, J. Guilhem, C. Pascard and J.-P. Sauvage, *Angew. Chem. Int. Ed. Engl.* **1990**, *29*, 1154-1156.
- [7] S. Richeter, C. Jeandon, J.-P. Gisselbrecht, R. Ruppert and H. J. Callot, *J. Am. Chem. Soc.* **2002**, *124*, 6168-6179.
- [8] H. Dekkiche, A. Buisson, A. Langlois, P.-L. Karsenti, L. Ruhlmann, R. Ruppert and P. D. Harvey, *Chem. Eur. J.* **2016**, *22*, 10484-10493.
- [9] M. A. Carvalho, H. Dekkiche, S. Richeter, C. Bailly, L. Karmazin, D. McKearney, D. B. Leznoff, G. Rogez, B. Vilen, S. Choua and R. Ruppert, *J. Porphyrins Phthalocyanines*, **2020**, *24*, 238-246.
- [10] M. A. Carvalho, H. Dekkiche, M. Nagasaki, Y. Kikkawa and R. Ruppert, *J. Am. Chem. Soc.* **2019**, *141*, 10137-10141.

**Publication :**

Jordan L. Appleton, Vincent Silber, Lydia Karmazin, Corinne Bailly, Jean-Claude Chambron, Jean Weiss, and Romain Ruppert, *Eur. J. Org. Chem.* 2020, **47**, 7320–7326.

**Communications orales :**

- GECOM Concoord 2022, 02/05/22 – 06/05/22, Annecy (France) (Prix de la communication orale)
- 54<sup>th</sup> Annual Conference of the RSC ESR Interest Group, CARDIFF (UK), 12/04/21 - 16/04/21, Flash presentation
- ARPE Online Summer School, 14/06/21 - 18/06/21, Flash Presentation

**Communications par posters :**

- Metal-radical interactions in molecular magnetism, Hirschegg (Austria), 20/06/22 -22/06/22,
- 54<sup>th</sup> Annual Conference of the RSC ESR Interest Group, Cardiff (UK), 12/04/21 - 16/04/21
- 30<sup>th</sup> Edition of the International Conference on Photochemistry, Geneva (Switzerland), 19/07/21 - 23/07/21
- 11<sup>th</sup> International Conference of Porphyrins and Phthalocyanines, ICPP-11, Buffalo (USA), 28/06/21 - 03/07/21
- ARPE Online Summer School, 14/06/21 - 18/06/21

## Experimental part

### General materials and methods

All reagents and solvents were purchased from commercial sources and were used as received. 1-Bromo-4-*tert*-butyl-2,6-dimethylbenzene,<sup>1</sup> 2,6-dimethyl-4-*tert*-butylbenzaldehyde,<sup>2</sup> 2-bromo[6]helicene,<sup>3</sup> methyl-2-formylbenzoate,<sup>4</sup> dipyrrolylalkyl<sup>5</sup> and nickel(II) enaminoketone porphyrin<sup>6</sup> were prepared following previously published procedures. The MnO<sub>2</sub> was from Honeywell Fluka (G1890). Dichloromethane was distilled from calcium hydride, THF and toluene from sodium/benzophenone ketyl. Most of the experiments were carried out under inert atmosphere by using standard Schlenk techniques. Chromatographic separations were performed using Merck silica gel (40-63 µm). Size exclusion chromatography was performed using BioBeads SX-1 cross-linked polystyrene microspheres and toluene. Very pure metal salts (99.99%) were bought for the EPR studies.

<sup>1</sup>H and <sup>13</sup>C were performed on Bruker Avance 400, 500 or 600 MHz spectrometers equipped with a cryoprobe. CDCl<sub>3</sub> was used as a solvent and the spectra were recorded at 25 °C. Chemical shifts ( $\delta$  (ppm)) are shown relative to TMS. UV-visible spectra were recorded on a Cary 5000 UV/vis/NIR double-beam spectrometer in dichloromethane. Emission and lifetime studies were carried out on a HORIBA scientific fluoromax spectrofluorometer in distilled dichloromethane. Lifetime studies were carried out using a nanoLED at 456 nm and a colloidal silica suspension in water as a prompt. ESI MS were collected on a Bruker Daltonics MicroTOF and MALDI MS were collected on a Bruker Autoflex II TOF-TOF instrument in positive ionisation mode with dithranol as a matrix. Measurements were carried out by S. Coutin (Service de Spectrométrie de Masse, Institut de Chimie, Université de Strasbourg). Elemental analysis was performed on a ThermoFischer Scientific Flash2000 by the Service d'Analyses de l'Institut de Chimie de Strasbourg (M. Hienrich, N. Bourgeois). Electrochemical measurements were carried out using a glassy carbon working electrode in distilled dichloromethane with NBu<sub>4</sub>PF<sub>6</sub> (0.1 M) as the electrolyte and ferrocenium/ferrocene (Fc<sup>+</sup>/Fc) couple as an internal reference. The three electrodes were connected to a computerised electrochemical device (Biologic SP-150). X-ray analysis was performed by Drs L. Karmazin, C. Bailly and N. Gruber (Service de radiocristallographie, Institut de Chimie, Strasbourg) using a Bruker APEX II DUO Kappa-CCD diffractometer.

X-band continuous wave EPR spectra were recorded on an EMXplus spectrometer (Bruker Biospin GmbH), equipped with a high sensitivity resonator (4119HSW) and an ESR900 continuous flow cryostat controlled with an Oxford ITC503S apparatus (Oxford Instrument). Samples were introduced into 4 mm outer diameter clear fused quartz tube (Wilmad-LabGlass). Modulation

frequency and amplitude were respectively of 100 kHz and 0.4 mT. The *g* factor was calibrated using the Bruker strong pitch (*g* = 2.0028).

X-band pulsed EPR spectra were recorded on an Elexsys E580 spectrometer equipped with a 4118X-MD5 resonator (Bruker Biospin GmbH) and a CF935 continuous flow cryostat controlled by a Mercury ITC (Oxford Instrument). The pulses were amplified using a 1 kW pulsed travelling wave tube (TWT) amplifier. The shot repetition time was set to at least 5 times  $T_1$  and the number of shots per point was adjusted according to the signal to noise ratio. Unless said otherwise,  $\pi/2$  and  $\pi$  pulses were 16 ns and 32 ns respectively. Echo detected field sweep (EDFS) were recorded using Hahn echo sequence ( $\pi/2 - \tau - \pi - \tau - \text{echo}$ ) where the delay  $\tau$  was set at 350 ns.  $T_2$  were also recorded using Hahn echo sequence where the delay  $\tau$  started at 210 ns and was incremented by steps of 4 to 12 ns depending on the temperature.  $T_1$  were measured using the picket fence saturation recovery sequence ( $\pi - t - \dots - \pi/2 - \tau - \pi - \tau - \text{echo}$  where  $n$  is 28,  $t$  is equal to 100 ns and  $\tau$  equal to 350 ns). Nutation experiments were recorded by applying a nutation pulse  $p_{\text{nut}}$  of incremented duration followed by a Hahn echo sequence applied after a long decoherence time  $t_{\text{dec}} > 5*T_m$  ( $t_{\text{nut}} - t_{\text{dec}} - \pi/2 - \tau - \pi - \tau - \text{echo}$ ). The length of the  $\pi/2$  and  $\pi$  pulses were adapted to get the maximum intensity of the echo at each power.

Curves were fitted using a Matlab (MathWorks) homemade routing.  $T_2$  curve were fitted with a mono exponential function of the form:

$$M_z(t) = M_0 e^{-t/T_2} \quad (\text{Eq. 6})$$

Where  $M_0$  is the amplitude.

$T_1$  were fitted with stretched exponential of the form:

$$M_z(t) = M_0 (1 - e^{-(t/T_1)^\beta}) \quad (\text{Eq. 7})$$

Where  $M_0$  is the amplitude and  $\beta$  is the stretch factor.

Nutations were fitted using the following model:

$$M_z(t) = M_{R_1} e^{t/T_{R_1}} \cos(2\pi f_{R_1} t) + M_{R_2} e^{t/T_{R_2}} \cos(2\pi f_{R_2} t + \varphi_{R_2}) \quad (\text{Eq. 8})$$

Where  $M_{\text{nut}}$ ,  $T_{\text{nut}}$ ,  $f_{\text{nut}}$  are respectively the amplitude, the decay and the frequency of the nutation and  $M_{1H}$ ,  $T_{1H}$ ,  $f_{1H}$ ,  $\varphi_{1H}$  are respectively the amplitude, the decay, the frequency and the phase of the oscillations due to weak hyperfine coupling with protons.

Scanning Tunnelling Microscopy (STM) images were recorded at ambient pressure and temperature with a Veeco Multimode III (Bruker) equipped with a 1- $\mu\text{m}$  range piezoelectric scanner (A-Piezo, Veeco) and connected to a STM head. The STM was operated in constant current mode with tips that were mechanically cut from Pt/Ir (80 : 20) wire with a diameter of 0.25 mm supplied by Goodfellow. The highly oriented pyrolytic graphite (HOPG) substrates (Momentive Performance) were glued with

silver paste to a metal disc that was magnetically attached to the STM base. STM experiments were performed at the solid/liquid interface of HOPG and a phenyloctane solution (typically around 1 mM) of the porphyrin derivative that was dropped on the substrate with a pipette. In our instrumental configuration, the sample is grounded and the voltage bias (V) and tunnelling current (I) are applied from the tip. The STM image processing was done on SPIP software from Image Metrology. The experimental drift of the images was corrected by in-situ calibration of the underlying HOPG lattice (V: 35 mV, I: 35 pA). Unit cell constants for each lattice were estimated by Fourier analysis and subsequent averaging of multiple images collected at different scan angles.

## DFT Calculations

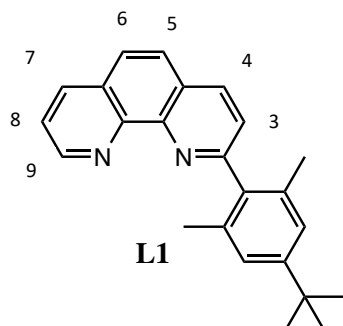
The calculations were performed with the ADF 2019 package at DFT level of theory using the B3LYP functional.<sup>7</sup> Scalar relativistic effects were included using zero order regular approximated (ZORA) Hamiltonian.<sup>8</sup> All atoms were described by the TZP basis set. Solvent corrections (dichloromethane) were introduced through a PCM (Polarisable Continuum Model). Van der Waals forces were described through Grimme's corrections.<sup>9</sup> All structures were fully optimized. Absorption spectra were computed by means of TD-DFT on these optimised structures and spin-orbit coupling added by perturbation of the TD-DFT results. Excited state geometries were optimized in the same conditions. The nature of the computed electronic transitions was determined by means of TheoDORE analysis<sup>10</sup> of the TD-DFT results.

A second set of calculations were performed with GAUSSIAN 09 (version D.01) at DFT level of theory (B3LYP functional). All atoms were described by 6-31+G\*\* basis set. Solvent corrections (dichloromethane) were introduced through a PCM (Polarisable Continuum Model). Van der Waals forces were described through Grimme's corrections. The structures were fully optimised. Non-covalent interactions were studied by means of NCIPlot<sup>11</sup> performed on the wavefunction of the optimized structures.

REFERENCES:

- (1) J. E. Field, T. J Hill and D. Venkataraman, *J. Org. Chem.* 2003, **68**, 6071-6078.
- (2) Q. Lui, M. Lu, F. Sun, J. Li Y. Zhoa, *Synth. Commun.*, 2008, **38**, 4188.
- (3) M. Jakubec, T. Beránek, P. Jakubík, J. Sykora, J. Zádny, V. Církva and J. Storch, *J. Org. Chem.* 2018, **83**, 3607-3616.
- (4) A. Osuka, S. Nakajima and K. Maruyama, *J. Org. Chem.*, 1992, **57**, 7355-7359.
- (5) C-H. Lee and J. S. Lindsey, *Tetrahedron*, 1994, **50**, 11427-11440.
- (6) H. Dekkiche, M-A. Carvalho, C. Jeandon, L. Karmazin, C. Boudon, L. Ruhlmann, R. Ruppert, *J. Porphyrins Phthalocyananines*, 2021, **25**, 1133-1142.
- (7) A.D. Becke, *J. Chem. Phys.*, 1993, **98**, 5648-5652.
- (8) ADF, SCM, Theoretical Chemistry, Vrije Universiteit, Amsterdam, The Netherlands.  
Available online: <https://www.scm.com/doc/ADF/index.html> (accessed on 1 June 2019).
- (9) S. Grimme, J. Antony, S. Ehrlich, H. Krieg, *J. Chem. Phys.* **2010**, *132*, 154104.
- (10) F. Plasser *J. Chem. Phys.*, 2020, **152**, 08418.
- (11) J. Contreras-García, E.R. Johnson, S. Keinan, R. Chaudret, J-P, Piquemal, D. N. Beratan and W. Yang, *J. Chem. Theory Comput.*, 2011, **7**, 625-632.

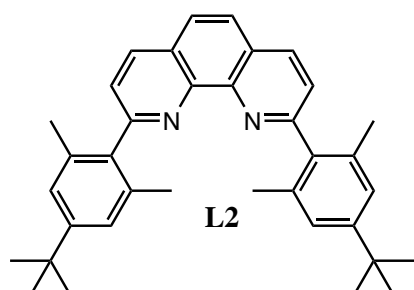
2-(4-(*tert*-butyl)-2,6-dimethylphenyl)-1,10-phenanthroline (**L1**) and 2,9-bis(4-(*tert*-butyl)-2,6-dimethylphenyl)-1,10-phenanthroline (**L2**)



Chemical formula: C<sub>24</sub>H<sub>24</sub>N<sub>2</sub>

Exact mass: 340.19

Molecular weight: 340.47



Chemical formula: C<sub>36</sub>H<sub>40</sub>N<sub>2</sub>

Exact mass: 500.32

Molecular weight: 500.73

Under argon and at 0 °C, a solution of 2-bromo-5-(*tert*-butyl)-1,3-dimethylbenzene (12.2 g, 50.6 mmol) in dry diethyl ether (115 mL) was added dropwise to a mixture of lithium (1.58 g, 0.23 mmol) in dry diethyl ether (70 mL). The resulting grey solution was stirred for 16 h at rt. A solution of 1,10-phenanthroline (2.14 g, 11.9 mmol) dissolved in dry toluene (100 mL) was slowly added and the solution was refluxed for 4 h and then stirred at rt for 16 h. Water (100 mL) was added and the layers were separated. The aqueous layer was extracted with dichloromethane. The combined organic layers were partially evaporated to eliminate ether and MnO<sub>2</sub> (60 g) was added. After 4 h of stirring at rt, MgSO<sub>4</sub> (65 g) was added and the suspension stirred for 2 h. The mixture was filtered and the solvent was evaporated, rendering a brown viscous oil which was purified by column chromatography (silica gel, from cyclohexane:dichloromethane 1:1 to 1% methanol in dichloromethane) to afford **L1** (1.61 g, 4.73 mmol, 40%) and **L2** (1.18 g, 2.36 mmol, 20%).

## L1

<sup>1</sup>H NMR (500 MHz, CDCl<sub>3</sub>) δ 9.19 (dd, *J* = 4.4, 1.8 Hz, 1H, H<sub>9</sub>), 8.29 (d, *J* = 8.0 Hz, 1H, H<sub>4</sub>), 8.25 (dd, *J* = 8.1, 1.8 Hz, 1H, H<sub>7</sub>), 7.85 and 7.81 (2d, 2H, *J* = 9.5 Hz, H<sub>5</sub> or 6 and H<sub>5</sub> or 6), 7.62 (d, *J* = 8.0 Hz, 1H, H<sub>3</sub>), 7.61 (dd, *J* = 4.4, 8.1 Hz, 1H, H<sub>8</sub>), 7.13 (s, 2H, H<sub>Ar</sub>), 2.11 (s, 6H, H<sub>Me</sub>), 1.35 (s, 9H, H<sub>tBu</sub>).

<sup>13</sup>C NMR (125 MHz, CDCl<sub>3</sub>) δ 160.9, 150.7, 150.42 (CH), 146.5, 146.4, 138.5, 136.1 (CH), 135.9 (CH), 135.6, 128.9, 127.0, 126.5 (CH), 126.2 (CH), 124.7 (CH), 124.5 (CH), 122.8 (CH), 34.4 (CH<sub>3</sub>), 31.4, 20.8 (CH<sub>3</sub>).

Anal. calcd for C<sub>24</sub>H<sub>24</sub>N<sub>2</sub>: C, 70.59; H, 6.16; N, 6.59. Found: C, 70.29; H, 6.04; N, 6.63.

## L2

<sup>1</sup>H NMR (500 MHz, CDCl<sub>3</sub>) δ 8.28 (d, *J* = 8.2 Hz, 2H, H<sub>4</sub> and H<sub>7</sub>), 7.85 (s, 2H, H<sub>5</sub> and H<sub>6</sub>), 7.61 (d, *J* = 8.2 Hz, 2H, H<sub>3</sub> and H<sub>8</sub>), 7.11 (s, 4H, H<sub>Ar</sub>), 2.17 (s, 12H, H<sub>Me</sub>), 1.32 (s, 18H, H<sub>tBu</sub>).

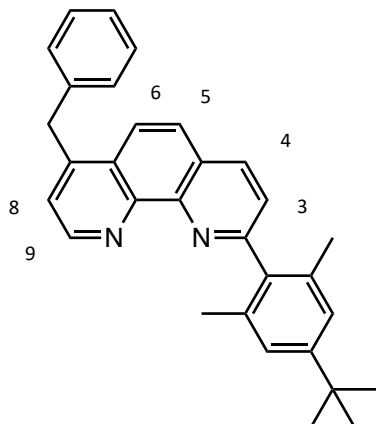
<sup>13</sup>C NMR (125 MHz, CDCl<sub>3</sub>) δ 160.2, 150.7, 146.3, 138.2, 135.9, 135.7 (CH), 127.1, 126.2 (CH), 124.9 (CH), 124.8 (CH), 34.37, 31.4 (CH<sub>3</sub>), 21.0 (CH<sub>3</sub>).

Anal. calcd for C<sub>36</sub>H<sub>40</sub>N<sub>2</sub>: C, 86.35; H, 8.05; N, 5.59. A tiny amount of residual water was always present in the samples, giving very close, but not exact analyses (> 0.4%).

HRMS ESI: calcd for C<sub>36</sub>H<sub>41</sub>N<sub>2</sub> (M + H<sup>+</sup>) 501.3264; obsd 501.3235.

Crystal data from Et<sub>2</sub>O/CH<sub>2</sub>Cl<sub>2</sub> for **L2**. C<sub>36</sub>H<sub>40</sub>N<sub>2</sub>; M = 500.70 g.mol<sup>-1</sup>, triclinic, space group P -1, *a* = 9.1339(4) Å, *b* = 13.3692(6) Å, *c* = 13.6625(7) Å,  $\alpha$  = 111.7100(10)°,  $\beta$  = 105.2060(10)°,  $\gamma$  = 94.184(2)°, V = 1468.63(12) Å<sup>3</sup>, Z = 2,  $\rho_{\text{calc}}$  = 1.132 Mg/m<sup>3</sup>, T = 173(2) K, MoK<sub>α</sub> = 0.71073 Å, 1.670 <  $\theta$  < 29.385, transmission factors: T<sub>min</sub>/T<sub>max</sub> = 0.7458/0.7007, 55514 reflections measured, 7931 unique reflections, R<sub>1</sub> = 0.0633, wR<sub>2</sub> = 0.1318, GoF = 1.033.

7-Benzyl-2-(4-(*tert*-butyl)-2,6-dimethylphenyl)-1,10-phenanthroline (**L3**)



Chemical formula: C<sub>31</sub>H<sub>30</sub>N<sub>2</sub>

Exact mass: 430.24

Molecular weight: 430.60

Under argon and at -78 °C, *t*-BuLi (19 mL of a 1.7 M solution, 32.3 mmol) was added slowly to a solution of 1-bromo-4-(*tert*-butyl)-2,6-dimethylbenzene (4.00 g, 16.6 mmol) in dry THF (30 mL). The solution was then stirred for 2 h. A degassed solution of 1,10-phenanthroline (1.00 g, 5.55 mmol) in dry toluene (50 mL) was added to the solution *via* cannula transfer. The solution was heated to 50 °C to distill off the ether, and then further heated at 65 °C under argon for 16 h. The same procedure as carried out for **L1**, was used for the work up to afford **L3** (1.34 g, 3.11 mmol, 56%) and **L2** (0.724 g, 1.45 mmol, 26%).

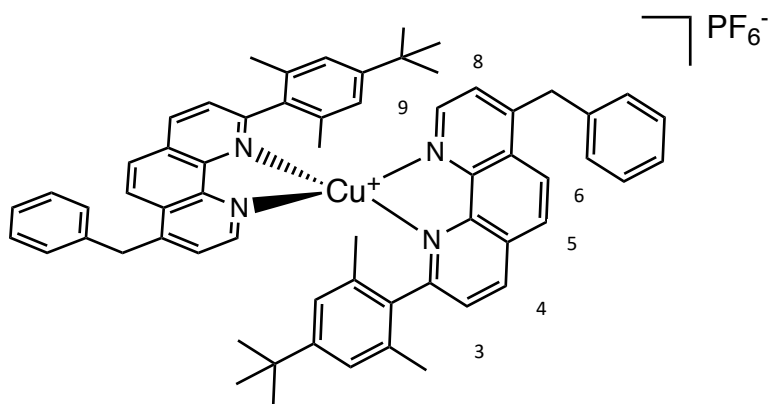
### L3

<sup>1</sup>H NMR (500 MHz, CDCl<sub>3</sub>) δ 9.12 (d, *J* = 4.5 Hz, 1H, H<sub>9</sub>), 8.26 (d, *J* = 8.2 Hz, 1H, H<sub>4</sub>), 8.03 (d, *J* = 9.1 Hz, 1H, H<sub>5 or 6</sub>), 7.81 (d, *J* = 9.1 Hz, 1H, H<sub>5 or 6</sub>), 7.59 (d, *J* = 8.2 Hz, 1H, H<sub>3</sub>), 7.39 (d, *J* = 4.5 Hz, 1H, H<sub>8</sub>), 7.33 – 7.29 (m, 2H, H<sub>ortho</sub>), 7.26 – 7.20 (m, 3H, H<sub>meta</sub> and H<sub>para</sub>), 7.13 (s, 2H, H<sub>Af</sub>), 4.54 (s, 2H, CH<sub>2</sub>), 2.10 (s, 6H, H<sub>Me</sub>), 1.35 (s, 9H, H<sub>tBu</sub>).

<sup>13</sup>C NMR (125 MHz, CDCl<sub>3</sub>) δ 161.0, 150.7, 150.2 (CH), 146.7, 146.2, 138.8, 138.6, 135.9 (CH), 135.6, 128.8 (CH), 127.9, 126.7 (CH), 126.6, 126.4 (CH), 124.7 (CH), 124.7, 124.5 (CH), 124.0 (CH), 122.2 (CH), 38.7, 34.4, 31.4 (CH<sub>3</sub>), 20.8 (CH<sub>3</sub>).

Anal. calcd for C<sub>36</sub>H<sub>40</sub>N<sub>2</sub>: C, 86.47; H, 7.02; N, 6.51. Found: C, 86.15; H, 7.04; N, 6.56.

[Cu(7-benzyl-2-(4-(*tert*-butyl)-2,6-dimethylphenyl)-1,10-phenanthroline)<sub>2</sub>]PF<sub>6</sub> (**C1**)



Under argon, a degassed solution of **L3** (138 mg, 0.32 mmol) in dichloromethane (10 mL) was added *via* cannula transfer to a degassed solution of [Cu(CH<sub>3</sub>CN)<sub>4</sub>]PF<sub>6</sub> (58 mg, 0.16 mmol) in dichloromethane (20 mL). The solution turned immediately red and was further stirred for 1 h. The solvent was evaporated and the solid was dissolved in the minimum amount of dichloromethane and precipitated by addition of a diethyl ether/pentane (1:1) solution, to afford complex **C1** (142 mg, 0.15 mmol, 94%).

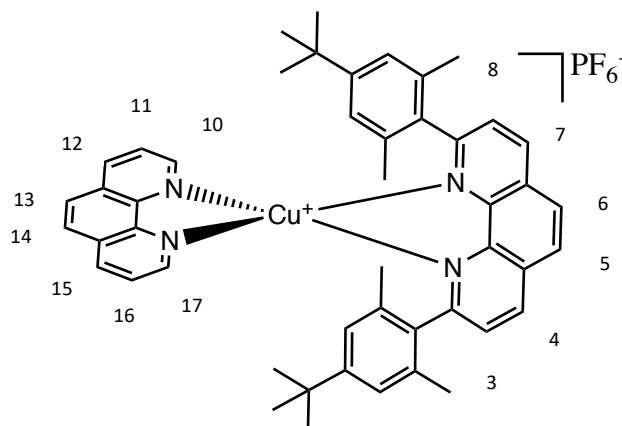
<sup>1</sup>H NMR (500 MHz, CDCl<sub>3</sub>) δ 8.76 (d, *J* = 4.9 Hz, 2H, H<sub>9</sub>), 8.49 (d, *J* = 8.2 Hz, 2H, H<sub>4</sub>), 8.12 (d, *J* = 9.2 Hz, 2H, H<sub>5 or 6</sub>), 8.00 (d, *J* = 9.2 Hz, 2H, H<sub>5 or 6</sub>), 7.54 – 7.51 (m, 4H, H<sub>3</sub> and H<sub>8</sub>), 7.37 – 7.34 (m, 4H, H<sub>Ph</sub>), 7.29 – 7.23 (m, 6H, H<sub>Ph</sub>), 6.42 (s, 2H, H<sub>Ar</sub>), 6.27 (s, 2H, H<sub>Ar</sub>), 4.63 (d, *J* = 16.0 Hz, 2H, CH<sub>2</sub>), 4.41 (d, *J* = 16.0 Hz, 2H, CH<sub>2</sub>), 1.68 (s, 6H, H<sub>Me</sub>), 1.38 (s, 6H, H<sub>Me</sub>), 1.08 (s, 18H, H<sub>tBu</sub>).

<sup>13</sup>C NMR (125 MHz, CDCl<sub>3</sub>) δ 159.3, 150.8, 148.3 (CH), 147.9, 143.9, 143.7, 137.3, 137.1 (CH), 135.5, 135.3, 133.2, 129.1 (CH), 129.0 (CH), 127.9, 127.2 (CH), 127.0, 126.9 (CH), 126.5 (CH), 125.6 (CH), 123.7 (CH), 123.4 (CH), 122.9 (CH), 38.6 (CH<sub>2</sub>), 34.0, 31.2 (CH<sub>3</sub>), 20.8 (CH<sub>3</sub>), 20.2 (CH<sub>3</sub>).

Anal. calcd for C<sub>62</sub>H<sub>60</sub>CuF<sub>6</sub>N<sub>4</sub>P: C, 69.62; H, 5.65; N, 5.24. Found: C, 69.64; H, 5.69; N, 5.22.

Crystal data from Et<sub>2</sub>O/CH<sub>2</sub>Cl<sub>2</sub> for Et<sub>2</sub>O/CH<sub>2</sub>Cl<sub>2</sub> for **C1**. C<sub>62</sub>H<sub>60</sub>CuF<sub>6</sub>N<sub>4</sub>P, M = 1239.50 g.mol<sup>-1</sup> monoclinic, space group P21, *a* = 12.8784(5) Å, *b* = 13.8188(5) Å, *c* = 17.4807(6) Å,  $\alpha$  = 90°,  $\beta$  = 107.243(2) °,  $\gamma$  = 90°, V = 2971.12(19) Å<sup>3</sup>, Z = 2,  $\rho_{\text{calc}}$  = 1.385 Mg/m<sup>3</sup>, T = 173(2) K, MoK<sub>α</sub> = 0.71073 Å, 2.22 <  $\theta$  < 29.01, transmission factors: T<sub>min</sub>/T<sub>max</sub> = 0.6223/0.7458, 15289 reflections measured, 10224 unique reflections, R<sub>1</sub> = 0.0995, wR<sub>2</sub> = 0.1205, GoF = 0.995.

[Cu(2,9-(4-(*tert*-butyl)-2,6-dimethylphenyl)-1,10-phenanthroline)(1,10-phenanthroline)]PF<sub>6</sub> (**C2**)



Chemical formula: C<sub>48</sub>H<sub>48</sub>CuF<sub>6</sub>N<sub>4</sub>P

Exact mass: 888.28

Molecular weight: 889.45

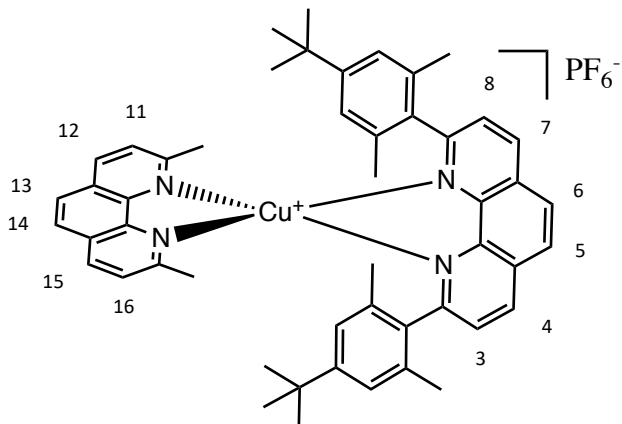
Under argon and at rt, to a solution of [Cu(CH<sub>3</sub>CN)<sub>4</sub>]PF<sub>6</sub> (58 mg, 0.16 mmol) in dichloromethane (20 mL) was added, *via* cannula transfer, a degassed solution of ligand **L2** (86 mg, 0.17 mmol) in dichloromethane (10 mL). The solution turned yellow and was stirred for 1 h. A solution of 1,10-phenanthroline (28 mg, 0.16 mmol) in degassed dichloromethane (10 mL) was then added *via* cannula transfer, rendering the solution red. The solution was once again stirred for 1 h. Solvent was then evaporated and the solid was dissolved in the minimum amount of dichloromethane and precipitated by addition of diethyl ether/pentane (1:1) to afford complex **C2** (98 mg, 0.11 mmol, 69%).

<sup>1</sup>H NMR (500 MHz, CDCl<sub>3</sub>) δ 8.70 (d, *J* = 8.0 Hz, 2H, H<sub>4</sub> and H<sub>7</sub>), 8.55 (dd, *J* = 4.7, 1.5 Hz, 2H, H<sub>10</sub> and H<sub>17</sub>), 8.36 (dd, *J* = 8.1, 1.5 Hz, 2H, H<sub>12</sub> and H<sub>15</sub>), 8.23 (s, 2H, H<sub>5</sub> and H<sub>6</sub>), 7.83 (d, *J* = 8.0 Hz, 2H, H<sub>3</sub> and H<sub>8</sub>), 7.78 (dd, *J* = 4.7, 8.1, 2H, H<sub>11</sub> and H<sub>16</sub>), 7.79 (s, 2H, H<sub>13</sub> and H<sub>14</sub>), 6.15 (s, 4H, H<sub>Ar</sub>), 1.77 (s, 12H, H<sub>Me</sub>), 0.62 (s, 18H, H<sub>tBu</sub>).

<sup>13</sup>C NMR (125 MHz, CDCl<sub>3</sub>) δ 159.1, 151.1, 147.7 (CH), 143.9, 142.8, 137.4 (CH), 137.0, 136.2 (CH), 134.2, 128.3, 127.9, 126.8 (CH), 126.6 (CH), 126.3 (CH), 124.7 (CH), 123.1 (CH), 33.6, 30.7 (CH<sub>3</sub>), 20.4 (CH<sub>3</sub>).

Anal. calcd for C<sub>48</sub>H<sub>48</sub>CuF<sub>6</sub>N<sub>4</sub>P: C, 64.82; H, 5.44; N, 6.30. Found: C, 64.59; H, 5.47; N, 6.22.

**[Cu(2,9-(4-(*tert*-butyl)-2,6-dimethylphenyl)-1,10-phenanthroline)(2,9-dimethyl-1,10-phenanthroline)]PF<sub>6</sub> (C3)**



Chemical formula: C<sub>50</sub>H<sub>52</sub>CuF<sub>6</sub>N<sub>4</sub>P

Exact mass: 916.31

Molecular weight: 917.50

Complex **C3** was synthesised using the same method as for **C2**, with the addition of 2,9-dimethyl-1,10-phenanthroline (29 mg, 0.14 mmol) as opposed to 1,10-phenanthroline to yield **C3** (90 mg, 0.098 mmol, 61%).

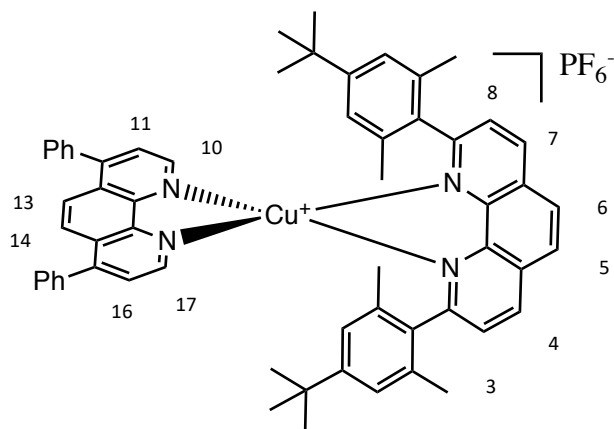
<sup>1</sup>H NMR (500 MHz, CDCl<sub>3</sub>) δ 8.73 (d, *J* = 8.2 Hz, 2H, H<sub>4</sub> and H<sub>7</sub>), 8.25 (s, 2H, H<sub>5</sub> and H<sub>6</sub>), 8.21 (d, *J* = 8.2 Hz, 2H, H<sub>12</sub> and H<sub>15</sub>), 7.84 (d, *J* = 8.2 Hz, 2H, H<sub>11</sub> and H<sub>16</sub>), 7.74 (s, 2H, H<sub>13</sub> and H<sub>14</sub>), 7.51 (d, *J* = 8.2 Hz, 2H, H<sub>3</sub> and H<sub>8</sub>), 6.31 (s, 4H, H<sub>Ar</sub>), 2.21 (s, 6H, H<sub>Me</sub>), 1.66 (s, 12H, H<sub>Me</sub>), 0.78 (s, 18H, H<sub>tBu</sub>).

<sup>13</sup>C NMR (500 MHz, CDCl<sub>3</sub>) δ 159.5, 156.8, 151.3, 143.8, 142.4, 137.6 (CH), 136.6, 136.6 (CH), 134.3, 128.2, 127.1 (CH), 126.9 (CH), 126.7, 125.6 (CH), 124.8 (CH), 123.3 (CH), 33.8, 30.8 (CH<sub>3</sub>), 26.5 (CH<sub>3</sub>), 20.2 (CH<sub>3</sub>).

Anal. calcd for C<sub>50</sub>H<sub>52</sub>CuF<sub>6</sub>N<sub>4</sub>P: C, 65.45; H, 5.21; N, 6.11. Found: C, 65.34; H, 5.75; N, 6.08.

Crystal data from Et<sub>2</sub>O/CH<sub>2</sub>Cl<sub>2</sub> for **C3**. C<sub>54</sub>H<sub>62</sub>CuF<sub>6</sub>N<sub>4</sub>P, M = 991.58 g.mol<sup>-1</sup> monoclinic, space group P21/c, *a* = 13.4772(6) Å, *b* = 19.4894 (8) Å, *c* = 19.6875(9) Å,  $\alpha$  = 90°,  $\beta$  = 105.2060(10)°,  $\gamma$  = 103.534(2)°, V = 5027.6(4) Å<sup>3</sup>, Z = 4,  $\rho_{\text{calc}}$  = 1.310 Mg/m<sup>3</sup>, T = 173(2) K, MoK $\alpha$  = 0.71073 Å, 1.873670 <  $\theta$  < 29.204, transmission factors: T<sub>min</sub>/T<sub>max</sub> = 0.6888/0.7458, 99929 reflections measured, 13604 unique reflections, R<sub>1</sub> = 0.0731, wR<sub>2</sub> = 0.1854, GoF = 1.038.

[Cu(2,9-(4-(*tert*-butyl)-2,6-dimethylphenyl)-1,10-phenanthroline)(bathophenanthroline)]PF<sub>6</sub> (**C4**)



Complex **C4** was synthesised using the same method as for **C2**, with the addition of bathophenanthroline (57 mg, 0.17 mmol) as opposed to 1,10-phenanthroline. Complex **C4** was isolated as orange-red plates (120 mg, 0.12 mmol, 75%).

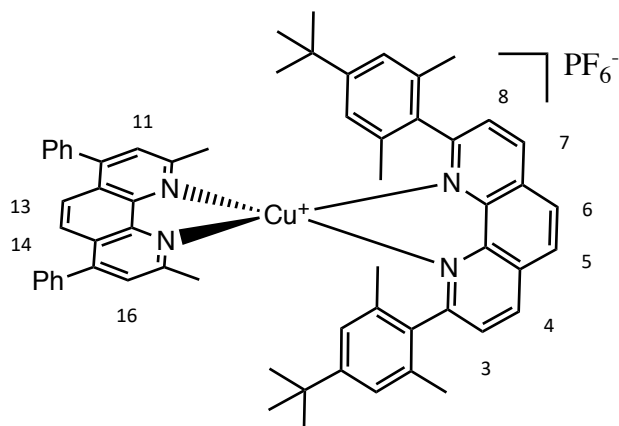
<sup>1</sup>H NMR (500 MHz, CDCl<sub>3</sub>) δ 8.74 (d, *J* = 8.3 Hz, 2H, H<sub>4</sub> and H<sub>7</sub>), 8.63 (d, *J* = 4.9 Hz, 2H, H<sub>10</sub> and H<sub>17</sub>), 8.26 (s, 2H, H<sub>5</sub> and H<sub>6</sub>), 7.86 (d, *J* = 8.3 Hz, 2H, H<sub>3</sub> and H<sub>8</sub>), 7.85 (s, 2H, H<sub>13</sub> and H<sub>14</sub>), 7.71 (d, *J* = 4.9 Hz, 2H, H<sub>11</sub> and H<sub>16</sub>), 7.62 – 7.57 (m, 6H, H<sub>meta</sub> and H<sub>para</sub>), 7.53 – 7.47 (m, 4H, H<sub>ortho</sub>), 6.23 (s, 4H, H<sub>Ar</sub>), 1.85 (s, 12H, H<sub>Me</sub>), 0.66 (s, 18H, H<sub>tBu</sub>).

<sup>13</sup>C NMR (125 MHz, CDCl<sub>3</sub>) δ 158.9, 150.9, 148.7, 147.4 (CH), 143.9, 143.4, 137.5 (CH), 137.4, 136.3, 134.5 (CH), 129.5 (CH), 129.4, 129.1 (CH), 128.0, 126.9 (CH), 126.3 (CH), 126.0, 124.9 (CH), 124.3 (CH), 123.1 (CH), 33.7, 30.8 (CH<sub>3</sub>), 20.6 (CH<sub>3</sub>).

Anal. calcd for C<sub>60</sub>H<sub>56</sub>CuF<sub>6</sub>N<sub>4</sub>P.H<sub>2</sub>O: C, 67.68; H, 5.52; N, 5.29. Found: C, 67.68; H, 5.33; N, 5.27.

Crystal data from Et<sub>2</sub>O/CH<sub>2</sub>Cl<sub>2</sub> for **C4**. C<sub>60</sub>H<sub>56</sub>CuF<sub>6</sub>N<sub>4</sub>P, M = 1041.59 g.mol<sup>-1</sup> monoclinic, space group P21/c, *a* = 10.9274(3) Å, *b* = 22.7485(6) Å, *c* = 21.5054(6) Å, α = 90°, β = 107.212(2) °, γ = 90°, V = 5106.4(2) Å<sup>3</sup>, Z = 4, ρ<sub>calc</sub> = 1.355 Mg/m<sup>3</sup>, T = 173(2) K, MoK<sub>α</sub> = 1.54178 Å, 2.898 < θ < 66.688, transmission factors: T<sub>min</sub>/T<sub>max</sub> = 0.6010/0.7528, 65968 reflections measured, 8989 unique reflections, R<sub>1</sub> = 0.0658, wR<sub>2</sub> = 0.1478, GoF = 1.028.

[Cu(2,9-(4-(*tert*-butyl)-2,6-dimethylphenyl)-1,10-phenanthroline)(bathocuproine)]PF<sub>6</sub> (**C5**)



Chemical formula: C<sub>62</sub>H<sub>60</sub>CuF<sub>6</sub>N<sub>4</sub>P

Exact mass: 1068.38

Molecular weight: 1069.70

Complex **C5** was synthesised using the same method as for **C2**, with the addition of bathocuproine (50 mg, 0.14 mmol) as opposed to 1,10-phenanthroline to yield **C5** (86 mg, 0.080 mmol, 50%).

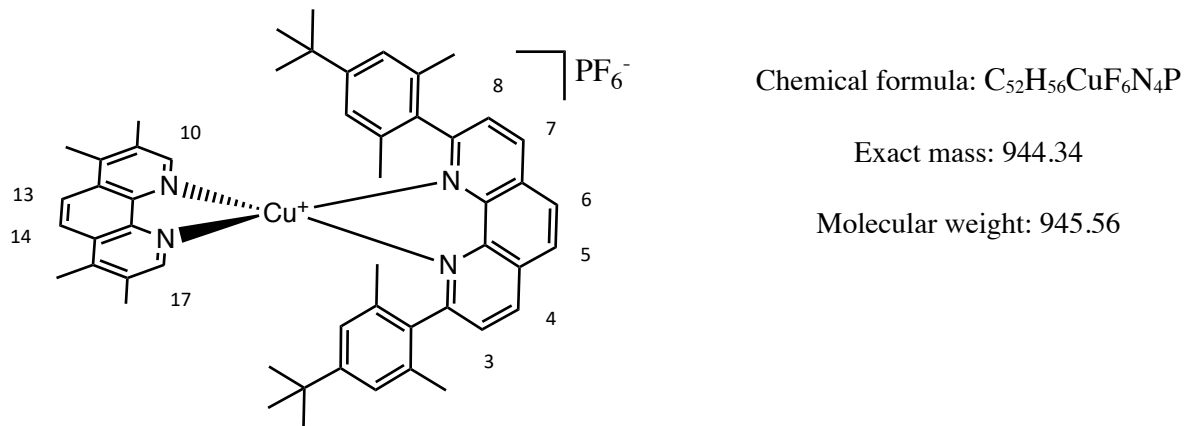
<sup>1</sup>H NMR (500 MHz, CDCl<sub>3</sub>) δ 8.77 (d, *J* = 8.2 Hz, 2H, H<sub>4</sub> and H<sub>7</sub>), 8.29 (s, 2H, H<sub>5</sub> and H<sub>6</sub>), 7.88 (d, *J* = 8.2 Hz, 2H, H<sub>3</sub> and H<sub>8</sub>), 7.79 (s, 2H, H<sub>11</sub> and H<sub>16</sub>), 7.58 - 7.46 (m, 12H, H<sub>ph</sub>, H<sub>13</sub> and H<sub>14</sub>), 6.38 (s, 4H, H<sub>Ar</sub>), 2.29 (s, 6H, H<sub>Me</sub>), 1.76 (s, 12H, H<sub>Me</sub>), 0.79 (s, 18H, H<sub>tBu</sub>).

<sup>13</sup>C NMR (125 MHz, CDCl<sub>3</sub>) δ 159.3, 156.3, 151.2, 148.9, 143.8, 143.2, 137.8 (CH), 136.8, 136.5, 134.5, 129.5 (CH), 129.3 (CH), 129.0 (CH), 128.3, 127.3 (CH), 126.9 (CH), 125.1 (CH), 124.5, 123.3 (CH), 123.3 (CH), 33.8, 31.0 (CH<sub>3</sub>), 26.8 (CH<sub>3</sub>), 20.4 (CH<sub>3</sub>).

MS ESI: calcd for C<sub>62</sub>H<sub>60</sub>CuN<sub>4</sub> (M - PF<sub>6</sub>)<sup>+</sup> 923.41; obsd 923.42.

Crystal data from Et<sub>2</sub>O/CH<sub>2</sub>Cl<sub>2</sub> for **C5**. C<sub>62</sub>H<sub>60</sub>CuF<sub>6</sub>N<sub>4</sub>P, M = 1069.65 g.mol<sup>-1</sup>, monoclinic, space group P21/c, *a* = 11.1445(5) Å, *b* = 21.9682(9) Å, *c* = 22.5256(9) Å,  $\alpha$  = 90°,  $\beta$  = 108.285(3)°,  $\gamma$  = 90°, V = 5236(4) Å<sup>3</sup>, Z = 4,  $\rho_{\text{calc}}$  = 1.357 Mg/m<sup>3</sup>, T = 173(2) K, MoK<sub>α</sub> = 0.71073, 2.4390 <  $\theta$  < 24.30, transmission factors: T<sub>min</sub>/T<sub>max</sub> = 0.6331/0.7456, 12676 reflections measured, 7892 unique reflections, R<sub>1</sub> = 0.0564, wR<sub>2</sub> = 0.1135, GoF = 1.050.

[Cu(2,9-(*tert*-butyl)-2,6-dimethylphenyl)-1,10-phenanthroline](3,4,7,8-tetramethyl-1,10-phenanthroline)]PF<sub>6</sub> (**C6**)



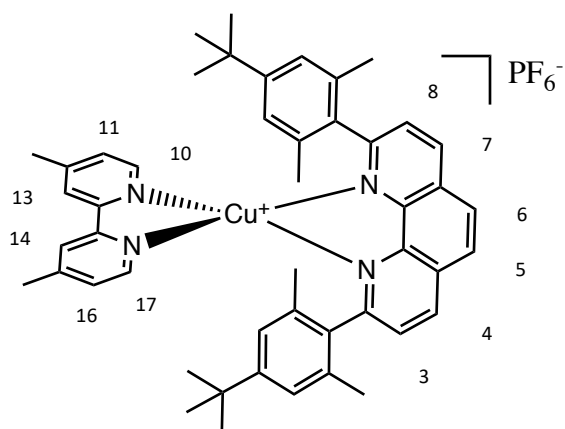
Complex **C6** was synthesised using the same method as for **C2**, with the addition of 3,4,5,6-tetramethyl-1,10-phenanthroline (40 mg, 0.17 mmol) as opposed to 1,10-phenanthroline to yield **C6** (127 mg, 0.13 mmol, 83%).

<sup>1</sup>H NMR (500 MHz, CDCl<sub>3</sub>) δ 8.70 (d, *J* = 8.2 Hz, 2H, H<sub>4</sub> and H<sub>7</sub>), 8.23 (s, 2H, H<sub>10</sub> and H<sub>17</sub>), 8.22 (s, 2H, H<sub>5</sub> and H<sub>6</sub>), 7.94 (s, 2H, H<sub>13</sub> and H<sub>14</sub>), 7.84 (d, *J* = 8.2 Hz, 2H, H<sub>3</sub> and H<sub>8</sub>), 6.17 (s, 4H, H<sub>Ar</sub>), 2.65 (s, 6H, H<sub>Me</sub> of phenanthroline), 2.49 (s, 6H, H<sub>Me</sub> of phenanthroline), 1.80 (s, 12H, H<sub>Me</sub> of aryl), 0.65 (s, 18H H<sub>tBu</sub>).

<sup>13</sup>C NMR (125 MHz, CDCl<sub>3</sub>) δ 158.8, 150.8, 148.7 (CH), 143.9, 142.5, 141.7, 137.2 (CH), 137.0, 134.3, 132.2, 128.0, 126.9 (CH), 126.5, 126.4 (CH), 123.2 (CH), 122.3 (CH), 33.6, 30.6 (CH<sub>3</sub>), 20.4 (CH<sub>3</sub>), 17.5 (CH<sub>3</sub>), 14.7 (CH<sub>3</sub>).

MS ESI: calcd for C<sub>52</sub>H<sub>56</sub>CuN<sub>4</sub> (M – PF<sub>6</sub>)<sup>+</sup> 799.38; obsd 799.38.

[Cu(2,9-(4-(*tert*-butyl)-2,6-dimethylphenyl)-1,10-phenanthroline)(4,4'-dimethyl-2,2'-bipyridine)]PF<sub>6</sub> (**C7**)



Chemical formula:  $C_{48}H_{52}CuF_6N_4P$

Exact mass: 892.31

Molecular weight: 893.48

Complex **C7** was obtained by using the procedure followed for **C2**, replacing 1,10-phenanthroline by 4,4'-dimethyl-2,2'-bipyridine (35 mg 0.17 mmol). Complex **C7** was isolated as an orange-red solid (96 mg, 0.13 mmol, 83%).

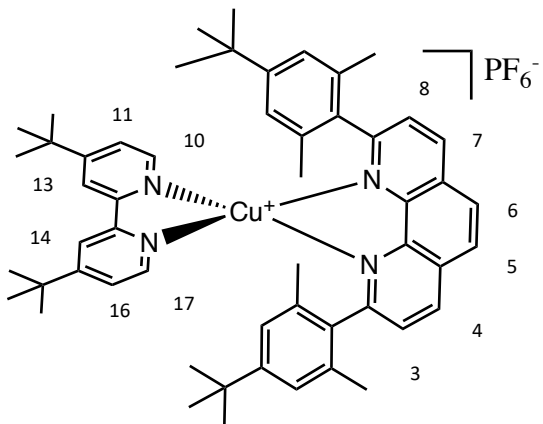
<sup>1</sup>H NMR (500 MHz, CDCl<sub>3</sub>) δ 8.66 (d, *J* = 8.1 Hz, 2H, H<sub>4</sub> and H<sub>7</sub>), 8.18 (s, 2H, H<sub>5</sub> and H<sub>6</sub>), 7.96 (d, *J* = 5.2 Hz, 2H, H<sub>10</sub> and H<sub>17</sub>), 7.83 (d, *J* = 8.1 Hz, 2H, H<sub>3</sub> and H<sub>8</sub>), 7.59 (s, 2H, H<sub>13</sub> and H<sub>14</sub>), 7.17 (d, *J* = 5.2 Hz, 2H, H<sub>11</sub> and H<sub>16</sub>), 6.45 (s, 4H, H<sub>Ar</sub>), 2.45 (s, 6H, H<sub>Me</sub>), 1.78 (s, 12H, H<sub>Me</sub>), 0.98 (s, 18H, H<sub>tBu</sub>).

<sup>13</sup>C NMR (125 MHz, CDCl<sub>3</sub>) δ 158.9, 151.1, 150.8, 148.9, 147.6 (CH), 143.8, 137.1 (CH), 137.0, 134.4, 127.8, 126.7 (CH), 126.4 (CH), 126.0 (CH), 123.6 (CH), 121.4 (CH), 34.0, 31.0 (CH<sub>3</sub>), 21.3 (CH<sub>3</sub>), 20.5 (CH<sub>3</sub>).

Anal. calcd for  $C_{48}H_{52}CuF_6N_4P \cdot H_2O$ : C, 64.53; H, 5.87; N, 6.27. Found: C, 64.24; H, 5.87; N, 6.23.

Crystal data from Et<sub>2</sub>O/CH<sub>2</sub>Cl<sub>2</sub> for **C7**. C<sub>48</sub>H<sub>52</sub>CuF<sub>6</sub>N<sub>4</sub>P, M = 893.44 g·mol<sup>-1</sup>, orthorhombic, space group Pbca,  $a = 20.1400(4)$  Å,  $b = 19.3338(4)$  Å,  $c = 23.5931(4)$  Å,  $\alpha = 90^\circ$ ,  $\beta = 90^\circ$ ,  $\gamma = 90^\circ$ , V = 9186.7(3) Å<sup>3</sup>, Z = 8,  $\rho_{\text{calc}} = 1.292$  Mg/m<sup>3</sup>, T = 173(2) K, MoK<sub>α</sub> = 0.71073,  $3.68 < \theta < 63.84$ , transmission factors: T<sub>min</sub>/T<sub>max</sub> = 0.5553/0.7528, 8127 reflections measured, 5749 unique reflections, R<sub>1</sub> = 0.0606, wR<sub>2</sub> = 0.1595, GoF = 1.048.

**[Cu(2,9-(4-(*tert*-butyl)-2,6-dimethylphenyl)-1,10-phenanthroline)(4,4'-(*tert*-butyl)-2,2'-bipyridine)]PF<sub>6</sub> (C8)**



Chemical formula: C<sub>54</sub>H<sub>64</sub>CuF<sub>6</sub>N<sub>4</sub>P

Exact mass: 976.41

Molecular weight: 977.64

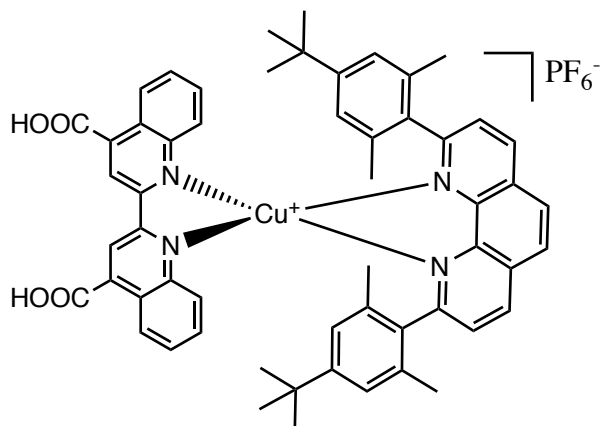
Complex **C8** was obtained by using the procedure followed for **C2**, replacing 1,10-phenanthroline by 4,4'-ditert-butyl-2,2'-bipyridine (46 mg, 0.17 mmol). Complex **C8** was isolated as an orange-red solid in 83% yield (85 mg, 0.087 mmol, 54%).

<sup>1</sup>H NMR (500 MHz, CDCl<sub>3</sub>) δ 8.70 (d, *J* = 8.2 Hz, 2H, H<sub>4</sub> and H<sub>7</sub>), 8.23 (s, 2H, H<sub>5</sub> and H<sub>6</sub>), 8.12 (d, *J* = 5.5 Hz, 2H, H<sub>10</sub> and H<sub>17</sub>), 7.84 (d, *J* = 8.2 Hz, 2H, H<sub>3</sub> and H<sub>8</sub>), 7.64 (d, *J* = 1.8 Hz, 2H, H<sub>13</sub> and H<sub>14</sub>), 7.42 (dd, *J* = 5.6, 1.8 Hz, 2H, H<sub>11</sub> and H<sub>16</sub>), 6.42 (s, 4H, H<sub>Ar</sub>), 1.81 (s, 12H, H<sub>Me</sub>), 1.43 (s, 18H, H<sub>tBu</sub>), 0.99 (s, 18H, H<sub>tBu</sub>).

<sup>13</sup>C NMR (125 MHz, CDCl<sub>3</sub>) δ 161.4, 158.8, 150.9, 150.9, 148.1 (CH), 143.8, 137.3 (CH), 137.3 (CH), 134.5, 127.9, 126.8 (CH), 126.3 (CH), 123.3 (CH), 122.6 (CH), 116.6 (CH), 35.3, 34.0, 31.1 (CH), 30.5 (CH), 20.5 (CH).

MS ESI: calcd for C<sub>54</sub>H<sub>64</sub>CuN<sub>4</sub> (M – PF<sub>6</sub>)<sup>+</sup> 831.44 obsd 831.44

[Cu(2,9-(4-(*tert*-butyl)-2,6-dimethylphenyl)-1,10-phenanthroline)(2,2'-Biquinoline-4,4'-dicarboxylic acid)]PF<sub>6</sub> (**C9**)



Chemical formula: C<sub>56</sub>H<sub>52</sub>CuF<sub>6</sub>N<sub>4</sub>PO<sub>4</sub>

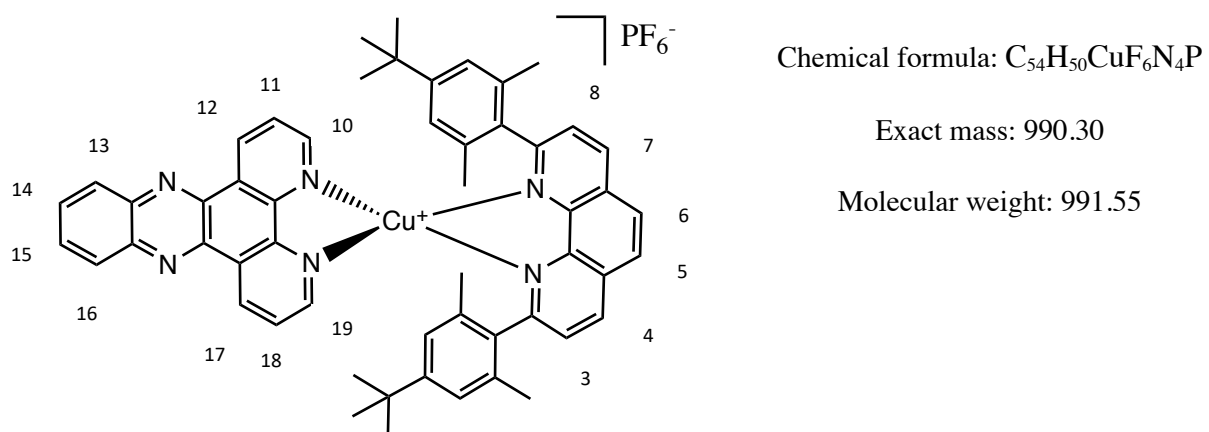
Exact mass: 907.33

Molecular weight: 908.60

The carboxylic acid group present on the biquinoline meant that the NMR was exceedingly broad. On addition of a base, in order to prevent this problem, the complex partially broke down into the ligand and hence made characterisation difficult. Therefore, characterisation could not be shown for this complex.

MS ESI: calcd for C<sub>54</sub>H<sub>64</sub>CuN<sub>4</sub> (M – PF<sub>6</sub>)<sup>+</sup> 907.33 obsd 907.33

[Cu(2,9-(4-(*tert*-butyl)-2,6-dimethylphenyl)-1,10-phenanthroline)(dipyridophenazine)]PF<sub>6</sub> (**C10**)



Complex **C10** was synthesised using the same method as for **C2**, with the addition of dipyridophenazine (44 mg, 0.16 mmol) as opposed to 1,10-phenanthroline to yield **C10** (100 mg, 0.10 mmol, 63%).

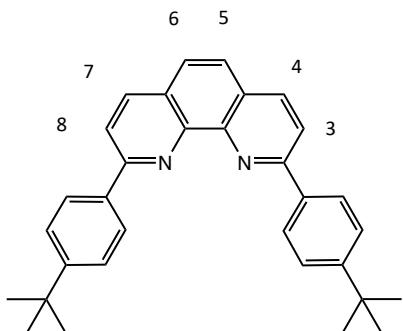
<sup>1</sup>H NMR (500 MHz, CDCl<sub>3</sub>) δ 9.64 (dd, *J* = 8.1, 1.5 Hz, 2H, H<sub>10</sub> and H<sub>19</sub>), 8.72 (d, *J* = 8.2 Hz, 2H, H<sub>4</sub> and H<sub>7</sub>), 8.66 (dd, *J* = 4.9, 1.5 Hz, 2H, H<sub>12</sub> and H<sub>18</sub>), 8.42 (dd, *J* = 6.5, 3.5 Hz, 2H, H<sub>13</sub> and H<sub>16</sub>), 8.25 (s, 2H, H<sub>5</sub> and H<sub>6</sub>), 8.04 (dd, *J* = 6.5, 3.5 Hz, 2H, H<sub>14</sub> and H<sub>15</sub>), 7.95 (dd, *J* = 8.1, 4.9 Hz, 2H, H<sub>11</sub> and H<sub>18</sub>), 7.85 (d, *J* = 8.2 Hz, 2H, H<sub>3</sub> and H<sub>7</sub>), 6.23 (s, 4H, H<sub>Ar</sub>), 1.83 (s, 12H, H<sub>Me</sub>), 0.41 (s, 18H, H<sub>tBu</sub>).

<sup>13</sup>C NMR (125 MHz, CDCl<sub>3</sub>) δ 159.0, 151.1, 149.5 (CH), 144.7, 143.9, 142.6, 139.6, 137.6 (CH), 137.2, 134.5, 133.7 (CH), 131.7 (CH), 129.7 (CH), 128.0, 127.8, 126.9 (CH), 126.4 (CH), 125.9 (CH), 123.2 (CH), 33.5, 30.4 (CH), 20.5 (CH).

MS ESI: calcd for C<sub>54</sub>H<sub>50</sub>CuN<sub>6</sub> (M – PF<sub>6</sub>)<sup>+</sup> 845.34; obsd 845.34.

Crystal data from Et<sub>2</sub>O/CH<sub>2</sub>Cl<sub>2</sub> for **C10**. C<sub>56</sub>H<sub>54</sub>Cl<sub>4</sub>CuF<sub>6</sub>N<sub>4</sub>P, M = 1161.36 g.mol<sup>-1</sup>, monoclinic, space group P 21/c, *a* = 10.5002(4) Å, *b* = 40.819(2) Å, *c* = 12.7406(6) Å, α = 90°, β = 96.385(2) °, γ = 90°, V = 5426.9(4) Å<sup>3</sup>, Z = 4, ρ<sub>calc</sub> = 1.421 Mg/m<sup>3</sup>, T = 120(2) K, MoK<sub>α</sub> = 0.71073, 2.20 < θ < 27.87, transmission factors: T<sub>min</sub>/T<sub>max</sub> = 0.7151/0.7456, 13008 reflections measured, 10771 unique reflections, R<sub>1</sub> = 0.0597606, wR<sub>2</sub> = 0.1628, GoF = 1.033.

2,9-bis(4-(*tert*-butyl)phenyl)-1,10-phenanthroline (**L4**)



Chemical formula: C<sub>32</sub>H<sub>32</sub>N<sub>2</sub>

Exact mass: 444.26

Molecular weight: 444.62

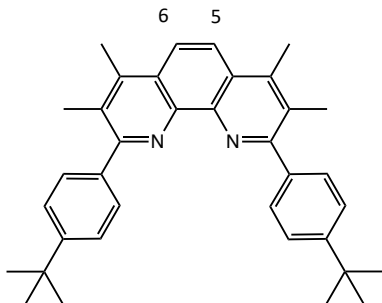
Under argon and at 0 °C, lithium (1.00 g, 0.139 mol) was added in small chunks to degassed dry diethyl ether (40 mL). 1-bromo-4-*tert*-butyl-benzene (4.8 mL, 0.0277 mol) in dry diethyl ether (20 mL) was added dropwise. The resulting solution turned grey as it was stirred at room temperature for 16 h. A broken pipette Pasteur helped break up the chunks of lithium. This solution was then transferred into an addition funnel *via* cannula and added dropwise to a solution of 1,10-phenanthroline (1.00 g, 5.55 mmol) in dry toluene (50 mL) at 0 °C. The resulting red solution was stirred at rt for 24 h under argon. Water (50 mL) was slowly added, rendering a yellow solution. The organic phase was extracted and washed with dichloromethane (3x 50 mL). MnO<sub>2</sub> (20 g) was added to the combined organic phases and the resulting suspension was stirred for 4 h. MgSO<sub>4</sub> (25 g) was added and the solution was stirred for half an hour. The solution was then filtered over a pad of MgSO<sub>4</sub> and the solvent was evaporated. After column chromatography (SiO<sub>2</sub>; 1:1 cyclohexane:dichloromethane to dichloromethane) titled product was obtained (1.88 g, 4.24 mmol, 76%).

<sup>1</sup>H NMR (500 MHz, CDCl<sub>3</sub>) δ 8.40 (d, *J* = 8.5 Hz, 4H, H<sub>Ar</sub>), 8.29 (d, *J* = 8.4 Hz, 2H, H<sub>4</sub> and H<sub>7</sub>), 8.13 (d, *J* = 8.4 Hz, 2H, H<sub>3</sub> and H<sub>8</sub>), 7.77 (s, 2H, H<sub>5</sub> and H<sub>6</sub>), 7.62 (d, *J* = 8.5 Hz, 4H, H<sub>Ar</sub>), 1.42 (s, 18H, H<sub>tBu</sub>).

<sup>13</sup>C NMR (125 MHz, CDCl<sub>3</sub>) δ 156.8, 152.6, 146.2, 136.8 (CH), 136.8, 127.8, 127.4 (CH), 125.9 (CH), 125.8 (CH), 119.8 (CH), 34.8, 31.4 (CH<sub>3</sub>).

MS ESI: calcd for C<sub>32</sub>H<sub>32</sub>N<sub>2</sub> (M + H<sup>+</sup>) 445.2638 obsd 445.2661

2,9-bis(4-(*tert*-butyl)phenyl)-3,4,7,8-tetramethyl-1,10-phenanthroline (**L5**)



Chemical formula: C<sub>36</sub>H<sub>40</sub>N<sub>2</sub>

Exact mass: 500.32

Molecular weight: 500.73

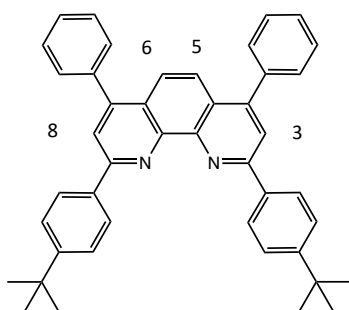
**L5** was obtained by using the procedure followed for **L4**, replacing 1,10-phenanthroline with 3,4,7,8-tetramethyl-1,10-phenanthroline (1.50 g, 6.35 mmol) to afford the titled product (2.70 g, 5.4 mmol, 85%).

<sup>1</sup>H NMR (500 MHz, CDCl<sub>3</sub>) δ 8.04 (s, 2H, H<sub>5</sub> and H<sub>6</sub>), 7.64 – 7.60 (m, 4H, H<sub>Ar</sub>), 7.50 – 7.45 (m, 4H, H<sub>Ar</sub>), 2.74 (s, 6H, H<sub>Me</sub>), 2.49 (s, 6H, H<sub>Me</sub>), 1.37 (s, 18H, H<sub>tBu</sub>).

<sup>13</sup>C NMR (126 MHz, CDCl<sub>3</sub>) δ 159.5, 150.6, 142.3, 138.9, 129.5 (CH), 128.7, 126.2, 124.8 (CH), 121.8 (CH), 34.7, 31.4 (CH<sub>3</sub>), 18.0, (CH<sub>3</sub>), 15.3 (CH<sub>3</sub>).

MS ESI: calcd for C<sub>36</sub>H<sub>40</sub>N<sub>2</sub> (M +H<sup>+</sup>) 501.3264 obsd 501.3253

2,9-bis(4-(*tert*-butyl)phenyl)-4,7-diphenyl-1,10-phenanthroline (**L6**)



Chemical formula: C<sub>44</sub>H<sub>40</sub>N<sub>2</sub>

Exact mass: 596.32

Molecular weight: 596.82

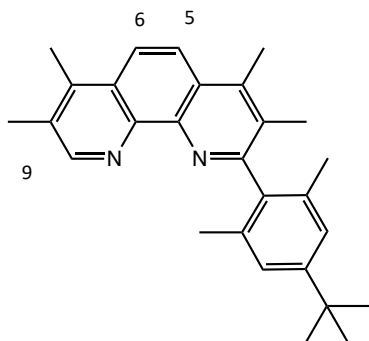
**L6** was obtained by using the procedure followed for **L4**, replacing 1,10-phenanthroline with bathophenanthroline (935 mg, 2.80 mmol) to afford the titled product (1.142 g, 1.91 mmol, 68%).

<sup>1</sup>H NMR (500 MHz, CDCl<sub>3</sub>) δ 8.47 – 8.42 (m, 4H, H<sub>Ar</sub>), 8.07 (s, 2H, H<sub>5</sub> and H<sub>6</sub>), 7.79 (s, 2H, H<sub>3</sub> and H<sub>8</sub>), 7.64 – 7.61 (m, 4H, H<sub>Ar</sub>), 7.61 – 7.48 (m, 10H), 1.43 (s, 18H, H<sub>tBu</sub>).

<sup>13</sup>C NMR (125 MHz, CDCl<sub>3</sub>) δ 156.2, 152.6, 149.0, 146.9, 138.7, 136.9, 129.8 (CH), 128.6 (CH), 128.4 (CH), 127.5 (CH), 125.8 (CH), 125.7, 123.4 (CH), 120.4 (CH), 34.8, 31.4 (CH<sub>3</sub>).

MS ESI: calcd for C<sub>44</sub>H<sub>40</sub>N<sub>2</sub> (M + H<sup>+</sup>) 597.3264 obsd 597.3257

2-(4-(*tert*-butyl)-2,6-dimethylphenyl)-3,4,7,8-tetramethyl-1,10-phenanthroline (**L7**)



Chemical formula: C<sub>28</sub>H<sub>32</sub>N<sub>2</sub>

Exact mass: 396.26

Molecular weight: 396.58

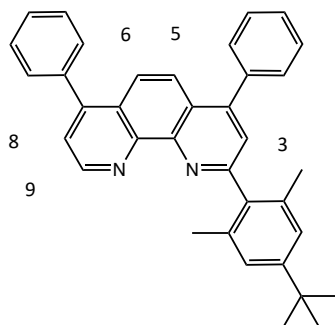
**L7** was obtained by using the procedure followed for **L1**, replacing 1,10-phenanthroline with 3,4,7,8-tetramethylphenanthroline (750 mg, 3.17 mmol). A column (SiO<sub>2</sub>; cyclohexane:dichloromethane 1:1 to 1% methanol in dichloromethane) afforded the titled product (768 mg, 19.94 mmol, 61%).

<sup>1</sup>H NMR (500 MHz, CDCl<sub>3</sub>) δ 8.92 (s, 1H, H<sub>9</sub>), 8.08 (d, *J* = 9.5 Hz, 1H, H<sub>5 or 6</sub>), 8.03 (d, *J* = 9.5 Hz, 1H, H<sub>5 or 6</sub>), 7.08 (s, 2H, H<sub>aryl</sub>), 2.75 (s, 3H, H<sub>Me</sub>), 2.69 (s, 3H, H<sub>Me</sub>), 2.50 (s, 3H, H<sub>Me</sub>), 2.22 (s, 3H, H<sub>Me</sub>), 1.96 (s, 6H, H<sub>Me</sub>), 1.34 (s, 9H, H<sub>tBu</sub>).

<sup>13</sup>C NMR (125 MHz, CDCl<sub>3</sub>) δ 160.6, 151.6 (CH), 150.0, 141.5, 141.2, 138.4, 135.1, 130.2, 129.9, 127.0, 126.0, 124.4 (CH), 122.3 (CH), 121.5 (CH), 34.3, 31.5, 31.4 (3 x CH<sub>3</sub>), 20.3 (2 x CH<sub>3</sub>), 17.5 (CH<sub>3</sub>), 16.1 (CH<sub>3</sub>), 15.1 (CH<sub>3</sub>), 14.5 (CH<sub>3</sub>).

MS ESI: calcd for C<sub>28</sub>H<sub>32</sub>N<sub>2</sub> (M + H<sup>+</sup>) 397.2638 obsd 397.2663

2-(4-(*tert*-butyl)-2,6-dimethylphenyl)-4,7-diphenyl-1,10-phenanthroline (**L8**)



Chemical formula: C<sub>36</sub>H<sub>32</sub>N<sub>2</sub>

Exact mass: 492.26

Molecular weight: 492.67

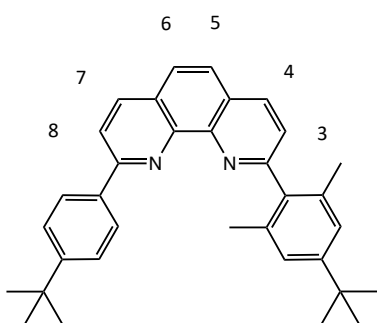
**L8** was obtained by using the procedure followed for **L1**, replacing 1,10-phenanthroline with bathophenanthroline (750 mg, 2.26 mmol) and using only 2 eq. of the ArLi in order to favour the monosubstituted product. A column (SiO<sub>2</sub>; cyclohexane:dichloromethane 1:1 to 1% methanol in dichloromethane) afforded the titled product (973 mg, 1.97 mmol, 87%).

<sup>1</sup>H NMR (500 MHz, CDCl<sub>3</sub>) δ 9.25 (d, *J* = 4.5 Hz, 1H, H<sub>9</sub>), 7.94 (d, *J* = 9.5 Hz, 1H, H<sub>5 or 6</sub>), 7.86 (d, *J* = 9.4 Hz, 1H, H<sub>5 or 6</sub>), 7.60 (s, 1H, H<sub>3</sub>), 7.58 – 7.47 (m, 11H, H<sub>ph</sub> and H<sub>8</sub>), 7.15 (s, 2H, H<sub>aryl</sub>), 2.19 (d, *J* = 0.6 Hz, 6H, H<sub>Me</sub>), 1.36 (s, 9H, H<sub>tBu</sub>).

<sup>13</sup>C NMR (125 MHz, CDCl<sub>3</sub>) δ 160.3, 150.8, 149.8 (CH), 148.4, 148.3, 147.0, 138.4, 138.2, 138.1, 135.7, 135.7, 129.8 (2 x CH), 129.7 (2 x CH), 128.6 (4 x CH), 128.4 (CH), 128.4 (CH), 126.6, 125.1 (CH), 124.8, 124.6 (CH), 124.0 (CH), 123.7 (CH), 123.3 (CH), 34.4, 31.4 (CH<sub>3</sub>), 21.0 (CH<sub>3</sub>).

MS ESI: calcd for C<sub>36</sub>H<sub>32</sub>N<sub>2</sub> (M + H<sup>+</sup>) 493.2638 obsd 493.2637

2-(4-(*tert*-butyl)-2,6-dimethylphenyl)-9-(4-(*tert*-butyl)phenyl)-1,10-phenanthroline (**L9**)



Chemical formula: C<sub>34</sub>H<sub>36</sub>N<sub>2</sub>

Exact mass: 472.29

Molecular weight: 472.68

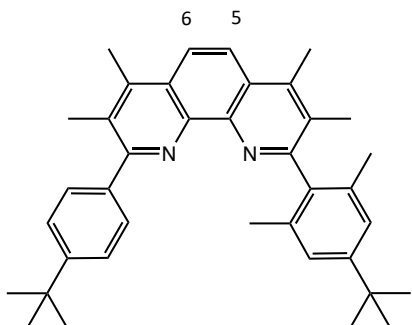
**L9** was obtained by using the procedure followed for **L4**, replacing 1,10-phenanthroline with **L1** (2.00 g, 5.87 mmol) to afford the titled product (621 mg, 1.31 mmol, 22%).

<sup>1</sup>H NMR (500 MHz, CDCl<sub>3</sub>) δ 8.27 (2d, *J* = 8.4 Hz, 2H, H<sub>4</sub> and H<sub>7</sub>), 8.23 – 8.20 (m, 2H, H<sub>aryl</sub>), 8.07 (d, *J* = 8.4 Hz, 1H, H<sub>8</sub>), 7.80 (s, 2H, H<sub>5</sub> and H<sub>6</sub>), 7.62 (d, *J* = 8.1 Hz, 1H, H<sub>3</sub>), 7.55 – 7.52 (m, 2H, H<sub>aryl</sub>), 7.20 (s, 2H, H<sub>aryl</sub>), 2.28 (d, *J* = 0.7 Hz, 6H, H<sub>Me</sub>), 1.39 (s, 9H, H<sub>tBu</sub>), 1.37 (s, 9H, H<sub>tBu</sub>).

<sup>13</sup>C NMR (125 MHz, CDCl<sub>3</sub>) δ 159.9, 157.4, 152.3, 150.7, 138.0, 137.2, 136.6 (CH), 136.0, 135.6 (CH), 127.6 (CH), 127.5, 127.2, 126.2, 126.0 (CH), 125.9 (CH), 125.7 (CH), 125.4, 125.0 (CH), 124.9 (CH), 120.2 (CH), 34.7, 34.4, 31.4 (CH<sub>3</sub>), 31.3 (CH<sub>3</sub>), 21.3 (CH<sub>3</sub>).

MS ESI: calcd for C<sub>34</sub>H<sub>36</sub>N<sub>2</sub> (M + H<sup>+</sup>) 473.2951 obsd 473.2958

2-(4-(*tert*-butyl)-2,6-dimethylphenyl)-9-(4-(*tert*-butyl)phenyl)-3,4,7,8-tetramethyl-1,10-phenanthroline (**L10**)



Chemical formula: C<sub>38</sub>H<sub>44</sub>N<sub>2</sub>

Exact mass: 528.35

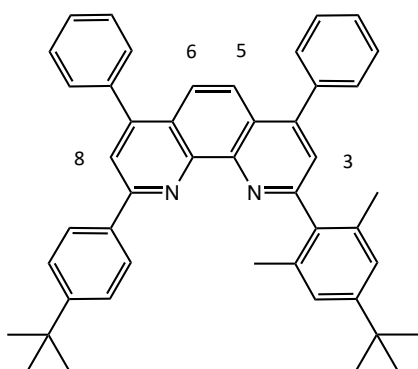
Molecular weight: 528.78

Under argon and at -78 °C, n-BuLi (3.5 mL of a 1.6 M solution, 5.54 mmol) was added slowly to a solution of 1-bromo-4-*tert*-butyl-benzene (0.9 mL, 5.04 mmol) in dry THF (15 mL). The solution was then stirred for 2 h. A degassed solution of **L7** (400 mg, 1.01 mmol) in dry toluene (30 mL) was added to the solution via cannula transfer. The solution was stirred at rt under argon for 16 h. The same procedure as carried out for isolating **L1** was used for the work up to afford **L10** (52 mg, 0.049 mmol, 5%)

<sup>1</sup>H NMR (300 MHz, CDCl<sub>3</sub>) δ 8.06 (s, 2H, H<sub>5</sub> and H<sub>6</sub>), 7.56 (m, 2H, H<sub>aryl</sub>), 7.45 (m, 2H, H<sub>aryl</sub>), 7.10 (s, 2H, H<sub>aryl</sub>), 2.75 (2s, 6H, H<sub>Me</sub>), 2.47 (s, 3H, H<sub>Me</sub>), 2.22 (s, 3H, H<sub>Me</sub>), 2.01 (s, 6H, H<sub>Me</sub>), 1.35 (2s, 18H, H<sub>tBu</sub>).

<sup>13</sup>C NMR (125 MHz, CDCl<sub>3</sub>) δ 159.9, 159.6, 150.5, 149.9, 144.6, 144.3, 142.2, 141.4, 138.8, 138.0, 135.3, 129.7, 129.5 (CH), 128.7, 126.2, 124.9 (CH), 124.4 (CH), 121.9 (CH), 121.7 (CH), 34.6, 34.4, 31.5 (CH<sub>3</sub>), 31.4 (CH<sub>3</sub>), 26.9, 20.5 (CH<sub>3</sub>), 18.0, 16.1 (CH<sub>3</sub>), 15.3 (CH<sub>3</sub>), 15.2 (CH<sub>3</sub>).

2-(4-(*tert*-butyl)-2,6-dimethylphenyl)-9-(4-(*tert*-butyl)phenyl)-4,7-diphenyl-1,10-phenanthroline  
**(L11)**



Chemical formula: C<sub>46</sub>H<sub>44</sub>N<sub>2</sub>

Exact mass: 624.35

Molecular weight: 624.87

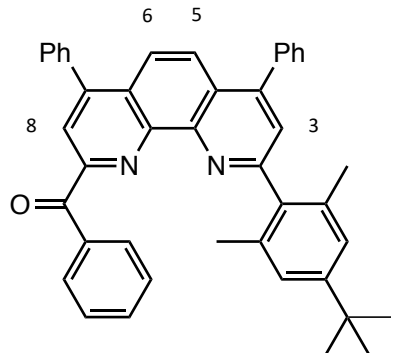
**L11** was obtained by using the procedure followed for **L1**, replacing 1,10 phenanthroline with **L8** (750 mg, 1.52 mmol) to afford the titled product (574 mg, 0.92 mmol, 61%).

<sup>1</sup>H NMR (500 MHz, CDCl<sub>3</sub>) δ 8.28 – 8.24 (m, 2H, H<sub>Ar</sub>), 8.02 (s, 1H, H<sub>8</sub>), 7.88 (d, *J* = 9.3 Hz, 1H H<sub>5</sub> or 6), 7.83 (d, *J* = 9.3 Hz, 1H, H<sub>5</sub> or 6), 7.61 (s, 1H, H<sub>3</sub>), 7.60 – 7.46 (m, 12H, H<sub>Ph</sub>), 7.22 (s, 2H, H<sub>Ar</sub>), 2.39 (s, 6H H<sub>Me</sub>), 1.39 (s, 9H, H<sub>tBu</sub>), 1.38 (s, 9H, H<sub>tBu</sub>).

<sup>13</sup>C NMR (125 MHz, CDCl<sub>3</sub>) δ 159.2, 156.7, 152.4, 150.7, 148.9, 147.7, 147.1, 146.8, 138.7, 138.4, 138.0, 137.2, 136.1, 129.8 (CH), 129.7 (CH), 128.6 (CH), 128.6 (CH), 128.4 (CH), 128.3 (CH), 127.7 (CH), 125.7 (CH), 125.4 (CH), 125.0 (CH), 123.6 (CH), 123.4 (CH), 120.8 (CH), 34.8, 34.4, 31.4 (CH<sub>3</sub>), 31.3 (CH<sub>3</sub>), 21.4 (CH<sub>3</sub>).

MS ESI: calcd for C<sub>36</sub>H<sub>32</sub>N<sub>2</sub> (M + H<sup>+</sup>) 625.3582 obsd 625.3577

(2-(4-(*tert*-butyl)-2,6-dimethylphenyl)-4,7-diphenyl-9-benzoyl-1,10-phenanthroline (**L12**)



Chemical formula: C<sub>43</sub>H<sub>36</sub>N<sub>2</sub>O

Exact mass: 596.28

Molecular weight: 596.77

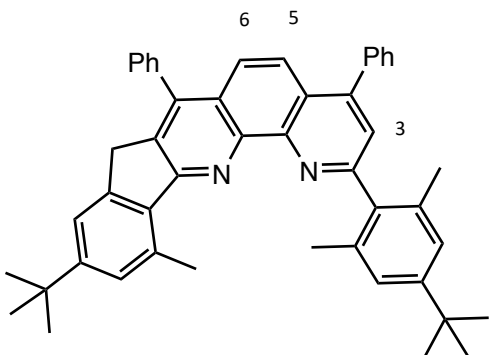
When 5 eq. of the aryl substituent was added with the same amount of bathophenanthroline (750 mg, 2.26 mmol), the synthesis of **L8** also led to the formation of **L12** (13 mg, 0.0218 mmol, 1%)

<sup>1</sup>H NMR (500 MHz, CDCl<sub>3</sub>) δ 8.70 – 8.64 (m, 2H, H<sub>benzoyl</sub>), 8.35 (s, 1H, H<sub>8</sub>), 8.07 (d, *J* = 9.5 Hz, 1H, H<sub>5</sub>), 7.97 (d, *J* = 9.5 Hz, 1H, H<sub>6</sub>), 7.69 (s, 1H, H<sub>3</sub>), 7.66 – 7.39 (m, 13H, H<sub>Ph</sub> and H<sub>benzoyl</sub>), 7.18 (s, 2H, H<sub>Ar</sub>), 2.38 (s, 6H, H<sub>Me</sub>), 1.37 (s, 9H, H<sub>tBu</sub>).

<sup>13</sup>C NMR (125 MHz, CDCl<sub>3</sub>) δ 192.8 (CO), 159.9, 154.0, 151.0, 149.6, 148.0, 146.9, 145.6, 138.0, 137.8, 137.6, 136.5, 136.0, 136.0, 133.0 (CH), 132.3 (CH), 129.8 (CH), 129.8 (CH), 128.8 (CH), 128.8 (CH), 128.7 (CH), 128.6 (CH), 128.1 (CH), 127.8, 126.1 (CH), 126.0 (CH), 125.0 (CH), 123.5 (CH), 123.4 (CH), 34.4, 31.4 (CH<sub>3</sub>), 21.4 (CH<sub>3</sub>).

MS ESI: calcd for C<sub>43</sub>H<sub>36</sub>N<sub>2</sub>O (M + H<sup>+</sup>) 597.29 obsd 597.29

### Cyclised phenanthroline (**L13**)



Chemical formula: C<sub>48</sub>H<sub>46</sub>N<sub>2</sub>

Exact mass: 650.37

Molecular weight: 650.91

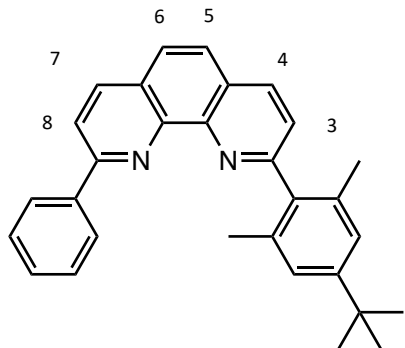
When 5 eq. of the aryl substituent was added with the same amount of bathophenanthroline (750 mg, 2.26 mmol), the synthesis of **L8** also led to the formation of **L13** (21 mg, 0.032 mmol, 1%)

<sup>1</sup>H NMR (500 MHz, CDCl<sub>3</sub>) δ 7.82 (d, *J* = 9.3 Hz, 1H, H<sub>5</sub> or 6), 7.65 (d, *J* = 9.3 Hz, 1H, H<sub>5</sub> or 6), 7.62 (s, 1H, H<sub>3</sub>), 7.60 – 7.45 (m, 10H, H<sub>Ph</sub>), 7.38 (s, 1H, H<sub>aryl</sub>), 7.31 (s, 1H, H<sub>aryl</sub>), 7.24 (s, 2H, H<sub>aryl</sub>), 3.87 (s, 2H, CH<sub>2</sub>), 3.27 (s, 3H, H<sub>Me</sub>), 2.49 (s, 6H, H<sub>Me</sub>), 1.40 (2s, 18H, H<sub>tBu</sub>).

<sup>13</sup>C NMR (125 MHz, CDCl<sub>3</sub>) δ 162.7, 158.5, 152.4, 150.6, 147.4, 146.7, 146.6, 145.4, 142.8, 138.7, 137.8, 137.0, 136.4, 136.4, 136.3, 135.3, 129.8 (CH), 129.5 (CH), 128.7 (CH), 128.6 (CH), 128.2 (CH), 128.1 (CH), 127.0, 125.3 (CH), 125.2, (CH) 124.9 (CH), 124.3 (CH), 124.0 (CH), 122.4 (CH), 119.1 (CH), 34.9, 34.5, 34.2 (CH<sub>2</sub>), 31.5 (CH<sub>3</sub>), 31.5 (CH<sub>3</sub>), 26.9 (CH<sub>3</sub>), 21.6 (CH<sub>3</sub>), 19.7 (CH<sub>3</sub>).

MS ESI: calcd for C<sub>48</sub>H<sub>46</sub>N<sub>2</sub> (M + H<sup>+</sup>) 651.38 obsd 651.37

2-(4-(*tert*-butyl)-2,6-dimethylphenyl)-9-phenyl-1,10-phenanthroline (**L14**)



Chemical formula: C<sub>30</sub>H<sub>28</sub>N<sub>2</sub>

Exact mass: 416.23

Molecular weight: 416.57

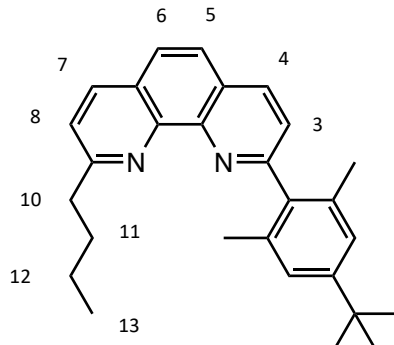
Under argon and at 0 °C, PhLi (5.9 mmol, 3.3 mL, 1.8 M in dibutyl ether) was added dropwise to a solution of **L1** (500 mg, 1.47 mmol) in dry toluene (10 mL). The black solution was stirred for 16 h at rt. A work up similar to the one described for **L1** afforded **L14** (242 mg, 0.581 mmol, 40%).

<sup>1</sup>H NMR (500 MHz, CDCl<sub>3</sub>) δ 8.34 – 8.24 (m, 4H, H<sub>7</sub>, H<sub>4</sub> and H<sub>ortho</sub>), 8.09 (d, *J* = 8.3 Hz, 1H, H<sub>3</sub>), 7.82 (s, 2H, H<sub>5</sub> and H<sub>6</sub>), 7.64 (d, *J* = 8.1 Hz, 1H, H<sub>8</sub>), 7.50-7.53 (m, 2H, H<sub>meta</sub>), 7.46 – 7.40 (m, 1H, H<sub>para</sub>), 7.20 (s, 2H, H<sub>Ar</sub>) 2.30 (s, 6H, H<sub>Me</sub>), 1.38 (s, 9H, H<sub>tBu</sub>).

<sup>13</sup>C NMR (125 MHz, CDCl<sub>3</sub>) δ 159.9, 157.2, 150.7, 146.4, 146.1, 139.9, 138.0, 136.7 (CH), 136.1, 135.5 (CH), 129.2 (CH), 128.7 (CH), 127.9 (CH), 127.6, 127.2, 126.1 (CH), 126.0 (CH), 125.1 (CH), 124.9 (CH), 120.3 (CH), 34.4, 31.4 (CH<sub>3</sub>), 21.4 (CH<sub>3</sub>).

HRMS ESI: calcd for C<sub>30</sub>H<sub>28</sub>N<sub>2</sub> (M + H<sup>+</sup>) 417.2325; obsd 417.2312.

2-(4-(*tert*-butyl)-2,6-dimethylphenyl)-9-butyl-1,10-phenanthroline (**L15**)



Chemical formula: C<sub>28</sub>H<sub>32</sub>N<sub>2</sub>

Exact mass: 396.26

Molecular weight: 296.58

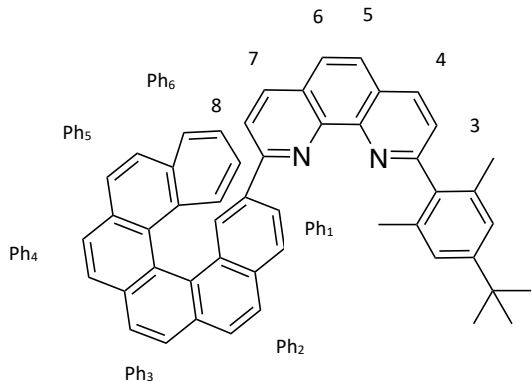
Under argon and at 0 °C, n-BuLi (7.8 mL, 1.6 M in hexane) was added dropwise to **L1** (500 mg, 1.47 mmol) in dry toluene (10 mL). The black solution was stirred for 16 h at r.t. The same procedure as carried out for **L1** was used for the work up to afford **L4** (190 mg, 0.479 mmol, 33%)

<sup>1</sup>H NMR (500 MHz, CDCl<sub>3</sub>) δ 8.25 (d, *J* = 8.2 Hz, 1H, H<sub>4</sub>), 8.14 (d, *J* = 8.2 Hz, 1H, H<sub>7</sub>), 7.76 (s, 2H, H<sub>5</sub> and H<sub>6</sub>), 7.59 (d, *J* = 8.2 Hz, 1H, H<sub>3</sub>), 7.50 (d, *J* = 8.2 Hz, 1H, H<sub>8</sub>), 7.16 (s, 2H, H<sub>Ar</sub>), 3.15 (t, *J* = 8.0 Hz, 2H, H<sub>10</sub>), 2.22 (s, 6H, H<sub>Me</sub>), 1.84 (m, 2H, H<sub>11</sub>), 1.43 (m, 2H, H<sub>12</sub>), 1.37 (s, 9H, H<sub>tBu</sub>), 0.95 (t, *J* = 7.5 Hz, 3H, H<sub>13</sub>).

<sup>13</sup>C NMR (125 MHz, CDCl<sub>3</sub>) δ 163.4, 159.8, 150.2, 146.0, 138.2, 136.1 (CH), 136.0, 135.7 (CH), 127.1, 127.0, 126.2 (CH), 125.4 (CH), 124.8 (CH), 124.7 (CH), 122.8 (CH), 39.0 (CH<sub>2</sub>), 34.4, 32.3 (CH<sub>2</sub>), 31.4 (CH<sub>3</sub>), 31.4, 22.6 (CH<sub>2</sub>), 21.2 (CH<sub>3</sub>), 14.1 (CH<sub>3</sub>).

Anal. calcd for C<sub>28</sub>H<sub>32</sub>N<sub>2</sub>: C, 84.80; H, 8.13; N, 7.06. Found: C, 84.41; H, 8.19; N, 6.63.

2-(4-(*tert*-butyl)-2,6-dimethylphenyl)-9-(hexahelicen-11-yl)-1,10-phenanthroline (**L16**)



Chemical formula: C<sub>50</sub>H<sub>38</sub>N<sub>2</sub>

Exact mass: 666.30

Molecular weight: 666.87

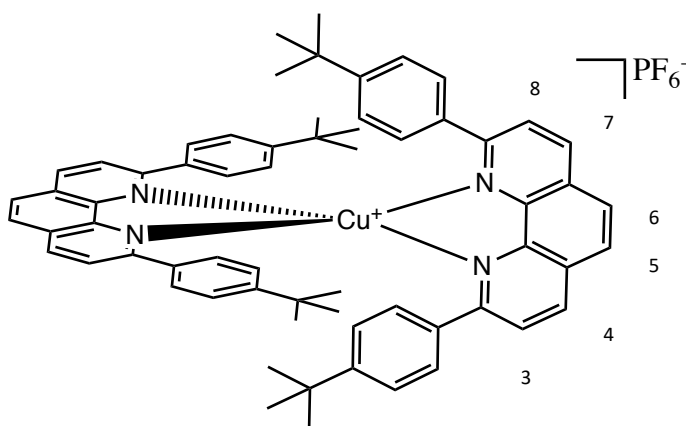
At -78 °C and under argon, n-BuLi (0.57 mL, 1.1 eq.) was added to a colourless solution of the 2-bromo[6]helicene (359 mg, 0.88 mmol) in dry THF (20 mL). The solution turned red and was stirred at -78 °C for half an hour. **L1** (100 mg, 0.293 mmol) was added and the solution was stirred at -78 °C for half an hour and then at rt for 20 h. Water (20 mL) was then added and the organic phase was extracted (3 x dichloromethane). MnO<sub>2</sub> (3.0 g) was added to the organic phase and the suspension was stirred at rt for 4 h. MgSO<sub>4</sub> (5.0 g) was then added and the solution was stirred for half an hour at rt. The solution was then filtered over a pad of MgSO<sub>4</sub>. The solvent was evaporated. A column (1:1 cyclohexane:dichloromethane) afforded the titled product (34 mg, 0.05 mmol, 17%)

<sup>1</sup>H NMR (600 MHz, CDCl<sub>3</sub>) δ 8.53 (d, *J* = 8.3 Hz, 1H, H<sub>7</sub>), 8.41 (s, 1H, H<sub>Ph1</sub>), 8.07 (d, 1H, H<sub>4</sub>), 8.06 – 8.01 (m, 6H, H<sub>Ph1</sub>, H<sub>Ph2</sub> and H<sub>Ph3</sub>), 8.00 (d, *J* = 8.3 Hz, 1H, H<sub>8</sub>), 7.99 – 7.93 (m, 3H, H<sub>Ph4</sub> and H<sub>Ph5</sub>), 7.86 (s, 1H, H<sub>5 or 6</sub>), 7.80 (s, 1H, H<sub>5 or 6</sub>), 7.77 – 7.72 (m, 2H, H<sub>Ph6</sub>), 7.68 (d, 1H, H<sub>3</sub>), 7.19 (s, 2H, H<sub>Ar</sub>), 7.11 (ddd, 1H, H<sub>Ph6</sub>), 6.84 (d, 1H, H<sub>Ph5</sub>), 6.72 (ddd, 1H, H<sub>Ph6</sub>), 2.23 (s, 6H, H<sub>Me</sub>), 1.38 (s, 9H, H<sub>tBu</sub>).

<sup>13</sup>C NMR (125 MHz, CDCl<sub>3</sub>) δ 156.6, 136.6, 136.1, 133.4, 132.7, 132.3, 131.6, 131.5, 129.6, 129.5, 128.6 (CH), 128.4, 128.1, 127.8 (CH), 127.7 (CH), 127.6 (CH), 127.5 (CH), 127.5 (CH), 127.4 (CH), 127.4 (CH), 127.2 (CH), 127.2 (CH), 127.1 (CH), 126.8 (CH), 126.2 (CH), 126.0 (CH), 125.7, 125.2, (CH) 125.1 (CH), 124.0, 34.5, 31.4 (CH<sub>3</sub>), 21.2 (CH<sub>3</sub>). The complexity of **L16** means that not all the quaternary carbon signals are distinguishable.

ESI: calcd for  $C_{50}H_{38}N_2 (M + H^+)$  666.3; obsd 666.4

[Cu(2,9-bis(4-(*tert*-butylphenyl)-1,10-phenanthroline)<sub>2</sub>]PF<sub>6</sub> (**C11**)



Chemical formula: CuC<sub>64</sub>H<sub>64</sub>N<sub>2</sub>PF<sub>6</sub>

Exact mass: 1096.40

Molecular weight: 1097.75

Under argon and at rt, a degassed solution of **L4** (150 mg, 0.34 mmol) in dichloromethane (10 mL) was added *via* cannula transfer to a degassed solution of [Cu(CH<sub>3</sub>CN)<sub>4</sub>]PF<sub>6</sub> (63 mg, 0.17 mmol) in dichloromethane (20 mL). The resulting red solution was stirred for 1 h under argon. Solvent was evaporated and the solid was redissolved in the minimum amount of dichloromethane and precipitated by addition of diethyl ether/pentane (1:1) to afford complex **C11** (138 mg, 0.126 mmol, 74%)

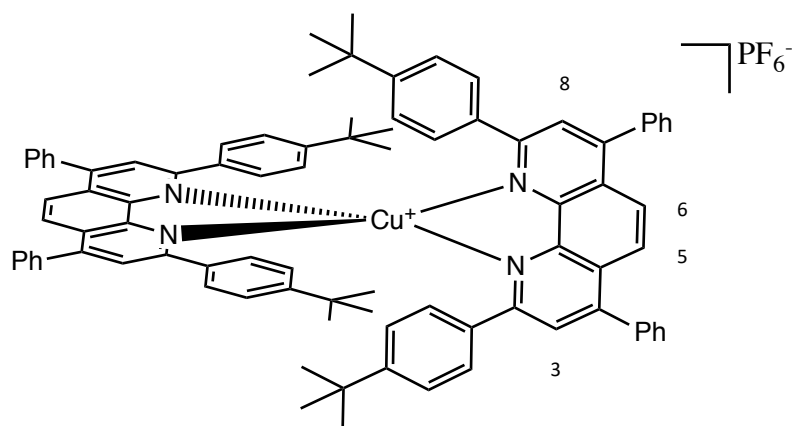
<sup>1</sup>H NMR (500 MHz, CDCl<sub>3</sub>) δ 8.46 (d, *J* = 8.4 Hz, 4H, H<sub>4</sub> and H<sub>7</sub>), 8.04 (s, 4H, H<sub>5</sub> and H<sub>6</sub>), 7.84 (d, *J* = 8.3 Hz, 4H, H<sub>3</sub> and H<sub>8</sub>), 7.45 – 7.40 (m, 8H, H<sub>Ar</sub>), 6.58 – 6.52 (m, 8H, H<sub>Ar</sub>), 0.95 (s, 36H, H<sub>tBu</sub>).

<sup>13</sup>C NMR (125 MHz, CDCl<sub>3</sub>) δ 156.5, 152.7, 143.3, 137.2 (CH), 135.6, 128.1, 127.9 (CH), 126.4 (CH), 124.5 (CH), 124.0 (CH), 34.3, 30.9 (CH<sub>3</sub>).

HRMS ESI: calcd for CuC<sub>64</sub>H<sub>64</sub>N<sub>4</sub> (M-PF<sub>6</sub>) 951.4421; obsd 951.4414.

Crystal data from Et<sub>2</sub>O/CH<sub>2</sub>Cl<sub>2</sub> for **C11**. CuC<sub>64</sub>H<sub>64</sub>N<sub>4</sub>PF<sub>6</sub>; M = 1097.70 g.mol<sup>-1</sup>, triclinic, space group P-1, *a* = 14.7048(6) Å, *b* = 15.2234(6) Å, *c* = 15.6909(7) Å,  $\alpha$  = 66.5840(10) °,  $\beta$  = 65.2480(10) °,  $\gamma$  = 72.911(2) °, V = 2892.7(2) Å<sup>3</sup>, Z = 2,  $\rho_{\text{calc}}$  = 1.260 Mg/m<sup>3</sup>, T = 120(2) K, MoK<sub>α</sub> = 0.71073 Å, 2.42 <  $\theta$  < 27.53, transmission factors: T<sub>min</sub>/T<sub>max</sub> = 0.7012/0.7456, 13867 reflections measured, 11814 unique reflections, R<sub>1</sub> = 0.0680, wR<sub>2</sub> = 0.1427, GoF = 1.086.

[Cu(2,9-bis(4-(*tert*-butyl)phenyl)-4,7-diphenyl-1,10-phenanthroline)<sub>2</sub>]PF<sub>6</sub> (**C12**)



Chemical formula: CuC<sub>88</sub>H<sub>80</sub>N<sub>4</sub>PF<sub>6</sub>

Exact mass: 1338.51

Molecular weight: 1340.07

Complex **C12** was synthesised using the same method as for **C11**, with the addition of **L6** (150 mg, 0.25 mmol), as opposed to **L4**, and [Cu(CH<sub>3</sub>CN)<sub>4</sub>]PF<sub>6</sub> (47 mg, 0.13 mmol) to yield **C12** (159 mg, 0.119 mmol, 91%).

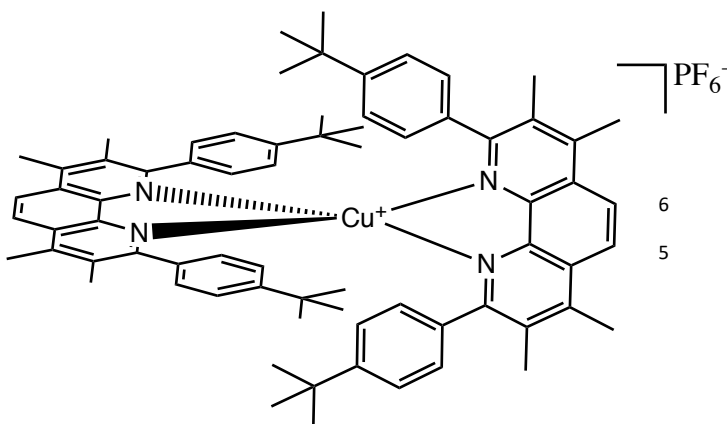
<sup>1</sup>H NMR (500 MHz, CDCl<sub>3</sub>) δ 8.05 (s, 2H, H<sub>5</sub> and H<sub>6</sub>), 7.84 (s, 2H, H<sub>3</sub> and H<sub>8</sub>), 7.66 – 7.58 (m, 10H, H<sub>Ph</sub>), 7.57 (d, *J* = 8.0 Hz, 4H, H<sub>Ar</sub>), 6.68 (d, *J* = 8.0 Hz, 4H, H<sub>Ar</sub>), 0.98 (s, 36H, H<sub>tBu</sub>).

<sup>13</sup>C NMR (125 MHz, CDCl<sub>3</sub>) δ 156.1, 152.6, 149.5, 144.2, 136.6, 136.1, 129.5 (CH), 129.5 (CH), 129.2 (CH), 127.8 (CH), 125.8, 125.2 (CH), 124.1 (CH), 124.1 (CH), 34.4, 31.17 (CH<sub>3</sub>).

HRMS ESI: calcd for C<sub>88</sub>H<sub>80</sub>CuN<sub>4</sub> (M-PF<sub>6</sub>) 1255.5673; obsd 1255.5686.

Crystal data from Et<sub>2</sub>O/CH<sub>2</sub>Cl<sub>2</sub> for **C12**. CuC<sub>88</sub>H<sub>80</sub>N<sub>4</sub>PF<sub>6</sub>; M = 1340.07 g·mol<sup>-1</sup>, monoclinic, space group P 21/n, *a* = 15.1109(4) Å, *b* = 16.1824(5) Å, *c* = 31.3521(8) Å, α = 90°, β = 99.2250(10)°, γ = 90°, V = 7567.4(4) Å<sup>3</sup>, Z = 4, ρ<sub>calc</sub> = 1.296 Mg/m<sup>3</sup>, T = 120(2) K, MoK<sub>α</sub> = 0.71073 Å, 2.34 < θ < 27.85, transmission factors: T<sub>min</sub>/T<sub>max</sub> = 0.956/0.963, 107912 reflections measured, 18100 unique reflections, R<sub>1</sub> = 0.0781, wR<sub>2</sub> = 0.1307, GoF = 1.019.

[Cu(2,9-bis(4-(*tert*-butyl)phenyl)-3,4,7,8-tetramethyl-1,10-phenanthroline)<sub>2</sub>]PF<sub>6</sub> (**C13**)



Chemical formula: CuC<sub>72</sub>H<sub>80</sub>N<sub>4</sub>PF<sub>6</sub>

Exact mass: 1208.53

Molecular weight: 1209.97

Complex **C13** was synthesised using the same method as for **C11**, with the addition of **L5** (150 mg, 0.30 mmol), as opposed to **L4**, and [Cu(CH<sub>3</sub>CN)<sub>4</sub>]PF<sub>6</sub> (56 mg, 0.15 mmol) to yield **C13** (111 mg, 0.094 mmol, 63%).

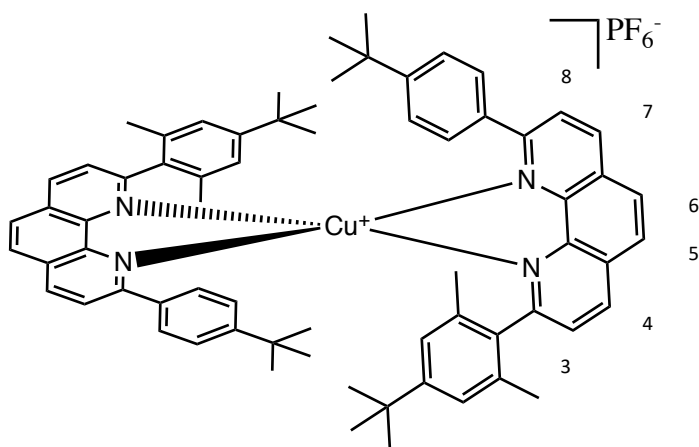
<sup>1</sup>H NMR (500 MHz, CDCl<sub>3</sub>) δ 8.04 (s, 2H, H<sub>5</sub> and H<sub>6</sub>), 7.62 (d, *J* = 8.3 Hz, 8H, H<sub>Ar</sub>), 7.47 (d, *J* = 8.3 Hz, 8H, H<sub>Ar</sub>), 2.74 (s, 12H, H<sub>Me</sub>), 2.49 (s, 12H, H<sub>Me</sub>), 1.37 (s, 36H, H<sub>tBu</sub>).

<sup>13</sup>C NMR (125 MHz, CDCl<sub>3</sub>) δ 159.9, 151.0, 144.4, 142.7, 139.2, 129.9, 129.1 (CH), 126.6, 125.2 (CH), 122.2 (CH), 35.0, 31.8 (CH<sub>3</sub>), 18.4 (CH<sub>3</sub>), 15.6 (CH<sub>3</sub>).

HRMS ESI: calcd for C<sub>72</sub>H<sub>80</sub>CuN<sub>4</sub> (M - PF<sub>6</sub>) 1063.5673; obsd 1063.5688.

Crystal data from Et<sub>2</sub>O/CH<sub>2</sub>Cl<sub>2</sub> for **C13**. CuC<sub>72</sub>H<sub>80</sub>N<sub>4</sub>PF<sub>6</sub>; M = 1209.91 g.mol<sup>-1</sup>, triclinic, space group P - 1, *a* = 10.1378(4) Å, *b* = 16.7629(7) Å, *c* = 19.1290(7) Å,  $\alpha$  = 96.1040(10) °,  $\beta$  = 99.0600(10) °,  $\gamma$  = 105.1770(10) °, V = 3060.9(2) Å<sup>3</sup>, Z = 2,  $\rho_{\text{calc}}$  = 1.313 Mg/m<sup>3</sup>, T = 120(2) K, MoK<sub>α</sub> = 0.71073 Å, 2.121 <  $\theta$  < 27.939, transmission factors: T<sub>min</sub>/T<sub>max</sub> = 0.948/0.957, 86009 reflections measured, 14665 unique reflections, R<sub>1</sub> = 0.0499, wR<sub>2</sub> = 0.1147, GoF = 1.026.

[Cu(2-(4-(*tert*-butyl)-2,6-dimethylphenyl)-9-(4-(*tert*-butyl)phenyl)-1,10-phenanthroline)<sub>2</sub>]PF<sub>6</sub> (**C14**)



Chemical formula: CuC<sub>68</sub>H<sub>72</sub>N<sub>4</sub>PF<sub>6</sub>

Exact mass: 1152.46

Molecular weight: 1153.86

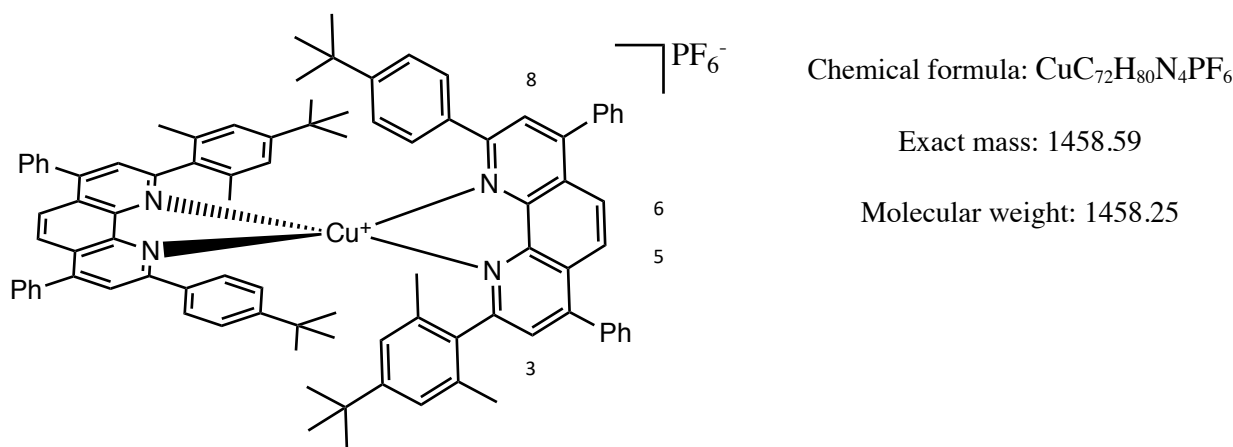
Complex **C14** was synthesised using the same method as for **C11**, with the addition of **L9** (40 mg, 0.085 mmol), as opposed to **L4**, and [Cu(CH<sub>3</sub>CN)<sub>4</sub>]PF<sub>6</sub> (16 mg, 0.048 mmol) to yield **C14** (25 mg, 0.022 mmol, 52%).

<sup>1</sup>H NMR (500 MHz, CDCl<sub>3</sub>) δ 8.56 (d, *J* = 8.1 Hz, 2H, H<sub>4</sub>), 8.41 (d, *J* = 8.5 Hz, 2H, H<sub>7</sub>), 8.12 (d, *J* = 8.8 Hz, 2H, H<sub>5</sub> or 6), 8.02 (d, *J* = 8.8 Hz, 2H, H<sub>5</sub> or 6), 7.96 (d, *J* = 8.5 Hz, 2H, H<sub>8</sub>), 7.86 (d, *J* = 8.5 Hz, 4H, H<sub>Ar</sub>), 7.45 (d, *J* = 8.1 Hz, 2H, H<sub>3</sub>), 6.91 – 6.86 (m, 4H, H<sub>Ar</sub>), 6.48 (s, 2H, H<sub>Ar</sub>), 6.08 (s, 2H, H<sub>Ar</sub>), 1.18 (2s, 24H, H<sub>tBu</sub> and H<sub>Me</sub>), 1.05 (s, 18H, H<sub>tBu</sub>), 0.88 (s, 6H, H<sub>Me</sub>).

<sup>13</sup>C NMR (125 MHz, CDCl<sub>3</sub>) δ 160.0, 156.2, 153.1, 150.5, 144.4, 144.1, 138.0 (CH), 137.7(CH), 135.7, 135.2, 135.0, 133.1, 128.4, 128.2 (CH), 127.7, 127.3 (CH), 127.2 (CH), 126.3 (CH), 124.8 (CH), 124.4 (CH), 124.2 (CH), 122.9 (CH), 34.5 (CH<sub>3</sub>), 34.1, 31.3, 31.0 (CH<sub>3</sub>), 20.0 (CH<sub>3</sub>), 19.8 (CH<sub>3</sub>).

HRMS ESI: calcd for C<sub>68</sub>H<sub>72</sub>CuN<sub>4</sub> (M- PF<sub>6</sub>) 1007.5047; obsd 1007.5023.

[Cu(2-(4-(*tert*-butyl)-2,6-dimethylphenyl)-9-(4-(*tert*-butyl)phenyl)-4,7-diphenyl-1,10-phenanthroline)<sub>2</sub>]PF<sub>6</sub> (**C15**)



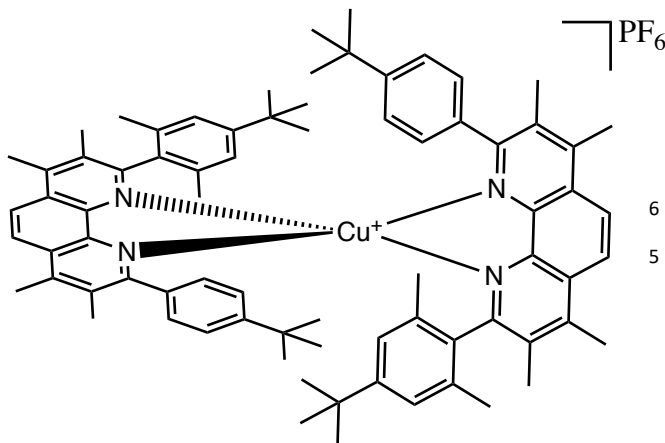
Complex **C15** was synthesised using the same method as for **C11**, with the addition of **L11** (30 mg, 0.048 mmol), as opposed to **L4**, and [Cu(CH<sub>3</sub>CN)<sub>4</sub>]PF<sub>6</sub> (9 mg, 0.024 mmol) to yield **C15** (21 mg, 0.016 mmol, 67%).

<sup>1</sup>H NMR (500 MHz, CDCl<sub>3</sub>) δ 8.13 (s, 4H, H<sub>5</sub> or <sub>6</sub> and H<sub>5</sub> or <sub>6</sub>), 7.94 (s, 2H, H<sub>3</sub>), 7.78 (d, *J* = 8.5 Hz, 4H, H<sub>Ar</sub>), 7.69 – 7.56 (m, 20H, H<sub>Ph</sub>), 7.50 (s, 2H, H<sub>8</sub>), 6.87 (d, *J* = 8.5 Hz, 4H, H<sub>Ar</sub>), 6.54 (s, 2H, H<sub>Ar</sub>), 6.21 (s, 2H, H<sub>Ar</sub>), 1.34 (s, 6H, H<sub>Me</sub>), 1.23 (s, 6H, H<sub>Me</sub>), 1.06 (s, 18H, H<sub>tBu</sub>), 1.00 (s, 18H H<sub>tBu</sub>).

<sup>13</sup>C NMR (125 MHz, CDCl<sub>3</sub>) δ 159.3, 155.9, 153.1, 151.0, 150.3, 145.4, 144.9, 136.5, 129.9 (CH), 129.5 (CH), 129.2 (CH), 129.2 (CH), 128.2 (CH), 127.4, 126.3, 125.1 (CH), 124.9 (CH), 124.7 (CH), 124.3 (CH), 123.3 (CH), 34.6 (CH<sub>3</sub>), 34.1, 31.2, 31.0 (CH<sub>3</sub>), 20.4 (CH<sub>3</sub>), 20.2 (CH<sub>3</sub>).

HRMS ESI: calcd for C<sub>72</sub>H<sub>80</sub>CuN<sub>4</sub> (M- PF<sub>6</sub>) 1311.6299; obsd 1311.6301.

[Cu(2-(4-(*tert*-butyl)-2,6-dimethylphenyl)-9-(4-(*tert*-butyl)phenyl)-3,4,7,8-tetramethyl-1,10-phenanthroline)<sub>2</sub>]PF<sub>6</sub> (**C16**)



Chemical formula: CuC<sub>76</sub>H<sub>88</sub>N<sub>4</sub>PF<sub>6</sub>

Exact mass: 1234.59

Molecular weight: 1236.07

Complex **C16** was synthesised using the same method as for **C11**, with the addition of **L10** (30 mg, 0.057 mmol), as opposed to **L4**, and [Cu(CH<sub>3</sub>CN)<sub>4</sub>]PF<sub>6</sub> (11 mg, 0.028 mmol) to yield **C16** (21mg, 0.018 mmol, 66%).

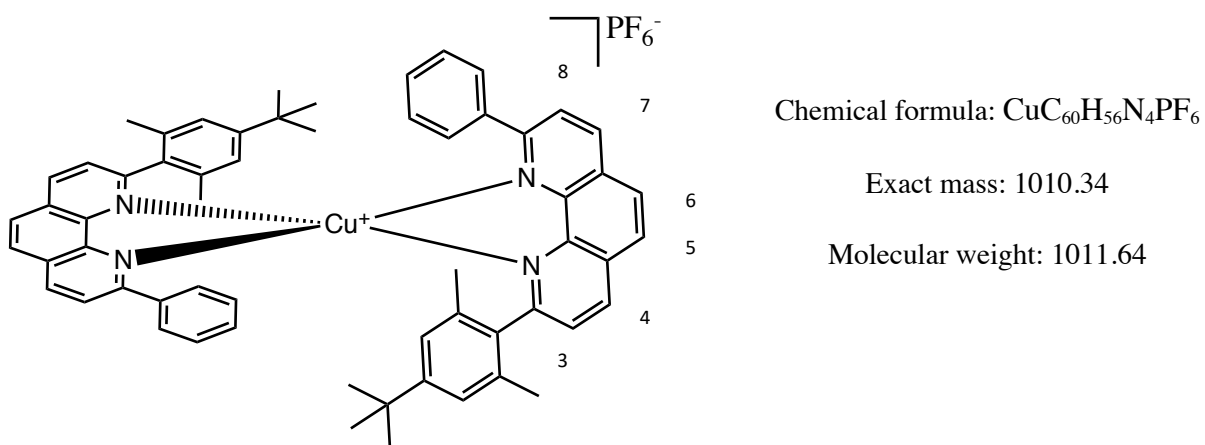
<sup>1</sup>H NMR (500 MHz, CDCl<sub>3</sub>) δ 8.27 (d, *J* = 9.5 Hz, 2H, H<sub>5 or 6</sub>), 8.19 (d, *J* = 9.5 Hz, 2H, H<sub>5 or 6</sub>), 6.69 (s, br, 8H, H<sub>Ar</sub>), 6.52 (s, 2H, H<sub>Ar</sub>), 5.95 (s, 2H, H<sub>Ar</sub>), 2.83 (s, 6H, H<sub>Me</sub>), 2.73 (s, 6H, H<sub>Me</sub>), 2.32 (s, 6H, H<sub>Me</sub>), 1.89 (s, 6H, H<sub>Me</sub>), 1.16 (s, 6H, H<sub>Me</sub>), 1.07 (s, 18H, H<sub>tBu</sub>), 0.96 (s, 18H, H<sub>tBu</sub>), 0.82 (s, 6H, H<sub>Me</sub>).

<sup>13</sup>C NMR (125 MHz, CDCl<sub>3</sub>) δ 159.3, 156.6, 151.3, 150.2, 144.2, 143.6, 142.9, 141.8, 136.9, 135.6, 134.6, 133.4, 133.1, 130.7, 129.4, 127.4, 126.2, 124.2 (CH), 123.6 (CH), 122.9 (CH), 122.9 (CH), 122.3 (CH), 34.3, 33.9, 31.2 (CH<sub>3</sub>), 30.9 (CH<sub>3</sub>), 20.1 (CH<sub>3</sub>), 19.7 (CH<sub>3</sub>), 19.2 (CH<sub>3</sub>), 16.0 (CH<sub>3</sub>), 15.8 (CH<sub>3</sub>), 15.7 (CH<sub>3</sub>).

HRMS ESI: calcd for CuC<sub>76</sub>H<sub>88</sub>N<sub>4</sub> (M- PF<sub>6</sub>) 1119.6299; obsd 1119.6259

Crystal data from Et<sub>2</sub>O/CH<sub>2</sub>Cl<sub>2</sub> for **C16**. CuC<sub>76</sub>H<sub>88</sub>N<sub>4</sub>PF<sub>6</sub>; M = 1236.07 g.mol<sup>-1</sup>, monoclinic, space group P 21/n, *a* = 16.3215(7) Å, *b* = 16.0909(6) Å, *c* = 27.0726(11) Å,  $\alpha$  = 90°,  $\beta$  = 101.344(2)°,  $\gamma$  = 90°, V = 6971.1(5) Å<sup>3</sup>, Z = 4,  $\rho_{\text{calc}}$  = 1.287 Mg/m<sup>3</sup>, T = 120(2) K, MoK<sub>α</sub> = 0.71073 Å, 25.242 <  $\theta$  < 27.91, transmission factors: T<sub>min</sub>/T<sub>max</sub> = 0.7078/0.7857, 16666 reflections measured, 10979 unique reflections, R<sub>1</sub> = 0.0567, wR<sub>2</sub> = 0.1255, GoF = 1.021.

[Cu(2-(4-(*tert*-butyl)-2,6-dimethylphenyl)-9-phenyl-1,10-phenanthroline)<sub>2</sub>]PF<sub>6</sub> (**C17**)



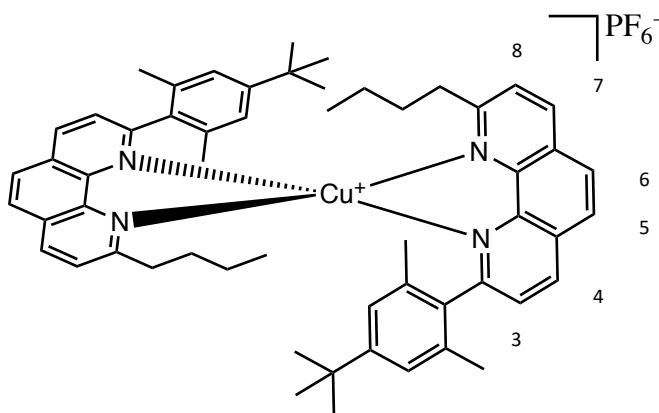
Complex **C17** was synthesised using the same method as for **C11**, with the addition of **L14** (18 mg, 0.038 mmol), as opposed to **L4**, and [Cu(CH<sub>3</sub>CN)<sub>4</sub>]PF<sub>6</sub> (7 mg, 0.019 mmol) to yield **C17** (12 mg, 0.012 mmol, 62%).

<sup>1</sup>H NMR (500 MHz, CDCl<sub>3</sub>) δ 8.58 (d, *J* = 8.2 Hz, 2H, H<sub>4</sub>), 8.46 (d, *J* = 8.5 Hz, 2H, H<sub>7</sub>), 8.14 (d, *J* = 8.8 Hz, 2H, H<sub>5</sub>), 8.05 (d, *J* = 8.8 Hz, 2H, H<sub>6</sub>), 8.00 (d, *J* = 8.5 Hz, 2H, H<sub>8</sub>), 7.97 – 7.94 (m, 4H, H<sub>Ph</sub>), 7.48 (d, *J* = 8.2 Hz, 2H, H<sub>3</sub>), 7.15 (m, 2H, H<sub>Ph</sub>), 7.00 (m, 4H, H<sub>Ph</sub>), 6.55 (s, 2H, H<sub>Ar</sub>), 6.07 (s, 2H, H<sub>Ar</sub>), 1.21 (s, 18H, H<sub>Me</sub>), 1.16 (s, 6H, H<sub>Me</sub>), 0.86 (s, 6H, H<sub>Me</sub>).

<sup>13</sup>C NMR (125 MHz, CDCl<sub>3</sub>) δ 160.2, 156.2, 150.6, 144.3, 144.1, 139.0, 138.0 (CH), 137.9 (CH), 135.2, 135.1, 133.1, 130.0 (CH), 128.5 (CH), 128.4, 128.2 (CH), 127.9, 127.2 (CH), 127.2 (CH), 126.6 (CH), 124.5 (CH), 124.4 (CH), 122.8 (CH), 34.1, 31.2 (CH<sub>3</sub>), 20.2 (CH<sub>3</sub>), 19.7 (CH<sub>3</sub>).

HRMS ESI: calcd for CuC<sub>76</sub>H<sub>88</sub>N<sub>4</sub> (M - PF<sub>6</sub>) 895.38; obsd 895.37

[Cu(2-(4-(*tert*-butyl)-2,6-dimethylphenyl)-9-butyl-1,10-phenanthroline)<sub>2</sub>]PF<sub>6</sub> (**C18**)



Chemical formula: CuC<sub>56</sub>H<sub>64</sub>N<sub>4</sub>PF<sub>6</sub>

Exact mass: 1000.40

Molecular weight: 1001.66

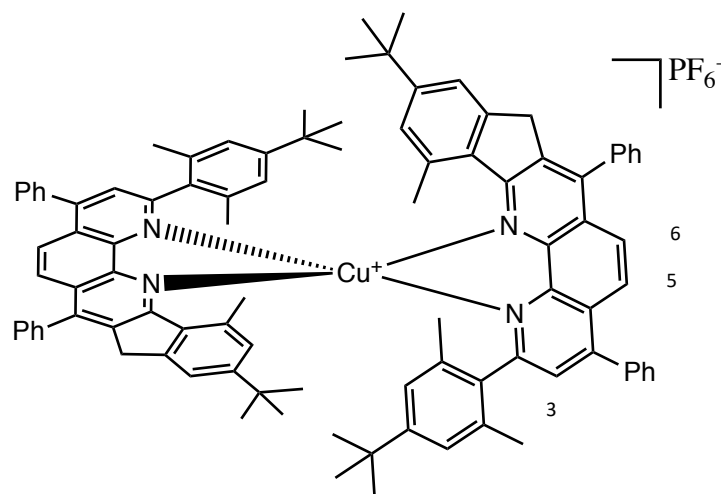
Complex **C18** was synthesised using the same method as for **C11**, with the addition of **L15** (30 mg, 0.076 mmol), as opposed to **L4**, and [Cu(CH<sub>3</sub>CN)<sub>4</sub>]PF<sub>6</sub> (14 mg, 0.038 mmol) to yield **C18** (28 mg, 0.033 mmol, 87 %).

<sup>1</sup>H NMR (500 MHz, CDCl<sub>3</sub>) δ 8.52 (d, *J* = 8.2 Hz, 2H, H<sub>4</sub>), 8.32 (d, *J* = 8.3 Hz, 2H, H<sub>7</sub>), 8.04 (d, *J* = 8.8 Hz, 2H, H<sub>5</sub>), 7.93 (d, *J* = 8.8 Hz, 2H, H<sub>6</sub>), 7.66 (d, *J* = 8.3 Hz, 2H, H<sub>8</sub>), 7.45 (d, *J* = 8.2 Hz, 2H, H<sub>3</sub>), 6.57 (s, 2H, H<sub>Ar</sub>), 6.09 (s, 2H, H<sub>Ar</sub>), 3.21 (ddd, *J* = 14.6, 10.9, 5.9 Hz, 2H, CH<sub>2</sub>), 3.10 (ddd, *J* = 14.6, 10.9, 5.7 Hz, 2H, CH<sub>2</sub>), 1.79 (qd, *J* = 12.4, 6.3 Hz, 4H, CH<sub>2</sub>), 1.62 (s, 6H, H<sub>Me</sub>), 1.45 – 1.33 (m, 4H, CH<sub>2</sub>), 1.19 (s, 18H, H<sub>tBu</sub>), 0.94 – 0.89 (m, 12H, CH<sub>3</sub> and H<sub>Me</sub>).

<sup>13</sup>C NMR (125 MHz, CDCl<sub>3</sub>) δ 161.4, 160.0, 151.1, 144.5, 143.8, 138.0 (CH), 137.7 (CH), 135.2, 133.5, 128.2, 127.7, 127.3 (CH), 127.2 (CH), 126.2 (CH), 124.5 (CH), 123.9 (CH), 123.5 (CH), 42.3 (CH<sub>2</sub>), 34.5, 31.8 (CH<sub>2</sub>), 31.6 (CH<sub>3</sub>), 23.5 (CH<sub>2</sub>), 21.0 (CH<sub>3</sub>), 20.0 (CH<sub>3</sub>), 14.3 (CH<sub>3</sub>).

HRMS ESI: calcd for CuC<sub>56</sub>H<sub>64</sub>N<sub>4</sub> (M - PF<sub>6</sub>) 855.44 obsd 855.44

[Cu(L13)<sub>2</sub>]PF<sub>6</sub> (C19)



Chemical formula: CuC<sub>96</sub>H<sub>96</sub>N<sub>4</sub>PF<sub>6</sub>

Exact mass: 1508.62

Molecular weight: 1510.33

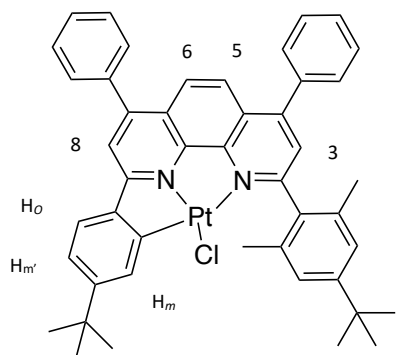
Complex **C19** was synthesised using the same method as for **C11**, with the addition of **L13** (18 mg, 0.027 mmol), as opposed to **L4**, and [Cu(CH<sub>3</sub>CN)<sub>4</sub>]PF<sub>6</sub> (5 mg, 0.014 mmol) to yield **C19** (8 mg, 0.0053 mmol, 39 %).

<sup>1</sup>H NMR (500 MHz, CDCl<sub>3</sub>) δ 7.82 (d, *J* = 9.3 Hz, 2H, H<sub>5</sub>), 7.65 (d, *J* = 9.3 Hz, 2H, H<sub>6</sub>), 7.62 (s, 2H, H<sub>3</sub>), 7.60 – 7.45 (m, 20H, H<sub>Ph</sub>), 7.38 (m, 2H, H<sub>Ar</sub>), 7.31 (s, 2H, H<sub>Ar</sub>), 7.24 (s, 4H, H<sub>Ar</sub>), 3.87 (s, 4H, CH<sub>2</sub>), 3.27 (s, 6H, CH<sub>3</sub>), 2.49 (s, 12H, H<sub>Me</sub>), 1.41 (s, 18H, H<sub>tBu</sub>), 1.38 (s, 18H, H<sub>tBu</sub>).

<sup>13</sup>C NMR (125 MHz, CDCl<sub>3</sub>) δ 158.8, 154.2, 150.9, 150.2, 146.8, 144.6, 144.2, 144.0, 139.1, 136.8, 135.9, 135.3, 134.7, 133.9, 130.0, 129.8 (CH), 129.5 (CH), 129.4 (CH), 129.3 (CH), 129.0 (CH), 128.8 (CH), 128.2 (CH), 127.2, 127.1 (CH), 125.7 (CH), 126.2, 123.5 (CH), 123.3 (CH), 123.1 (CH), 120.0 (CH), 34.7 (CH<sub>2</sub>), 34.0, 31.3 (CH<sub>3</sub>), 31.1 (CH<sub>3</sub>), 24.1 (CH<sub>3</sub>), 20.3 (CH<sub>3</sub>), 20.2 (CH<sub>3</sub>).

HRMS ESI: calcd for CuC<sub>96</sub>H<sub>96</sub>N<sub>4</sub> (M - PF<sub>6</sub>) 1364.66 obsd 1364.67

Pt 2-(4-(*tert*-butyl)-2,6-dimethylphenyl)-9-(4-(*tert*-butyl)phenyl)-4,7-diphenyl-1,10-phenanthroline chloride (**C20**)



Chemical formula: PtC<sub>46</sub>H<sub>43</sub>N<sub>2</sub>Cl

Exact mass: 853.28

Molecular weight: 854.40

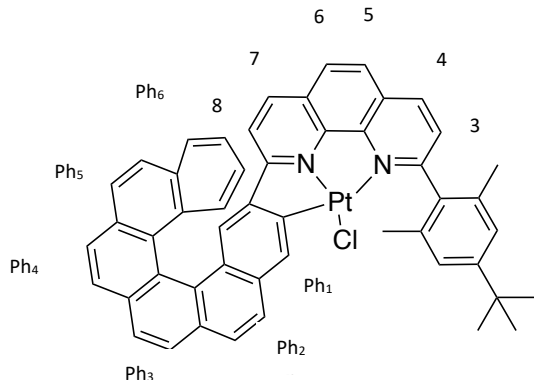
**L11** (20 mg, 0.019 mmol) and  $K_2PtCl_4$  (8 mg, 0.019 mmol) were refluxed in acetic acid (20 mL) for 24 h under argon. The solvent was evaporated and a column ( $SiO_2$ ; dichloromethane:cyclohexane 1:1) was carried out, followed by a recrystallisation (dichloromethane/pentane) to afford the titled product (11 mg, 0.013 mmol, 68%).

<sup>1</sup>H NMR (500 MHz, CDCl<sub>3</sub>) δ 8.03 – 7.96 (m, 1H, H<sub>m</sub>), 7.92 (d, *J* = 9.3 Hz, 1H, H<sub>5</sub>), 7.85 (d, *J* = 9.3 Hz, 1H, H<sub>6</sub>), 7.71 (s, 1H, H<sub>8</sub>), 7.69 (s, 1H, H<sub>3</sub>), 7.61 – 7.53 (m, 10H, H<sub>Ph</sub>), 7.38 (d, *J* = 8.2 Hz, 1H, H<sub>o</sub>), 7.20 (s, 2H, H<sub>Ar</sub>), 7.12 (dd, *J* = 8.1, 2.0 Hz, 1H, H<sub>m'</sub>), 2.21 (s, 6H, H<sub>Me</sub>), 1.41 (s, 9H, H<sub>tBu</sub>), 1.31 (s, 9H, H<sub>tBu</sub>).

<sup>13</sup>C NMR (125 MHz, CDCl<sub>3</sub>) δ 165.5, 163.6, 155.1, 152.1, 150.4, 150.1, 149.6, 147.0, 143.2, 138.9, 137.1, 136.1, 136.0, 135.0, 131.6 (CH), 129.6 (CH), 129.6 (CH), 129.4 (CH), 129.3 (CH), 129.3 (CH), 129.2 (CH), 129.1 (CH), 127.7, 125.6, 124.8 (CH), 124.7 (CH), 124.4 (CH), 124.4, 123.6 (CH), 121.2 (CH), 118.2 (CH), 35.5, 34.6, 31.5 (CH<sub>3</sub>), 31.2 (CH<sub>3</sub>), 20.8 (CH<sub>3</sub>).

HRMS ESI: calcd for PtC<sub>46</sub>H<sub>43</sub>N<sub>2</sub> (M - Cl) 818.3074; obsd 818.3073

Pt 2-(4-(*tert*-butyl)-2,6-dimethylphenyl)-9-(hexahelicen-11-yl)-1,10-phenanthroline chloride (**C21**)



Chemical formula:  $\text{PtC}_{50}\text{H}_{37}\text{N}_2\text{Cl}$

Exact mass: 895.23

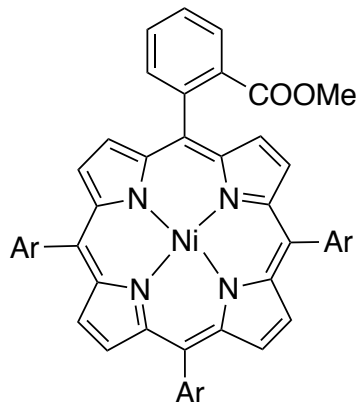
Molecular weight: 896.39

Complex **C21** was synthesised using the same method as for **C20**, with the addition of  $\text{K}_2\text{PtCl}_4$  (18 mg, 0.043 mmol) **L16** (26 mg, 0.039) as opposed to **L11** to afford the titled product (9 mg, 0.01 mmol, 23%)

$^1\text{H}$  NMR (500 MHz,  $\text{CDCl}_3$ )  $\delta$  8.51 (d,  $J = 8.2$  Hz, 1H, H<sub>7</sub>), 8.11 (s, 1H, H<sub>Ph1</sub>), 8.02 (d, 1H, H<sub>4</sub>), 8.01 – 7.96 (m, 6H, H<sub>Ph</sub>), 7.93 (d,  $J = 8.2$  Hz, 1H, H<sub>8</sub>), 7.89 – 7.83 (m, 3H, H<sub>3</sub> and H<sub>Ph</sub>), 7.77 – 7.71 (m, 2H, H<sub>Ph6</sub>), 7.48 (d, 1H, H<sub>5</sub>), 7.41 (d, 1H, H<sub>6</sub>), 7.23 (s, 2H, H<sub>Ar</sub>), 6.95 (ddd,  $J = 8.0, 6.8, 1.3$  Hz, 1H, H<sub>Ph6</sub>), 6.89 (d,  $J = 8.8$  Hz, 1H, H<sub>Ph</sub>), 6.70 (ddd,  $J = 8.0, 6.8, 1.3$  Hz, 1H, H<sub>Ph6</sub>), 2.23 (s, 3H, H<sub>Me</sub>), 2.19 (s, 3H, H<sub>Me</sub>), 1.44 (s, 9H, H<sub>tBu</sub>),

$^{13}\text{C}$  NMR (125 MHz,  $\text{CDCl}_3$ )  $\delta$  165.5, 152.7, 146.3, 142.7, 139.0, 138.7 (CH), 138.7 (CH), 136.0, 135.9, 135.7, 133.5, 131.9, 131.7, 131.6, 130.7, 130.5, 129.7 (CH) 128.9, 128.8, 128.7, 128.4, 127.9 (CH), 127.8 (CH), 127.8 (CH), 127.7 (CH), 127.6 (CH), 127.6 (CH), 127.6 (CH), 127.5 (CH), 127.4 (CH), 127.3 (CH), 127.0 (CH), 127.0 (CH), 126.7, 126.2, 126.1 (CH), 126.0, 125.0, 124.5 (CH), 124.4 (CH), 123.9, 119.6, 34.8, 31.5 (CH<sub>3</sub>), 21.5 (CH<sub>3</sub>).

HRMS ESI: calcd for  $\text{PtC}_{50}\text{H}_{37}\text{N}_2$  (M - Cl<sup>-</sup>) 860.2599; obsd 860.26031

**M1**Chemical formula: C<sub>64</sub>H<sub>66</sub>N<sub>4</sub>NiO<sub>2</sub>

Exact mass: 980.45

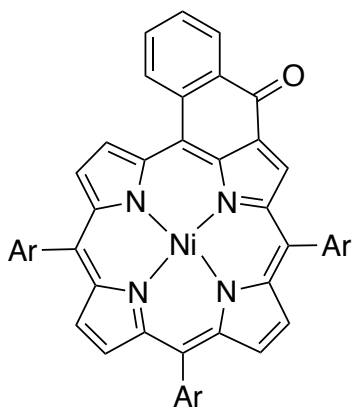
Molecular weight: 981.95

To a degassed solution of pyrrole (1.4 mL, 20.8 mmol), 2,6-dimethyl-4-tertbutylbenzaldehyde (2.97g, 15.6 mmol), methyl-2-formylbenzoate (854 mg, 5.2 mmol) in chloroform (780 mL), borontrifluoride etherate (5.7 mM) was added. The resulting orange-red solution was shielded from light and stirred for 2h under argon and at rt. Chloranil (3.7g, 15 mmol) was added and the resulting solution was refluxed for half an hour. On cooling, the solution was filtered through a pad of alumina (~20 cm). Solvent was then evaporated and the desired A<sub>3</sub>B porphyrin was obtained *via* column chromatography (SiO<sub>2</sub>; cyclohexane:dichloromethane, 80:20, 60:40, 50:50) to obtain the free-base purple porphyrin. This porphyrin was then dissolved in toluene (150 mL) with Ni(acac)<sub>2</sub> (1.4g, 5.5 mmol) and heated to reflux for 16 h. Solvent was then evaporated and excess nickel salts were removed *via* filtration of the porphyrin through an alumina column (dichloromethane) to obtain the titled product (1.17 g 1.1 mmol, 21%).

<sup>1</sup>H NMR (500 MHz, CDCl<sub>3</sub>) : δ 8.51-8.45 (m, 6H, H<sub>pyrr</sub>), 8.43 (d, *J* = 4.8 Hz, 2H, H<sub>pyrr</sub>), 8.25-8.15 (m, 1H, H<sub>Ph-ester</sub>), 8.06-7.95 (m, 1H, H<sub>Ph-ester</sub>), 7.73-7.66 (m, 2H, H<sub>Ph-ester</sub>), 7.35-7.28 (m, 6H, H<sub>Ar</sub>), 2.78 (s, 3H, COOCH<sub>3</sub>), 1.83 (s, 6H, H<sub>Me</sub>), 1.81 (s, 3H, H<sub>Me</sub>), 1.81 (s, 3H, H<sub>Me</sub>), 1.75 (s, 6H, H<sub>Me</sub>), 1.47 ppm (s, 27H, H<sub>tBu</sub>).

<sup>13</sup>C NMR (125 MHz, CDCl<sub>3</sub>) : δ 167.9, 150.8, 142.7, 142.62, 142.59, 142.5, 141.7, 138.63, 138.60, 138.59, 138.58, 137.42, 137.38, 135.5 (CH), 134.3, 134.0, 131.4 (CH), 131.3 (CH), 131.2 (CH), 131.0 (CH), 129.9 (CH), 129.7 (CH), 129.6 (CH), 128.6 (CH), 128.2 (CH), 126.5 (CH), 123.92 (CH), 123.90 (CH), 123.88 (CH), 117.5, 117.3, 117.1, 51.6 (CH<sub>3</sub>), 34.68, 31.7 (CH<sub>3</sub>), 22.0 (CH<sub>3</sub>), 21.9 (CH<sub>3</sub>), 21.8 ppm (CH<sub>3</sub>).

ESI-TOF: Calcd for C<sub>64</sub>H<sub>66</sub>N<sub>4</sub>NiO<sub>2</sub> (M<sup>+</sup>) 980.45; obsd 980.45

**M2**Chemical formula: C<sub>63</sub>H<sub>62</sub>N<sub>4</sub>NiO

Exact mass: 948.43

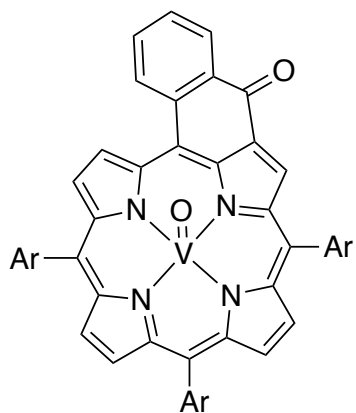
Molecular weight: 949.91

A suspension of **M1** (558 mg, 0.576 mmol) and lithium hydroxide (1g, excess) in a dioxane:water (8:2) solution was refluxed for 16 h. On cooling, dichloromethane (60 mL) was added and the organic phase was extracted (3 x dichloromethane), washed (3 x water) and dried over sodium sulphate. The solvent was then evaporated and the porphyrin was redissolved in dry toluene and heated at 50 °C under argon with oxalyl chloride (3 mL, excess). A dean-stark was used to remove excess oxalyl chloride. On cooling, tin(IV) chloride (1 mL, excess) was added and the solution turned instantly green. After half an hour of stirring at r.t. the solution was poured onto ice cold concentrated NaOH (150 mL). The organic phase was extracted (3 x dichloromethane), washed (3 x water) and dried over sodium sulphate. The solvent was evaporated and the titled product was purified *via* column chromatography (SiO<sub>2</sub>; 1:1 dichloromethane:cyclohexane) to afford the titled product (443 mg, 0.47 mmol, 81%).

<sup>1</sup>H NMR (500 MHz, CDCl<sub>3</sub>): δ 9.21 (d, *J* = 5.1 Hz, 1H, H<sub>pyrr</sub>), 8.97 (s, 1H, H<sub>pyrr</sub>), 8.47- 8.45 (m, 2H, H<sub>pyrr</sub> + H<sub>cyclPh</sub>), 8.28 (d, *J* = 4.9 Hz, 1H, H<sub>pyrr</sub>), 8.27 (d, *J* = 4.7 Hz, 1H, H<sub>pyrr</sub>), 8.22 (d, *J* = 4.9 Hz, 1H, H<sub>pyrr</sub>), 8.18 (d, *J* = 4.9 Hz, 1H, H<sub>pyrr</sub>), 8.06-7.95 (br dd, 1H, H<sub>cyclPh</sub>), 7.71-7.65 (br ddd, 1H, H<sub>cyclPh</sub>), 7.47-7.41 (br ddd, 1H, H<sub>cyclPh</sub>), 7.35 (s, 2H, H<sub>Ar</sub>), 7.32 (2s, 4H, H<sub>Ar</sub>), 1.94 (s, 6H, H<sub>Me</sub>), 1.91 (s, 6H, H<sub>Me</sub>), 1.90 (s, 6H, H<sub>Me</sub>), 1.51 (2s, 18H, H<sub>tBu</sub>), 1.43 ppm (s, 9H, H<sub>tBu</sub>)

<sup>13</sup>C NMR (125 MHz, CDCl<sub>3</sub>): δ 183.0, 151.3, 151.2, 145.1, 144.8, 143.9, 143.4, 142.8, 141.2, 141.0, 140.0, 138.9, 138.4, 138.18, 138.17, 135.9, 135.7, 135.34 (CH), 135.29, 135.26, 133.71 (CH), 133.70, 133.5 (CH), 133.1 (CH), 132.9 (CH), 132.84 (CH), 132.75 (CH), 132.1 (CH), 166, 131.3 (CH), 129.3 (CH), 127.4 (CH), 124.4, 124.12, 124.09, 119.8, 117.1, 108.3, 31.63 (CH<sub>3</sub>), 34.65, 34.64, 34.63, 31.59 (CH<sub>3</sub>), 21.9 (CH<sub>3</sub>), 21.79 (CH<sub>3</sub>), 21.78 (CH<sub>3</sub>)

ESI-TOF: Calcd for C<sub>63</sub>H<sub>62</sub>N<sub>4</sub>NiO (M<sup>+</sup>) 948.43; obsd 948.43

**M3**

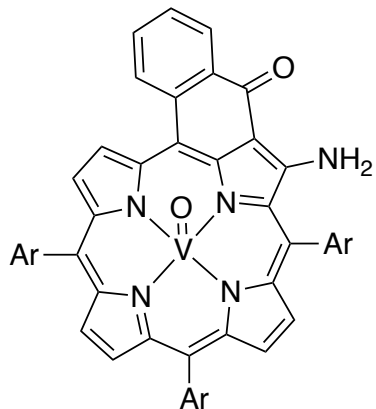
Chemical formula: C<sub>63</sub>H<sub>62</sub>N<sub>4</sub>O<sub>2</sub>V

Exact mass: 957.43

Molecular weight: 958.16

Vanadyl sulfate (162 mg, 0.640 mmol) and the free-base porphyrin (155 mg, 0.207 mmol) were heated to reflux in an acetic acid buffer (glacial acetic acid (27 mL) and sodium acetate (828 mg)) for 20h. Water (50 mL) was then added and the precipitate was filtered and washed with water in order to extract the vanadyl salts (washed until filtrate no longer blue). This afforded the titled product as a green solid (175mg, 0.183 mmol, 88%). Only one spot was present on the TLC plate.

MALDI-TOF: Calcd for C<sub>63</sub>H<sub>62</sub>N<sub>4</sub>O<sub>2</sub>V (M +H<sup>+</sup>) 958.44; obsd 958.398

**M4**Chemical formula: C<sub>63</sub>H<sub>63</sub>N<sub>5</sub>O<sub>2</sub>V

Exact mass: 972.44

Molecular weight: 973.17

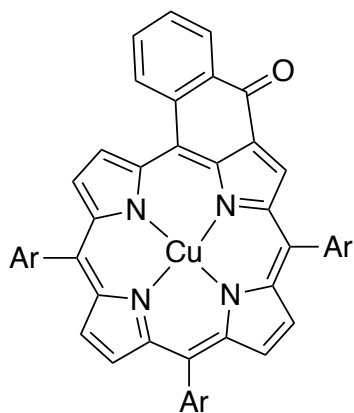
The **M3** (322 mg, 0.34 mmol), 4-amino-4H-1,2,4-triazole (565 mg, 6.72 mmol) and NaOH (1.4 g, 34 mmol) were refluxed for 2 h in toluene:ethanol (8:2) under argon. Water (50 mL) was then added and the organic phase was washed with water and dried over sodium sulphate. The solvent was evaporated and the porphyrin was purified by column chromatography (SiO<sub>2</sub>; dichloromethane:cyclohexane 2:1) to afford the titled product (310 mg, 0.32 mmol, 94%).

MALDI-TOF: Calcd for C<sub>63</sub>H<sub>63</sub>N<sub>5</sub>O<sub>2</sub>V (M +H<sup>+</sup>) 973.45; obsd 973.517

Crystal data from chlorobenzene/methanol for **M4**. C<sub>63</sub>H<sub>63</sub>N<sub>5</sub>O<sub>2</sub>V: M = 972.44 g·mol<sup>-1</sup>, monoclinic, space group P 21/c, *a* = 13.3217(5) Å, *b* = 9.9524(4) Å, *c* = 40.3311(17) Å,  $\alpha$  = 90°,  $\beta$  = 98.415(2)°,  $\gamma$  = 90°, V = 5289.6(4) Å<sup>3</sup>, Z = 2,  $\rho_{\text{calc}}$  = 1.222 Mg/m<sup>3</sup>, T = 120(2) K, MoK $\alpha$  = 1.54178 Å, 2.215 <  $\theta$  < 66.451, transmission factors: T<sub>min</sub>/T<sub>max</sub> = 0.6008/0.7528, 51339 reflections measured, 9306 unique reflections, R<sub>1</sub> = 0.0933, wR<sub>2</sub> = 0.2580, GoF = 1.249.

Crystal data for **M4** with phenyl groups as *meso* substituents:

Crystal data from chlorobenzene/methanol. C<sub>46</sub>H<sub>31</sub>N<sub>5</sub>O<sub>2</sub>V: M = 720.16 g·mol<sup>-1</sup>, monoclinic, space group P 21/c, *a* = 11.4999(4) Å, *b* = 9.21.6133(7) Å, *c* = 18.0899(6) Å,  $\alpha$  = 90°,  $\beta$  = 107.1730(10)°,  $\gamma$  = 90°, V = 4295.8(2) Å<sup>3</sup>, Z = 4,  $\rho_{\text{calc}}$  = 1.533 Mg/m<sup>3</sup>, T = 120(2) K, MoK $\alpha$  = 0.71073 Å, 2.36 <  $\theta$  < 28.02, transmission factors: T<sub>min</sub>/T<sub>max</sub> = 0.7179/0.7456, 10406 reflections measured, 8832 unique reflections, R<sub>1</sub> = 0.0540, wR<sub>2</sub> = 0.1392, GoF = 1.034.

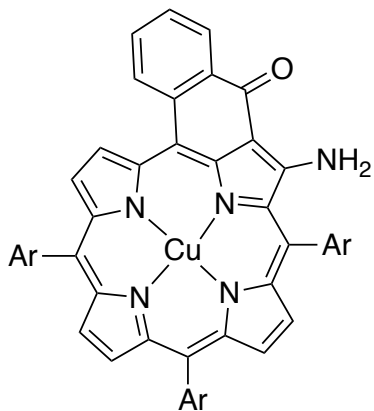
**M5**Chemical formula: C<sub>63</sub>H<sub>62</sub>N<sub>4</sub>OCu

Exact mass: 953.42

Molecular weight: 954.76

The free-base porphyrin (140 mg, 0.18 mmol) and Cu(OAc)<sub>2</sub> (85 mg, 0.47 mmol) were refluxed in toluene (50 mL) for 16 h. Solvent was evaporated and the product was purified *via* column chromatography (SiO<sub>2</sub>; dichloromethane:cyclohexane 1:1) to afford the titled product (141 mg, 0.17 mmol, 94%)

MALDI-TOF: Calcd for C<sub>63</sub>H<sub>62</sub>N<sub>4</sub>OCu (M<sup>+</sup>) 954.76; obsd 954.391

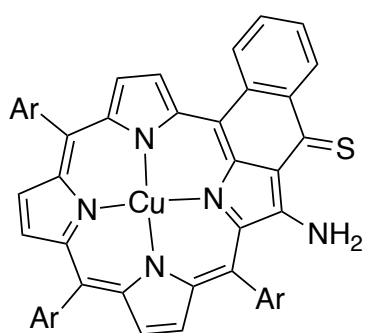
**M6**Chemical formula: C<sub>63</sub>H<sub>63</sub>N<sub>5</sub>OCu

Exact mass: 968.43

Molecular weight: 969.78

The **M5** (173 mg, 0.181 mmol), 4-amino-4H-1,2,4-triazole (304 mg, 3.62 mmol) and NaOH (724 mg, 18.1 mmol) were refluxed for 2 h in toluene:ethanol (8:2) under argon. Water (50 mL) was then added and the organic phase was washed with water and dried over sodium sulphate. The solvent was evaporated and the porphyrin was purified by column chromatography (SiO<sub>2</sub>; dichloromethane:cyclohexane 2:1) to afford the titled product (161mg, 0.167 mmol, 92%).

MALDI-TOF: Calcd for C<sub>63</sub>H<sub>63</sub>N<sub>5</sub>OCu (M +H<sup>+</sup>) 969.44; obsd 969.496

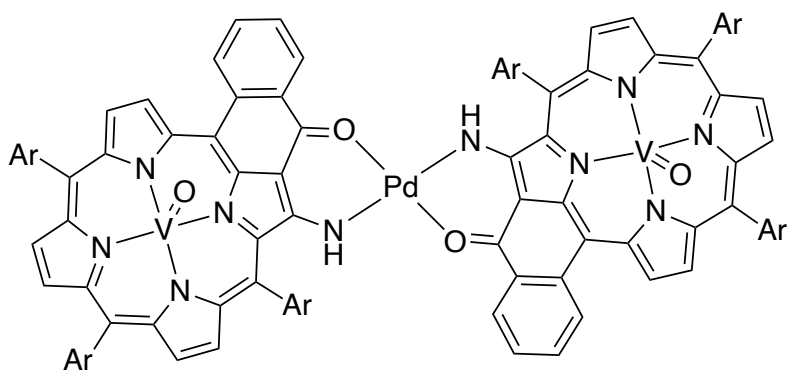
**M7**Chemical formula: C<sub>63</sub>H<sub>63</sub>N<sub>5</sub>SCu

Exact mass: 984.41

Molecular weight: 985.84

**M6** (65 mg, 0.067 mmol) and Lawesson's reagent (162 mg, 0.402 mmol) were heated to reflux in toluene for 2h under argon. On cooling, the solvent was evaporated and the product was purified by column chromatography (SiO<sub>2</sub>; cyclohexane:dichloromethane 1:1) to afford the titled product (57 mg, 0.058 mmol, 86%)

MALDI-TOF: Calcd for C<sub>63</sub>H<sub>63</sub>N<sub>5</sub>OCu (M +H<sup>+</sup>) 985.42; obsd 985.447

**D1**

Chemical formula:  $C_{126}H_{124}N_{10}O_4PdV_2$

Exact mass: 2048.77

Molecular weight: 2050.75

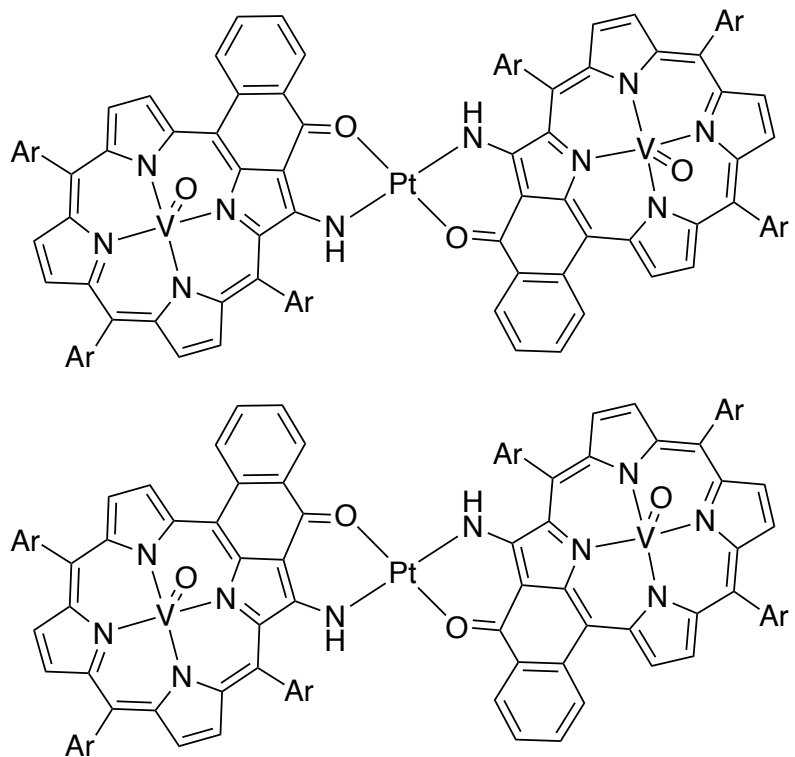
**M4** (25 mg, 0.026 mmol) and  $Pd(OAc)_2$  (3 mg, 0.14 mmol) were heated to reflux in toluene (10 mL) for 16 h under argon. On cooling, the solvent was evaporated and the product was purified by column chromatography ( $SiO_2$ ; cyclohexane:dichloromethane 60:40) to afford the titled product as a brown solid (11 mg, 5.36  $\mu$ mol, 42%)

MALDI-TOF: Calcd for  $C_{126}H_{124}N_{10}O_4PdV_2$  ( $M^{+}$ ) 2048.77; obsd 2048.573

The X-ray structure obtained was not suitable for publication so no crystal data will be provided. Yet it was apparent that the dimer was the  $\alpha,\beta$ .

The Crystal data for **D1** with *meso* substituents are as follows:

Crystal data from chlorobenzene/methanol for **D1**.  $C_{93}H_{55}N_5O_4V_2Pd$ ;  $M = 1903.80 \text{ g.mol}^{-1}$ , orthorhombic, space group  $P 21 21 21$ ,  $a = 38.6581(18) \text{ \AA}$ ,  $b = 13.7285(6) \text{ \AA}$ ,  $c = 15.4266(7) \text{ \AA}$ ,  $\alpha = 90^\circ$ ,  $\beta = 90^\circ$ ,  $\gamma = 90^\circ$ ,  $V = 8187.2(6) \text{ \AA}^3$ ,  $Z = 4$ ,  $\rho_{\text{calc}} = 1.545 \text{ Mg/m}^3$ ,  $T = 120(2) \text{ K}$ ,  $MoK\alpha = 1.54178 \text{ \AA}$ ,  $2.286 < \theta < 66.443$ , transmission factors:  $T_{\text{min}}/T_{\text{max}} = 0.5238/0.7528$ , 94102 reflections measured, 14408 unique reflections,  $R_1 = 0.0686$ ,  $wR_2 = 0.1724$ ,  $\text{GoF} = 1.090$ .

**D2**

Chemical formula:  $C_{126}H_{124}N_{10}O_4PtV_2$

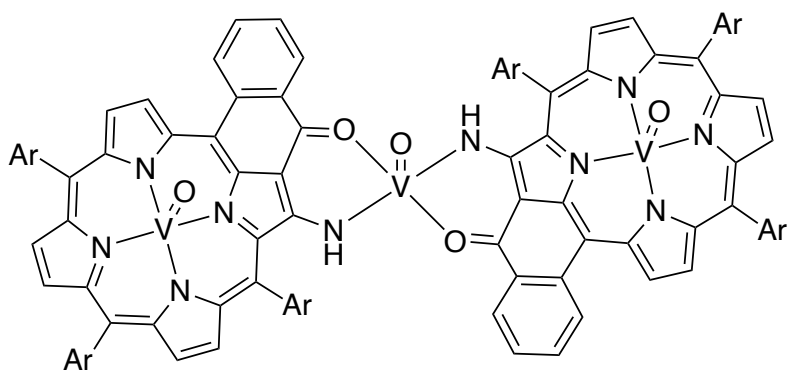
Exact mass: 2137.83

Molecular weight: 2139.41

**M4** (20 mg, 0.02 mmol) and  $Pt(acac)_2$  (4.4 mg, 0.011 mmol) were heated in 1,2-dichlorobenzene (5 mL) in a microwave (180 °C, 200 mW) for 5 h under argon. On cooling, the solvent was evaporated by trap to trap distillation and the product was purified by column chromatography ( $SiO_2$ ; cyclohexane:dichloromethane 60:40) to afford the titled product in two forms  $\alpha,\beta$  (2 mg, 0.93  $\mu$ mol, 10%) and  $\alpha,\alpha$  (5 mg, 2  $\mu$ mol, 20%) both as brown solids.

MALDI-TOF: Calcd for  $\alpha,\beta C_{126}H_{124}N_{10}O_4PtV_2 (M + H^+)$  2134.84; obsd 2138.773

MALDI-TOF: Calcd for  $\alpha,\alpha C_{126}H_{124}N_{10}O_4PtV_2 (M + H^+)$  2138.84; obsd 2138.858

**D3**

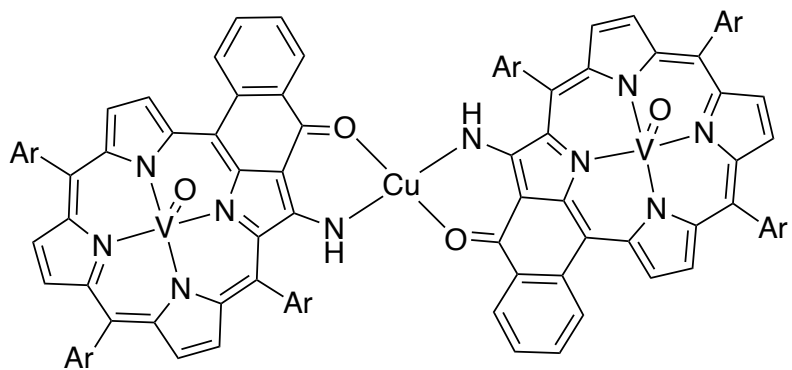
Chemical formula:  $C_{126}H_{124}N_{10}O_5V_3$

Exact mass: 2009.81

Molecular weight: 2011.27

**M4** (10 mg, 0.01 mmol) and vanadyl sulfate (1.4 mg, 5.6  $\mu$ mol) were refluxed in an acetic acid buffer (20 mL) for 24h under argon. On cooling, the solvent was evaporated and the product was purified by size exclusion chromatography (toluene) to afford the titled product as a deep green solid (3 mg, 1.5  $\mu$ mol, 30%).

Breakdown of dimer on ionisation only monomer was observed in mass spectrometry (MALDI and ESI)



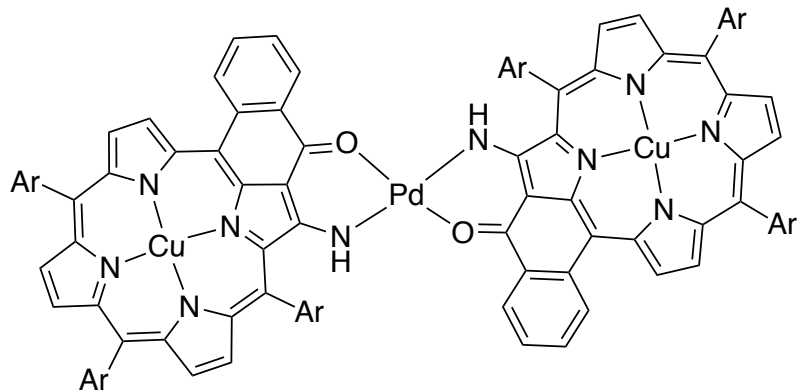
Chemical formula:  $C_{126}H_{124}N_{10}O_4CuV_2$

Exact mass: 2005.80

Molecular weight: 2007.87

**M4** (25 mg, 0.026 mmol) and  $Cu(OAc)_2$  (3 mg, 0.014 mmol) were heated to reflux in toluene for 24 h under argon. On cooling, the solvent was evaporated and the product was purified by size exclusion chromatography (toluene) to afford the titled product as a deep green solid (23 mg, 0.011 mmol, 88%).

MALDI-TOF: Calcd for  $C_{126}H_{124}N_{10}O_4PtV_2 (M^{+})$  2005.80; obsd 2005.808

**D5**

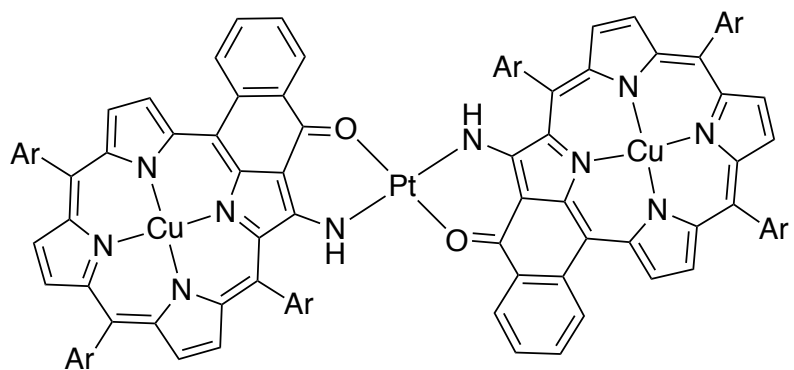
Chemical formula:  $C_{126}H_{124}N_{10}O_2PdCu_2$

Exact mass: 2040.75

Molecular weight: 2043.96

**M7** (35 mg, 0.036 mmol) and  $Pd(OAc)_2$  (4 mg, 0.018 mmol) were heated to reflux in toluene (20 mL) for 16 h under argon. On cooling, the solvent was evaporated and the product was purified by column chromatography ( $SiO_2$ ; cyclohexane:dichloromethane 60:40) to afford the titled product as a brown solid (13 mg, 6.4  $\mu$ mol, 36%).

MALDI-TOF: Calcd for  $C_{126}H_{124}N_{10}O_4PdCu_2$  ( $M^{+}$ ) 2040.75; obsd 2040.924



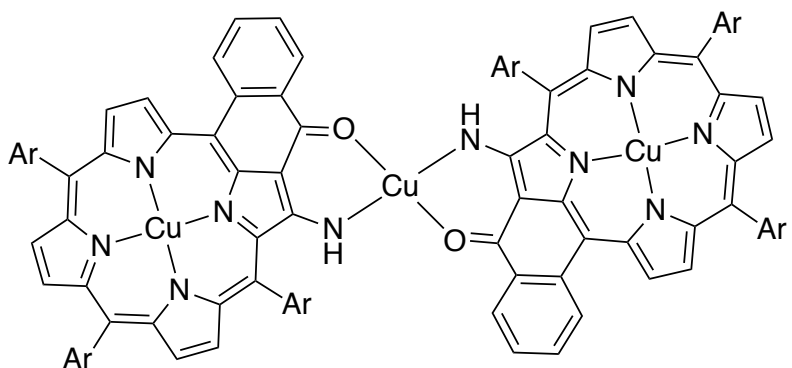
Chemical formula: C<sub>126</sub>H<sub>124</sub>N<sub>10</sub>O<sub>2</sub>CuPt

Exact mass: 2129.81

Molecular weight: 2132.62

**M7** (10 mg, 0.01 mmol) and Pt(acac)<sub>2</sub> (2 mg, 5.6 umol) were heated to reflux in 1,2-dichlorobenzene for 4 days under argon. On cooling, the solvent was evaporated by trap to trap distillation and the product was purified by column chromatography (SiO<sub>2</sub>; cyclohexane:dichloromethane 60:40) to afford the titled product as a brown solid (2 mg, 0.94  $\mu$ mol, 18%)

MALDI-TOF: Calcd for C<sub>126</sub>H<sub>124</sub>N<sub>10</sub>O<sub>4</sub>PdCu<sub>2</sub> (M<sup>+</sup>) 2132.62; obsd 2132.901



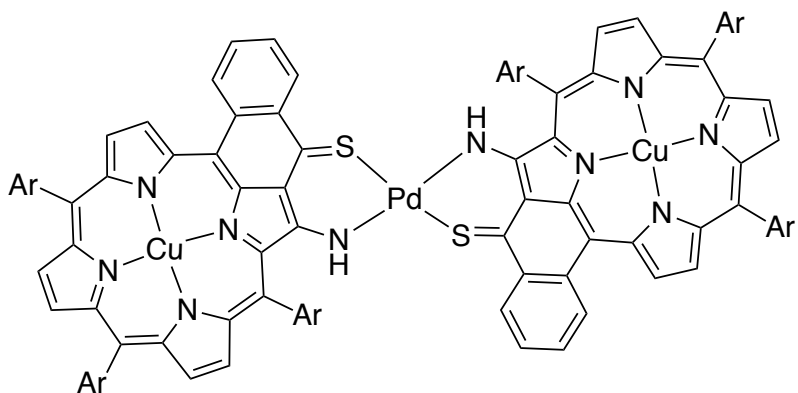
Chemical formula: C<sub>126</sub>H<sub>124</sub>N<sub>10</sub>O<sub>2</sub>Cu<sub>3</sub>

Exact mass: 1997.78

Molecular weight: 2001.08

**M7** and Cu(OAc)<sub>2</sub> were heated to reflux in toluene for 16 h under argon. On cooling, the solvent was evaporated and the product was purified by size exclusion chromatography (toluene) to afford a deep green solid (18 mg, 9 µmol, 86%).

MALDI-TOF: Calcd for  $C_{126}H_{124}N_{10}O_4Cu_3 (M^+)$  1997.79; obsd 1997.806



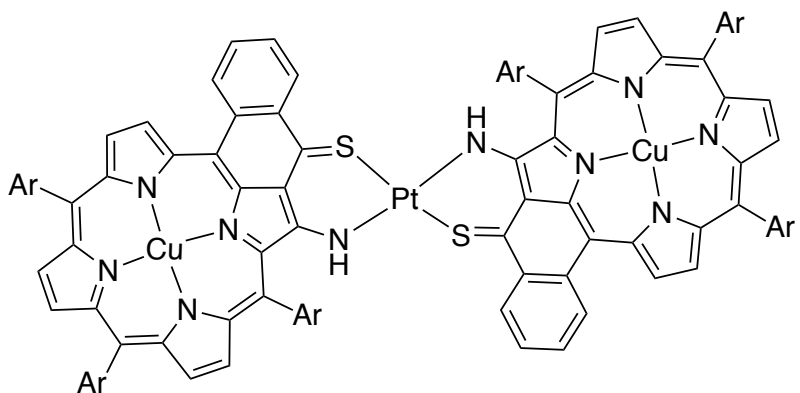
Chemical formula:  $C_{126}H_{124}N_{10}S_2PdCu_2$

Exact mass: 2072.71

Molecular weight: 2076.08

**M8** (15 mg, 0.016 mmol) and  $Pd(OAc)_2$  (2 mg, 8.6 umol) were heated to reflux in toluene for 1 h under argon. On cooling, the solvent was evaporated and the product was purified by column chromatography ( $SiO_2$ ; cyclohexane:dichloromethane 1:1) to afford the titled product (5 mg, 2.4  $\mu$ mol, 57%).

MALDI-TOF: Calcd for  $C_{126}H_{124}N_{10}S_4PdCu_2 (M^{+})$  2072.71; obsd 2072.117



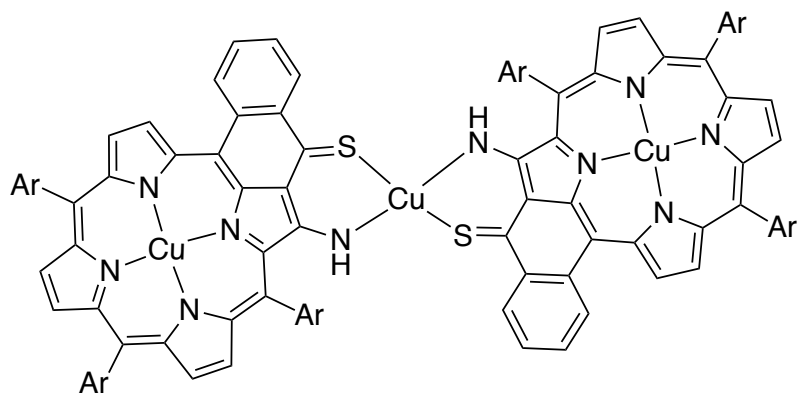
Chemical formula:  $C_{126}H_{124}N_{10}S_2PtCu_2$

Exact mass: 2161.77

Molecular weight: 2164.74

**M8** (8 mg, 8.4 umol) and Pt(acac)<sub>2</sub> (1.8 mg, 4.6 umol) were heated to reflux in 1,2-dichlorobenzene for 4 h under argon. On cooling, the solvent was evaporated by trap to trap distillation and the product was purified by column chromatography (SiO<sub>2</sub>; cyclohexane:dichloromethane 1:1) to afford the titled product as a deep red solid (4 mg, 1.89  $\mu$ mol, 45%).

MALDI-TOF: Calcd for  $C_{126}H_{124}N_{10}S_4PtCu_2$  ( $M^{+}$ ) 2161.77; obsd 2161.712



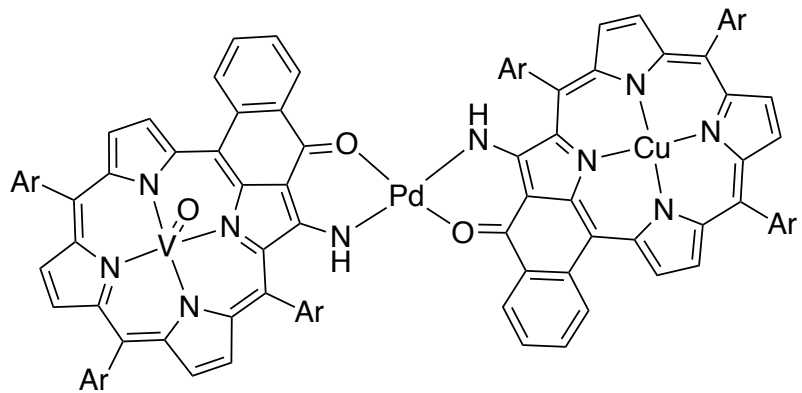
Chemical formula:  $C_{126}H_{124}N_{10}S_2Cu_3$

Exact mass: 2029.73

Molecular weight: 2033.21

**M8** (15 mg, 0.016 mmol) and  $Cu(OAc)_2$  (1.5 mg, 8.6  $\mu$ mol) were heated to reflux in toluene for 1h under argon. On cooling, the solvent was evaporated and the product was purified by size exclusion chromatography (toluene) (11 mg, 5.4  $\mu$ mol, 63%)

MALDI-TOF: Calcd for  $C_{126}H_{124}N_{10}S_4Cu_3$  ( $M + H^+$ ) 2030.74; obsd 2030.094

**D11**

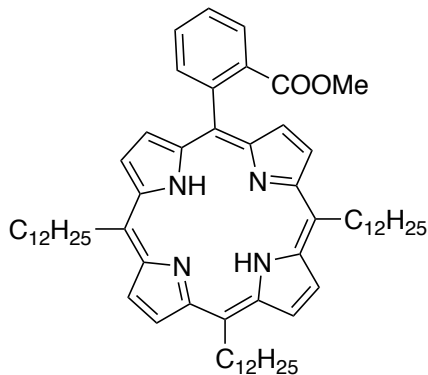
Chemical formula:  $C_{126}H_{124}N_{10}O_3PdVCu$

Exact mass: 2044.76

Molecular weight: 2047.35

**M4** (30 mg, 0.031 mmol), **M6** (30 mg, 0.031 mmol),  $PdCl_2(PhCN)_2$  (12 mg, 0.031 mmol) and sodium carbonate (16 mg, 0.155 mmol) were dissolved in toluene (30 mL) and refluxed for 16 h under argon. A column ( $SiO_2$ ; dichloromethane:cyclohexane 1:1) separated the 3 potential products to afford the titled product (18 mg, 8.8  $\mu$ mol, 28%).

MALDI-TOF: Calcd for  $C_{126}H_{124}N_{10}O_3PdVCu$  ( $M^{+}$ ) 2046.766; obsd 2046.611

**M8**Chemical formula: C<sub>64</sub>H<sub>92</sub>N<sub>4</sub>O<sub>2</sub>

Exact mass: 948.72

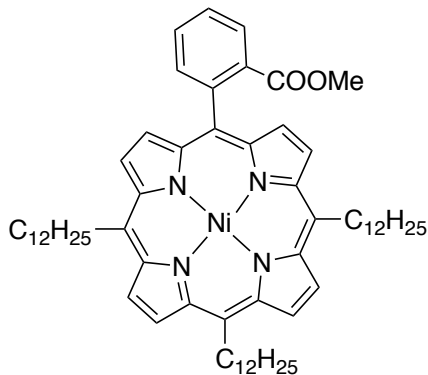
Molecular weight: 949.47

A solution of freshly distilled dichloromethane (1.5 L) containing dipyrromethane (6.141 g, 19.5 mmol) and methyl-2-formylbenzoate (4.18 g, 25 mmol) was degassed by bubbling argon through the solution for 20 minutes. After addition of BF<sub>3</sub> etherate (15 drops), the solution was stirred under argon in the dark for one hour. 2,3-Dichloro-5,6-dicyanoquinone (DDQ) (8.9 g, 39 mmol) was added and the solution was stirred for 1 h. The reaction mixture was then filtered through an alumina column and the solvents evaporated. After column chromatography (SiO<sub>2</sub>; from cyclohexane:dichloromethane, 8:2 to dichloromethane), the tetraalkylporphyrin (72 mg, 0.073 mmol) and the desired monoester porphyrin **M8** (545 mg, 0.574 mmol) were isolated and recrystallised from dichloromethane and methanol.

<sup>1</sup>H NMR (CDCl<sub>3</sub>, 400 MHz):  $\delta$  9.53 (d, *J* = 5.2 Hz, 2H, H<sub>pyrr</sub>), 9.49 (d, *J* = 5.2 Hz, 2H, H<sub>pyrr</sub>), 9.33 (d, *J* = 4.8 Hz, 2H, H<sub>pyrr</sub>), 8.62 (d, *J* = 4.8 Hz, 2H, H<sub>pyrr</sub>), 8.37 (dd, *J* = 8 and 1.5 Hz, 1H, H<sub>Ar</sub>), 8.10 (dd, *J* = 7.2 and 1.5 Hz, 1H, H<sub>Ar</sub>), 7.87 (ddd, *J* = 8, 8 and 1.5 Hz, 1H, H<sub>Ar</sub>), 7.81 (ddd, *J* = 7.5, 8 and 1.5 Hz, 1H, H<sub>Ar</sub>), 5.00 (m, 2H, CH<sub>2</sub>), 4.93 (m, 4H, CH<sub>2</sub>), 2.67 (s, 3H, OCH<sub>3</sub>), 2.61-2.45 (m, 6H, CH<sub>2</sub>), 1.89-1.74 (m, 6H, CH<sub>2</sub>), 1.6-1.2 (m, 48H, CH<sub>2</sub>), 0.87 (t, *J* = 6.8 Hz, 9H, CH<sub>3</sub>), -2.56 (s, 2H, NH).

<sup>13</sup>C NMR (CDCl<sub>3</sub>, 125 MHz):  $\delta$  168.4 (CO), 143.0, 136.2 (CH), 134.5, 129.7 (CH), 129.6 (CH), 128.3 (CH), 119.6, 119.2, 117.0, 51.6 (OCH<sub>3</sub>), 39.1 (CH<sub>2</sub>), 38.9 (CH<sub>2</sub>), 36.0 (CH<sub>2</sub>), 35.6 (CH<sub>2</sub>), 32.09 (CH<sub>2</sub>), 32.07 (CH<sub>2</sub>), 30.85 (CH<sub>2</sub>), 30.78 (CH<sub>2</sub>), 29.91 (CH<sub>2</sub>), 29.89 (CH<sub>2</sub>), 29.88 (CH<sub>2</sub>), 29.87 (CH<sub>2</sub>), 29.86 (CH<sub>2</sub>), 29.83 (CH<sub>2</sub>), 29.81 (CH<sub>2</sub>), 29.79 (CH<sub>2</sub>), 29.52 (CH<sub>2</sub>), 29.50 (CH<sub>2</sub>), 22.85 (CH<sub>2</sub>), 22.83 (CH<sub>2</sub>), 14.28 (CH<sub>3</sub>), 14.27 (CH<sub>3</sub>). The signals of the pyrrolic carbons are missing due to the NH tautomeric exchange.

Anal. calcd for C<sub>64</sub>H<sub>92</sub>N<sub>4</sub>O<sub>2</sub>: C, 80.96; H, 9.77; N, 5.90; obsd C, 80.73; H, 9.73; N, 6.01

**M9**Chemical formula: NiC<sub>64</sub>H<sub>90</sub>N<sub>4</sub>O<sub>2</sub>

Exact mass: 1004.64

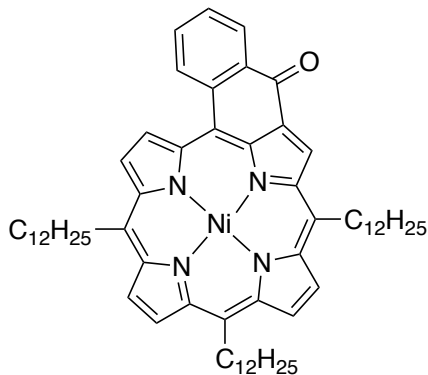
Molecular weight: 1006.14

A solution of free base **M8** (102 mg, 0.107 mmol) and Ni(acac)<sub>2</sub> (80 mg, 0.31 mmol) in toluene (50 mL) was refluxed for 16 h. After cooling, the solution was passed through a short pad of alumina and the toluene evaporated. After recrystallisation from dichloromethane and methanol, an orange solid was isolated (102 mg, 0.101 mmol, 95%).

<sup>1</sup>H NMR (CDCl<sub>3</sub>, 500 MHz):  $\delta$  9.30 (d, *J* = 5.0 Hz, 2H, H<sub>pyrr</sub>), 9.28 (d, *J* = 5.0 Hz, 2H, H<sub>pyrr</sub>), 9.15 (d, *J* = 5.0 Hz, 2H, H<sub>pyrr</sub>), 8.47 (d, *J* = 5.0 Hz, 2H, H<sub>pyrr</sub>), 8.26 (m, 1H, H<sub>Ar</sub>), 8.01 (m, 1H, H<sub>Ar</sub>), 7.77 (m, 2H, H<sub>Ar</sub>), 7.81 (ddd, *J* = 7.5, 8 and 1.5 Hz, 1H, H<sub>Ar</sub>), 4.53 (m, 2H, CH<sub>2</sub>), 4.49 (m, 4H, CH<sub>2</sub>), 2.87 (s, 3H, OCH<sub>3</sub>), 2.32-2.21 (m, 6H, CH<sub>2</sub>), 1.64-1.53 (m, 6H, CH<sub>2</sub>), 1.47-1.37 (m, 6H, CH<sub>2</sub>), 1.33-1.18 (m, 42H, CH<sub>2</sub>), 0.87 (t, *J* = 7.0 Hz, 3H, CH<sub>3</sub>), 0.86 (t, *J* = 7.0 Hz, 6H, CH<sub>3</sub>).

<sup>13</sup>C NMR (CDCl<sub>3</sub>, 125 MHz):  $\delta$  167.7 (CO), 141.85, 141.8, 141.5, 141.4, 141.5, 135.5 (CH), 133.7, 131.5 (CH), 130.0 (CH), 129.8 (CH), 129.70 (CH), 129.67 (CH), 129.59 (CH), 128.2 (CH), 117.8, 1176, 116.1, 51.8 (OCH<sub>3</sub>), 37.58 (CH<sub>2</sub>), 37.52 (CH<sub>2</sub>), 34.32 (CH<sub>2</sub>), 34.24 (CH<sub>2</sub>), 32.06 (CH<sub>2</sub>), 32.04 (CH<sub>2</sub>), 30.58 (CH<sub>2</sub>), 30.54 (CH<sub>2</sub>), 29.82 (CH<sub>2</sub>), 29.80 (CH<sub>2</sub>), 29.78 (CH<sub>2</sub>), 29.76 (CH<sub>2</sub>), 29.75 (CH<sub>2</sub>), 29.74 (CH<sub>2</sub>), 29.71 (CH<sub>2</sub>), 29.49 (CH<sub>2</sub>), 29.47 (CH<sub>2</sub>), 22.83 (CH<sub>2</sub>), 22.82 (CH<sub>2</sub>), 14.26 (CH<sub>3</sub>), 14.25 (CH<sub>3</sub>).

Anal. calcd for NiC<sub>64</sub>H<sub>90</sub>N<sub>4</sub>O<sub>2</sub>: C, 76.40; H, 9.02; N, 5.57; obsd C, 76.11; H, 8.99; N, 5.62

**M10**Chemical formula: NiC<sub>63</sub>H<sub>86</sub>N<sub>4</sub>O

Exact mass: 972.62

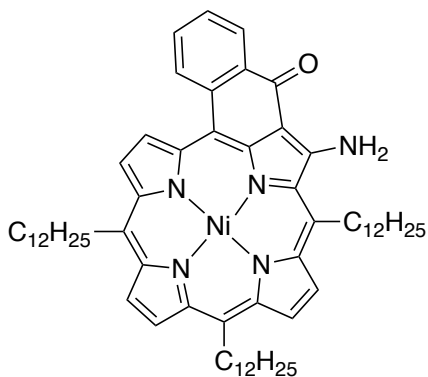
Molecular weight: 974.10

A suspension of **M9** (98 mg, 0.097 mmol) and lithium hydroxide (500 mg, excess) in a dioxane:water (8:2) solution was refluxed for 16 h. On cooling, dichloromethane (50 mL) was added and the organic phase was extracted (3 x dichloromethane), washed (3 x water) and dried over sodium sulphate. The solvent was then evaporated and the porphyrin was redissolved in benzene and heated at 50 °C under argon with oxalyl chloride (1 mL, excess). A Dean-Stark was used to remove excess oxalyl chloride. On cooling, tin(IV) chloride (0.5 mL, excess) was added and the solution turned instantly green. After half an hour of stirring at r.t., the solution was poured on to ice cold concentrated NaOH (50 mL). The organic phase was extracted (3 x dichloromethane), washed (3 x water) and dried over sodium sulphate. The solvent was evaporated and the titled product was purified *via* column chromatography (SiO<sub>2</sub>; 1:1 dichloromethane:cyclohexane) to afford the titled product (76 mg, 0.078 mmol, 80%).

<sup>1</sup>H NMR (400 MHz, CDCl<sub>3</sub>) δ 9.41 (s, 1H, H<sub>pyrr</sub>), 8.98 (d, *J* = 5.1 Hz, 1H, H<sub>pyrr</sub>), 8.94 (d, *J* = 5.1 Hz, 1H, H<sub>pyrr</sub>), 8.88 (d, *J* = 5.1 Hz, 1H, H<sub>pyrr</sub>), 8.87 – 8.83 (m, 2H, H<sub>pyrr</sub> and H<sub>CycPh</sub>), 8.81 (d, *J* = 5.1 Hz, 1H, H<sub>pyrr</sub>), 8.39 (dd, *J* = 7.5, 1.5 Hz, 1H, H<sub>CycPh</sub>), 7.64 (d, *J* = 5.1 Hz, 1H, H<sub>Pyrr</sub>), 7.58 (ddd, *J* = 7.5, 1.5, 1.5 Hz, 1H, H<sub>CycPh</sub>), 7.43 – 7.34 (m, 1H, H<sub>CycPh</sub>), 4.15 (m, 4H, CH<sub>2</sub>), 4.10 (m, 2H, CH<sub>2</sub>) 4.29 – 4.03 (m, 6H, CH<sub>2</sub>), 2.23 – 1.88 (m, 6H, CH<sub>2</sub>), 1.43 – 1.34 (m, 2H, CH<sub>2</sub>), 1.31 – 1.14 (m, 46H), 0.87 (m, 9H, CH<sub>3</sub>).

<sup>13</sup>C NMR (125 MHz, CDCl<sub>3</sub>) δ 182.4 (CO), 144.3, 143.5, 142.8, 142.0, 142.0, 140.6, 140.0, 138.5, 138.0, 135.2, 134.7 (CH), 133.3, 132.6 (CH), 132.4 (CH), 131.6 (CH), 131.3 (CH), 130.9 (CH), 130.2 (CH), 129.7 (CH), 129.0 (CH), 128.9 (CH), 126.9 (CH), 125.5, 121.2, 117.5, 106.8, 37.6 (CH<sub>2</sub>), 37.2 (CH<sub>2</sub>), 37.1 (CH<sub>2</sub>), 33.8 (CH<sub>2</sub>), 33.7 (CH<sub>2</sub>), 33.5 (CH<sub>2</sub>), 31.9 (CH<sub>2</sub>), 30.4, 30.4 (CH<sub>2</sub>), 30.3 (CH<sub>2</sub>), 29.7 (CH<sub>2</sub>), 29.7 (CH<sub>2</sub>), 29.6 (CH<sub>2</sub>), 29.6 (CH<sub>2</sub>), 29.5 (CH<sub>2</sub>), 29.4 (CH<sub>2</sub>), 22.7 (CH<sub>2</sub>), 14.2 (CH<sub>3</sub>).

MS MALDI: calcd for NiC<sub>63</sub>H<sub>86</sub>N<sub>4</sub>O (M + H<sup>+</sup>) 973.632 obsd 973.675

**M11**Chemical formula:  $\text{NiC}_{63}\text{H}_{87}\text{N}_5\text{O}$ 

Exact mass: 987.63

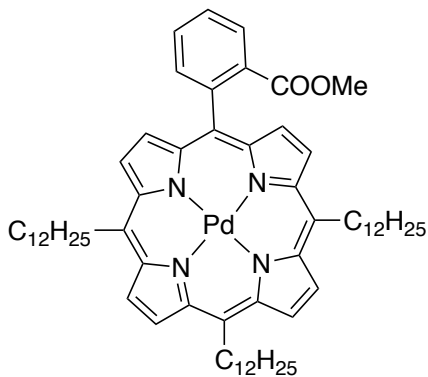
Molecular weight: 989.12

The same procedure as **M4** was used to afford the titled product in 81% yield.

<sup>1</sup>H NMR (500 MHz,  $\text{CDCl}_3$ )  $\delta$  9.08 (d,  $J$  = 5.1 Hz, 1H, H<sub>pyrr</sub>), 9.05 (d,  $J$  = 5.1 Hz, 1H, H<sub>pyrr</sub>), 9.01 (d,  $J$  = 4.9 Hz, 1H, H<sub>pyrr</sub>), 8.96 (d,  $J$  = 4.9 Hz, 1H, H<sub>pyrr</sub>), 8.90 (2d, 2H, H<sub>pyrr</sub>) 8.57 (dd,  $J$  = 7.8, 1.5 Hz, 1H, H<sub>CycPh</sub>), 7.97 (d,  $J$  = 7.8 Hz, 1H, H<sub>CycPh</sub>), 7.93 (s, br, 2H, NH<sub>2</sub>), 7.73 – 7.67 (m, 1H, H<sub>CycPh</sub>), 7.54 – 7.47 (m, 1H, H<sub>CycPh</sub>), 4.28 (t,  $J$  = 8.1 Hz, 2H, CH<sub>2</sub>), 4.22 (t,  $J$  = 8.1 Hz, 2H, CH<sub>2</sub>), 4.10 (t,  $J$  = 8.3 Hz, 2H, CH<sub>2</sub>), 2.17 (dq,  $J$  = 15.2, 7.7 Hz, 4H, CH<sub>2</sub>), 2.07 (t, 2H, CH<sub>2</sub>), 1.41 (s, 6H, CH<sub>2</sub>), 1.33 – 1.22 (m, 48H, CH<sub>2</sub>), 0.96 – 0.76 (m, 9H, CH<sub>3</sub>).

<sup>13</sup>C NMR (125 MHz,  $\text{CDCl}_3$ )  $\delta$  181.3 (CO), 160.2, 143.4, 142.9, 141.2, 140.2, 140.2, 140.1, 139.5, 138.9, 134.4 (CH), 133.3, 132.5 (CH), 131.8 (CH), 131.6 (CH), 129.9 (CH), 129.1, 128.7 (CH), 128.2 (CH), 127.5 (CH), 127.2 (CH), 125.9 (CH), 123.4, 120.7, 118.5, 113.0, 101.7, 36.9 (CH<sub>2</sub>), 36.7 (CH<sub>2</sub>), 33.7 (CH<sub>2</sub>), 33.5 (CH<sub>2</sub>), 33.2 (CH<sub>2</sub>), 31.9 (CH<sub>2</sub>), 30.3 (CH<sub>2</sub>), 29.6 (CH<sub>2</sub>), 29.6 (CH<sub>2</sub>), 29.5 (CH<sub>2</sub>), 29.5 (CH<sub>2</sub>), 29.3 (CH<sub>2</sub>), 22.7 (CH<sub>2</sub>), 14.1 (CH<sub>3</sub>).

MS MALDI: calcd for :  $\text{NiC}_{63}\text{H}_{87}\text{N}_5\text{O}$  ( $\text{M} + \text{H}^+$ ) 988.64 obsd 988.577

**M12**Chemical formula:  $\text{PdC}_{64}\text{H}_{90}\text{N}_4\text{O}_2$ 

Exact mass: 1052.61

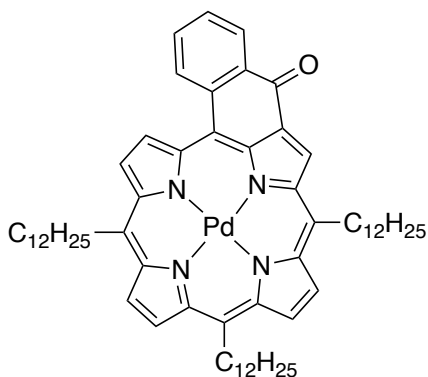
Molecular weight: 1053.87

A solution of free base **M8** (102 mg, 0.107 mmol) and  $\text{Pd}(\text{PhCN})_2\text{Cl}_2$  (49 mg, 0.127 mmol) in toluene (40 mL) was refluxed for 20 h. After cooling, the solution was passed through a short pad of alumina and the toluene evaporated. After recrystallization from dichloromethane and methanol, an orange solid was isolated (103 mg, 0.98 mmol, 91%).

$^1\text{H}$  NMR ( $\text{CDCl}_3$ , 500 MHz):  $\delta$  9.47 (d,  $J = 5.0$  Hz, 2H,  $\text{H}_{\text{pyrr}}$ ), 9.45 (d,  $J = 5.0$  Hz, 2H,  $\text{H}_{\text{pyrr}}$ ), 9.32 (d,  $J = 5.0$  Hz, 2H,  $\text{H}_{\text{pyrr}}$ ), 8.60 (d,  $J = 5.0$  Hz, 2H,  $\text{H}_{\text{pyrr}}$ ) 8.36 (dd,  $J = 7.5$  and 1.5 Hz, 1 H,  $\text{H}_{\text{Ar}}$ ), 8.13 (dd,  $J = 7$  and 1.5 Hz, 1H,  $\text{H}_{\text{Ar}}$ ), 7.86 (ddd,  $J = 7.5$ , 7 and 1.5 Hz, 1H,  $\text{H}_{\text{Ar}}$ ), 7.81 (ddd,  $J = 7.5$ , 7 and 1.5 Hz, 1H,  $\text{H}_{\text{Ar}}$ ), 4.86 (m, 6H,  $\text{CH}_2$ ), 2.60 (s, 3H,  $\text{OCH}_3$ ), 2.51 (m, 6H,  $\text{CH}_2$ ), 1.80 (m, 6H,  $\text{CH}_2$ ), 1.54 (m, 6H,  $\text{CH}_2$ ), 1.40-1.23 (m, 42H,  $\text{CH}_2$ ), 0.89 (t,  $J = 7.0$  Hz, 3H,  $\text{CH}_3$ ), 0.88 (t,  $J = 7.0$  Hz, 6H,  $\text{CH}_3$ ).

$^{13}\text{C}$  NMR ( $\text{CDCl}_3$ , 125 MHz):  $\delta$  168.1 (CO), 142.5, 141.12, 141.06, 140.59, 140.58, 135.7 (CH), 134.3, 130.2 (CH), 129.9 (CH), 129.7 (CH), 128.34 (CH), 128.30 (CH), 128.14 (CH), 128.09 (CH), 120.86, 120.66, 119.0, 51.55 ( $\text{OCH}_3$ ), 38.54 ( $\text{CH}_2$ ), 38.46 ( $\text{CH}_2$ ), 35.58 ( $\text{CH}_2$ ), 35.47 ( $\text{CH}_2$ ), 32.10 ( $\text{CH}_2$ ), 32.08 ( $\text{CH}_2$ ), 29.90 ( $\text{CH}_2$ ), 29.88 ( $\text{CH}_2$ ), 29.87 ( $\text{CH}_2$ ), 29.85 ( $\text{CH}_2$ ), 29.82 ( $\text{CH}_2$ ), 29.80 ( $\text{CH}_2$ ), 29.53 ( $\text{CH}_2$ ), 29.51 ( $\text{CH}_2$ ), 22.86 ( $\text{CH}_2$ ), 22.85 ( $\text{CH}_2$ ), 14.29 ( $\text{CH}_3$ ), 14.28 ( $\text{CH}_3$ ).

MS HR-ESI: calcd for  $\text{PdC}_{64}\text{H}_{90}\text{N}_4\text{O}_2(\text{M}^+)$ : 1052.6093; obsd 1052.6097

**M12**Chemical formula:  $\text{PdC}_{63}\text{H}_{86}\text{N}_4\text{O}$ 

Exact mass: 1020.58

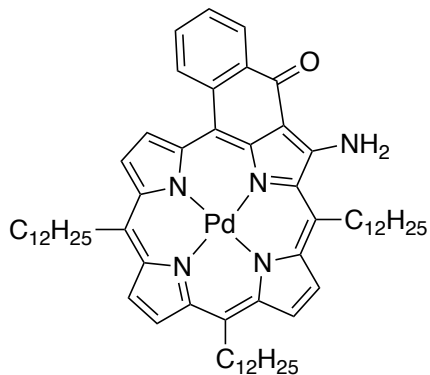
Molecular weight: 1021.83

A procedure analogous to that of **M10** was used to synthesise **M12**, replacing **M9** with **M11** (108 mg, 0.104 mmol), to afford the titled product (75 mg, 0.073 mmol 71%).

$^1\text{H}$  NMR (500 MHz,  $\text{CDCl}_3$ )  $\delta$  9.01 (s, 1H,  $\text{H}_{\text{pyrr}}$ ), 8.78 (d,  $J$  = 5.0 Hz, 1H,  $\text{H}_{\text{pyrr}}$ ), 8.71 (d,  $J$  = 5.0 Hz, 1H,  $\text{H}_{\text{pyrr}}$ ), 8.64 (d,  $J$  = 5.0 Hz, 1H,  $\text{H}_{\text{pyrr}}$ ), 8.61 (d,  $J$  = 5.0 Hz, 1H,  $\text{H}_{\text{pyrr}}$ ), 8.57 - 8.54 (m, 2H,  $\text{H}_{\text{CyclPh}}$  and  $\text{H}_{\text{pyrr}}$ ), 8.39 (dd,  $J$  = 7.6, 1.5 Hz, 1H,  $\text{H}_{\text{CyclPh}}$ ) 7.59 (d,  $J$  = 5.0 Hz, 1H,  $\text{H}_{\text{pyrr}}$ ), 7.56 (dd,  $J$  = 7.6, 1.5 Hz, 1H,  $\text{H}_{\text{CyclPh}}$ ), 7.40 (ddd,  $J$  = 6.9, 1.5, 1.5 Hz, 1H,  $\text{H}_{\text{CycPh}}$ ), 4.14 (t,  $J$  = 8.3 Hz, 2H,  $\text{CH}_2$ ), 4.02 (t,  $J$  = 8.3 Hz, 2H,  $\text{CH}_2$ ), 3.92 (t,  $J$  = 8.3 Hz, 2H,  $\text{CH}_2$ ), 2.23 (q,  $J$  = 7.8 Hz, 2H,  $\text{CH}_2$ ), 2.15 (q,  $J$  = 6.8 Hz, 2H,  $\text{CH}_2$ ), 2.01 (q,  $J$  = 7.7 Hz, 2H,  $\text{CH}_2$ ), 1.77 - 1.51 (m, 6H,  $\text{CH}_2$ ), 1.37 - 1.22 (m, 48H), 0.89 (2t,  $J$  = 6.8 Hz, 9H).

$^{13}\text{C}$  NMR (125 MHz,  $\text{CDCl}_3$ )  $\delta$  182.6 (CO), 142.7, 141.6, 141.5, 141.3, 140.6, 140.3, 139.0, 137.6, 136.1, 136.0 (CH), 133.4, 132.4, 132.3 (CH), 130.0 (CH), 129.1 (CH), 129.0 (CH), 128.8 (CH), 128.4 (CH), 128.1 (CH), 128.0 (CH), 127.3 (CH), 126.8, 126.6 (CH), 123.0, 119.8, 109.3, 38.4 (CH<sub>2</sub>), 37.9 (CH<sub>2</sub>), 37.9 (CH<sub>2</sub>), 34.8 (CH<sub>2</sub>), 34.6 (CH<sub>2</sub>), 34.6 (CH<sub>2</sub>), 32.0 (CH<sub>2</sub>), 32.0 (CH<sub>2</sub>), 30.6 (CH<sub>2</sub>), 30.6 (CH<sub>2</sub>), 30.5 (CH<sub>2</sub>), 29.8 (CH<sub>2</sub>), 29.8 (CH<sub>2</sub>), 29.7 (CH<sub>2</sub>), 29.7 (CH<sub>2</sub>), 29.7 (CH<sub>2</sub>), 29.7 (CH<sub>2</sub>), 29.6 (CH<sub>2</sub>), 29.4 (CH<sub>2</sub>), 29.4 (CH<sub>2</sub>), 26.9 (CH<sub>2</sub>), 22.7 (CH<sub>2</sub>), 22.7 (CH<sub>2</sub>), 14.2 (CH<sub>3</sub>), 14.2 (CH<sub>3</sub>).

MS MALDI: calcd for  $\text{PdC}_{63}\text{H}_{86}\text{N}_4\text{O}$  ( $\text{M} + \text{H}^+$ ) 1021.59 obsd 1021.692

**M13**Chemical formula:  $\text{PdC}_{63}\text{H}_{87}\text{N}_5\text{O}$ 

Exact mass: 1035.59

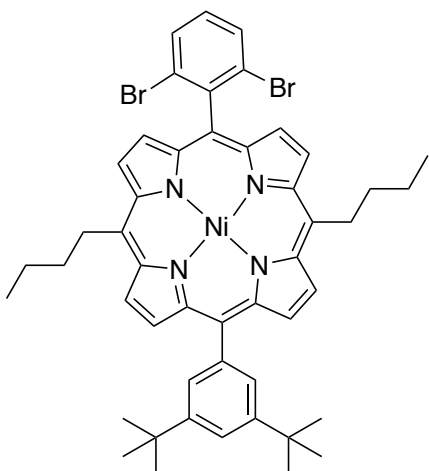
Molecular weight: 1036.84

The same procedure as **M4** was used to afford the titled product, replacing **M10** with **M12** (70 mg, 0.069 mmol) in 60% yield (41 mg, 0.04 mmol, 58%).

<sup>1</sup>H NMR (400 MHz,  $\text{CDCl}_3$ )  $\delta$  9.05 (s, br, 1H  $\text{H}_{\text{pyrr}}$ ), 8.97 (s, br, 1H,  $\text{H}_{\text{pyrr}}$ ), 8.89 (s, br, 3H,  $\text{H}_{\text{pyrr}}$ ), 8.70 (s, 1H,  $\text{H}_{\text{pyrr}}$ ), 8.58 (s, br, 1H,  $\text{H}_{\text{Ar}}$ ), 8.03 (s, br, 1H,  $\text{H}_{\text{Ar}}$ ), 7.67 (s, br, 1H,  $\text{H}_{\text{Ar}}$ ), 7.51 (s, br 1H,  $\text{H}_{\text{Ar}}$ ), 4.43 (s, 2H,  $\text{CH}_2$ ), 4.31 (s, 2H,  $\text{CH}_2$ ), 3.74 (s, 2H,  $\text{CH}_2$ ), 2.34 (s, 4H,  $\text{CH}_2$ ), 1.71 (s, 4H,  $\text{CH}_2$ ), 1.37 – 1.21 (m, 52H,  $\text{CH}_2$ ), 0.89 (t, 9H,  $\text{CH}_3$ ).

<sup>13</sup>C NMR (125 MHz,  $\text{CDCl}_3$ )  $\delta$  181.3 (CO), 157.8, 141.2, 140.8, 140.0, 139.9, 138.9, 138.7, 138.2, 135.6 (CH), 133.1 (CH), 130.9 (CH), 129.4 (CH), 127.6 (CH), 127.1 (CH), 126.8 (CH), 126.6 (CH), 125.4 (CH), 124.9 (CH), 121.3, 120.6, 103.9, 38.1 (CH<sub>2</sub>), 37.9 (CH<sub>2</sub>), 32.0 (CH<sub>2</sub>), 32.0 (CH<sub>2</sub>), 30.7 (CH<sub>2</sub>), 30.4 (CH<sub>2</sub>), 29.8 (CH<sub>2</sub>), 29.8 (CH<sub>2</sub>), 29.8 (CH<sub>2</sub>), 29.7 (CH<sub>2</sub>), 29.7 (CH<sub>2</sub>), 29.7 (CH<sub>2</sub>), 29.7 (CH<sub>2</sub>), 29.4 (CH<sub>2</sub>), 29.4 (CH<sub>2</sub>), 22.8 (CH<sub>2</sub>), 22.7 (CH<sub>2</sub>), 14.2 (CH<sub>3</sub>), 14.2 (CH<sub>3</sub>).

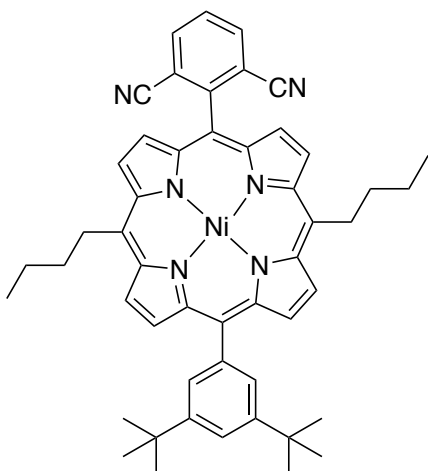
MS MALDI: calcd for  $\text{PdC}_{63}\text{H}_{87}\text{N}_5\text{O}$  ( $\text{M}^{+}$ ) 1035.59 obsd 1035.630

**M14**Chemical formula:  $\text{NiC}_{48}\text{H}_{50}\text{N}_4\text{Br}_2$ 

Exact mass: 898.18

Molecular weight: 901.46

The dipyrromethane (1.24 g, 6.14 mmol), 2,6-dibromobenzaldehyde (810 mg, 3.07 mmol) and 3,5-*ditert*-butylbenzaldehyde (670 mg, 3.07 mmol) were degassed in dichloromethane (900 mL) for 30 mins. TFA (10 mmol/L) was added and the solution was stirred under argon and shielded from light for 3 h. The yellow solution turned red over this time. DDQ (1.5 g 6.75 mmol) was added and the solution was stirred for 45 mins. The solution was filtered through a pad of alumina. The solvent was filtered and the mixture of porphyrins were metallated with  $\text{Ni}(\text{acac})_2$  in toluene (150 mL) at reflux for 16 h. The products could not be separated by column chromatography.

**M15**Chemical formula:  $\text{NiC}_{50}\text{H}_{50}\text{N}_6$ 

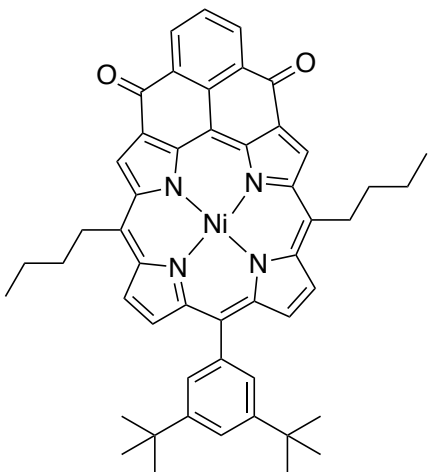
Exact mass: 793.35

Molecular weight: 793.69

The porphyrin mixture (473 mg) and CuCN (excess) was dissolved in NMP (2 mL). The resulting red solution was placed in a microwave (200 °C, 200 mW) for 5 h. The colour changed from red to blue. On cooling, the resulting solution was diluted in dichloromethane (50 mL) and the organic phase was washed with water (5 x 70 mL). The organic phase was dried over  $\text{Na}_2\text{SO}_4$  and the solvent was evaporated. Column chromatography ( $\text{SiO}_2$ ; 2:1 to 1:1 dichloromethane:cyclohexane) afforded the titled product.

$^1\text{H}$  NMR (500 MHz,  $\text{CDCl}_3$ )  $\delta$  9.34 (d,  $J = 5.0$  Hz, 2H,  $\text{H}_{\text{pyrr}}$ ), 9.28 (d,  $J = 5.0$  Hz, 2H,  $\text{H}_{\text{pyrr}}$ ), 8.83 (d,  $J = 5.0$  Hz, 2H,  $\text{H}_{\text{pyrr}}$ ), 8.37 (d,  $J = 5.0$  Hz, 2H,  $\text{H}_{\text{pyrr}}$ ), 8.18 (d,  $J = 8.0$  Hz, 2H,  $\text{H}_{\text{Ph}}$ ), 7.90 (t,  $J = 8.0$  Hz, 1H,  $\text{H}_{\text{Ph}}$ ), 7.86 (d,  $J = 1.8$  Hz, 2H,  $\text{H}_{\text{Ar}}$ ), 7.74 (t,  $J = 1.8$  Hz, 1H,  $\text{H}_{\text{Ar}}$ ), 4.65 – 4.39 (m, 4H,  $\text{CH}_2$ ), 2.44 – 2.22 (m, 4H,  $\text{CH}_2$ ), 1.63 (q, 4H,  $\text{CH}_2$ ), 1.50 (s, 18H,  $\text{H}_{\text{Ar}}$ ), 1.05 (t,  $J = 7.4$  Hz, 6H,  $\text{CH}_3$ ).

$^{13}\text{C}$  NMR (125 MHz,  $\text{CDCl}_3$ )  $\delta$  149.0, 148.3, 143.1, 142.4, 141.9, 140.2, 139.6, 135.1 (CH), 133.4 (CH), 131.1 (CH), 129.7 (CH), 129.6 (CH), 129.4 (CH), 128.7 (CH), 128.3, 121.2 (CH), 120.8, 119.0, 118.8, 116.2, 107.1, 39.6 ( $\text{CH}_2$ ), 35.0, 34.0 ( $\text{CH}_2$ ), 31.7 ( $\text{CH}_3$ ), 26.9 ( $\text{CH}_2$ ), 23.5 ( $\text{CH}_2$ ), 14.0 ( $\text{CH}_3$ ).

**M16**Chemical formula:  $\text{NiC}_{50}\text{H}_{48}\text{N}_4\text{O}_2$ 

Exact mass: 794.31

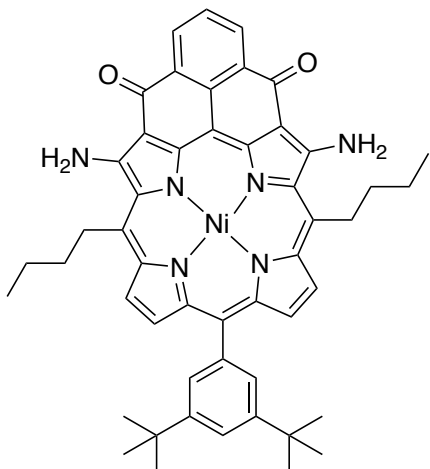
Molecular weight: 795.65

A TFA/H<sub>2</sub>SO<sub>4</sub> (1:1) solution (20 mL) was added to **M15** (34 mg, 0.04 mmol) turning the red solid to a blue solution. Acetic acid (30 mL) was then added and the TFA and acetic acid were evaporated using a rotary evaporator. An acetic acid:water (16:4) solution (20 mL) was then added and the solution was refluxed for 24 h. Dichloromethane (30 mL) was then added and the organic phase was extracted (3 x dichloromethane (30 mL) and washed with NaHCO<sub>3</sub> solution (5 x 30 mL). The colour changed from green to violet/brown. The organic phase was dried over Na<sub>2</sub>SO<sub>4</sub> and the solvent was evaporated. The solid was then dissolved in dry toluene (15 mL) and heated at 50 °C under argon with oxalyl chloride (0.5 mL, excess). A Dean-Stark was used to remove excess oxalyl chloride. On cooling, tin(IV) chloride (0.1 mL, excess) was added and the solution turned instantly green. After half an hour of stirring at rt, the solution was poured onto ice cold concentrated NaOH (50 mL). The organic phase was extracted (3 x dichloromethane), washed (3 x water) and dried over sodium sulphate. The solvent was evaporated and the titled product was purified *via* column chromatography (SiO<sub>2</sub>; dichloromethane) to afford the titled product (5 mg, 0.00628 mmol, 16%).

<sup>1</sup>H NMR (500 MHz, CDCl<sub>3</sub>) δ 8.76 (s, 2H, H<sub>pyrr</sub>), 8.65 (d, *J* = 5.0 Hz, 2H, H<sub>pyrr</sub>), 8.31 (d, *J* = 5.0 Hz, 2H, H<sub>pyrr</sub>), 7.94 (d, *J* = 7.4 Hz, 2H, H<sub>Cyclph</sub>) 7.82 (s, 2H, H<sub>Ar</sub>), 7.76 (t, *J* = 1.8 Hz, 1H, H<sub>Ar</sub>), 7.11 (t, *J* = 7.4 Hz, 1H, H<sub>Cyclph</sub>), 3.77 (t, *J* = 8.4 Hz, 4H, CH<sub>2</sub>), 2.12 – 1.89 (m, 4H, CH<sub>2</sub>), 1.60 (q, *J* = 7.4 Hz, 4H, CH<sub>2</sub>), 1.55 (s, 18H, H<sub>tBu</sub>), 1.02 (t, *J* = 7.4 Hz, 6H, CH<sub>3</sub>).

<sup>13</sup>C NMR (126 MHz, CDCl<sub>3</sub>) δ 180.4 (CO), 149.4, 146.1, 145.7, 141.6, 139.2, 139.1, 133.5 (CH), 132.1, 132.0 (CH), 131.0, 130.0 (CH), 129.6 (CH), 128.4 (CH), 127.0 (CH), 125.7, 121.7 (CH) 53.4, 40.1 (CH<sub>2</sub>), 35.1, 34.1 (CH<sub>2</sub>), 31.8 (CH<sub>3</sub>), 23.7 (CH<sub>2</sub>), 14.0 (CH<sub>3</sub>).

MS ESI NiC<sub>50</sub>H<sub>48</sub>N<sub>4</sub>O<sub>2</sub> (M + H<sup>+</sup>) calcd: 795.3203 obsd 795.3186

**M17**Chemical formula:  $\text{NiC}_{50}\text{H}_{50}\text{N}_6$ 

Exact mass: 824.33

Molecular weight: 825.68

The porphyrin (5mg, 6.28  $\mu\text{mol}$ ) and 4-amino-4H-1,2,4-triazole (26 mg, 0.31 mmol) were refluxed in a toluene/ethanol solution (8:2) in basic conditions (NaOH, 15mg, 0.38 mmol) for 2 h and then under acidic conditions (TFA, 0.1 mL) for 1 h. Water (20 mL) was then added and the organic phase was washed with water and dried over sodium sulphate. The solvent was evaporated and the porphyrin was purified by column chromatography ( $\text{SiO}_2$ ; dichloromethane:cyclohexane 1:1) to afford the titled product (2 mg, 2.42  $\mu\text{mol}$ , 39%).

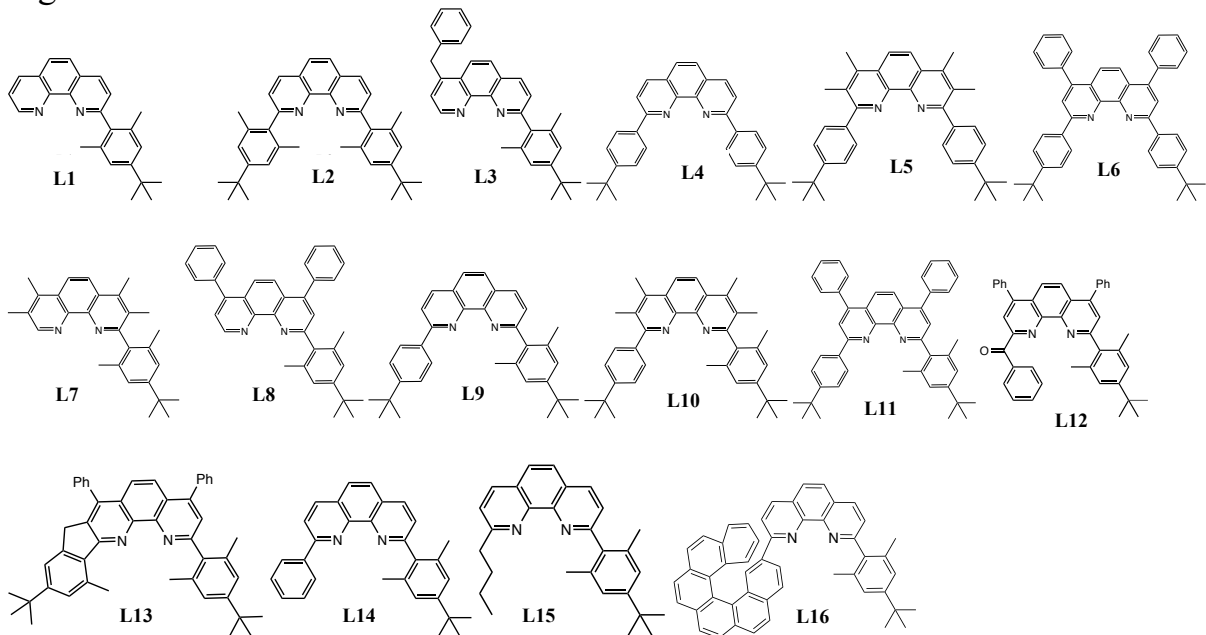
$^1\text{H}$  NMR (500 MHz,  $\text{CDCl}_3$ )  $\delta$  8.30 (m, 5H,  $\text{H}_{\text{pyrr}}$  and  $\text{H}_{\text{Ar}}$ ), 8.18 (d,  $J = 4.7$  Hz, 2H,  $\text{H}_{\text{Ph}}$ ), 7.69 (t,  $J = 1.7$  Hz, 2H,  $\text{H}_{\text{Ar}}$ ), 7.42 (t,  $J = 7.0$  Hz, 1H,  $\text{H}_{\text{Ph}}$ ), 2.93 (s, 4H,  $\text{CH}_2$ ), 1.98 (s, 4H,  $\text{CH}_2$ ), 1.72-1.64 (m, 2H,  $\text{CH}_2$ ), 1.49 (s, 18H,  $\text{H}_{\text{tBu}}$ ), 1.09 (t, 6H,  $\text{CH}_3$ ).

$^{13}\text{C}$  NMR (125 MHz,  $\text{CDCl}_3$ )  $\delta$  179.8 (CO), 158.4, 149.3, 145.7, 142.1, 140.3, 139.2, 131.4 (CH), 130.8, 130.5, 130.3 (CH), 127.8 (CH), 127.2, 125.6 (CH), 125.1 (CH), 121.5 (CH), 121.4, 109.9, 35.1 (CH<sub>2</sub>), 34.5 (CH<sub>2</sub>), 31.7 (CH<sub>3</sub>), 31.1 (CH<sub>2</sub>), 29.7 (CH<sub>2</sub>), 23.7 (CH<sub>2</sub>), 13.9 (CH<sub>3</sub>).

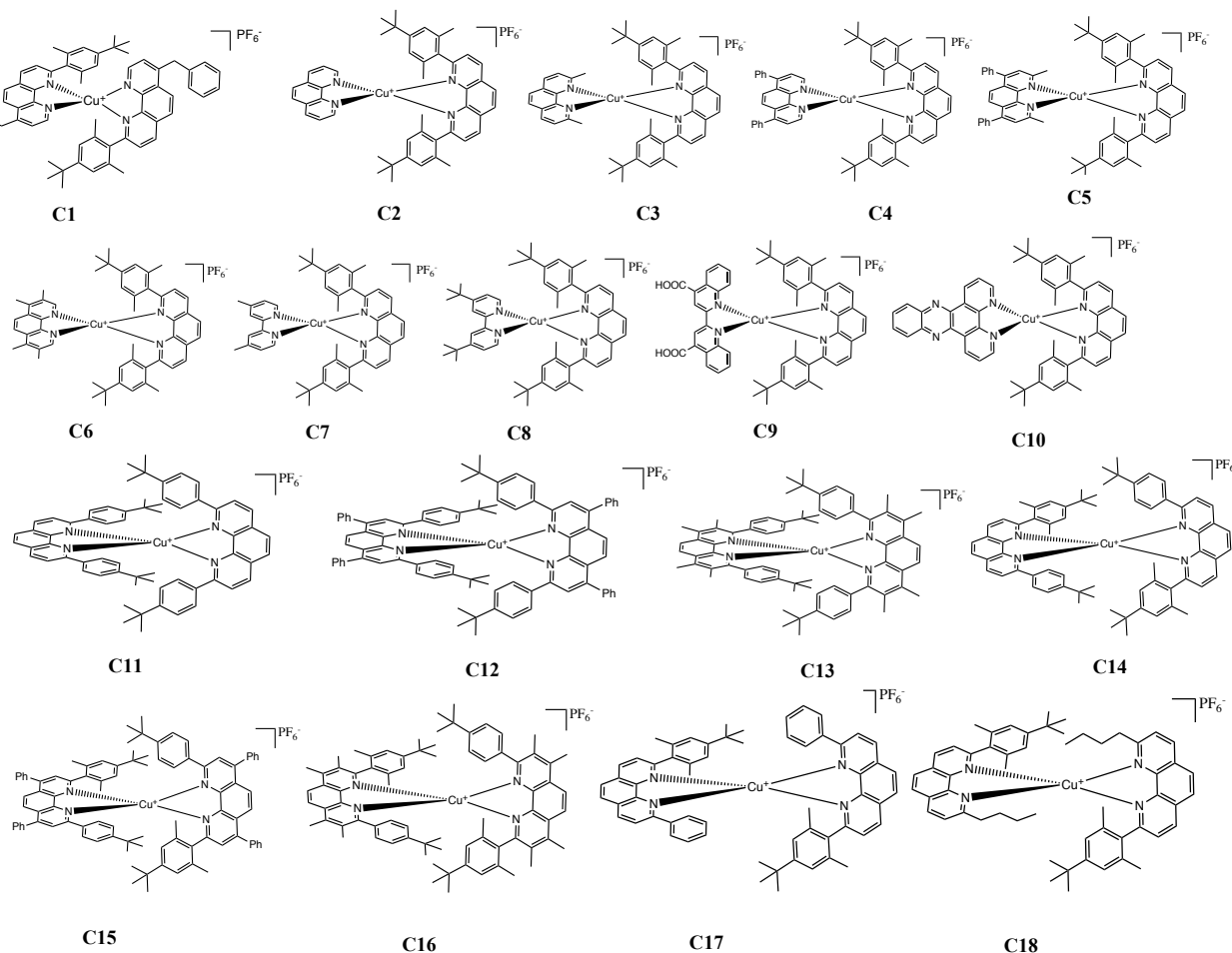
MS ESI  $\text{NiC}_{50}\text{H}_{51}\text{N}_6\text{O}_2$  ( $\text{M} + \text{H}^+$ ) calcd: 825.3421 obsd 825.3403

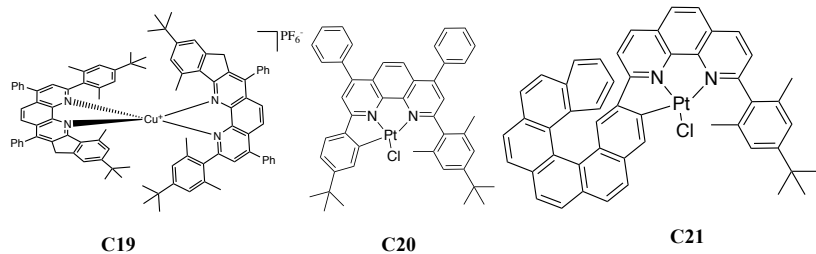
## List of molecules

Ligands:

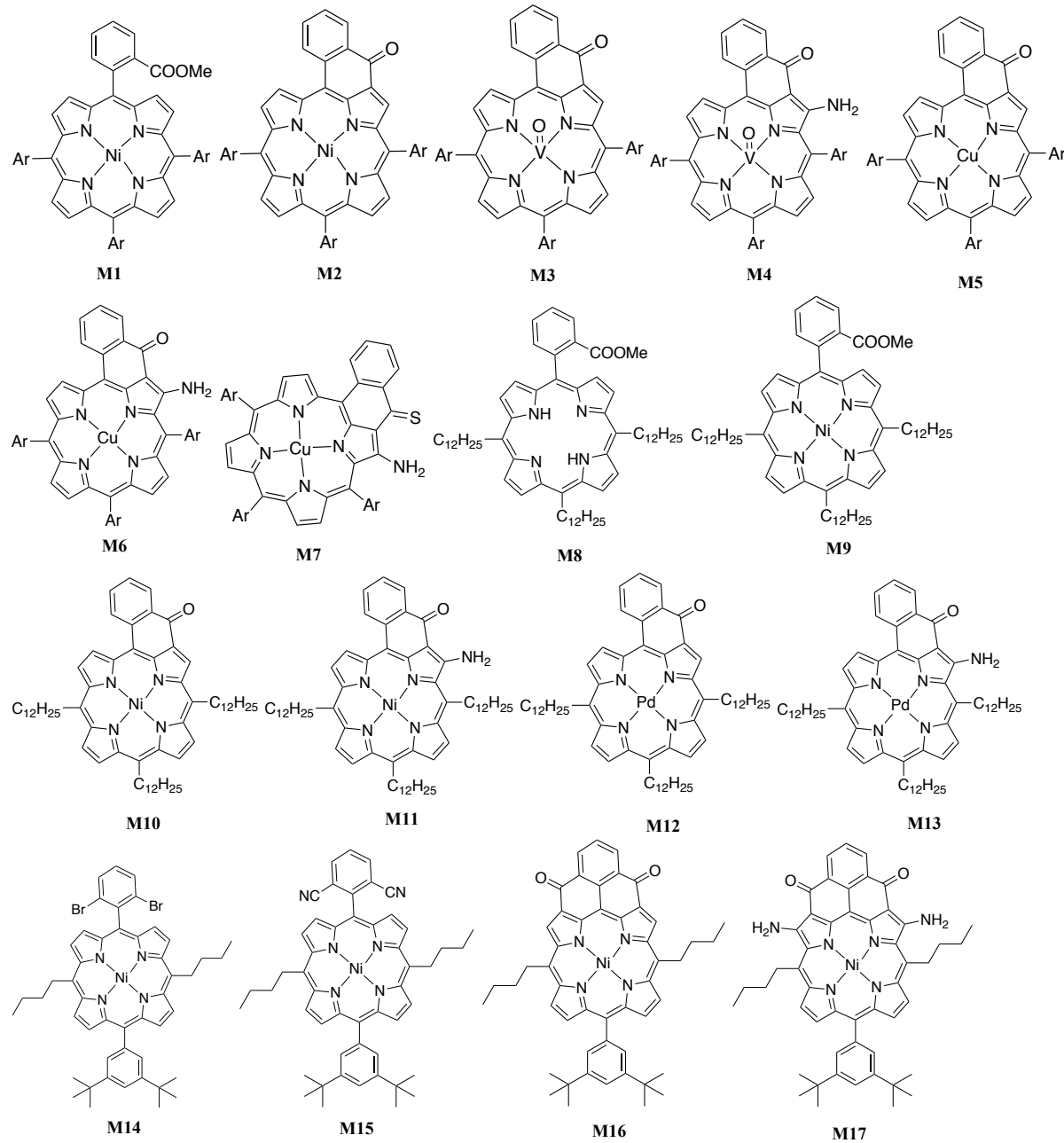


Complexes:

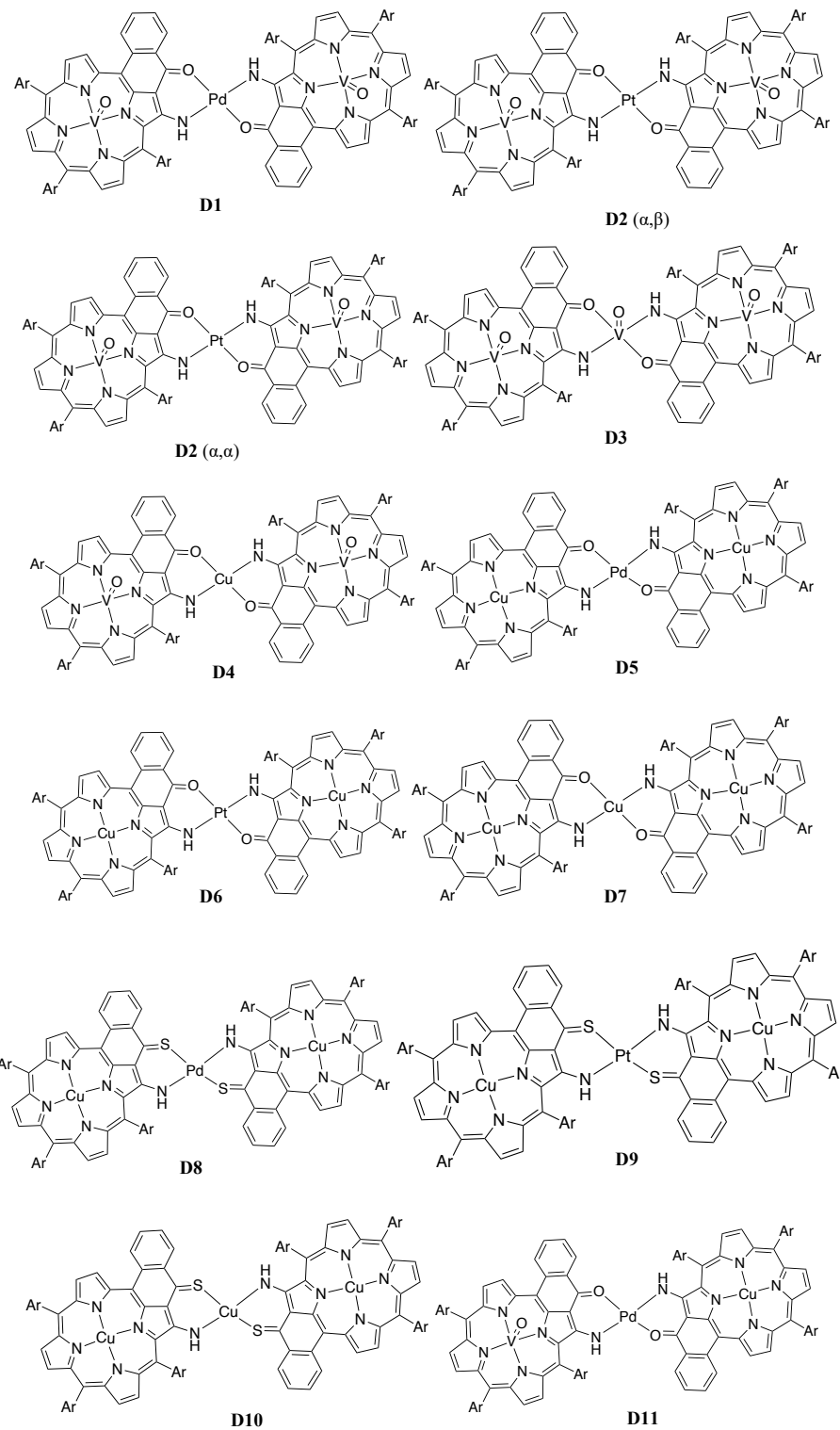




### Porphyrin monomers:



Porphyrin dimers:



# Interactions électroniques et magnétiques dans des dimères de porphyrines et nouveaux complexes de cuivre(I) luminescents

## Résumé

La synthèse de dimères de porphyrines reliées par des cations métalliques a été effectuée. Les propriétés électroniques et magnétiques de ces dimères ont été comparées à celles des monomères. Des études électrochimiques, de spectroscopie électronique et de résonance paramagnétique électronique (RPE) ont permis de mettre en évidence les facteurs influençant l'ampleur de la communication électronique et/ou magnétique entre les sous-unités. Des études RPE plus poussées, pour démontrer les applications de ces composés dans le domaine des qubits, ont été réalisées. Finalement, des porphyrines monomères et dimères comportant des chaînes alkyles ont été auto-assemblées à l'interface solide/liquide et ont conduit à des structures régulières de très grandes dimensions qui ont été visualisées à l'aide de techniques STM (microscopie à effet tunnel).

Le second projet a concerné la synthèse de phénanthrolines et leur utilisation pour former des complexes stables de cuivre(I). Différentes approches ont été utilisées pour étudier ces photosensibilisateurs : électrochimie, spectroscopie électronique, fluorescence, diffraction des rayons X et calculs DFT.

Mots-clefs : Porphyrines, cuivre(I), phénanthroline, chimie de coordination, RPE, photochimie, électrochimie, études STM, calculs DFT

## Résumé en anglais

The synthesis of porphyrin dimers linked by a metal cation has been carried out. The electronic and magnetic properties of these dimers have been compared with the properties of the porphyrin monomers. Electrochemical studies, electronic spectroscopy and electron paramagnetic resonance (EPR) spectroscopy have shown the influential factors that maximise electronic and/or magnetic communication between the two porphyrin moieties. Further EPR studies with pulsed EPR techniques showed a potential application in the field of qubits. Finally, porphyrin monomers and dimers with alkyl chains self-assembled at a solid/liquid interface formed large motifs that were visualised with STM (Scanning Tunneling Microscopy) techniques.

For the second project, phenanthroline ligands were synthesised and used to form stable copper(I) complexes. A wide variety of techniques were utilised in order to determine the optical properties of these photosensitisers: electrochemistry, electronic spectroscopy, fluorescence, X-ray crystallography and DFT calculations.

Keywords: Porphyrins, copper(I), phenanthroline, coordination chemistry, EPR, photochemistry, electrochemistry, STM studies, DFT calculations